Computational physics of **bacterial chromosome organization** by **condensin**

Christiaan Adrianus
Miermans

München
2020

LMU
LUDWIG-
MAXIMILIANS-
UNIVERSITÄT
MÜNCHEN

Computational physics of bacterial chromosome organization by condensin

Christiaan Adrianus Miermans

A dissertation submitted
to the Faculty of Physics
of the Ludwig-Maximilians-Universität München
for the degree of
DOCTOR RERUM NATURALIUM

Munich, 28 February 2020

First referee: Prof. Dr. Chase Broedersz
Second referee: Prof. Dr. Jan Lipfert
Daf of submission: 28 February 2020
Day of the oral examination: 22 June 2020

Zusammenfassung

Das bakterielle Chromosom ist kein zufällig angeordnetes Polymer, sondern ein komplexes und heterogenes Nichtgleichgewichtssystem. Eine Vielzahl von nukleoid-assoziierten Proteinen (nucleoid-associated proteins - NAPs) verleihen der chromosomalen DNA sowohl durch energetische Interaktionen als auch durch enzymatische Aktivität faszinierende Organisationsmerkmale. Insbesondere bildet das Chromosom anomal große Schleifen aus, verfügt über robust positionierte, lokal verdichtete Kügelchen und zeigt ballistische Bewegung während der Chromosomentrennung. Im Großen und Ganzen untersucht diese Arbeit eine Methode zur Simulation solcher Nichtgleichgewichtspolymere und Möglichkeiten für deren Anwedung zur Aufklärung der Organisation des Chromosoms durch bakterielles Kondensin. Genauer gesagt beschreiben wir zunächst einige der zentralen Fragestellungen zur Organisation des bakteriellen Chromosoms mit Schwerpunkt auf der Wirkung von Kondensin, und welche Arten von empirischen Daten verwendet werden können, um diese offenen Fragen zu klären. Dann entwickeln, implementieren und testen wir im Detail eine kinetische Monte-Carlo-Methode zur Simulation eines Minimalmodells für die chromosomale Organisation durch Kondensin: ein Gitterpolymer mit gleitenden elastischen Ringen, so genannten "Slip-Links", deren Bewegung die Wirkung einzelner Kondensine modelliert. Wir verwenden diesen Simulationsrahmen, um den Einfluss von diffusiven und motorischen Slip-Links zu verstehen und zeigen, dass die molekulare Wirkung dieser Slip-Links die großräumigen organisatorischen Merkmale des Chromosoms beeinflusst. Schließlich präsentieren wir unsere unvollendete Arbeit darüber, wie sich DNA-Schleifen, die von Proteinclustern ausgehen, auf die Ausdehnung des Chromosoms unter Kraft auswirken können. Die folgenden vier Themen bilden die Hauptteile dieser Arbeit:

Part I Chapters 1–5. Hier stellen wir den biologischen Kontext vor, der uns die Fragestellungen, die die theoretische Physik aufzuklären helfen kann, vorgibt, und bestimmt, welche numerischen Methoden wir (nicht) verwenden können. Wir beginnen damit, das bakterielle Chromosom als einfachen Random Walk im thermodynamischen Gleichgewicht zu modellieren, und zeigen, dass dieses Modell auf spektakuläre Weise daran scheitert, empirische Daten des bakteriellen Chromosoms zu berücksichtigen. Wir zeigen, dass andere physikalische Effekte mit einbezogen werden müssen, wie sterische Wechselwirkungen, die Anwesenheit von DNA-bindenden Proteinen und nicht-adiabatische externe Kräfte. Wir führen auch eine Vernetzungstechnik namens Hi-C ein, die einen Fingerabdruck der chromosomalen Organisation erstellt. Dieses Werkzeug liefert uns experimentelle Daten, die für diese Arbeit von Bedeutung sind.

Part II Chapters 6–8.3. Eine detaillierte Untersuchung eines gitterkinetischen lattice kinetic Monte-Carlo (LKMC) Modells, mit besonderem Schwerpunkt auf der Verwendung von durch Slip-Links gebundenen Polymeren für die Simulation in Gleichgewicht und Nichtgleichgewicht. Das durch Slip-Links gebundene Polymer bietet nicht nur ein realistisches Benchmark für unser LKMC-Modell, sondern dient uns auch als toy model in späteren Kapiteln. Unsere Diskussion des LKMC ist in drei Teile gegliedert, die logisch aufeinander aufbauen: (i) Design und Implementierung, (ii) Testen und (iii) Ausloten der Grenzen des LKMC. Im Großen und Ganzen stellen wir fest, dass das LKMC Daten produziert, die mit Brownian Dynamics Simulationen übereinstimmen, dass sich jedoch sehr weit vom Gleichgewicht die Grenzen der Lesitungsfähigkeit des LKMC zeigen. Diese Einschränkungen lassen sich hauptsächlich in zwei Kategorien einteilen: Gittereffekte und Kinetik, die einschränken können, wie weit das System aus Gleichgewicht getrieben werden kann.
Verwandte Publikationen und Beitragende. Diese Arbeit wurde in Zusammenarbeit mit Prof. C.P. Broedersz durchgeführt und in der folgenden Forschungsarbeit veröffentlicht: "*A lattice kinetic Monte-Carlo method for simulating chromosomal dynamics and other (non-)equilibrium bio-assemblies*", Soft Matter **16** (2020).

Part III Chapters 9–12. Wir verwenden das LKMC-Modell, das wir in den vorhergehenden Kapiteln entwickelt haben, um die Organisation des bakteriellen Chromosoms durch Kondensin aufzuklären. Wir konstruieren ein Minimalmodell, wobei wir vom einfachst möglichen Modell ausgehen und Schritt für Schritt Komplexität hinzufügen. Die ersten

Modelle, die wir betrachten, befinden sich im thermodynamischen Gleichgewicht, mit Beschränkung durch ein externes Potential und diffundierende Slip-Links. Wir zeigen, dass diese Modelle die in lebenden Zellen beobachtete großräumige Organisation nicht nachbilden können. Dann fügen wir Nicht-Gleichgewichtsaktivität durch über einen aktiven SMC-Lademechanismus hinzu, ein Modell, das für die molekulare Wirkung des Kondensins vorgeschlagen wurde. Überraschenderweise sehen wir, dass diffusive Slip-Links mit aktiver Ladung eine robuste, nebeneinander liegende Anordnung der Chromosomen erzeugen können, wenn auch nicht unter physiologischen Bedingungen. Die Anzahl der Kondensine, die benötigt werden damit dieser Mechanismus funktioniert, übersteigt die Anzahl an Kondensinen, die in lebenden Zellen zur Verfügung steht, und die Geschwindigkeit der dynamischen Reorganisation ist weitaus langsamer als die in vivo beobachtete. Dann fügen wir motorische Aktivität zu den Slip-Links hinzu, wie sie in vitro für eukaryotisches Kondensin beobachtet wurde. Tatsächlich stimmt die Organisation durch motorische Slip-Links gut mit den empirischen Daten überein, sowohl in Bezug auf die erforderliche Anzahl von Kondensinen als auch auf die Geschwindigkeit der Reorganisation. Insgesamt legt unsere Forschung nahe, dass die bakteriellen Kondensine motorische Aktivität benötigen, um das Chromosom so effizient und schnell zu organisieren, wie es in den in vivo-Daten beobachtet wird.

Verwandte Publikationen und Beitragende. Diese Arbeit wurde in Zusammenarbeit mit Prof. C.P. Broedersz durchgeführt und in der folgenden Forschungsarbeit veröffentlicht: "*Bacterial chromosome organization by collective dynamics of SMC condensins*", *J. R. Soc. Interface* **15** (2018).

Part IV Chapter 13. Wir präsentieren unveröffentlichte Ergebnisse für das Kraft-Ausdehnungsverhalten eines DNA-Moleküls mit einem großen, daran gebundenen Proteincluster. Wir zeigen, dass große DNA-Schleifen in einer "Rosette" von dem Proteincluster ausgehen und dabei DNA von den Ketten, die unter Zug stehen, entfernen. Wir charakterisieren das Kraft-Ausdehnungsverhalten durch die Federkonstante. Wir stellen fest, dass die Federkonstante von den Bindungsenergien der Proteine abhängt, aber nur in einer Kombination, die der Nettoenergie der Schleifenbildung entspricht. Das führt uns zur Hypothese, dass Proteininteraktionen die Steifigkeit von DNA mit daran gebundenen großen Proteingebilden beeinflussen, indem sie die Schwierigkeit der Schleifenbildung und -vernichtung beeinflussen.

Summary

Far from being a random polymer, the bacterial chromosome is a complex, heterogeneous and non-equilibrium system. Through both energetic interactions and enzymatic activity, a variety of nucleoid-associated proteins (NAPs) impart fascinating organizational features onto chromosomal DNA. In particular, the chromosome has anomolously large loops, has robustly positioned locally compacted globules and displays ballistic motion during chromosome segregation. Broadly, this thesis explores a method to simulate such non-equilibrium polymers and how it can be applied to elucidate chromosome organization by bacterial condensin. In more detail, we start by describing some of the central puzzles in bacterial chromosome organization with a focus on the action of condensin, and which types of empirical data can be used to address these open questions. Then, we develop, implement and test in detail a kinetic Monte-Carlo method to simulate a minimal model for chromosome organization by condensin: a lattice polymer with sliding elasting rings called 'slip-links', whose movement models the action of single condensins. We use this simulation framework to understand the impact of diffusive and motor slip-links, and show that the molecular action of these slip-links affects the large-scale organizational features of the chromosome. Finally, we present our unfinished work of how DNA loops emanating from protein clusters can affect its force-extension behavior. These four topics compose the main parts of this thesis:

Part I Chapters 1–5. Here, we introduce the biological context, which guides the types of computational frameworks we can(not) use and the puzzles that theoretical physics can help elucidate. We start by modeling the bacterial chromosome as a simple random walk in thermodynamic equilibrium, and show that this model spectacularly fails to account for empirical data from the bacterial chromosome. We show that other physical effects have to included, such as steric interactions, the presence of DNA-binding proteins and non-adiabatic external forcing. We also introduce a crosslinking technique called Hi-C that produces a fingerprint of chromosome organization, a tool that provides experimental data instrumental to this thesis.

Part II Chapters 6–8.3. A detailed exploration of a lattice kinetic Monte-Carlo (LKMC) framework, with particular focus on usage for the simulation of equilibrium and non-equilibrium slip-linked polymers. The slip-linked polymer not only provides a realistic benchmark for our LKMC framework, it also serves as our toy-model for later chapters. Our discussion of LKMC is decomposed into three parts that logically follow one another: (i) design and implementation, (ii) testing and (iii) probing the limits of LKMC. Broadly, we find that LKMC produces data consistent with Brownian dynamics simulations, but that very far from equilibrium the limitations of LKMC are manifested. These limitations mainly fall into two categories: lattice effects and kinetics, that can limit how far the system can be driven from equilibrium.

Related publication and contributors. This work was carried out in collaboration with Prof. C.P. Broedersz and published in the research paper: "*A lattice kinetic Monte-Carlo method for simulating chromosomal dynamics and other (non-)equilibrium bio-assemblies*", Soft Matter **16** (2020).

Part III Chapters 9–12. We use the LKMC framework that we developed in the previous chapters to elucidate bacterial chromosome organization by condensin. We build up a minimal model, starting from the simplest possible model and gradually adding complexity. The first models we consider live in thermodynamic equilibrium, with confinement by an external potential and diffusive slip-links. We show that these models cannot account for the large-scale organization observed in live cells. Then, we add non-equilibrium activity through an active loading mechanism, a proposed model for the molecular action of condensin. Surprisingly, we see that diffusive slip-links with active loading can generate robust juxtaposed chromosome organization, albeit not under physiologal constraints. The number of condensins to make this mechanism work exceeds the number that are available in live cells, and the speed of dynamic re-organization is far slower than observed *in vivo*. Then, we add motor activity to the slip-links, as has been observed *in vitro* for eukaryotic condensin. Indeed, the organization by motor slip-links matches well with the

empirical data, both in terms of the required number of condensins, as well with as the speed of re-organization. Overall, our research suggests that bacterial condensins need motor activity to efficiently and rapidly organize the chromosome.

Related publication and contributors. This work was carried out in collaboration with Prof. C.P. Broedersz and published in the research paper: "*Bacterial chromosome organization by collective dynamics of SMC condensins*", *J. R. Soc. Interface* **15** (2018).

Part IV Chapter 13. We present unpublished results for the force-extension behavior of a DNA molecule with a large protein cluster bound to it. We show that large DNA loops emanate from the protein cluster in a 'rosette', removing DNA from the chains that are being pulled on. We characterize the force-extension behavior through the spring constant. We find that the spring constant depends on the protein binding energies, but only in a combination that corresponds to the net energy of loop creation. Thus, we hypothesize that protein interactions affect the stiffness of DNAs with large protein droplets bound to it, by setting the difficulty of loop creation and annihilation.

Acknowledgements

That you are reading this thesis means that I (almost) completed the intense, long and challenging adventure of doing a PhD. By my word choice, you can probably already infer that it wasn't always easy, and it wasn't always fun. Looking back, I can see how much it has brought me in my technical, scientific and personal development. But, in retrospect, many things appear easy—in the moment, it was often difficult to keep my head level. What in the end kept me sane were, to a large extent, the wonderful people around me. I'd like to take a moment to thank those people that made a valuable and unforgettable impact on my life.

First things first: my supervisor Chase Broedersz was close to the best supervisor I could have wished for. It was through his patience and ability to steer me away from dead ends during the first two years that I was able to succesfully complete my first project. I often found it difficult to discern interesting research avenue from distracting detail, but Chase helped me acquire some of his skill in this regard. Now, I believe this comes much more naturally to me, largely in part to Chase's excellent guidance.

Then, I'd like to take a moment to thank all the people in both the Broedersz and Frey groups for creating a challenging yet friendly work atmosphere. In particular, I'm thankful to Silke Bergeler, Federico Gnesotto, Felix Kempf, Isabella Krämer, Borislav Polovnikov, David Muramatsu and Patrick Wilke for the extensive work- and non-work related discussions, and the activities that we organized. Also, thank you to my two former students, Srikanth Subramanian and Žan Kokalj for pursuing their projects with me—I hope both of you are doing well!

To my Dutch friends, Joris Scheers, Thom Bijsterbosch & Lisa van Kessel, Mark van Ninhuijs, Carline van Breugel, Koen van Gils, Michelle Verhoeks, Maarten Lubbers and Louise Janssen, I always looked forward to seeing each and every one of you whenever I went back to The Netherlands. During the last few years, we danced to overdriven techno in former Soviet atomic bunkers, were told we 'had the wrong entrance' at Berghain, had long walks in a cold autumn Vondelpark, did a brewery tour amongst bachelor parties several hours too early in the morning, learned to perform a traditional Greek dance, and many more unforgettable memories. You know me well enough to know that I don't really take pictures, but you can be sure I frequently think back to those moments.

Despite my time in Munich covering only a few years, I've had the privilege of meeting some incredible people that I hope to know for the rest of my life. Thank you Peter Baumgartner, Mareike Berger, David Bondesson, Robert Borrmann, George Dadunashvili, Daniel Devlitsarov, Aurore Dupin, Andreas Häfner, Tobias Hermann, Mona Hoyos, Hanna Kratzat, Timo Krüger, Marie-Lena Marstaller, Joris Messelink, Fabian Meyer, Federica Mura, Martin Rossa, Tobias Stöber, Anika & Valerie Schöttle, Matthaüs Schwarz-Schilling, Muriel van Teeseling and Philipp Weber. You made my time in Munich worthwile! I started writing personal notes to each of you here, but it quickly became apparant that this page wouldn't cover the stories I'd like to retell, and the appreciation I'd like to express. That just goes to show how many wonderful memories we already shared! Instead, let us reminisce after the defense. Each and every one of you occupy a warm place in my heart.

Although they have all been mentioned already, I'd like to say "thank you" again to Joris Messelink, Isabella Krämer, Felix Kempf and Mona Hoyos for their kind help with writing this thesis. Undoubtedly, it improved because of your help. I'm also honored to have Mareike Berger and George Dadunashvili be my paranymphs, and grateful for their help in organizing the celebrations.

Last but not least, both my parents and brother were always there to support me. Always. If you're being challenged, it can be a life-saver to know that some people will always have your back, no matter what happens. Through many calls, they gave me a connection to home in spirit, far away from home in body.

Contents

I Introduction 13

1 The Bacterial Chromosome: A Brief Overview 14

2 Bacterial Chromosomes are not Random Walks 16
- 2.1 Size scaling of a random walk . . . 16
- 2.2 DNA is a semiflexible polymer . . . 17
- 2.3 Steric interactions play an important role in the chromosome . . . 19
- 2.4 DNA-binding proteins remodel the chromosome . . . 21

3 The Chromosome is not a System in Thermal Equilibrium 24

4 Crosslinking of DNA Loci Reveals Organization 27

5 Goals and Significance 30

II The Design, Testing and Limitations of Lattice Kinetic Monte-Carlo 36

6 Ingredients of a Lattice Kinetic Monte-Carlo Simulation for Slip-Linked Polymers 37
- 6.1 Recipe for the Gillespie Method . . . 37
- 6.2 Updating time in Gillespie algorithms . . . 39
- 6.3 Using Locality to Boost Efficiency . . . 40
- 6.4 Implementing Polymer Dynamics . . . 42
- 6.5 Implementing Energetic Effects using Metropolis-Hastings Kinetics . . . 43
- 6.6 Combining Multiple Degrees for More Realistic Kinetics . . . 44

7 Verifying the Validity of Stochastic Dynamics in LKMC 46
- 7.1 Controls on Time-Averaged Quantities in Equilibrium . . . 46
- 7.2 Controls on Polymer Dynamics in Equilibrium . . . 48
- 7.3 Control on Slip-Link Dynamics in Equilibrium . . . 50
- 7.4 Control on Particle Dynamics in Potential Landscapes . . . 51
- 7.5 Controls on Particle and Polymer Dynamics out of Equilibrium . . . 52
- 7.6 Comparison of LKMC with Brownian Dynamics for Non-Equilibrium Loop Extrusion . . . 53

8 Probing the Limits of LKMC for Non-Equilibrium Systems 55
- 8.1 Metropolis-Hastings Kinetics Limits the Maximum Speed of Particle Movement . . . 55
- 8.2 Metropolis-Hastings Kinetics Underestimates the Entropy Production at Large Forces . . . 56
- 8.3 Lattice Discretization can Result in Unphysical Jamming far from Equilibrium . . . 58

III Bacterial Chromosome Organization by Condensin 64

9 Minimal Models for DNA Organization by SMC 65
9.1 Quantifying Loop Topology . . . 67

10 Slip-Linked Polymers in Equilibrium do not Display Juxtaposed Organization 69
10.1 Equilibrium Implementation of Diffusive Slip-Links do not Produce Juxtaposed Organization . . . 69
10.2 Confinement and Diffusive Slip-Links do not Produce Juxtaposed Organization . . . 70

11 Steady-State Organization by Diffusive and Motor Slip-Links Out of Equilibrium 72
11.1 Diffusive Slip-Links Can Organize the Chromosome at High Densities . . . 72
11.2 Motor Slip-Links are Effective at Organizing the Chromosome at all Densities . . . 79

12 Dynamic Re-Organization of Chromosomes by Diffusive and Motor Slip-Links 82
12.1 SMC condensin requires motor activity to rapidly re-organize the chromosome . . . 82
12.2 DNA Relaxation Dynamics Can Limit Slip-Link Velocity . . . 83
12.3 Motor condensins without a loading site transiently juxtapose the polymer . . . 84

IV Force-Extension Behavior of the ParB-DNA System 89

13 Polymer Looping affects the Force-Extension Relation of the DNA-ParB System 90

V Conclusion and Outlook 96

14 Conclusion 97

15 Outlook 99
15.1 Rouse Dynamics of Circular Polymer Chains . . . 99
15.2 Impact of Looping on Force-Extension Behavior of ParB-DNA System . . . 99
15.3 Interaction Between Slip-Links . . . 101

Appendices 105

A Measurement of Simulation and Empirical Data 106
A.1 Converting Empirical Data to Simulation Parameters . . . 106
A.2 Converting Simulation Data to Metrics . . . 107

B Rouse Model for Circular Polymer Chains 110

C Response Function of Sub-Chains of Circular Polymers 112

D Controls on Equilibrium Monte-Carlo Model for Globular Polymers 114
D.1 Force-Extension of Naked Polymer . . . 114
D.2 Binding Isotherm of Non-Interacting, Repulsive Particles . . . 117
D.3 Binding Isotherm of Particles with Spreading Interactions . . . 118
D.4 Binding Isotherm of Particles with Bridging Interactions . . . 119
D.5 Internal Scaling of Globular Polymer . . . 120

Part I

Introduction

1

The Bacterial Chromosome: A Brief Overview

The bacterial chromosome is a circular polymer that contains the cell's genetic material. It is not contained in a nucleus, as in the case of eukaryotic cells, but rather lives in the dense and dynamic middle of the cell called the *nucleoid*. Its name stems from its similarity in function to that of the nucleus in eukaryotes. Although the nucleoid is distinguished from the nucleus by the absence of a separate enclosure, the nucleoid does have an increased concentation of various proteins [23]. These proteins perform tasks related to organization, segregation and maintenance of the chromosome [33, 36, 44, 70, 76].

For a long time, the bacterial chromosome was believed to be unorganized [38]. This notion stemmed from the lack of organelles in bacteria, in addition to the rather amorphous or globular nucleoid [38]. However, upon puncturing the cell wall (cell lysis), a more detailed look at the DNA of the lysed cell showed domains of intricately twisted DNA [70]. More recently, a crosslinking technique called Hi-C has been developed that can probe the organization of live cells (chapter 4). Data from these methods and others have uncovered a variety of types of organization on different length-scales, such as: bending, bridging, twisting and condensing [17, 30, 36, 49]. Some of these types of organization are vital to cell survival, whereas others play a more elusive role. These various types of organization are effected by a variety of *nucleoid-associated proteins* (NAPs), covered in more detail in section 2.4.

On the largest scale, chromosome organization pertains to the positioning and alignment of the whole chromosome within the cell. Two special regions on the DNA called the origin (*ori*) and terminus (*ter*) regions (figure 1.1), whose biological function are respectively starting and stopping points of DNA replication [3, 33, 70, 76], serve as markers to uniquely define the alignment of the chromosome. In bacteria such as *B. subtilis* and *C. crescentus* [46, 73, 78, 79], but not in *E. coli* [48], the *ori–ter* axis is aligned with the cell's global shape (figure 1.1) [3, 33, 70, 76]. Still on a megabasepair-scale, the two chromosomal arms in many bacteria are juxtaposed along the *ori–ter* axis [46, 78, 79]. We discuss a possible mechanism for such arm–arm juxtaposition in great detail in part III of this thesis. Whatever the mechanism, it is clear from a combination of gene deletion and protein incubation experiments that the NAP called *structural maintenance of chromosomes* (SMC) is responsible for this large-scale organization [46, 78, 79]. On a yet smaller scale, kilobase-sized stretches of DNA are organized in *macrodomains* that are composed of highly compacted, twisted motifs called *plectonemes*. Plectonemes are not statically folded—rather, they are dynamically wound and unwound by NAPs called *gyrases*. There is growing evidence that the role of these plectonemes is not simply to make the DNA more compact, but also to regulate gene transcription by making the DNA locally less accessible to transcription factors [46]. The chromosome organization on these various length- and time-scales is not simply a biological problem—the NAPs involved leverage physical principles such as steric repulsion, diffusion, bending and twisting to produce the complex spatiotemporal organization of bacterial chromosomes.

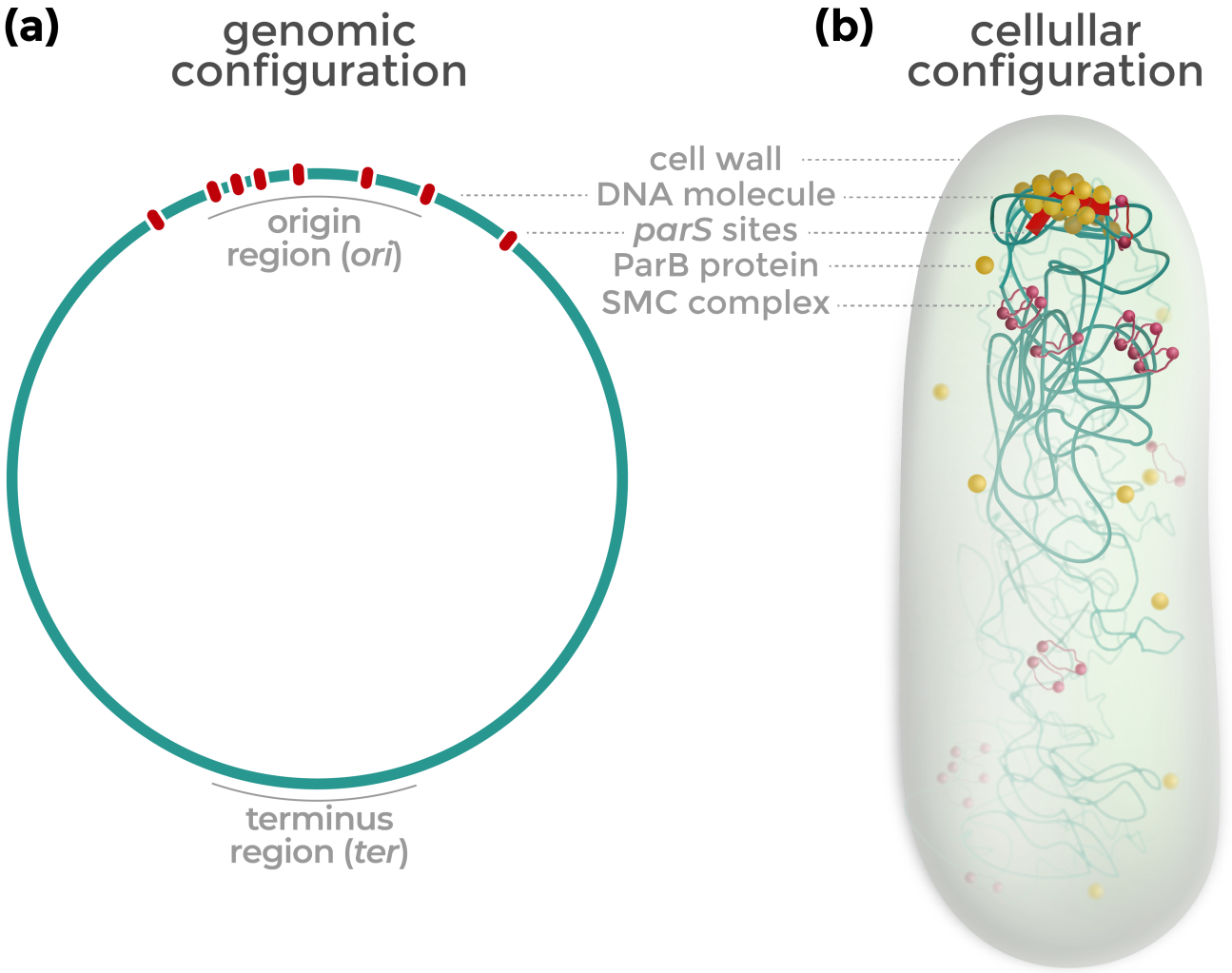

Figure 1.1: **The bacterial nucleoid is composed of a densely compacted circular polymer with proteins binding to and interacting with it. (a)** Topology of the bacterial chromosome: a circular polymer, with the *ori* and *ter* regions defining a unique axis. Array of *parS* sites based on approximate locations in *B. subtilis* is shown in red. **(b)** Illustration of the nucleoid inside a cell. In this particular illustration, the origin region coincides with one of the cell poles through DivIVA tethering proteins (not shown), which follows the geometry of bacteria such as *B. subtilis* [76]. All the elements shown in this figure are discussed in this thesis: how to simulate the spatial organization of DNA (part II), DNA organization by SMCs and/or cellullar confinement (part III) and DNA looping from ParB clusters (part IV).

2

Bacterial Chromosomes are not Random Walks

Chapter summary: *We discuss three key ways in which the bacterial chromosome is not a random walk: local polymer persistence, steric interactions and DNA-binding proteins.*

The simplest possible model of a polymer is the *random walk*, and is therefore a useful measuring stick by which any other model for the chromosome can be compared. In this chapter, we will first derive the size of a random walk (section 2.1). Then, we show that several key assumptions in the random walk model are contradicted by the presence of additional effects in the chromosome: the presence of stiffness in the DNA backbone (section 2.2), steric interactions between parts of DNA proximate in space (section 2.3) and the presence of DNA-binding proteins that locally remodel DNA (section 2.4). Inclusion of these three physical effects results in a description that has been successfully used for the study of DNA organization [9, 13].

2.1 Size scaling of a random walk

The random walk can be defined in multiple ways: on-lattice, off-lattice but with discrete segments and as a continuous path. Here, we analyze an off-lattice discrete random walk with n steps of size ℓ and net displacement $\mathbf{R}(n)$ that starts at the origin ($\mathbf{R}(0) \equiv 0$). We assume no correlations whatsoever between adjacent segments, so the polymer is simply the path of a randomly diffusing particle taking n steps of size ℓ. Without computing the distribution of end-to-end vector $\mathbf{R}$ after n steps $p(\mathbf{R}(n))$ yet, we know that it must obey several key symmetry properties:

rotational symmetry — There is no aligning field or other system property that breaks rotational symmetry.

translational symmetry — Since the particle is equally likely to go to the left or the right (or up or down, etc.), its average position must lie at its starting point, $\langle \mathbf{R} \rangle = 0$. Note that this is a corollary of rotational symmetry, and not a separate constraint, because for any rotationally invariant distribution $\langle \mathbf{R} \rangle = \int d\mathbf{R}\, \mathbf{R} p(\mathbf{R}) = 0 \forall p(R)$.

Furthermore, since the random walk is composed of many independent steps from the same single-step distribution, the central limit applies: the distribution of the *net displacement* is a Gaussian as $n \to \infty$, even if the *individual* steps are not Gaussian [74]. Then, the condition of either rotational or translational symmetry sets the mean of this Gaussian to zero. Whereas the one-dimensional Gaussian distribution is written as $\exp(-x^2/2\sigma^2)/\sqrt{2\pi\sigma^2}$ with a scalar variance σ^2, in d dimensions the Gaussian distribution contains a covariance matrix $^\circ$. Van Kampen [74] shows that, using $^\circ$, the distribution can be written as

$$p(\mathbf{R}(n)) = \frac{1}{\sqrt{(2\pi)^d |\mathbf{\Sigma}|}} \exp\left(-\tfrac{1}{2}\mathbf{R}^T \mathbf{\Sigma}^{-1} \mathbf{R}\right), \tag{2.1}$$

where $|\cdot|$ is the determinant. For a rotationally symmetric distribution, $\mathbf{\Sigma}$ must be a diagonal matrix with identical components, $\mathbf{\Sigma} = \sigma_1^2 I$, where σ_1^2 is the variance of the vector $\mathbf{R}$ when projected any single one of the d dimensions and I is the identity matrix. Moreover, again using the diagonal form of $\mathbf{\Sigma}$, we have $|\mathbf{\Sigma}| = (\sigma_1^2)^d$. Since $\mathbf{R}^2 = \sum_i R_i^2$, we have $\sigma(\mathbf{R})^2 = d\sigma_1^2$. This results in the much more tractable expression

$$p(\mathbf{R}(n)) = \frac{1}{\sqrt{(2\pi/d)^d \sigma(\mathbf{R})^{2d}}} \exp\left(-\frac{d\mathbf{R}^2}{2\sigma(\mathbf{R})^2}\right), \tag{2.2}$$

where the variance $\sigma(\mathbf{R})^2$ is as of yet unknown. However, since the walk's individual steps are all independent, the total variance obeys the summation rule $\mathrm{var}[\mathbf{R}] = \sum_i \mathrm{var}[\mathbf{R}(i) - \mathbf{R}(i-1)] = n\mathrm{var}[\Delta\mathbf{R}]$ where in the last step we used translation invariance. The single-step variance is, by definition,

$$\mathrm{var}[\Delta\mathbf{R}] = \left\langle \Delta\mathbf{R}^2 \right\rangle - \langle \Delta\mathbf{R} \rangle^2 ,$$

where each step traverses the same Euclidean distance $\Delta\mathbf{R}^2 = \ell^2$ and each step must be translationally invariant so that $\langle \Delta\mathbf{R} \rangle = 0$. Thus, we find for a random walk composed of n steps of size ℓ a variance $\mathrm{var}[\mathbf{R}] = \left\langle \mathbf{R}^2 \right\rangle = n\ell^2$. Importantly, the *size scaling* behavior that we found here is *universal*, i.e. the relationship $R^2 \sim n$ holds for a random walk irrespective of dimensionality and lattice topology.[1]

2.2 DNA is a semiflexible polymer

To map the random walk model to an actual polymer, we need to know how to relate the model parameter ℓ to a measurable quantity. Since the random walk performs rigid steps of size ℓ, ℓ will be proportional to the length-scale on which the DNA polymer starts to appear 'straight'. Given that our discrete model for random walks with no correlations between the directions of subsequent polymer segments results in a scale-free geometry, there is no emergent length-scale (that is not equal to ℓ) on which the random walk polymer is straight. Thus, ℓ cannot be determined self-consistently from the random walk model. However, images of nicked DNA on mica surfaces show that DNA is not a chain of rigid segments, but rather shows clearly visible correlations between tangent vectors along the arc-length of the polymer (Figure 2.1a–b), suggesting that a smallest length-scale does exist. This is because DNA is a *semiflexible polymer*: bending the DNA backbone is energetically penalized [32], resulting in few places with a large curvature.

The angular correlations, quantified as $g(s, s+\Delta s) \equiv \langle \mathbf{t}(s) \cdot \mathbf{t}(s+\Delta s) \rangle$ for a tangent vector $\mathbf{t}(s) \equiv \partial_s \mathbf{r}(s)$ at arc-length s, follow an approximately exponential decay $g(s, s+\Delta s) \approx \exp(-\Delta s/\ell_p)$ (Figure 2.1d) [84]. The lack of a dependency on s in $g(s, s+\Delta s)$ is consistent with a necessary translational invariance of homopolymers. The typical length-scale $\langle s \rangle = \ell_p$ that captures the decay length of this correlator is called the *persistence length*. The definition of the inner product: $\mathbf{t}(s) \cdot \mathbf{t}(s+\Delta s) = \cos\theta(s, s+\Delta s)$ (where $\theta(s, s+\Delta s)$ is the angle between the tangent vectors at arc-lengths $s, s+\Delta s$, Figure 2.1c), provides a clear interpretation of ℓ_p. Namely, ℓ_p is the amount of arc-length that needs to be traversed for the angle to change substantially. In particular, after a distance $s = \ell_p$, the angle will have changed approximately by an amount $\Delta\theta \approx \arccos e^{-1} \approx 68°$.[2]. For length-scales below this ℓ_p, mechanical stiffness of the polymer dominates, whereas above it, thermal fluctuations randomize the polymer direction. The persistence length ℓ_p of double-stranded DNA is $\approx 50\,\mathrm{nm}$ in typical physiological conditions [50], but can be reduced to as low as 15 nm at unphysiologically high salt concentrations [4, 12, 50]. The rigid segments in the random walk model are called *Kuhn monomers* with a segment length known as the *Kuhn length* ℓ [22, 64]. After equating the end-to-end distance of a semiflexible polymer to that of a model with rigid segments but identical total length, it is found that $\ell = 2\ell_p$ [64].

[1] The coefficient between R^2 and n is *non-universal* [74]. This effective step-size will depend on details of how the random walk is constructed, such as whether the walk is on-lattice or off-lattice, whether each step has the same size, dimensionality, etc..

[2] We specifically added the word "approximately" because $\langle \cos\Delta\theta \rangle \neq \cos\langle \Delta\theta \rangle$, so the angle can strictly not be found by simple inversion as we did here.

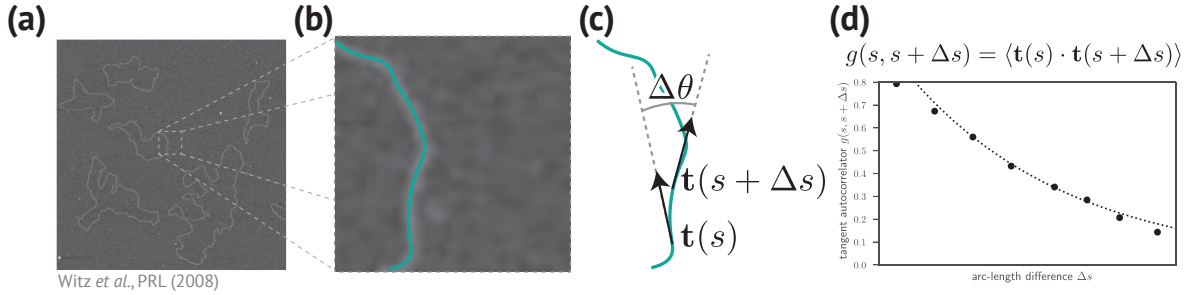

Figure 2.1: **DNA polymers display rigidity on small length-scales, characterized by a typical length-scale. (a)** Image of plasmids (small circular DNA polymers) deposited on a mica substrate. **(b)** Zoom of panel (a), with a trace of the curve $\mathbf{r}(s)$ superimposed (red). **(c)** The tangent vector $\mathbf{t}(s)$ is defined as $\mathbf{t}(s) = \partial_s \mathbf{r}(s)$. **(d)** The autocorrelator of the tangent vector follows an exponential decay, with a typical length-scale $\langle s \rangle$ that is called the *persistence length* ℓ_p. Left two images of DNA on mica adapted from [84] with permission from the publisher.

Because the tangent–tangent correlations decay exponentially, the local stiffness of polymers can in many, but not all, cases be neglected on length-scales $L \gg \ell_p$. They cannot be neglected even for these large length-scales L if, for example, other reaction coordinates couple to the bending energy such that the bending energy induces correlations on this length-scale L. One practical example of this involves proteins that preferentially bind to pieces of DNA with a certain curvature [85]. Parts of DNA with this particular curvature can then nucleate large protein clusters, establishing correlations that are not limited by local polymer persistence but rather by collective DNA-protein effects [9].

Now that we found the size of a Kuhn monomer for double stranded DNA, we can compute the size of a bacterial chromosome within the random walk model. For the total length of a 5 Mbp *E. coli* chromosome [56] at 0.34 nm per basepair [1], the total length is 1.7 mm, or $n = L/(2\ell_p) = 17 \cdot 10^3$ Kuhn monomers. Plugging this in our previously found size scaling (section 2.1), we find $R \approx 13\ \mu$m, more than an order of magnitude larger than an entire *E. coli* cell (Figure 2.2). This already shows that the bacterial chromosome cannot be a random walk: it's confinement is > 1000 times too small in volume to contain its DNA in an uncompacted form.

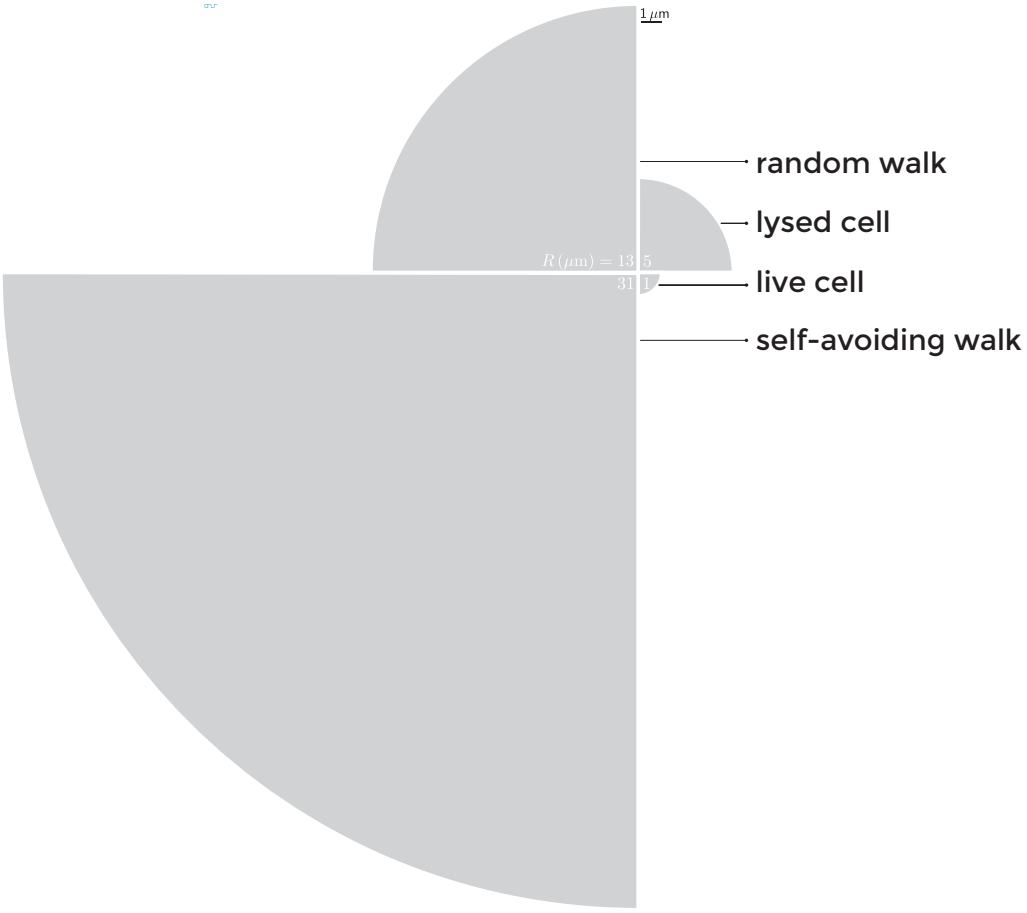

Figure 2.2: **Typical sizes of DNA molecules in various conditions**. Inside a live cell, the entire chromosome is ca. 1 μm in size [56]; after lysing (dissolving the cell wall), it spans ca. 5 μm (visually estimated from the image in [70]); a random walk with $17 \cdot 10^3$ Kuhn monomers has a typical size of ca. 13 μm and a self-avoiding walk of that size is about 31 μm in size (equation (2.3)). Radii in μm of different polymer models indicated inside quadrants (white).

2.3 Steric interactions play an important role in the chromosome

One strong assumption that we made in our discussion of random walks is that the polymer segments do not interact with one another. However, biopolymers are composed of hydrocarbon subsegments, which strongly repel each other at short distances—in other words, biopolymers exhibit *steric repulsion* [64]. A simple extension to incorporate this effect is to take the random walk model, but to add an infinitely strong repulsion between monomers at a distance ℓ' apart. Such walks are called *self-avoiding*.

Before we analyze the physics of self-avoiding walks, we point out that these contacts are expected to play a strong role for a typical bacterial chromosome. Given the monomer size $\ell_p \approx 50\,\text{nm}$ [84], there are about $n \approx 17 \cdot 10^3$ monomers in an *E. coli* chromosome [56]. Covering the DNA molecule with spheres of a diameter $2\ell_p$ (Figure 2.3a), we find an excluded volume for this beads-on-a-string model of $V \approx n \cdot \frac{4}{3}\pi {\ell_p}^3 \approx 8.9\,\mu\text{m}^3$. Based on a typical *E. coli* cellullar volume of $0.5\text{–}5\,\mu\text{m}^3$ [56], we find that a fraction of 178 – 1780% of the cytosol is occupied by the excluded volume of these Kuhn monomers. Clearly, a fraction of cytosolic volume occupied by DNA greater than 100% is impossible, which already suggests a role for various compaction factors inside the cell. Given the ensuing high densities following this high degree of compaction, we expect steric effects to play a significant role—indeed, intracellullar restrictions are believed to substantially affect polymer dynamics [60] and DNA geometry [65].

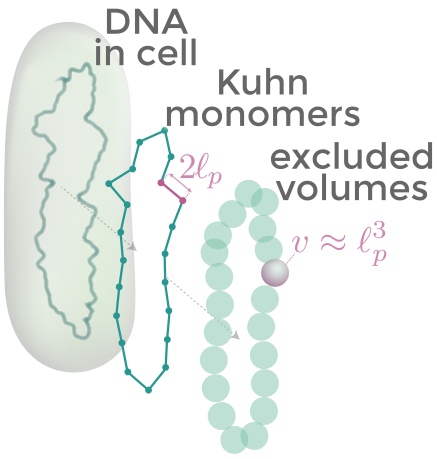

(a) **Polymers are characterized by an excluded volume that can be estimated using Kuhn monomers.** The DNA fluctuating inside a cell can be coarse-grained to a discrete set of Kuhn monomers of size $b = 2\ell_p$ [64]. Each Kuhn monomer has an excluded volume of $\approx \ell_p^3$.

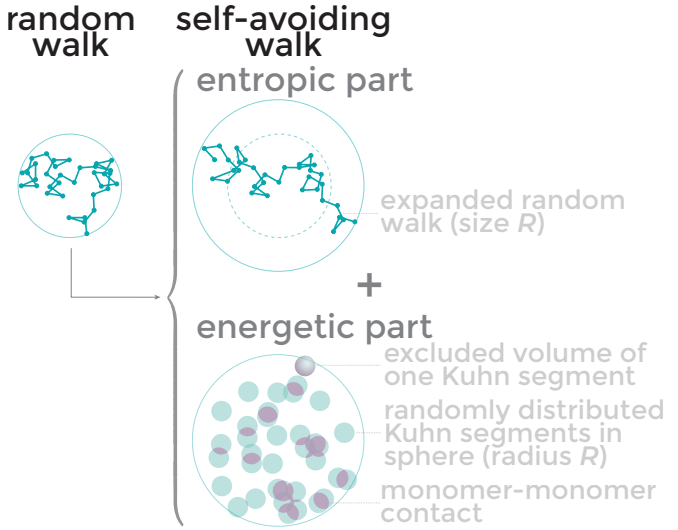

(b) **A Flory theory approximates the free energy of an expanded polymer by combining estimates for the monomer-monomer interactions and loss of entropy upon expansion. Top**: A random walk with an expanded size will disproportionally explore microstates with a large typical radius R, resulting in a decreased entropy. **Bottom**: Flory theories assume that the Kuhn monomers are randomly distributed throughout a sphere of radius R, allowing for straightforward calculation of the number of monomer-monomer contacts.

Figure 2.3

Naively, one might imagine that a short-ranged repulsion in 3D space will result in short-range correlations along the polymer chain. If this were the case, the self-avoiding walk will still be a random walk, but with a renormalized monomer size $\ell' > \ell$, where the size increase ℓ'/ℓ is related to the strength and length-scale of the steric interactions. It turns out that this is not the case: polymers with short-ranged steric repulsion exhibit long-ranged, power-law decay of correlations with arc-length [37]. The polymer geometry of self-avoiding walks thus displays qualitatively different behavior than a random walk, with a scaling $R \sim n^\nu$ with $\nu > \frac{1}{2}$.

There are different methods to find the scaling exponents ν of such self-avoiding walks such as renormalization group calculations [24], self-consistently by balancing terms in a scale-invariant fashion [5] and path-integral formalisms [81]. Here, however, we use a mean-field-theoretical approach called a *Flory theory* [64]. Although such a mean-field theory ignores correlated fluctuations, and can therefore introduce systematic biases in our calculations, it has the benefit of simplicity. Broadly, a Flory theory proposes a free-energy *Ansatz* $F(R) = F_{\text{RW}}(R) + F_{\text{ints.}}(R)$ (Figure 2.3b) where:

- F_{RW} is the change in the free-energy of a random walk if it is extended or compressed to a size R (Figure 2.3b, top). Since a random walk does not have energetic interactions, this free-energy is purely entropic. Moreover, since the entropy of a random walk is maximized, F_{RW} will increase as R deviates from the random walk size.
- $F_{\text{ints.}}$ is a mean-field estimate for the energetic monomer-monomer interactions that we include in our model (Figure 2.3b, bottom).

The term F_{RW} can be found from the probability distribution (equation (2.1)) as $F_{\text{RW}}(R) = -TS_{\text{RW}}(R)$ where the Boltzmann entropy conditioned on a size R is $S_{\text{RW}}(R) = k_B \log \Omega(R)$ with $\Omega(R) \sim p(R)$ the number of microstates with size R. To get $p(R)$ from $p(\mathbf{R})$, we use the formula for the conservation of probability:

$$p(R)\mathrm{d}R = \int \mathrm{d}\mathbf{r} p(\mathbf{r})\delta(|\mathbf{r}| - R) = 4\pi p(\mathbf{r})|_{|\mathbf{r}|=R} R^2 \mathrm{d}R,$$

where we used the sieve property of the Dirac delta and assumed rotational invariance. Plugging this into our expression for the entropy, we find

$$S_{\text{RW}}(R) = k_B(2\log(R/\mathfrak{r}) - R^2/2\sigma^2 + \ldots),$$

where $\mathfrak{r}$ is a constant that makes the logarithm argument dimensionless and the ellipsis represents terms that do not depend on R. Then, for the interactions, we penalize each monomer-monomer contact with a constant energy ϵ (Figure 2.3a), with a total number of N_c monomer-monomer contacts, resulting in an interaction energy $F_{\text{ints.}} = \epsilon N_c$. What is the mean-field expression for N_c? For each of the n monomers, the probability of overlapping with any of the other $(n-1)$ monomers is $p_c^{\text{MF}} = (n-1)v/(R^d - v) \approx nv/R^d$, where v is the excluded volume of a monomer and d is the dimensionality of space. The total number of contacts is therefore $N_c \approx \frac{1}{2} n p_c^{\text{MF}}$, where the prefactor $\frac{1}{2}$ prevents double-counting the contacts. Combining these two different free-energies, we find

$$F(R) \approx k_B T - \left(2 \log R + \frac{R^2}{\ell^2 n} + \ldots\right) + \epsilon \frac{n^2 v}{2R^d}.$$

The value of R for which the free-energy is minimized is then found by solving $R^* : 0 = \partial_R F(R)|_{R=R*}$:

$$\begin{aligned} 0 &= \partial_R F(R) \\ &= k_B T \left(\underbrace{-\frac{2}{R}}_{\text{term (i)}} + \underbrace{\frac{2R}{2\ell^2 n}}_{\text{term (ii)}} \right) - \epsilon d \underbrace{\frac{n^2 v}{2R^{d+1}}}_{\text{term (iii)}}. \end{aligned}$$

For sufficiently long chains $n \gg 1$, we expect that $R \gg \ell$ so that term (i) $\sim 1/R \ll 1$. For a random walk, the $R \sim n^{1/2}$ scaling implies that term (ii) $R/n \sim 1/R$. Thus, term (i) and (ii) will have the same scaling if a self-avoiding walk exhibits random walk scaling. On the contrary, if the scaling exponent of the self-avoiding walk $\nu > \frac{1}{2}$, then term (ii) will dominate over (i). For now, we assume that term (ii) indeed dominates over (i) and show that this assumption is justified later. The term that scales as n^2/R^{d+1} cannot be neglected for self-avoiding walks in $d \leq 3$, because even a random walk in $d = 3$ obeys $n^2/R^{d+1} \sim O(1)$. Then, solving for R, we find

$$\begin{aligned} R &\approx \left(\frac{1}{2} \frac{\epsilon}{k_B T} \ell^2 v d \right)^{1/(d+2)} n^{3/(d+2)} \\ &\equiv \ell' n^{\nu^{\text{MF}}}. \end{aligned} \tag{2.3}$$

Importantly, we find that the Flory theory suggests our intuition about the role of monomer-monomer repulsion was incorrect: although ϵ does only affect the size of the renormalized monomer size ℓ' in the above expression, an arbitrarily small $\epsilon > 0$ already produces a different scaling $\nu^{\text{MF}} = 3/(d+2) = 0.6$ for $d = 3$. This shows that, at least according to this mean-field picture, steric interactions—even if they are weak and operate on a small scale, cannot be neglected on length-scales much larger than the length-scale of that interaction. Both measurements of self-avoiding polymers [64] as well as detailed simulations [31] show that ν^{MF} is remarkably close to the one of the most accurate measurements $\nu = 0.587597(7)$ [15]. However, the closeness of ν^{MF} to the currently accepted value is due to a fortuitous cancellation of errors [5].

Although the scaling exponent of self-avoiding polymers is only < 18% different to that of a random walk, this small difference in the scaling exponent can result in quite a drastic increase in total volume for large n: The size of a self-avoiding walk with the size of a DNA polymer is $R \approx 31\,\mu$m, more than twice the size of a random walk of the same contour length. This means that a self-avoiding walk of the size of an *E. coli* chromosome has to be compacted by a ratio of $\approx 30 \cdot 10^3$ for it to fit inside its cellullar volume. These large degrees of compaction imply that cellullar processes must somehow regulate the density for the DNA to fit inside its container, possibly by proteins that can locally compact DNA.

2.4 DNA-binding proteins remodel the chromosome

There are additional clues that the bacterial chromosome is more than a simple homopolymer. One such clue we already saw in Figure 2.2; even after lysis, the DNA is much more compact than both the random and self-avoiding walks, suggesting the membrane is not the only compaction force. Another indication is that after tagging certain nucleoid-associated proteins (NAPs) with a fluorescent dye, bright foci consistently are found on opposite sides of the cell (Figure 2.4a). Additionally, fluorescent molecules that bind to particular binding regions on the genome are found to arrange in a linear pattern along the cell's major axis [82]. Additional insight comes from Hi-C contact maps, which reveal the proximity of different genetic loci [21]—more details follow in section 4. Still on a cell-wide scale, these Hi-C data reveals that the two chromosomal arms

are *juxtaposed* in many bacteria (*B. subtilis* [78], *C. crescentus* [71] and others but not *E. coli* [48]; Figure 2.4b). On a smaller length-scale, high-frequency regions in Hi-C contact maps can be seen that correspond to *plectonemes*: highly folded and twisted segments of DNA that are locally compacted (Figure 2.4c). On an even smaller scale, individual proteins twist, bend and bridge DNA [17, 30] (Figure 2.4d). On all these length-scales, the DNA organization is largely due to the action of NAPs [3, 30, 36, 76].

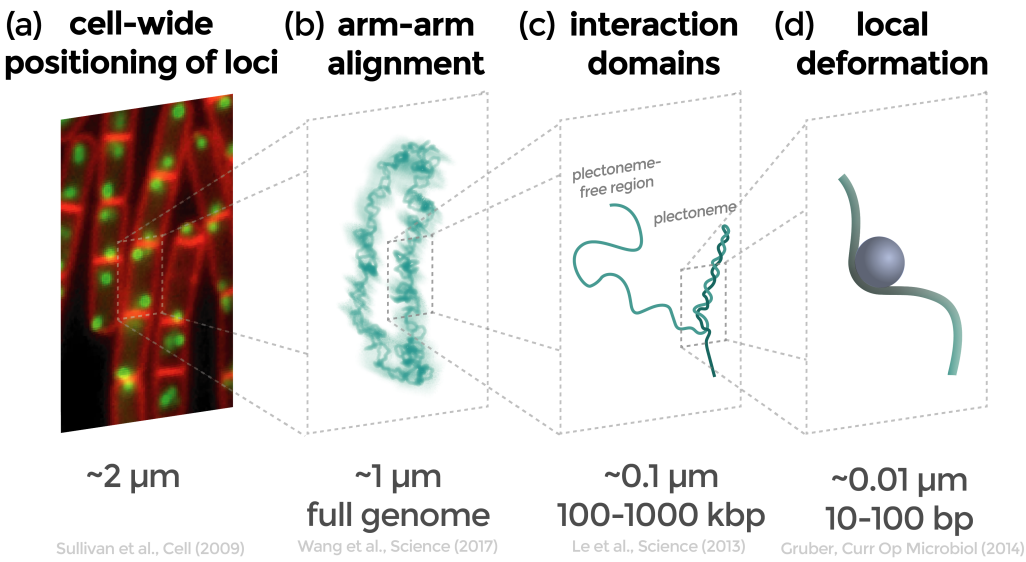

Figure 2.4: **The bacterial chromosome is organized across multiple length-scales. (a)** Fluorescently tagged loci (green) in *B. subtilis* are robustly positioned at the cell poles [68]. Image reused from Sullivan et al. [68] with permission from the publisher. **(b)** The chromosome is in an approximately juxtaposed configuration, with many long-range contacts between the two chromosomal arms [79]. **(c)** Highly compacted, supercoiled regions of DNA called *plectonemes* are observed in the 100 – 1000 kbp range. Less compacted *plectoneme-free regions* connect these interaction domains. **(d)** Single nucleoid-associated proteins locally twist and bend DNA, e.g. the highly abundant HU generates sharp kinks in the DNA backbone across a $\approx$ 36 bp stretch of DNA [30].

In figure 2.4, we show a selection of the wide variety of organizational features effected by various NAPs. In this thesis, we mostly restrict ourselves to an NAP called *structural maintenance of chromosomes* (SMC) that is responsible for the juxtaposed organization (Figure 2.4) [78, 79]. Juxtaposition of the chromosomal arms is believed to play an important role in resolution of replicated origins and chromosome segregation [35, 36, 76, 77]. SMC does not operate as a single protein; rather, it is one unit in a more complicated ring-shaped protein complex called *condensin*.

Condensin is such a fascinating complex, in part, because it is so efficient: only 3–30 condensins are needed to organize a full bacterial chromosome [83]. Additionally, dynamic re-organization by condensin is fast: starting from a state lacking juxtaposed organization, it aligns the chromosomal arms in $T \approx 30$ mins [79]. Whatever the translocation mechanism of condensin on a molecular scale may be, this timescale does imply a certain effective traversed distance per hydrolyzed ATP molecule. Based on the ATP hydrolysis rate of condensin $k_{\text{cat}} \approx 2\,\text{s}^{-1}$ [69], the re-organization time T corresponds to an average step size of $\approx$ 30 bp per hydrolyzed ATP molecule [69]. This stands in stark contrast to the $\sim$ 1 bp step sizes for many common DNA motor proteins [66].

It has been doubted that condensin has motor activity, (i) because of the discrepancy between the step size of known DNA motor proteins and the step size of condensin [69], and (ii) because attempts at finding motor activity in condensin for a long time did not yield positive results [41]. Instead, other models for collective condensin translocation on the chromosome have been proposed, such as DNA loop capture and diffusive motion with active loading at the origin region [14, 55, 83]. For a contemporary review of different models for condensin, we refer to Dame et al. [18]. However, for many of these models the organizational impact of condensin on the chromosome were, to the best of our knowledge, not quantitatively investigated. Luckily, the model with active loading and diffusive sliding has been thoroughly investigated using Brownian dynamics simulations and Fokker-Planck methods [7, 8, 10]. The non-equilibrium loading, combined with mutual steric repulsion, generates an "osmotic ratchet" that promotes loop extrusion, even in the absence of bias in the

microscopic molecular diffusion [10]. This theoretical analysis shows that condensins might not need motor activity for their organizational function.

Since then, motor activity in yeast condensin has been experimentally demonstrated [26, 69], although direct evidence for motor activity in bacterial condensin is still lacking [18]. Nevertheless, active loop extrusion has emerged as a popular model for bacterial condensin [11, 18, 79, 80]. Marko et al. [53] propose a molecular model for how condensin might pull off this feat based on a coupling of condensin shape to fluctuations in the DNA. In this thesis, however, we take a more coarse-grained approach, and only investigate the impact of different types of condensin translocation on DNA organization. In part III, we investigate both the motor and active loading models for SMC, and show that motor activity is consistent with *in vivo* data, whereas the active loading model isn't.

3

The Chromosome is not a System in Thermal Equilibrium

Chapter summary: *The bacterial chromosome is driven out of equilibrium by enzymes. We discuss the relationship between polymer relaxation and being out of equilibrium.*

All our previous polymer models (sections 2.1–2.3) have lived in *thermodynamic equilibrium*. Can the bacterial chromosome be approximated as a polymer in equilibrium with its environment? Of course, any living system is strictly not in thermodynamic equilibrium, but how closely the dynamics can be modeled as an equilibrium system depends on a few key parameters. Before we discuss those key parameters, it's insightful to point out that there are experimental demonstrations of non-equilibrium activity involved in chromosome organization.

One of the most obvious cases of a non-equilibrium process is that of chromosome segregation: two (nearly) replicated chromosomes are actively pulled apart [77], exhibiting ballistic motion [42] (relevant time-scales: $10^3 - 10^4$ s in *E. coli* [42]). Lesser well known, but not less impressive, the two chromosomal arms are known to be 'zipped up' in many bacteria by SMC enzymes in a ballistic fashion [79] (relevant time-scales: $10^3 - 10^4$ s in *B. subtilis* [79]). On a smaller scale, the dynamics of individual DNA loci depends on metabolism (relevant time-scales: $1 - 100$ s [60]), exhibiting non-ergodic dynamics in some cases [60]. In many cases, the non-equilibrium dynamics stem from the activity of enzymatic nucleoid-associated proteins (NAPs) such as SMCs [36], MukBEFs [58], topoisomerases [43] and, as recently shown, even ParBs [39, 67]. These *in vivo* data show that non-equilibrium dynamics are manifest across multiple orders of magnitude.

Despite living in a non-equilibrium environment, theoretical analyses of e.g. plectonemes are succesful in predicting key features of plectonemes even in the assumption of equilibrium [16, 34, 52, 62]. The success of equilibrium frameworks inside a non-equilibrium system shows that not all aspects of chromosome dynamics are equally far removed from equilibrium. A primary reason for this is that some processes relax so fast that their outside environment appears quasi-static. In this case, the comparatively slow non-equilibrium activity only sets up quasi-static constraints for the fast dynamics. Well-known from thermodynamics, such quasi-static changes are called *adiabatic* [63]. The fast dynamics are then in equilibrium with the adiabatic process.

Whether a process has fast relaxation dynamics often depends on the length-scale. In particular, small polymer sub-chains (size s_-) have proportionally fewer degrees of freedom than larger chains ($s_+ > s_-$). Everything else being equal, a subsystem with fewer degrees of freedom will require a shorter time to equilibrate [22, 40, 59, 64]. Thus, we expect an *ordering* of the relaxation time-scales of polymer sub-chains based on their respective sizes $s_- < s_+ \iff t(s_-) < t(s_+)$.

The above analysis of relaxation time-scales shows that, for long enough polymer chains, there are always length-scales whose relaxation times are comparable to the time-scale τ_e of active forcing (Figure 3.1). Although we did not find experimental measurements of this, theoretical models of polymer dynamics show that length-scales with relaxation times much shorter or much longer than τ_e will exhibit thermal-like dynamics, whereas length-scales s_p with $t(s_p) \approx \tau$ will be slow enough so that their degrees of freedom will couple to the non-equilibrium process in a non-adiabatic fashion [59].[1]

[1] In more detail, Osmanović [59] shows that pumping energy with a typical time-scale τ_e into a polymer (in the form of an additional local noise source,

What can we learn from the above discussion about relaxation times? We argued that short length-scale processes in the chromosome can be modeled using equilibrium methods, but that the slower, collective variables can nevertheless exhibit non-equilibrium dynamics. The fact that DNA polymer dynamics is frequently driven away from equilibrium by enzymatic activity changes the type of simulation tools we can use. For example, standard (equilibrium) Monte-Carlo assumes detailed balance, and therefore cannot be used for non-equilibrium processes [57]. Other methods exist to simulate such non-equilibrium systems such as Molecular Dynamics [61] and Brownian Dynamics [29]. Luckily, some of the tools from the field of equilibrium Monte-Carlo simulation can still be used for non-equilibrium processes as long as there exists *local equilibrium* [20, 75]. In part II of this thesis, we take on that challenge by leveraging the concept of local equilibrium: we will develop, implement and test all ingredients necessary for a framework for the non-equilibrium simulation of heterogeneous bio-assemblies.

exponentially correlated with a decorrelation time τ_e) affects the polymer dynamics in the following ways: (i) Modes become coupled, where the amount of coupling depends on a balance between τ_e and the mode relaxation times; (ii) The energy stored in a given mode now depends on a combination of τ_e and the mode length-scale, i.e. equipartition is broken—the very slow modes simply 'see' a higher effective temperature and the very fast modes are unchanged; (iii) How far away from the non-equilibrium source the external driving can still be observed depends on τ_e—with higher τ_e corresponding to a larger 'observational radius'.

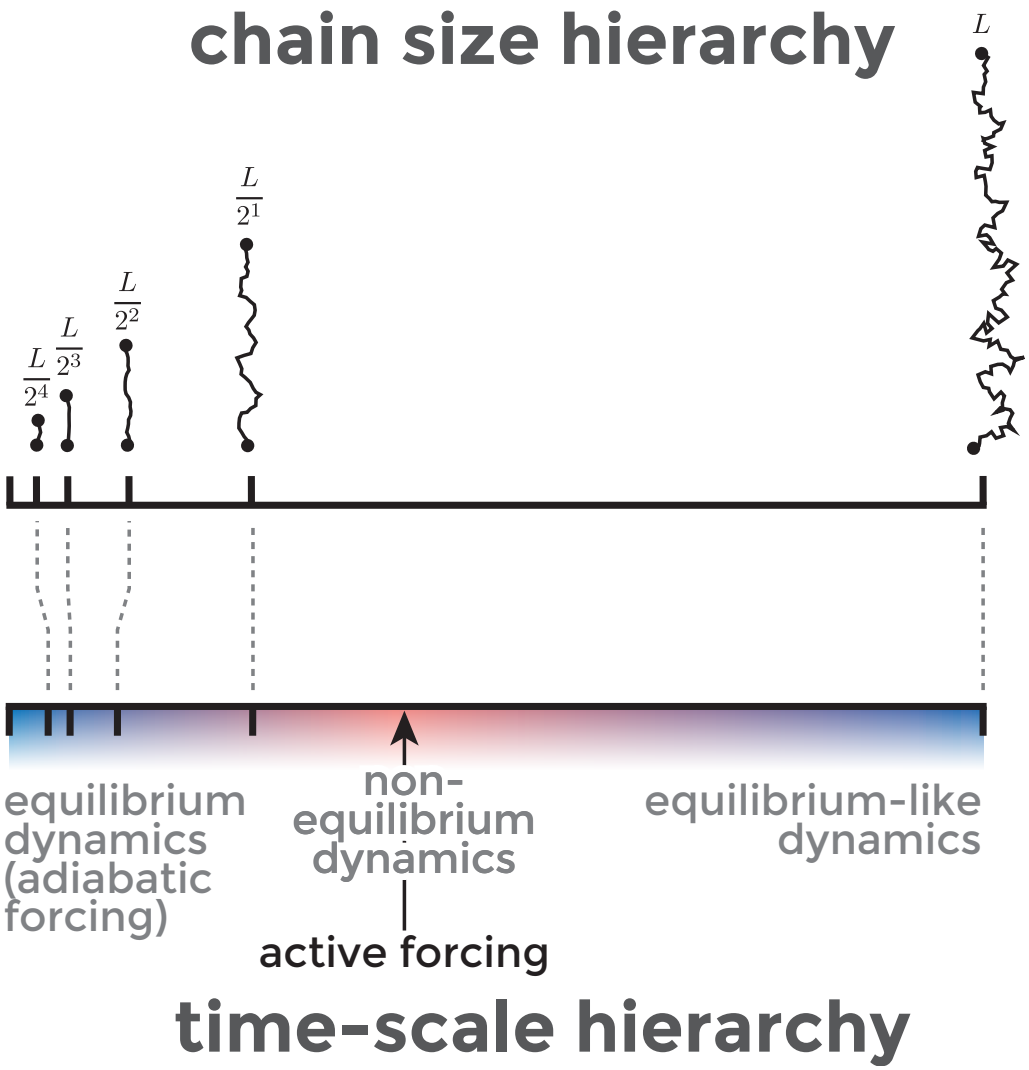

Figure 3.1: **In the presence of active forcing, polymers of a certain size are driven away from equilibrium, whereas others remain close to equilibrium. Left**: Hypothetical polymer with contour lengths $L/2^p$. **Right**: The largest relaxation time of these chains is $\tau_p = \tau_1/p^2$ (assuming these are random walks). A hypothetical active forcing (zero mean) takes place on a time-scale $\tau_4 \ll \tau_e \ll \tau_1$. The dynamics of polymers with largest time-scales $\tau_p \approx \tau_e$ are driven away from equilibrium (most prominently in this figure, τ_2). The chains p with $\tau_p \ll \tau_e$ are close to equilibrium because they observe the active forcing as an adiabatic change. The chains p with $\tau_p \gg \tau_e$ are close to equilibrium because their dynamics does not register the quickly changing active forcing.

4

Crosslinking of DNA Loci Reveals Organization

Chapter summary: *Contact frequency maps from DNA cross-linking experiments provide a fingerprint of chromosome organization, showing that the chromosome has structure across multiple length-scales.*

How can we gain insight into the spatial organization of chromosomes? This question has been addressed by using different forms of imaging: electron micrographs, fluorescent imaging and confocal microscopy. All these methods have the distinct disadvantage of only providing a two-dimensional projection of a three-dimensional system. Amongst these, fluorescent imaging can track individual genetic loci, but not all loci simultaneously. This lack of data inhibited modeling, and much of the understanding was qualitative rather than quantitative. A major recent advancement to gain more direct insight into the three-dimensional structure of the chromosome has been the development of the *chromosome conformation capture* (3C) method and improved 3C-like methods [21]. In 3C, a fingerprint of the three-dimensional organization is generated in the form of a map of DNA–DNA contacts. Conceptually, the procedure of 3C(-like) methods is displayed in figure 4.1. The result of is a collection of small DNA fragments that were in proximity to one another before the protocol was started—hence, this process generates an ensemble of DNA–DNA contacts. Once sequenced, the list of DNA–DNA contacts can be sorted by sequence position and counted to generate a histogram: the contact frequency matrix ('contact map' for short).[1] Since the contact map is an encoding of how close pairs of DNA loci are, it is a fingerprint of chromosomal organization. The surge of data coming from 3C(-like) methods has generated not just a more detailed picture of the chromosome—it has enabled both quantitative modeling of the bacterial chromosome as well as comparison with other techniques, which has lead to surprising insights [46, 48, 51, 72].

[1] Strictly speaking, the sequenced data is usually fed through additional algorithms and filters, so that Hi-C maps in the literature do not strictly represent the contact frequency [45].

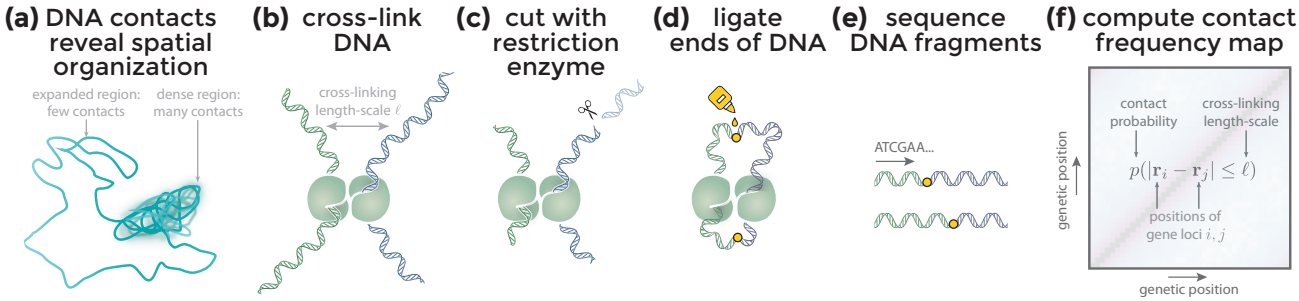

Figure 4.1: **Schematic of Hi-C method for generating contact maps. (a)** The frequency of DNA-DNA contacts in the chromosome is related to how compacted that region is. **(b)** Two loci are chemically cross-linked, resulting in covalent bonds between proximate DNA loci—although this may be more subtle than previously thought [54]. **(c)** A restriction enzyme cuts the DNA at a certain basepair sequence. **(d)** The 'sticky ends' of the cut DNA are now *ligated* (glued together) and marked at the point of ligation. **(e)** The DNA fragments containing a number of basepairs from either side of the ligation point are sequenced. **(f)** The sequences that were ligated are defined to be *in contact*, and this is registered as a hit in the contact frequency map. Figure inspired by [47].

What do we expect for the contact probability $P_c(i,j)$ of a random polymer?[2] As we did in section 2.1 for size scaling exponents, we use a discrete random walk (nth coordinate $\mathbf{R}(n)$) as a toy-model to explore this property. We define the contact probability as the probability for $\mathbf{R}(n)$ to return to a hypersphere of radius ℓ. Before we derive the precise form of $P_c(i,j)$, several properties of $P_c(i,j)$ can be postulated:

$P_c(i,j) = P_c(|i-j|)$ Homopolymers must be translationally invariant in a global displacement along the arc-length.

$P_c(1) = 1$ We consider inextensible segments, where each segment advances the polymer by a fixed distance $|\mathbf{R}(i+1) - \mathbf{R}(i)| = \ell$.

$P_c(n) \sim n^{\delta}$ Polymers are scale-invariant objects.

$\delta = f(d)$ For a one-dimensional random walk, only segments along one dimension have to return to the origin; for a two-dimensional walk, the segments in *both* dimensions must return—a stronger condition. Thus, we expect that $|\delta_{d=2}| > |\delta_{d=1}|$.

As we derived in section 2.1, the probability density function of the displacement vector $\mathbf{R}$ of a random walk ($n \gg 1$ steps) follows a Gaussian:

$$p(\mathbf{R}(n)) = \frac{1}{\sqrt{(2\pi/d)^d \sigma(n)^{2d}}} \exp\left(-\frac{d\mathbf{R}^2}{2\sigma(n)^2}\right).$$

The translationally invariant form of $p(\mathbf{R}(n))$ implies that $P_c(n)$ must be translationally invariant, as previously postulated. This contact probability is simply the probability mass found inside the sphere with all coordinates $\mathbf{R} \in \{|\mathbf{R}| \leq \ell\}$:

$$P_c(n) = \int \mathrm{d}\mathbf{R}\, \theta(\ell - |\mathbf{R}|) p(\mathbf{R}(n)),$$

where $\theta(x)$ is the Heaviside theta. For $\ell \ll \sigma$, the $p(\mathbf{R}(n))$ is approximately constant around $|\mathbf{R}| = 0$, so that we can write

$$\begin{aligned} P_c(n) &\approx p(0) \int \mathrm{d}\mathbf{R}\, \theta(\ell - |\mathbf{R}|) \\ &= \frac{\ell^d V_d(1)}{\sqrt{(2\pi/d)^d}} \frac{1}{\sigma(n)^d} \\ &\sim n^{-d/2}, \end{aligned}$$

[2] We use a capital "P" to make explicit that this is *not* a probability density but a probability proper, since we define two monomers to be either in contact or not.

where $V_d(1)$ is the volume of a $d-$dimensional unit-sphere and the approximation in the first line improves with increasing $\sigma(n)/\ell$. We thus see that the contact probability of random walks exhibits a power-law with an exponent $\delta = -d/2$ that, unlike the size scaling exponent of random walks, depends on the dimensionality of space. As a rough approximation, we can again use the above formula for the contact probability for a general size scaling exponent ν in $\sigma(n) \sim n^{\nu}$, leading to $\delta = -\nu d$. Despite arriving at this result through a naive substitution, it is to the best of my knowledge, used as the currently accepted value [6, 19].

Now that we have an expectation for $P_c(n)$, we can examine how Hi-C data from live cells compares to such a power-law. Indeed, we find that a large portion of the data shows a power-law with exponent $\delta \approx -1$ which would correspond to a compact object ($\nu \approx 1/3$) in three dimensions (Figure 4.2a). There are, however, clear deviations from this power-law at length-scales $\sim$ 100 kbp ($\approx 680\ell_p$ [1, 50]). This is unlikely to be a boundary effect, as these length-scales far exceed the local persistence ℓ_p of the DNA molecule. The decay of P_c at these length-scales has a $|\delta| < 1$, which would correspond to a $\nu < 1/3$ according to $\delta = -d\nu$—physically impossible as this represents more compaction than that of a space-filling object. Additionally, examining the contact frequencies in the full matrix form $P_c(i, j)$ (Figure 4.2b), we see that the contact frequencies for the bacterial chromosome do not exhibit translational invariance. Instead, there is a surprising cross-diagonal centered around the *ori* region, corresponding to the arm-arm alignment already discussed in section 2.4. More subtly visible in the contact map are also high-frequency regions around the main diagonal that correspond to highly compacted interaction domains (Figure 2.4c). Taken together, these properties of the *in vivo* Hi-C data indicate that the bacterial chromosome is far more interesting, and complex, than a simple homopolymer.

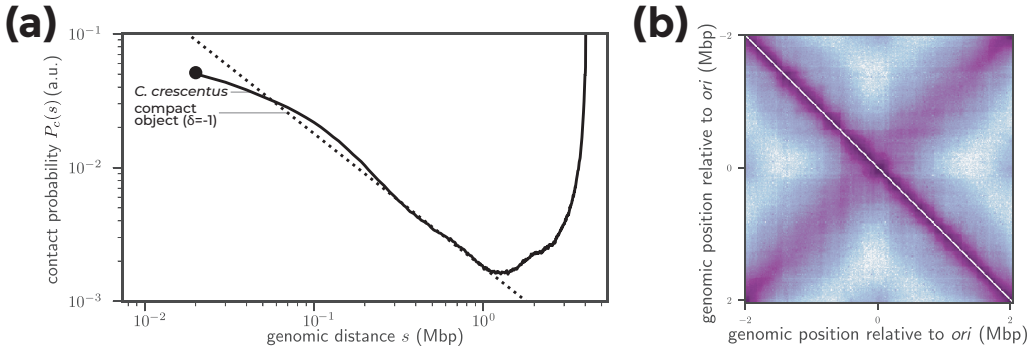

Figure 4.2: **Hi-C data from live cells show multiple types of spatial organization of the bacterial chromosome. (a)** Unnormalized contact probability versus genomic distance between loci for *C. crescentus* cells. For comparison, the contact probability for a fractal space-filling polymer ($\delta = -d\nu = -1$) is also shown. Contacts were not present for genomic distances below a certain length-scale marked by the black circle. **(b)** Full contact map $P_c(i, j)$ that was used to compute panel (a). Data was taken from wild-type *C. crescentus* swarmer cells (data accessible at NCBI GEO database [46], accession GSE45966).

5

Goals and Significance

There are many types of chromosome organization in bacteria across multiple length-scales [77], but we are particularly interested in the arm–arm juxtaposition present in e.g. *C. crescentus* and *B. subtilis* (Figure 4.2). Since *in vivo* studies have shown that SMC condensin is needed for this type of organization [78, 79], juxtaposition is attributed to the action of condensins. Surprisingly, there are typically only 3 – 30 condensins bound to the chromosome at any time [83], making condensins remarkably efficient at creating arm–arm contacts over millions of basepairs [78]. Additionally, these condensins are able to align the two chromosomal arms in less than half an hour post-induction [79]. The condensins accomplish this feat of dynamically structuring a less organized DNA polymer inside a confined environment, across DNA-bound obstacles [11]. Understanding how condensins achieve this level of speed and efficiency at organizing an entire DNA polymer is difficult to do *in vivo*— point mutations can be used to probe the role of protein functionality, but have multiple interpretations. Firstly, lack of viability can indicate that the mutation perturbs an essential function; secondly, the same mutation can also disturb interactions with other proteins, that are more directly responsible for cell fate. Our computational models neglect much of the complexity present in live cells, but can more directly probe the impact of various molecular mechanisms on chromosome organization. In sum, this thesis attempts to propose a model for juxtaposed organization by bacterial condensin with both the speed and efficiency as observed in live cells.

In this introduction, we started by exploring the phenomenology of a simple random walk, and demonstrated how it fails to account for several types of experimental data in the context of chromosome organization. Given the complexity of living systems, it should not come as a surprise that the simplest possible model has its drawbacks. Perhaps more surprising though, the random walk has been successfully modified in rather modest ways to provide new and meaningful insights into large-scale chromosome organization [2, 25, 27, 28, 53]. This raises the question: *which* essential ingredients should be added to reliably produce fast, efficient and robust juxtaposed organization? We address this puzzle by using a *minimal model approach*: rather than attempting to include as much of the complexity of the chromosome as possible, we gradually add ingredients to the simplest possible model, until it captures key features of the empirical data. Before we are able to do that, we need to develop a simulation framework that can simulate the interplay between the action of condensins and chromosome dynamics. Therefore, this thesis addresses the following questions:

> *What ingredients should a kinetic Monte-Carlo method contain for the simulation of chromosome organization by SMC condensins, and how far from equilibrium can the simulation be driven by these model condensins?*
>
> *What kind of minimal model for SMC condensin is consistent with the experimental data of juxtaposed organization in bacteria?*

Why is our reductionist approach, based on minimal models, useful? Firstly, we will see that several possible models for chromosome organization by condensin can plausibly be ruled out, based on disagreement with empirical data. In particular, we argue in section 11.1 that condensins that move diffusively can collectively organize large DNA molecules, but that its organizational mechanism is fundamentally density-driven. This dependence on condensin density makes diffusively moving condensins dramatically inefficient compared to condensin in live cells. Indeed, we find that condensins with motor activity organize the chromosome in a way consistent with the empirical data (section 11.2). Secondly, our simulations

could provide input for the design of reconstituted or *de novo* nucleoids. To that end, we provide state diagrams of chromosome organization across a wide variety of parameter values such as motor velocity and persistence (chapter 11.2), data difficult to acquire experimentally for many parameter values. Finally, during the development of our simulation framework we characterized several fundamental limitations of lattice-based kinetic Monte-Carlo methods for polymer dynamics far from equilibrium. To our knowledge, some of these simulation artifacts far-from-equilibrium have not previously been reported in the literature (chapter 8.3).

Bibliography

[1] B Alberts, A Johnson, J Lewis, D Morgan, M Raff, K Roberts, and P Walter. *Molecular Biology of the Cell, Sixth Edition*. Multidisciplinary Digital Publishing Institute (MDPI), nov 2014.

[2] Elnaz Alipour and John F Marko. Self-organization of domain structures by DNA-loop-extruding enzymes. *Nucleic acids research*, 40(22):11202–12, dec 2012. ISSN 1362-4962.

[3] Anjana Badrinarayanan, Tung B K Le, and Michael T Laub. Bacterial chromosome organization and segregation. *Annual review of cell and developmental biology*, 31:171–99, 2015. ISSN 1530-8995.

[4] C G Baumann, S B Smith, V A Bloomfield, and C Bustamante. Ionic effects on the elasticity of single DNA molecules. *Proceedings of the National Academy of Sciences of the United States of America*, 94(12):6185–90, jun 1997. ISSN 0027-8424.

[5] Somendra M Bhattacharjee, Achille Giacometti, and Amos Maritan. Flory theory for Polymers. *Journal of physics: Condensed Matter*, 25:503101, 2013.

[6] RALF. BLOSSEY BLOSSEY. *COMPUTATIONAL BIOLOGY : a statistical mechanics perspective.* CRC PRESS, 2019. ISBN 9780367390822.

[7] C A Brackley, J Johnson, D Michieletto, and D Marenduzzo. Effect of chromatin flexibility on diffusive loop extrusion via molecular slip-links. *bioRxiv*, page 275214, 2018.

[8] C. A. Brackley, J. Johnson, D. Michieletto, A. N. Morozov, M. Nicodemi, P. R. Cook, and D. Marenduzzo. Extrusion without a motor: a new take on the loop extrusion model of genome organization. *Nucleus*, 9(1):95–103, jan 2018. ISSN 1949-1034.

[9] Chris A Brackley, Stephen Taylor, Argyris Papantonis, Peter R Cook, and Davide Marenduzzo. Nonspecific bridging-induced attraction drives clustering of DNA-binding proteins and genome organization. *Proceedings of the National Academy of Sciences of the United States of America*, 110 (38):E3605–11, sep 2013. ISSN 1091-6490.

[10] Chris A Brackley, James Johnson, Davide Michieletto, Alexander N Morozov, Mario Nicodemi, Peter R Cook, and Davide Marenduzzo. Non-equilibrium chromosome looping via molecular slip-links. *Physical Review Letters*, 119(13):138101, 2017.

[11] Hugo B Brandão, Payel Paul, Aafke A van den Berg, David Z Rudner, Xindan Wang, and Leonid A Mirny. RNA polymerases as moving barriers to condensin loop extrusion. *Proceedings of the National Academy of Sciences of the United States of America*, 116(41):20489–20499, oct 2019. ISSN 1091-6490.

[12] Sanneke Brinkers, Heidelinde R. C. Dietrich, Frederik H. de Groote, Ian T. Young, and Bernd Rieger. The persistence length of double stranded DNA determined using dark field tethered particle motion. *The Journal of Chemical Physics*, 130(21):215105, jun 2009. ISSN 0021-9606.

[13] C. P. Broedersz, X. Wang, Y. Meir, J. J. Loparo, D. Z. Rudner, and N. S. Wingreen. Condensation and localization of the partitioning protein ParB on the bacterial chromosome. *Proceedings of the National Academy of Sciences*, 111(24):8809–8814, jun 2014. ISSN 0027-8424.

[14] Frank Bürmann, Alrun Basfeld, Roberto Vazquez Nunez, Marie-Laure Diebold-Durand, Larissa Wilhelm, and Stephan Gruber. Tuned SMC Arms Drive Chromosomal Loading of Prokaryotic Condensin. *Molecular Cell*, 65(5):861–872.e9, mar 2017. ISSN 10972765.

[15] Nathan Clisby. Accurate estimate of the critical exponent ν for self-avoiding walks via a fast implementation of the pivot algorithm. feb 2010.

[16] Simona Cocco, John F. Marko, and Rémi Monasson. Theoretical models for single-molecule DNA and RNA experiments: from elasticity to unzipping. *Comptes Rendus Physique*, 3(5):569–584, jan 2002. ISSN 1631-0705.

[17] Remus T. Dame. The role of nucleoid-associated proteins in the organization and compaction of bacterial chromatin, 2005. ISSN 0950382X.

[18] Remus T. Dame, Fatema-Zahra M. Rashid, and David C. Grainger. Chromosome organization in bacteria: mechanistic insights into genome structure and function. *Nature Reviews Genetics*, pages 1–16, nov 2019. ISSN 1471-0056.

[19] Pierre-Gilles de. Gennes. *Scaling concepts in polymer physics*. Cornell University Press, 1979. ISBN 080141203X.

[20] S.R. de Groot and P. Mazur. *Non-Equilibrium Thermodynamics*. North-Holland, Amsterdam, 1962.

[21] Job Dekker, Karsten Rippe, Martijn Dekker, and Nancy Kleckner. Capturing chromosome conformation. *Science (New York, N.Y.)*, 295(5558): 1306–11, feb 2002. ISSN 1095-9203.

[22] M. Doi and S. F. Edwards. *The Theory of Polymer Dynamics*. Clarendon Press, Oxford, 1986.

[23] Jay K Fisher, Aude Bourniquel, Guillaume Witz, Beth Weiner, Mara Prentiss, and Nancy Kleckner. Four-Dimensional Imaging of E.Â coli Nucleoid Organization and Dynamics in Living Cells. *Cell*, 153:882–895, 2013.

[24] Michael E Fisher. Shape of a Self-Avoiding Walk. *The Journal of Chemical Physics*, 44(2):104904–1321, 1966.

[25] Geoffrey Fudenberg, Maxim Imakaev, Carolyn Lu, Anton Goloborodko, Nezar Abdennur, and LeonidÂ A. Mirny. Formation of Chromosomal Domains by Loop Extrusion. *Cell Reports*, 15(9):2038–2049, 2016. ISSN 22111247.

[26] Mahipal Ganji, Indra A Shaltiel, Shveta Bisht, Eugene Kim, Ana Kalichava, Christian H Haering, and Cees Dekker. Real-time imaging of DNA loop extrusion by condensin. *Science*, 360(6384):102–105, feb 2018. ISSN 1095-9203.

[27] Anton Goloborodko, Maxim V Imakaev, John F Marko, and Leonid Mirny. Compaction and segregation of sister chromatids via active loop extrusion. *eLife*, 5, may 2016. ISSN 2050-084X.

[28] Anton Goloborodko, John F Marko, and Leonid A Mirny. Chromosome Compaction by Active Loop Extrusion. *Biophysical Journal*, 110, 2016.

[29] P. S. Grassia, E. J. Hinch, and L. C. Nitsche. Computer simulations of Brownian motion of complex systems. *Journal of Fluid Mechanics*, 282: 373–403, 1995. ISSN 1469-7645.

[30] Stephan Gruber. Multilayer chromosome organization through DNA bending, bridging and extrusion. *Current Opinion in Microbiology*, 22: 102–110, 2014. ISSN 13695274.

[31] Anthony J Guttmann. Self-Avoiding Walks and Polygons – An Overview. *Asia Pacific Mathematics Newsletter*, 2(4), 2012.

[32] Karin R. Hagerman and Paul J. Hagerman. Helix Rigidity of DNA: The Meroduplex as an Experimental Paradigm. *Journal of Molecular Biology*, 260(2):207–223, jul 1996. ISSN 0022-2836.

[33] Christine D Hardy, Nancy J Crisona, Michael D Stone, and Nicholas R Cozzarelli. Disentangling DNA during replication: a tale of two strands. *Philosophical Transactions of the Royal Society of London. Series B, Biological sciences*, 359(1441):39–47, jan 2004. ISSN 0962-8436.

[34] John E. Hearst and Nathaniel G. Hunt. Statistical mechanical theory for the plectonemic DNA supercoil. *The Journal of Chemical Physics*, 95(12): 9322–9328, dec 1991. ISSN 0021-9606.

[35] Tatsuya Hirano. At the heart of the chromosome: SMC proteins in action. *Nature Reviews Molecular Cell Biology*, 7(5):311–322, may 2006. ISSN 1471-0072.

[36] Tatsuya Hirano. Condensin-Based Chromosome Organization from Bacteria to Vertebrates. *Cell*, 164:847–857, 2016.

[37] Hsiao-Ping Hsu. Monte Carlo simulations of lattice models for single polymer systems. *The Journal of Chemical Physics*, 141(16):164903, oct 2014. ISSN 0021-9606.

[38] Michael Ingerson-Mahar and Zemer Gitai. A growing family: the expanding universe of the bacterial cytoskeleton. *FEMS Microbiology Reviews*, 36(1):256–266, jan 2012. ISSN 1574-6976.

[39] Adam S. B. Jalal, Ngat T. Tran, and Tung B. K. Le. ParB spreading on DNA requires cytidine triphosphate in vitro. *bioRxiv*, page 2019.12.11.865972, dec 2019.

[40] Mehran Kardar. *Statistical Physics of Particles*. Cambridge University Press, Cambridge, New York, 2007. ISBN 9780521873420.

[41] HyeongJun Kim and Joseph J. Loparo. Multistep assembly of DNA condensation clusters by SMC. *Nature Communications*, 7:10200, jan 2016. ISSN 2041-1723.

[42] Nancy Kleckner, Jay K. Fisher, Mathieu Stouf, Martin A. White, David Bates, and Guillaume Witz. The bacterial nucleoid: Nature, dynamics and sister segregation, 2014. ISSN 18790364.

[43] Fedor Kouzine, David Levens, and Laura Baranello. DNA topology and transcription. *Nucleus (Austin, Tex.)*, 5(3):195–202, jan . ISSN 1949-1042.

[44] Andrei Kuzminov. The precarious prokaryotic chromosome. *Journal of Bacteriology*, 196(10):1793–806, may 2014. ISSN 1098-5530.

[45] Bryan R. Lajoie, Job Dekker, and Noam Kaplan. The Hitchhiker's guide to Hi-C analysis: Practical guidelines. *Methods*, 72:65–75, jan 2015. ISSN 10462023.

[46] Tung B K Le, Maxim V Imakaev, Leonid A Mirny, and Michael T Laub. High-Resolution Mapping of the Spatial Organization of a Bacterial Chromosome. *Science*, 342(6159):731–734, nov 2013. ISSN 0036-8075.

[47] Erez Lieberman-Aiden, Nynke L van Berkum, Louise Williams, Maxim Imakaev, Tobias Ragoczy, Agnes Telling, Ido Amit, Bryan R Lajoie, Peter J Sabo, Michael O Dorschner, Richard Sandstrom, Bradley Bernstein, M A Bender, Mark Groudine, Andreas Gnirke, John Stamatoyannopoulos, Leonid A Mirny, Eric S Lander, and Job Dekker. Comprehensive mapping of long-range interactions reveals folding principles of the human genome. *Science (New York, N.Y.)*, 326(5950):289–93, oct 2009. ISSN 1095-9203.

[48] Virginia S Lioy, Axel Cournac, Olivier Espé, Fré Dé, Ric Boccard, Romain Koszul Correspondence, Martial Marbouty, Sté Phane Duigou, Julien Mozziconacci, and Romain Koszul. Multiscale Structuring of the E. coli Chromosome by Nucleoid-Associated and Condensin Proteins. *Cell*, 172: 771–783, 2018.

[49] Ana Losada and Tatsuya Hirano. Dynamic molecular linkers of the genome: the first decade of SMC proteins. *Genes & development*, 19(11): 1269–87, jun 2005. ISSN 0890-9369.

[50] Gerald S Manning. The persistence length of DNA is reached from the persistence length of its null isomer through an internal electrostatic stretching force. *Biophysical journal*, 91(10):3607–16, nov 2006. ISSN 0006-3495.

[51] Martial Marbouty, Antoine Le Gall, Diego I Cattoni, Axel Cournac, Alan Koh, Jean-Bernard Fiche, Julien Mozziconacci, Heath Murray, Romain Koszul, and Marcelo Nollmann. Condensin- and Replication-Mediated Bacterial Chromosome Folding and Origin Condensation Revealed by Hi-C and Super-resolution Imaging. *Molecular Cell*, 59(4):588–602, aug 2015. ISSN 1097-4164.

[52] John F Marko and Sébastien Neukirch. Global force-torque phase diagram for the DNA double helix: structural transitions, triple points, and collapsed plectonemes. *Physical review. E, Statistical, nonlinear, and soft matter physics*, 88(6):062722, dec 2013. ISSN 1550-2376.

[53] John F. Marko, Paolo De Los Rios, Alessandro Barducci, and Stephan Gruber. DNA-segment-capture model for loop extrusion by structural maintenance of chromosome (SMC) protein complexes. *bioRxiv*, page 325373, sep 2018.

[54] Joris J. B. Messelink, Jacqueline Janssen, Muriel C. F. van Teeseling, Martin Thanbichler, and Chase P. Broedersz. Resolving the degree of order in the bacterial chromosome using a statistical physics approach. *arXiv*, feb 2020.

[55] Anita Minnen, Frank Bürmann, Larissa Wilhelm, Anna Anchimiuk, Marie-Laure Diebold-Durand, and Stephan Grüber. Control of Smc Coiled Coil Architecture by the ATPase Heads Facilitates Targeting to Chromosomal ParB/parS and Release onto Flanking DNA. *Cell Reports*, 14, 2016.

[56] Uri Moran, Rob Phillips, and Ron Milo. SnapShot: Key Numbers in Biology. *Cell*, 141:1262–1262, 2010.

[57] Mej Newman and Gt Barkema. *Monte Carlo methods in statistical physics*. Clarendon Press, 1999. ISBN 0198517971.

[58] Sophie Nolivos and David Sherratt. The bacterial chromosome: architecture and action of bacterial SMC and SMC-like complexes Identification, initial characterization and distribution of Structural Maintenance of Chromosomes (SMC) complexes. *FEMS Microbiology Reviews*, 38:380–392, 2014.

[59] Dino Osmanović. Properties of Rouse polymers with actively driven regions. *The Journal of Chemical Physics*, 149(16):164911, oct 2018. ISSN 0021-9606.

[60] Bradley R. Parry, Ivan V. Surovtsev, Matthew T. Cabeen, Corey S. O'Hern, Eric R. Dufresne, Christine Jacobs-Wagner, R.H. Singer, T. Earnest, L. Shapiro, H. Löwen, and D. Vlassopoulos. The Bacterial Cytoplasm Has Glass-like Properties and Is Fluidized by Metabolic Activity. *Cell*, 156 (1-2):183–194, jan 2014. ISSN 00928674.

[61] Juan R Perilla, Boon Chong Goh, C Keith Cassidy, Bo Liu, Rafael C Bernardi, Till Rudack, Hang Yu, Zhe Wu, and Klaus Schulten. Molecular dynamics simulations of large macromolecular complexes. *Current Opinion in Structural Biology*, 31:64–74, 2015.

[62] Prashant K. Purohit. Plectoneme formation in twisted fluctuating rods. *Journal of the Mechanics and Physics of Solids*, 56(5):1715–1729, may 2008. ISSN 0022-5096.

[63] L. E. Reichl. *A Modern Course in Statistical Physics*, volume 67. Wiley, 4 edition, 2016. ISBN 978-3-527-40782-8.

[64] Michael Rubinstein and Ralph H. Colby. *Polymer Physics*. Oxford University Press, 2003.

[65] TylerÂ N. Shendruk, Martin Bertrand, HendrickÂ W. deÂ Haan, JamesÂ L. Harden, and GaryÂ W. Slater. Simulating the Entropic Collapse of Coarse-Grained Chromosomes. *Biophysical Journal*, 108(4):810–820, 2015. ISSN 00063495.

[66] Martin R. Singleton, Mark S. Dillingham, and Dale B. Wigley. Structure and Mechanism of Helicases and Nucleic Acid Translocases. *Annual Review of Biochemistry*, 76(1):23–50, jun 2007. ISSN 0066-4154.

[67] Young-Min Soh, Iain Finley Davidson, Stefano Zamuner, Jérôme Basquin, Florian Patrick Bock, Michael Taschner, Jan-Willem Veening, Paolo De Los Rios, Jan-Michael Peters, and Stephan Gruber. Self-organization of parS centromeres by the ParB CTP hydrolase. *Science (New York, N.Y.)*, 366(6469):1129–1133, nov 2019. ISSN 1095-9203.

[68] Nora L Sullivan, Kathleen A Marquis, and David Z Rudner. Recruitment of SMC by ParB-parS Organizes the Origin Region and Promotes Efficient Chromosome Segregation. *Cell*, 137(137):697–707, 2009.

[69] Tsuyoshi Terekawa, Shveta Bisht, Jorine Eeftens, Cees Dekker, Christian Haering, and Eric Greene. The Condensin Complex Is A Mechanochemical Motor That Translocates Along DNA. *Science*, 358(6363):672–676, 2017.

[70] Esteban Toro and Lucy Shapiro. Bacterial chromosome organization and segregation. *Cold Spring Harbor Perspectives in Biology*, 2(2):a000349, feb 2010. ISSN 1943-0264.

[71] Ngat T Tran, Michael T Laub, and Tung B K Le. SMC progressively aligns chromosomal arms in Caulobacter crescentus but is antagonized by convergent transcription.

[72] Marie Trussart, François Serra, Davide Baù, Ivan Junier, Luís Serrano, and Marc A Marti-Renom. Assessing the limits of restraint-based 3D modeling of genomes and genomic domains. *Nucleic acids research*, 43(7):3465–77, apr 2015. ISSN 1362-4962.

[73] Mark A. Umbarger, Esteban Toro, Matthew A. Wright, Gregory J. Porreca, Davide Baù, Sun-Hae Hong, Michael J. Fero, Lihua J. Zhu, Marc A. Marti-Renom, Harley H. McAdams, Lucy Shapiro, Job Dekker, and George M. Church. The Three-Dimensional Architecture of a Bacterial Genome and Its Alteration by Genetic Perturbation. *Molecular Cell*, 44(2):252–264, 2011. ISSN 10972765.

[74] N.G. Van Kampen. Stochastic Processes in Physics and Chemistry, 1981.

[75] Arthur F. Voter. INTRODUCTION TO THE KINETIC MONTE CARLO METHOD. In *Radiation Effects in Solids*, pages 1–23. Springer Netherlands, Dordrecht, 2007.

[76] Xindan Wang and David Z Rudner. Spatial organization of bacterial chromosomes. *Current Opinion in Microbiology*, 22:66–72, 2014.

[77] Xindan Wang, Paula Montero Llopis, and David Z Rudner. Organization and segregation of bacterial chromosomes. *Nature Reviews Genetics*, 14: 191–203, 2013.

[78] Xindan Wang, Tung B K Le, Bryan R. Lajoie, Job Dekker, Michael T. Laub, and David Z. Rudner. Condensin promotes the juxtaposition of dna flanking its loading site in Bacillus subtilis. *Genes and Development*, 29(15):1661–1675, 2015. ISSN 15495477.

[79] Xindan Wang, Hugo B. Brandão, Tung B. K. Le, Michael T. Laub, and David Z. Rudner. Bacillus subtilis SMC complexes juxtapose chromosome arms as they travel from origin to terminus. *Science*, 355(6324), 2017.

[80] Xindan Wang, Anna C. Hughes, Hugo B. Brandão, Benjamin Walker, Carrie Lierz, Jared C. Cochran, Martha G. Oakley, Andrew C. Kruse, and David Z. Rudner. In Vivo Evidence for ATPase-Dependent DNA Translocation by the Bacillus subtilis SMC Condensin Complex. *Molecular Cell*, 71(5):841–847.e5, sep 2018. ISSN 1097-2765.

[81] F.W. Wiegel. Introduction To Path Integral Methods In Physics And Polymer Science, 1986.

[82] Paul A Wiggins, Keith C Cheveralls, Joshua S Martin, Robert Lintner, and Jané Kondev. Strong intranucleoid interactions organize the Escherichia coli chromosome into a nucleoid filament. *Proceedings of the National Academy of Sciences of the United States of America*, 107(11):4991–5, mar 2010. ISSN 1091-6490.

[83] Larissa Wilhelm, Frank Bürmann, Anita Minnen, Ho-Chul Shin, Christopher P Toseland, Byung-Ha Oh, Stephan Gruber, E. Alipour, JF. Marko, P. Arumugam, and S. Gruber. SMC condensin entraps chromosomal DNA by an ATP hydrolysis dependent loading mechanism in Bacillus subtilis. *eLife*, 4:11202–11212, may 2015. ISSN 2050-084X.

[84] G Witz, K Rechendorff, J Adamcik, and G Dietler. Conformation of Circular DNA in 2 Dimensions. *Physical Review Letters*, 101(14):148103, 2008.

[85] Hisami Yamada, Shuji Muramatsu, and Takeshi Mizuno. An Escherichia coli Protein That Preferentially Binds to Sharply Curved DNA1. *The Journal of Biochemistry*, 108(3):420–425, sep 1990. ISSN 1756-2651.

Part II

The Design, Testing and Limitations of Lattice Kinetic Monte-Carlo

6

Ingredients of a Lattice Kinetic Monte-Carlo Simulation for Slip-Linked Polymers

Chapter summary: *We provide a detailed description of all tools needed to implement a Lattice Kinetic Monte-Carlo simulation for non-equilibrium slip-linked polymer dynamics.*

6.1 Recipe for the Gillespie Method

In this section we introduce an LKMC framework, which we specifically apply to describe the dynamics of proteins on a fluctuating DNA polymer. To describe the stochastic dynamics of such a system, this LKMC framework employs a Gillespie-type algorithm [5, 13, 15–17, 24, 41], where we assume that all the individual processes T_i have a Poissonian waiting-time distribution with rate k_i. These individual processes may include local configurational changes of the DNA polymer, (un)binding of proteins, or a movement of the protein along the DNA. The microscopic rates k_i will in general depend on the microstate of the system, which is further discussed in section 6.5. Given a set of such microscopic transitions $\Omega = \{T_i, k_i\}$, a process i is selected with a probability $k_i/\sum_i k_i$, i.e. faster processes are performed with a proportionally higher probability in a given time-step. This choice for selecting a microscopic transition guarantees that the stochastic dynamics of each microscopic transition i is Poissonian distributed with rate k_i.

After selecting a microscopic transition i, how do we advance the simulation time t? This depends on the rates of the system: for a set of exponential waiting-time distributions with rates $\{k_i\}$, the waiting time distribution $p(\Delta t)$ for any event to happen in time Δt is also exponential but with a rate $K = \sum_i k_i$ (Figure 6.1c, see appendix S1). Hence, after every reaction, the simulation time is advanced by a sample from an exponential distribution with mean K^{-1}.

Given a choice for the k_i, our LKMC framework consists in detail of the following steps (Figure 6.1):

1. Construct an initial configuration of the system.
2. Build a rate-catalog $\Omega = \{T_i, k_i\}$ of all possible microscopic transitions T_i, where k_i is the rate of that transition. This is done by looping over all particles in the system, and adding to Ω all possible transitions (displacements, changes of internal state and otherwise) that that particle can perform.
3. Perform an arbitrary number of iteration steps, consisting of steps (a)–(f):
   (a) Randomly select one of the transitions T_i from the rate-catalog Ω. The probability to perform T_i is k_i/K, where k_i is the rate of T_i and $K = \sum_i k_i$ is the total rate of the system. We implemented the selection procedure using tower-sampling, equivalent to a linear search on the cumulative distribution function [16, 25, 41], see Figure 6.1c.
   (b) Update the KMC time $t \to t + \Delta t$, where $\Delta t = -\log r/K$ with mean $\langle \Delta t \rangle = K^{-1}$, $r \in \langle 0, 1]$ a uniformly sampled random number [24, 41].

(c) This choice of updating the simulation is simply a random sample Δt from the waiting time distribution $p(\Delta t) = K \exp(-K\Delta t)$ for any event to occur within a time-interval Δt (appendix S1).

(d) Perform transition T_j that was selected in (a), which can affect the positions and/or internal states in the system.

(e) Update the entire rate-catalog of possible transitions Ω based on the transition T_j that was performed in step (c). This can be done in the same way as in step 2, but a more computationally efficient strategy consists of a *minimal local update* (see section 6.3).

(f) Return to step (a).

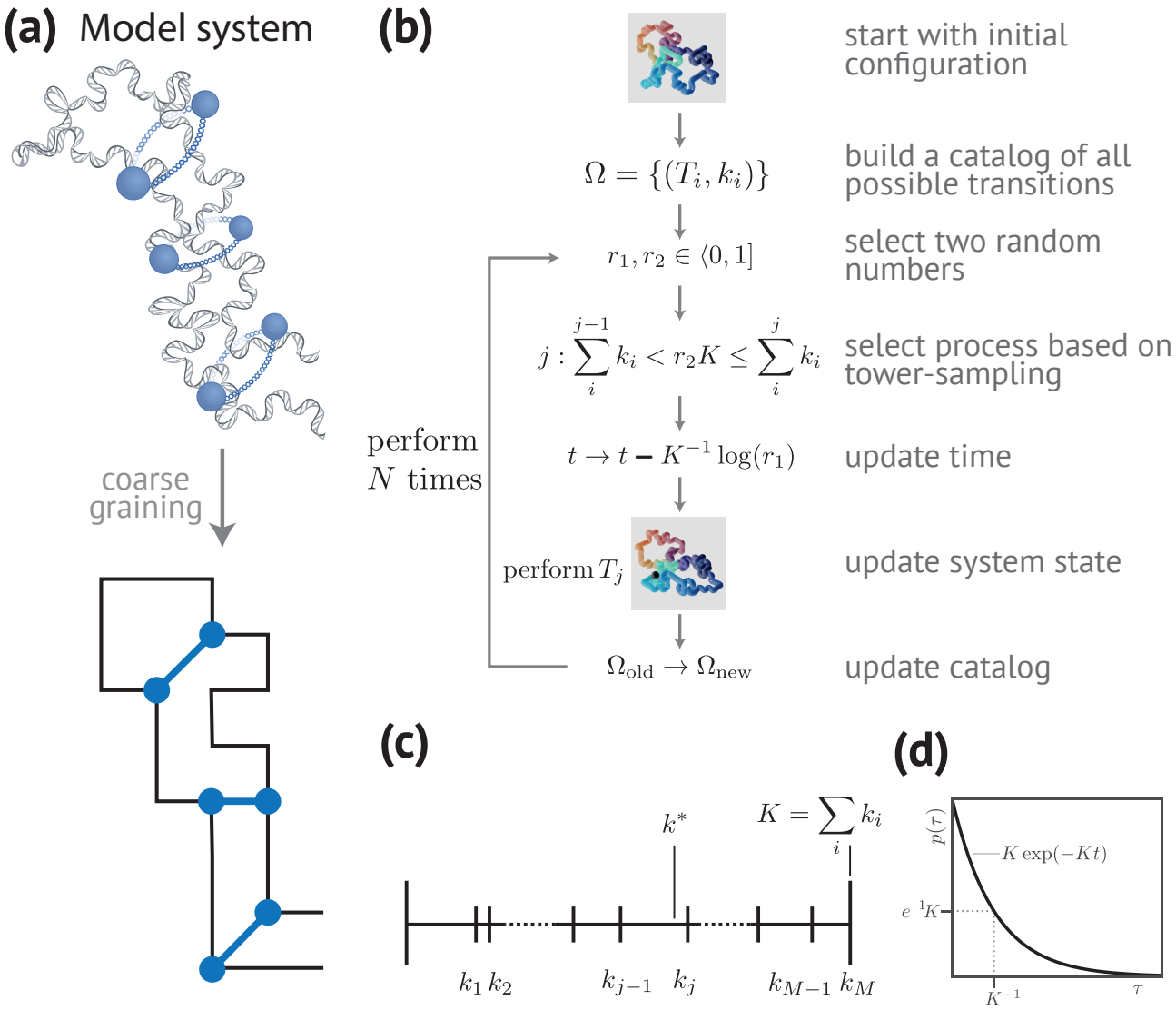

Figure 6.1: **Illustration of the LKMC algorithm. (a)** The Slip-link DNA model system that we employ to illustrate a biologically relevant application of LKMC. This model system consists of a DNA polymer with diffusing elastic rings, which interact with the polymer by trapping DNA loops (top); this is represented in the LKMC as a polymer on a cubic lattice with springs that can diffuse along the DNA polymer (bottom). **(b)** Flow-chart of a Gillespie algorithm with transitions T_i and rates k_i. **(c)** A process j with rate k_j is selected from all possible rates by tower sampling [25, 41]: First, all rates are stacked, producing an array of rate-intervals; then, a random number $k^\star \in [0, K\rangle$ is sampled from a uniform distribution; the location of the interval in which this $k^\star$ lies is located selects the process that will occur. **(d)** The waiting time distribution of any event to occur at time t is $K \exp(-Kt)$, where K is the total rate. The mean of this distribution is $\langle t \rangle = K^{-1}$, and is thus set by the decay rate of the waiting time distribution (see section 6.2).

6.2 Updating time in Gillespie algorithms

Below, we present a derivation for updating time in Gillespie simulations. Similar derivations can be found in e.g. Kratzer [24], Voter [41]. Consider two processes 1,2 with Poissonian waiting-time distributions with rates k_1, k_2. The probability distribution for an event to occur at time t is $p(1;t) = k_1 e^{-k_1 t}$, so that the probability for any event to occur in the time-interval $[0, \Delta t\rangle$ is $P(1;\Delta t) = \int_0^{\Delta t} \mathrm{d}t\, p(1;t) = 1 - \exp(-k_1 \Delta t)$. The probability for *either* process 1 or 2 to have occurred in

the time-interval $[0, \Delta t\rangle$ is

$$\begin{aligned} P(1 \vee 2; \Delta t) &= P(\overline{\bar{1} \vee \bar{2}}; \Delta t) \\ &= 1 - P(\bar{1} \vee \bar{2}; \Delta t) \\ &= 1 - P(\bar{1}; \Delta t) P(\bar{2}; \Delta t), \end{aligned}$$

where the overline is the "not-operator". Thus, we find

$$\begin{aligned} P(1 \vee 2 \Delta t) &= 1 - e^{-k_1 \Delta t} e^{-k_2 \Delta t} \\ &= 1 - e^{-(k_1 + k_2) t}, \end{aligned}$$

i.e. the probability for either process 1 or 2 to occur is again Poissonian, but now with rate $K = k_1 + k_2$. The proof is analogous for more than two processes.

Given that we can sample uniformly random numbers $r \in [0, 1\rangle$, how do we generate samples that are Poissonian distributed with rate K? The probability distribution for an event to occur at time t is $p(t) = Ke^{-Kt}$. To transform this distribution to a distribution for $p(r)$, we use the fact that probability must be conserved in both the r or t coordinates; this implies that $p(t)|\mathrm{d}t| = p(r)|\mathrm{d}r|$. Since $p(r) = 1$ on the corresponding interval, we find $p(t) = |\mathrm{d}r/\mathrm{d}t|$ or

$$\begin{aligned} r &= \pm \int \mathrm{d}t p(t) \\ &= \mp e^{-Kt}, \end{aligned}$$

but, since r must be positive, we find $r = e^{-Kt}$. Inverting this, we find $t = -K^{-1} \log r$.

6.3 Using Locality to Boost Efficiency

The full slip-link model system (Figure 6.1a) contains a DNA polymer, composed of $10^2 - 10^4$ Kuhn monomers *in vivo* [30, 46], and will thus typically also contain $\sim 10^2 - 10^4$ number of allowed transitions in the 'rate-catalog'. However, updating the entire rate-catalog after each time-step would make the LKMC method infeasible for these large particle numbers. Thus, in this section we develop a method to keep the rate-catalog up-to-date with a weaker dependency of the computational complexity on system-size.

Conceptual Description of Local Kinetics

The first time that the rate-catalog $\Omega = \{T_i, k_i\}$ is instantiated, we loop over all particles in the system and add all possible microscopic transitions T_i these particles can undergo. A naive approach to keep Ω updated is to perform this loop over all particles in the system after every microscopic transition. Many systems, however, only involve local kinetics, meaning that a transition T_i affecting a coordinate $\mathbf{r}$ will affect the state of the system only in a local neighborhood of $\mathbf{r}$. Systems involving only local kinetics exhibit a scaling form for the total rate $\langle K \rangle \sim N$ with respect to system size N. Indeed, we observe $\langle K \rangle \sim N$ for self-avoiding polymers (Figure 6.2c), reflecting the local kinetics of such polymers [12].

Systems can exhibit non-local kinetics either due to kinetics that carry an explicit time-dependence (since the entire rate catalog will have to be updated at each time-step), or systems with non-local interactions (because every particle in the system can now interact with every other particle). For such systems, the locality of kinetics cannot be used to increase computational efficiency. When applicable, however, the locality aspect of the kinetics can be leveraged to vastly increase the computational efficiency of the LKMC.

Once we established that a system exhibits local kinetics, how do we actually choose which processes occur, and with which rates? This question can be answered universally if there exists *local equilibrium*. Local equilibrium exists when, on an infinitesimal scale, all processes exhibit equilibrium dynamics [23]. Local equilibrium is a much weaker constraint than global equilibrium, since global equilibrium implies local equilibrium but not *vice versa* [23]. We will see many examples of this in part III of this thesis. Local equilibrium is leveraged to simulate non-equilibrium systems in certain flavors of kinetic Monte-Carlo, where the transition probabilities of microscopic processes are sampled from a distribution that assumes local, but not global thermodynamic equilibrium [24, 41]. As follows from the discussion in chapter 3, local equilibrium in the case of polymer dynamics amounts to the shortest polymer length-scales relaxing faster than the fastest non-equilibrium process. Thus, assuming local equilibrium sets a lower bound on the length-scales we can investigate under this assumption.

We stress that local kinetics and local equilibrium are separate assumptions. Non-local interactions even in thermodynamic equilibrium could occur in various cases: systems with long-range potentials, e.g. non-shielded Coulomb-potentials; systems where particles can displace to any other point in the system-size in a single move; systems with a global conservation law but not a corresponding local conservation law, such as particle unbinding and rebinding anywhere in a canonical ensemble. Conversely, a system can display local kinetics but not be in local thermodynamic equilibrium, for example the paradigmatic totally asymmetric exclusion process [9], the close-to-equilibrium polymer dynamics in section 7.5 and even the far-from-equilibrium systems that we investigate in chapter 8.

Recipe for Leveraging Local Kinetics to Boost Efficiency

To speed up the update step of the LKMC, for example in the case of our slip-link DNA model, we exploit the locality property of the kinetics by only re-computing the set of points $M = \{\mathbf{r}_i\}$ on the lattice that can be affected by the transition T_i. We call this the *minimal local update*, an idea similar to the next reaction method A. and Bruck [1], but applied to the set of reactions instead of the rate constants. The size of the local neighborhood that we have to consider, and hence the number of points in M, is determined by the maximal interaction range δr, which is the maximal length-scale at which particles can interact with each other in a single time-step (compare Figure 6.2a and Figure 6.2b).

The minimal local update involves a set of M coordinates that are updated after each LKMC iteration. If a microscopic transition T_i displaces a particle at coordinate $\mathbf{r}$ to a coordinate $\mathbf{r}'$, then $M = M_1 \cup M_2$, where $M_1 = \{\mathbf{r} + \mathbf{v}\}_{\forall |\mathbf{v}| \leq \delta r(\mathbf{r})}$ and $M_2 = \{\mathbf{r}' + \mathbf{v}\}_{\forall |\mathbf{v}| \leq \delta r(\mathbf{r})}$, i.e. M contains all points within the *maximal interaction ranges* $\delta r(\mathbf{r}), \delta r(\mathbf{r}')$ of the coordinates $\mathbf{r}, \mathbf{r}'$. The maximal interaction ranges $\delta r(\mathbf{r}), \delta r(\mathbf{r}')$ are not necessarily equal to the interaction range of the particle displaced by T_i, but rather by the largest possible interaction range of *all* particles in the system that are affected by T_i. In our slip-link model system for example, a slip-link only ever displaces one lattice site, but the crank-shaft move can displace a monomer by two lattice sites; hence, $\delta r = 1$ if a particular move only affects slip-links but $\delta r = 2$ if a monomer can be affected by the move.

Concretely, the maximal interaction ranges before and after the move are $\delta r(\mathbf{r}) = \max\{\delta r_j \cdot \theta(|\mathbf{r} - \mathbf{r}_j| \leq \delta r_j)\}$ and $\delta r(\mathbf{r}') = \max\{\delta r_j \cdot \theta(|\mathbf{r}' - \mathbf{r}_j| \leq \delta r_j)\}$, where $\theta(\mathbf{x})$ is the three-dimensional Heaviside theta function, the $\mathbf{r}_j$ are the coordinates of all particles in the system and δr_j their corresponding interaction ranges. However, to avoid having to compute the $\delta r(\mathbf{r}), \delta r(\mathbf{r}')$ after every transition T_i in this costly manner, and for the sake of simplicity, we always use $\delta r = \max\{\delta r_j\}$. In particular, for our slip-link model system we have $\max\{\delta r_j\} = 2$ corresponding to the crank-shaft move in the Verdier-Stockmayer move-set that we use for the simulation of polymer dynamics (Figure 6a).

For a system with a rate-catalog of size $|\Omega|$ and a number $|M|$ of points in the minimal local update, the minimal local update speeds up the update step by a factor of $f \approx |\Omega|/|M|$. Since $|M|$ is independent of system-size for local kinetics, we have $|M| \sim O(1)$ and hence, for a number of particles N, the speed-up from using the minimal local update is $f \sim O(N)$. In practice, we find that the minimum local update results in a constant computational time per iteration for $N \lesssim 2000$, but increases sub-linearly for $N \gtrsim 2000$ (Figure 6.2c). This increase of computational time per iteration can be traced to the increasing complexity of hash-table lookups with the number of hash-map elements.

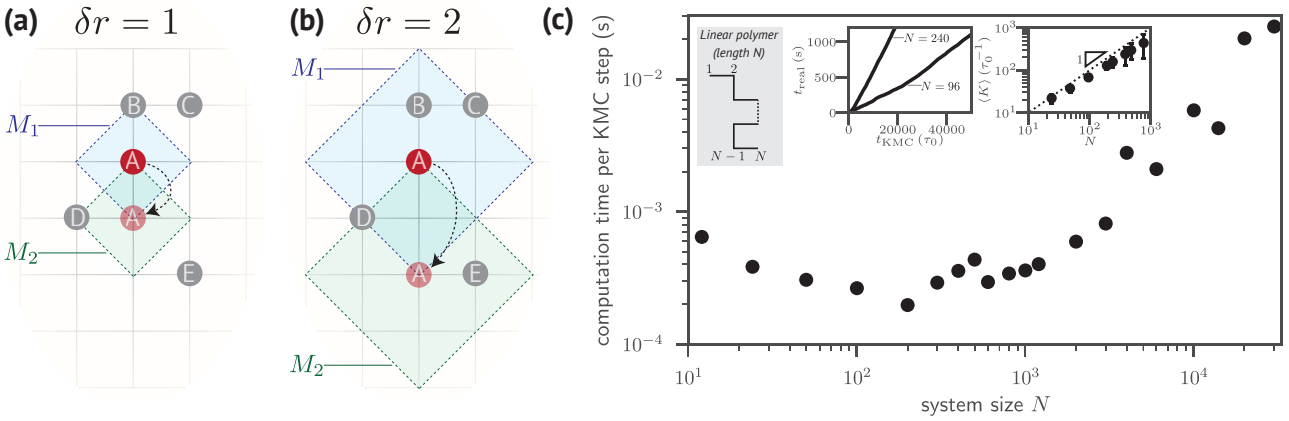

Figure 6.2: **The minimum local update results in a computational time per transition that is independent of system size for small systems and sub-linearly increasing for larger systems.** **(a)** Particles make 'hops' of one lattice step, e.g. particle A (red) can move one step downwards. Hence, the hopping distance $\delta r = 1$, which means that the minimal local update of the move considers the positions of particles A,B,D, but not C,E. **(b)** Particles can also 'hop' over a distance $\delta r = 2$, e.g. particle A (red) can move two steps downwards. The minimal local update of this move now involves an environment that contains all shown particles A,B,C,D,E. **(c)**: The amount of real time δt (units of seconds) per LKMC iteration versus system size N. We find a δt that is independent of N for $N \lesssim 2000$ and approximately linear with N for large $N \gtrsim 2000$. Left inset: The real time t_{real} (units of seconds) required to simulate to time t_{KMC} (units of the smallest time-scale τ_0) is approximately linear with t_{KMC} with a slope that depends on N. Right inset: The total rate of the system $\langle K \rangle$ is an extensive quantity, $\langle K \rangle \sim N$, indicating that this system exhibits local kinetics. For these data, we simulated the Rouse dynamics of a linear polymer of length N (with the move-set displayed in Figure 6) on a MacBook Pro, dual core Intel Core i7@3.1 GHz.

6.4 Implementing Polymer Dynamics

Now that we have established a computationally efficient method to update the rate-catalog for systems with local kinetics (Figure 6.2), we will develop a framework to simulate the DNA dynamics for our slip-link model system (Figure 6.1a). To leverage the computational efficiency of the local update, we require a Monte-Carlo move-set with local kinetics that correctly samples polymer dynamics. Fortunately, it can be shown that (non-self-avoiding) random walks lacking long-range (e.g. hydrodynamic) interactions can indeed be simulated using only local moves [12].

As our set of local polymer moves, we choose the Verdier–Stockmayer move-set containing a 'kink', 'end' and 'crankshaft' move [2, 39], as sketched in Figure 6.3a. We choose the attempt rate for the elementary polymer moves (Figure 6.3a) as follows: The kink move only displaces one monomer, and thus the attempt rate k_{kink} for the kink move sets the smallest time-scale for monomer displacement. For Rouse modes $p = 1, 2, \ldots, N$ on a polymer of length N, the hierarchy of relaxation times is given by $\tau_p = \tau_0 (N/p)^{1+2\nu}$ where ν is the scaling exponent [12, 32]. Thus, the monomer relaxation time τ_0 sets the smallest time-scale in the hierarchy of Rouse dynamics, and is therefore related to the kink move attempt rate as $\tau_0 = k_{\mathrm{kink}}^{-1}$. Since the end move also displaces only one monomer, we set $k_{\mathrm{kink}} = k_{\mathrm{end}}$. The crankshaft move, on the other hand, displaces two monomers and hence we use the attempt rate $k_{\mathrm{crank}} = k_{\mathrm{kink}} \log(4/3)$ (see section 6.6).

Lattice simulations of polymers with strict self-avoidance are non-ergodic if only local moves are included [27]. The source of this non-ergodicity lies in the inability of local moves to reach a set of highly folded configurations. To simulate self-avoiding polymers without this breaking of ergodicity, self-overlap can be included with an energy penalty J per contact (Figure 6.3b). The total Hamiltonian is now $H = \frac{1}{2} J \sum_{i,j} \delta_{\mathbf{r}_i, \mathbf{r}_j}$ where $\delta_{\mathbf{a},\mathbf{b}}$ is the Kronecker delta. For $J = 0$, we should recover random walk statistics, whereas the polymer should become a self-avoiding walk in the thermodynamic limit for $J > 0$ [4, 12]. Strict self-avoidance is recovered within this framework by setting $J \to \infty$. Indeed, the internal geometrical scaling of both random and self-avoiding polymers in our LKMC display these statistical properties (see section 7.1). In section 7.2, we show that the non-ergodicity for strictly self-avoiding polymers does not impact their dynamical scaling.

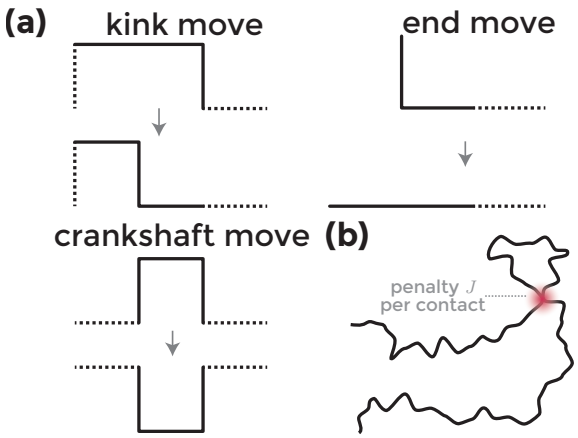

Figure 6.3: **The Verdier–Stockmayer move-set.** **(a)** Move-set that we use for linear polymers (circular polymers simply lack the end-move). **(b)** Each monomer-monomer contact is assigned an energetic penalty J, where 'contact' is defined as overlap on the same lattice point. [2, 39].

6.5 Implementing Energetic Effects using Metropolis-Hastings Kinetics

Proteins such as ParB and SMC are known to bind specifically to certain regions of DNA in bacteria [43]. To simulate such interactions in our slip-link model system [8, 29], we need to understand how attractive and/or repulsive potentials between particles affects the kinetics.

In our algorithm, energetic interactions between particles are encoded in how the rate-constants k_i of a microscopic transition T_i depend on the microstate of the system and, in particular, the internal energy of that microstate. Here, we assume that the transitions are thermally activated across a free-energy barrier, which captures the dynamics of particles coupled to a heat bath in thermal equilibrium. Since we assume the existence of a well-defined temperature and free-energy, these dynamics assume the existence of local equilibrium[40]. This results in so-called 'Metropolis-Hastings kinetics': $k_i = k_{i,0} \min(1, \exp(-\beta \Delta E))$, where $k_{i,0}$ is the attempt rate of the transition and $\beta \Delta E$ is the dimensionless height of the energy barrier of the microscopic transition [3]. In this expression, the value of the prefactor $k_{i,0}$ depends on molecular details and the level of coarse-graining, and can be found from e.g. all-atom molecular dynamics or experimental data. Thus, the time-scale of molecular motion within this type of kinetics establishes the rate-limiting factor ($k_i \leq k_{i,0}$) for a particular microscopic transition to occur [3, 24, 41].

6.6 Combining Multiple Degrees for More Realistic Kinetics

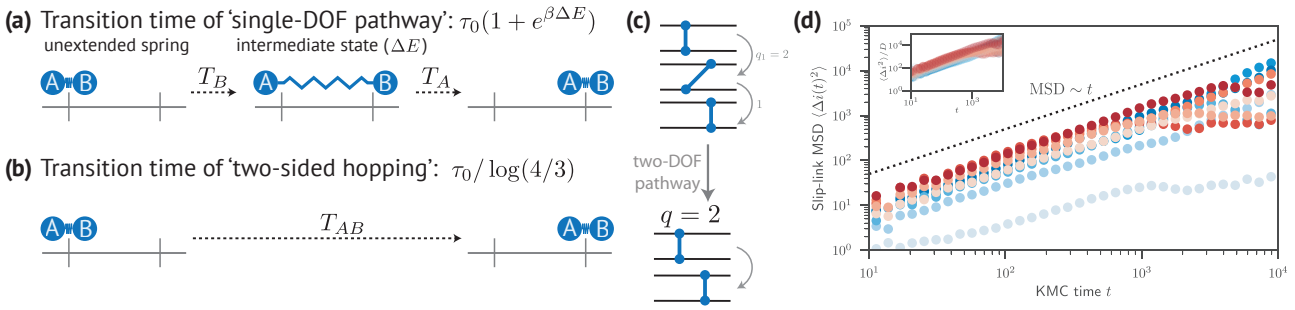

Figure 6.4: **Combining transitions leads to more accurate kinetics in the LKMC framework. (a)** Elastic dimer consisting of monomers A and B diffuses one lattice step to the right in a two-step process: extending the spring to an energy ΔE by displacing B and thereafter displacing part A. **(b)** Elastic dimer displaces to the right as a whole ('two-sided hopping'), where the diffusion of the whole dimer is characterized by a renormalized diffusion constant. **(c)** Example from our "slip-link model system", where a slip-link (blue) diffuses over two proximate polymer strands (black). A single-DOF pathway (top) is combined into a multi-DOF pathway with a renormalized movement attempt rate (bottom). Note that there are two single-DOF pathways for this example. To account for this, we add a prefactor $q = 2$ to the net movement attempt rate of the multi-DOF pathway. **(d)** Slip-link mean-square displacement $\langle \Delta i(t)^2 \rangle$ for various spring-constants of the slip-link using single-DOF kinetics (blue) and two-DOF kinetics as in panel (c) (red). Inset: Data-collapse using a rescaling $\langle \Delta i^2 \rangle / D$ where $D \sim \ell_0^2 k_+/(1+e^{\beta\Delta E})$ for the single-DOF kinetics (blue) and $D = \ell_0^2 K_{++}$ (orange).

The elementary moves in our polymer simulation (Figure 6.3a) contain both single-particle and two-particle displacements. Thus, we require an estimate for the attempt rate of such two-particle excitations, and how they depend on the smallest time-scale in the system. This question is also relevant for Monte-Carlo move-sets where merely single-particle excitations can already reach any end-state, because the presence of multi-particle excitations can still affect the dynamics. In fact, including the relevant pathways is regarded as one of the primary difficulties in designing KMC simulations [41]. Since the simulation data itself typically does not reveal which pathways are relevant unless we have already included them, physical intuition and domain knowledge have to be used to propose a realistic rate-catalog that includes the pathways that will be most commonly sampled [41]. In detail, a known source of inaccuracies in LKMC occurs when a particle or subsystem has multiple internal degrees of freedom (DOF) in which only microscopic transitions are taken into account that affect one DOF at a time ('single-DOF pathways') [28, 41]. This issue can be mitigated by including additional kinetic pathways where multiple DOFs are simultaneously affected ('multi-DOF pathways'). Such multi-DOF pathways are characterized by a renormalized attempt rate that accounts for the decreased probability of multiple processes occurring simultaneously.

How will the presence of two-particle excitations in the rate-catalog affect the overall dynamics? To make a quantitative comparison, we first consider diffusion of a dimer by only single-particle excitations. The dimer consists of two parts, A and B, which can both move in two directions $+,-$ (Figure 6.4a). We consider a slip-link with an internal energy of extension ΔE, and assume that the spring constant is so high that the slip-link will at most be extended by one lattice site (i.e. the likelihood of moves such as A_+B_- is assumed negligible). This assumption is inspired by the fact that our slip-links model SMC condensin, which have a maximum size of about one lattice size in our simulations (chapter 9). Pathways with a different ordering of transitions are distinguishable in the stochastic trajectories of the system—even if they result in the same endstate—and therefore have to be counted separately. There are four possible ways of having a net displacement after two Monte-Carlo moves: $A_+B_+, B_+A_+, A_-B_-, B_-A_-$ and four zero-displacement pathways that result in the same energy gain ΔE, namely $A_+A_-, A_-A_+, B_+B_-, B_-B_+$. Since there are four MC pathways that produce a net displacement and four that do not, on average, we have to perform twice two MC moves to achieve one displacement ℓ_0—either to the left or to the right. The average waiting time for each of these pathways at unit temperature is $T_0 = \tau_0(1+e^{\Delta E})$. To find the diffusion coefficient, we solve $\langle r^2 \rangle = 2Dt$ for D. As explained above, the dimer makes a displacement of size ℓ_0 after at time $t = 2T_0$, where the factor two is due to only 50% of two-step moves resulting in a net displacement. We thus find $\ell_0^2 = 4DT_0$. In sum, the diffusion constant using single-DOF kinetics is $D = \ell_0^2/[4\tau_0(1+e^{\Delta E})]$, which agrees well with the data from simulated slip-links (Figure 6.4d, blue data-points).

Through ΔE, the diffusion constant with only single-DOF pathways strongly depends on the elasticity of the slip-link.

However, the 'two-sided hopping' of AB as a whole will not depend on ΔE if the AB dimer diffuses without extending in the process (Figure 6.4d, orange data-points). This example illustrates the effect of including combined pathways. Such a procedure results in a more accurate (higher) effective rate of processes that involve multiple degrees of freedom, with an increase in accuracy that strongly depends on the internal energy of intermediate states.

How can multiple single pathways be combined into one effective combined pathway? We address this question in the particular case of two identical and uncorrelated independent single pathways, each of which is a two-state system $|-\rangle, |+\rangle$ with probabilities $p_-(t), p_+(t)$ and transition rates k_+ (rate of going from $|-\rangle$ to $|+\rangle$) and k_- (rate of going from $|+\rangle$ to $|-\rangle$). The master equation that describes a single two-state system reads

$$\partial_t p_+ = k_+ p_- - k_- p_+ \tag{6.1}$$

with $p_- = 1 - p_+$. In the stationary state, the probability $P^\star$ that the combined system is not in the state $|++\rangle$ is $P^\star = 1 - p_+^2$ where, from equation (6.1), $p_+ \to k_+/K$ with $K = k_- + k_+$. If the system does not start in $|++\rangle$, the probability it has not been in the state $|++\rangle$ during n statistically independent steps is

$$P_n^\star = (1 - p_+^2)^n. \tag{6.2}$$

The number of statistically independent steps over a time-interval t is $n = t/\Delta t$ where $\Delta t = K^{-1}$ is the decorrelation time. Thus, we can write equation (6.2) as

$$P_t^\star = (1 - p_+^2)^{Kt} = \exp(-K_{++} t), \tag{6.3}$$

so that, combining our results, the typical rate for the combined system to go into $|++\rangle$ is $K_{++} = -K \log(1 - k_+^2/K^2)$. For the particular case of symmetric two-state systems ($k_- = k_+$), which is the case for unbiased diffusion, we thus find the effective rate of a combined pathway from two single pathways to be $K_{++} = K \log(4/3) < K$.

How does this derivation based on discrete oscillators compare to continuous movement? For the continuous case, consider two particles $\alpha = a, b$ with position, velocity $\mathbf{r}_\alpha, \mathbf{v}_\alpha = \partial_t \mathbf{r}_\alpha$ experiencing overdamped kinetics and subject to a harmonic potential $V(|\mathbf{r}_a - \mathbf{r}_b|) = \frac{1}{2} k (\mathbf{r}_a - \mathbf{r}_b)^2$. The Langevin equations are $\gamma \mathbf{v}_\alpha = -\nabla_\alpha V + \boldsymbol{\eta}_\alpha$ where γ is a damping coefficient and $\boldsymbol{\eta}_\alpha$ is delta-correlated noise, $\langle \boldsymbol{\eta}_\alpha(t) \cdot \boldsymbol{\eta}_\alpha(t') \rangle = 2\gamma k_B T d \delta(t - t')$. The forces on the particle due to this potential are $\mathbf{f}_\alpha = -\nabla_\alpha V = -k(\mathbf{r}_\alpha - \mathbf{r}_\beta)$, $\beta \neq \alpha$. We thus find $\mathbf{f}_a = -\mathbf{f}_b$, so that we can sum the two Langevin equations together to find for the center-of-mass velocity

$$\begin{aligned} \mathbf{v}_{CM} &= \frac{1}{2}(\mathbf{v}_a + \mathbf{v}_b) \\ &= \frac{1}{2\gamma}(\boldsymbol{\eta}_a + \boldsymbol{\eta}_b), \end{aligned}$$

where the deterministic forces for the two particles have canceled each other out in the second line. The total center of mass displacement is $\mathbf{r}_{CM} = \int_0^t \mathrm{d}\tau \mathbf{v}_{CM}(\tau)$, so the mean-squared-displacement is

$$\begin{aligned} \langle \mathbf{r}_{CM}(t)^2 \rangle &= \int_0^t \int_0^t \mathrm{d}\tau \mathrm{d}\tau' \langle \mathbf{v}_{CM}(\tau) \cdot \mathbf{v}_{CM}(\tau') \rangle \\ &= \frac{2}{(2\gamma)^2} \int_0^t \int_0^t \mathrm{d}\tau \mathrm{d}\tau' \langle \boldsymbol{\eta}_\alpha(\tau) \cdot \boldsymbol{\eta}_\alpha(\tau') \rangle \\ &= \frac{d k_B T}{\gamma} t. \end{aligned}$$

Combined with the Einstein relation, $\gamma = D/k_B T$ [33], this gives $\langle \mathbf{r}_{CM}^2(t) \rangle = 2 d D_{CM} t$ with $D_{CM} = D/2$.

We can now compare the diffusion constant of a slip-link that moves by two-sided hopping $D_{++} = \ell^2 K_{++}$ to the diffusion constant of one that moves continuously D_{CM}. Based on our result $K_{++} = K \log(4/3)$, we find that the discrete case has a diffusion coefficient $D_{++}/D_{\text{cont.}} - 1 \approx 42\%$ lower than the continuous case. If single-particle motion has the same prior probability as two-particle motion, this results in a total rate for the discrete derivation that is $(k_0 + k_0 \log(4/3))/(k_0 + k_0/2) \approx 14\%$ lower than the continuous derivation. This discrete derivation is more appropriate when the dynamics of the underlying system already has discrete properties (e.g. diffusion of holes in a crystal [41] or stepping of a molecular motor [14]).

7

Verifying the Validity of Stochastic Dynamics in LKMC

Chapter summary: *We systematically check the validity of the (non-)equilibrium dynamics in LKMC, including a comparison to Brownian dynamics simulations.*

7.1 Controls on Time-Averaged Quantities in Equilibrium

The particles in our LKMC live on a lattice, thereby strictly speaking introducing a breaking of rotational symmetry. In order for the lattice simulation to simulate dynamics of an off-latice system (e.g. a polymer), the breaking of rotational symmetry should be negligible in the thermodynamic limit. To test whether angular symmetry is broken, we applied a force along the $z-$axis to both ends of a linear polymer (end-to-end vector $\mathbf{R}$) and measured the azimuthal angle θ defined implicitly as $\tan\theta = (\mathbf{R}\cdot\hat{\mathbf{y}})/(\mathbf{R}\cdot\hat{\mathbf{x}})$ (where $\hat{\mathbf{x}},\hat{\mathbf{y}}$ are unit vectors). Indeed, we find that the histogram of θ is a uniform distribution within one standard deviation (Figure 7.1a). This indicates that, although rotational symmetry is strictly broken by the lattice geometry (e.g. $\theta \approx -\pi, 0, \pi$ appear to have an increased $p(\theta)$), the breaking of rotational symmetry is less than the relevant fluctuation size.[1]

To test whether the internal geometry of polymers in LKMC displays the correct statistics, we measure the radius of gyration $R_g^2 = N^{-1}\sum_i(\mathbf{r}_i - \bar{\mathbf{r}})^2$ for a polymer of size N with coordinates $\mathbf{r}_i$ and center of mass $\bar{\mathbf{r}}$. Polymers are scale-free objects, displaying a geometrical scaling $R_g \sim \Delta^\nu$ for sub-chains of any size $1 \ll \Delta \leq N$. The scaling exponent ν differs between random and self-avoiding polymers where the monomers carry a mutual short-ranged repulsive energy J (section 2.3), with $J = 0$ corresponding to $\nu = 1/2$ and $J > 0$ to $\nu \approx 0.588$ [4, 34]. We implemented monomer-monomer interactions by allowing for multiple monomers on the same lattice point $\mathbf{r}_i$. Monomer overlap was penalized with the Hamiltonian $H = \frac{1}{2}\sum_{i,j} J\delta_{\mathbf{r}_i\mathbf{r}_j}$, where $\delta_{\mathbf{a},\mathbf{b}}$ is a Kronecker delta. For $J = 0$, we recover a random walk, whereas for any $J > 0$, the polymer should self-avoiding walk statistics [4], as verified by our simulations (Figure 7.1b).

[1] We do not claim that there is not a statistically significant breaking of rational symmetry, as this depends on the statistical power of the data—for sufficiently many samples of θ, an arbitrarily small breaking of rotational symmetry can always be distinguished. Rather, the data in figure 7.1a demonstrates that the size of the typical fluctuations $\delta p(\theta) \equiv \sqrt{\mathrm{var}[p(\theta)]_{\theta,\delta\theta}}$ (for the θ in the bin $[\theta - \frac{1}{2}\delta\theta, \theta + \frac{1}{2}\delta\theta\rangle$) for all θ are larger than the variation in $p(\theta)$ itself. This indicates that the random fluctuations in $p(\theta)$ (quantified as $\delta p(\theta)$) are larger than the systematic differences in $p(\theta)$ (quantified as $p(\theta_1) - p(\theta_2)$).

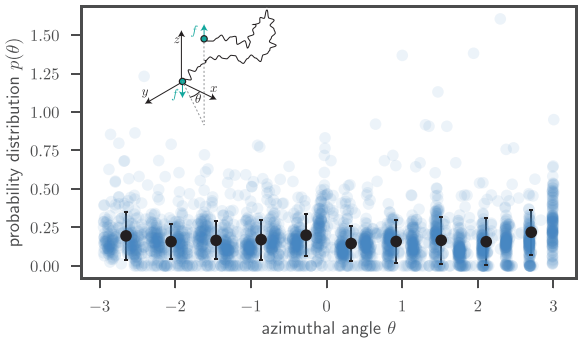

(a) **Our LKMC obeys rotational invariance.** We measured the azimuthal angle θ as indicated in the figure. Data was collected for polymer length $N = 12 \ldots 192$ and monomer overlap energy $J = 0 \ldots 20$ and generated individual histograms for each parameter set. All histograms were then combined (blue), and the average histogram of all parameter sets was computed (black, error bars: standard deviation).

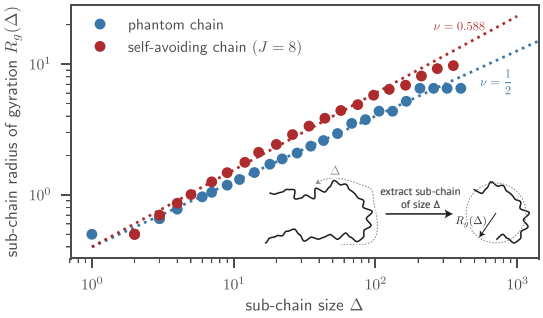

(b) **Ensemble-averaged polymer statistics of polymers with and without (partial) self-avoidance are in agreement with theory.** Two polymers were simulated: a phantom chain (blue) and a polymer with monomer overlap energy $J = 8$. The radius of gyration scaling of sub-chains within such the phantom and self-avoiding walk obey a scaling $R_g \sim \Delta^\nu$ with respectively $\nu = 1/2$ and $\nu \approx 0.588$.

Figure 7.1

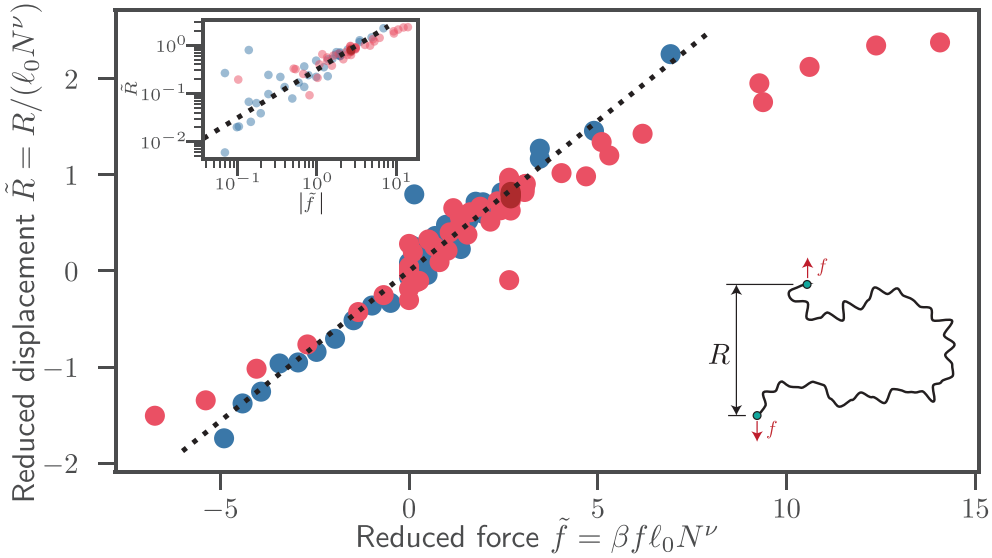

Figure 7.2: **Static response of polymers in our LKMC obeys the fluctuation-dissipation theorem.** Linear polymers of length N were simulated with monomer overlap energy J. **(a)** We measured the average end-to-end vector projected along the $z-$axis $\langle R \rangle$ in response to a force along the $z-$axis f for $J = 0$ (blue), $J = 2$ (light red) and $J = 4$ (dark red). Axes are scaled to dimensionless variables to make them independent of system size for small f.

As a final example, we consider the linear response of a polymer in response to static external forces. As the force is time-independent, the system remains in equilibrium—albeit it with a different free energy that includes the work done by the external force. We consider a linear polymer with end-to-end distance projected along the $z-$axis R. In equilibrium, we can define a partition function conditioned on R, which in turn defines a free energy F_R. Using this free energy, we will now compute the force-extension relation for small externally applied forces (along the $z-$axis) f.

We assume that the free energy is harmonic in R for small perturbative forces, $F_R = \frac{1}{2}kR^2 - fR$. In the unperturbed ensemble, and using a Gaussian integral, we find $\langle R^2 \rangle_0 = k_B T/k$ where $\langle R^2 \rangle_0 = \ell_0^2 N^{2\nu}$. These two expressions for $\langle R^2 \rangle_0$ relate the unperturbed size to the spring constant upon extension for arbitrarily small forces. For the harmonic free

energy that we assumed, the observed $\langle R \rangle_f$ follows from $0 = \langle \partial_R F_R \rangle_f$, giving a force-extension relation $f = k \langle R \rangle_f = k_B T \langle R \rangle_f / \langle R^2 \rangle_0$. Writing $\overline{R} = \sqrt{\langle R^2 \rangle_0}$, we propose a reduced force $\tilde{f} = \beta f \overline{R}$ and displacement $\tilde{R} = \langle R \rangle_f / \overline{R}$ that are independent of system size. Indeed, we find that linear response theory is accurately obeyed with the expected dependency of k on $\langle R \rangle$, N and ν for both random and self-avoiding polymers (Figure 7.2).

There are non-linearities in the force-extension relationship for forces $|f| \geq 1$ (Figure 7.2). These non-linearities appear superficially similar to those that we'll explore in chapter 8 for large forces. There, the non-linearities stem from the inability of LKMC to simulate far-from-equilibrium dynamics. The non-linearities in figure 7.2, however, have a fundamentally different origin: the finite maximum extension $R_{\max} = \ell_0 N$ of the polymer as $f \to \infty$ [12, 34]. The breakdown of linear response in Figure 7.2 thus reflects an intrinsic physical property of the polymer, unlike the breakdown of linear response due to the relevant type of kinetics far from equilibrium in Figure 8.1.

7.2 Controls on Polymer Dynamics in Equilibrium

Polymer sub-chains with a size far removed from both the smallest length-scale ℓ and system size L ($\ell \ll s_-, s_+ \ll L$) are self-similar objects with no intrinsic length-scale [11, 12, 34]. Across statistical physics, dynamical scaling is much more subtle, complex and less universal than static scaling [11, 22]. Nevertheless, the so-called *Rouse model* for random polymers does exhibit scale invariant dynamics [11, 12]. To satisfy this scale invariance, we expect a power-law dependency for the dynamical scaling of the chain relaxation time $t(s) \sim s^\alpha$, where $\alpha > 0$ to obey the ordering of time-scales that we postulated in chapter 3. If we assume that the relaxation is rate-limited by the time needed for fluctuations to propagate over the full length of the sub-chain by passive one-dimensional diffusion, then we expect $\alpha = 2$. Indeed, the Rouse model predicts a scaling $t_p \sim s_p^2$ for the relaxation time t_p of the normal mode with length-scale s_p [12, 34].

The dynamical scaling exponent is $\alpha = 2$ for *any* model with only localized interactions [12].[2] However, polymers with steric interactions such as DNA are more closely modeled as self-avoiding walks (section 2.3), which do not only have localized interactions: displacing a single monomer in a self-avoiding walk potentially involves rearranging the whole polymer to avoid any points of overlap. In agreement with this, computational studies of self-avoiding polymers find that $\alpha = 1 + 2\nu \geq 2$ for a size scaling exponent ν ($R \sim s^\nu$) [32].

To verify that our LKMC displays the correct physical dynamics of self-avoiding chains, we measure the monomeric displacement $\Delta\mathbf{r}(t)$ of polymers varying in length N_m, over a time-interval t. Self-overlap was penalized with an energetic penalty of J per monomer–monomer contact (also see Figure 6.3). All data can be collapsed onto a single master curve by a rescaling $\Delta\mathbf{r} \to \Delta\mathbf{r}/\Delta^\nu, t \to t/\Delta^{1+2\nu}$ (Figure 6.3b), indicating that polymers in our LKMC approach correctly exhibit Rouse dynamics of self-avoiding chains [32].

It is known in the literature that, in the limit of *strict* self-avoidance, the LKMC simulations with the Verdier-Stockmayer move-set (Figure 6.3) are no longer ergodic [27]. To test in more detail whether this breaking of ergodicity impacts polymer dynamics, we also generated simulation results with $J \to \infty$. Despite being strictly non-ergodic, we find that these data are described by the same dynamic scaling exponents as for finite J (Figure 6.3). This shows that, although our LKMC with strict self-avoidance breaks ergodicity, the inability of the algorithm to reach these states does not impact polymer dynamics within our statistical accuracy.

[2] Here, "localized" refers to local in the arc-length coordinate s, *not* in the space coordinates. Otherwise stated, there exists an intermonomeric potential $U(|s_1 - s_2|)$ between monomers at s_1, s_2 that has a typical size, but that is not a function of the space coordinates.

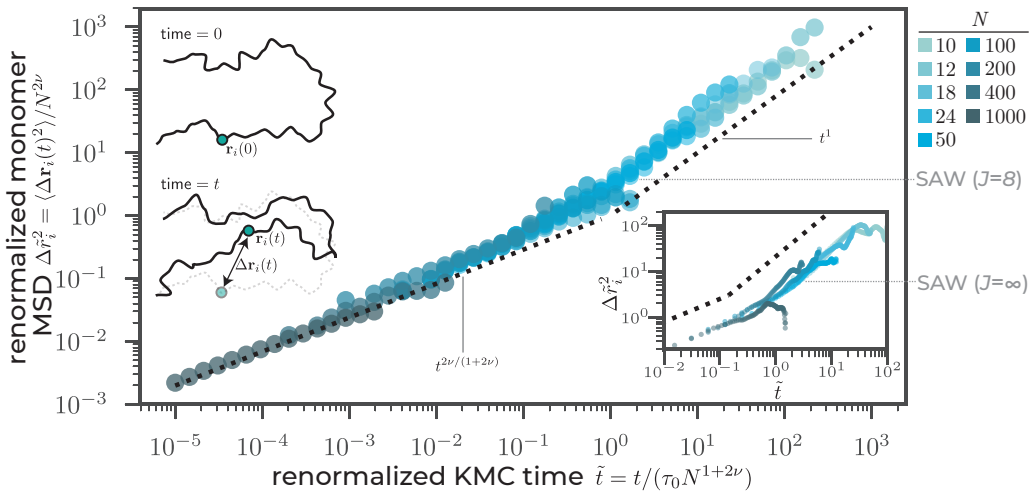

Figure 7.3: **Our LKMC captures Rouse-like dynamics for both random and self-avoiding polymers.** We measured the monomeric displacement $\Delta\mathbf{r}(t)$ for polymers of different lengths N_m with self-overlap energy $J = 8$ per contact. A rescaling using the Flory exponent ν indicates that these curves follow the expected scaling [32]. **Inset:** The same dynamic scaling exponents are observed for polymers with exclusive self-avoidance ($J \to \infty$). For these data, we used $N_m = 8 \ldots 512$.

We already verified that the diffusion of single monomers in a self-avoiding polymer is in agreement with the expected Rouse-like dynamics (Figure 7.3). We will now verify that not only a single monomer, but also *collective dynamics* of the self-avoiding walk displays the correct dynamic scaling. We do this in two ways: (i) Verify that the whole chain displays the expected diffusive motion, and (ii) Verify that sub-chains display the expected relaxation dynamics. In more detail, in the first test we check whether the whole polymer moves diffusively, and check the scaling of the diffusion coefficient with theory. We assume an overdamped limit, so that we have for the hydrodynamic force $f = \zeta_N v$ onto a polymer of length N moving at a velocity v, where the friction coefficient of a chain of size N by virtue of extensivity obeys $\zeta_N \approx \zeta_1 N$. Combined with the Einstein relation, this gives $D_N = D_1/N$, where D_N, D_1 are respectively the polymer and monomer diffusion coefficients. Thus, the quantity $N\langle \mathbf{R}_{CM}(t)^2 \rangle$ should be independent of N, which is indeed the case for our LKMC (Figure 7.4a). For the second test, we measure time-traces of the intermonomeric vector $\mathbf{r}_\Delta$ of sub-chains of size Δ. $\mathbf{r}_\Delta$ changes over time as $\mathrm{MSD}_\Delta(t) = \langle \Delta\mathbf{r}_\Delta(t)^2 \rangle \sim N^{2\nu}$ and where the time-dependency has a longest relaxation time $\tau_N \sim N^{1+2\nu}$ [31]. For times $t \gg \tau_N$, we simply recover the static subchain scaling $\langle \mathbf{r}_\Delta^2 \rangle \sim N^{2\nu}$. Thus, a plot of $\langle \Delta\mathbf{r}(t)^2 \rangle / N^{2\nu}$ versus t/τ_N should approximately collapse all data onto a single master-curve, which is indeed the case for our LKMC (Figure 7.4b). The two tests in Figure 7.4 indicate that not only single monomer motion, but also the collective dynamics of self-avoiding polymers display the expected dynamics in our LKMC.

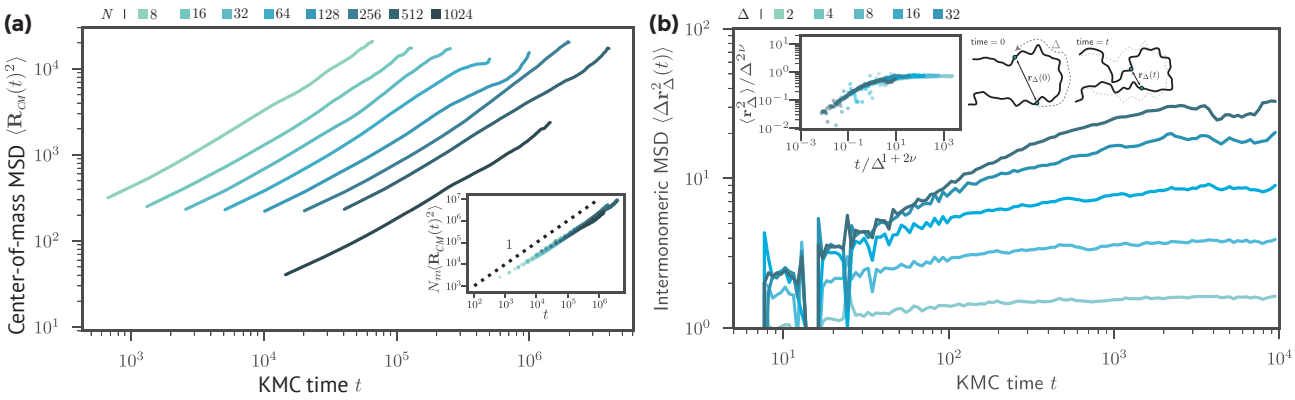

Figure 7.4: **Consistency checks of polymer dynamics using LKMC. (a)** Diffusion of the center of mass of a circular polymer. Center of mass $\mathbf{R}_{CM}(t)$ mean-square displacement (MSD) for polymers of various sizes is shown. Inset: Collapse onto universal master curve by a rescaling $D_N = D_1/N$. **(b)** Rouse dynamics of mean-squared displacement of the intermonomeric distance in a circular polymer. Linear distance between monomers is Δ. **Left inset:** Data collapse onto a single master-curve by a rescaling $\langle \Delta \mathbf{r}(t)^2 \rangle / N^{2\nu}$ versus t/τ_N, where τ_N is the whole-chain relaxation time [32]. **Right inset**: Schematic of the quantity that we measure. .

7.3 Control on Slip-Link Dynamics in Equilibrium

A necessary property of our LKMC framework must be that detailed balance is obeyed in thermodynamic equilibrium. For two microstates x, x', detailed balance in a Markov chain implies that

$$W(x'|x)p(x) = W(x|x')p(x'), \tag{7.1}$$

where $W(x'|x)$ is the transition rate from state x into state x' and $p(x)$ is the steady-state probability distribution of state x. Unfortunately, there are so many microstates (already $\sim 10^{34}$ for a 79−step self-avoiding walk [19]), that any individual microstate will typically be only observed once. We must find a different way of testing whether detailed balance is obeyed. Instead of checking detailed balance on microstates x, x', we measure detailed balance on lower-dimensional variables $i(x), j(x')$. In this lower-dimensional space, two different microstates $x_1, x_2, x_1 \neq x_2$ can have the same $i(x_1) = i(x_2)$. Since the current state in the lower-dimensional space does not uniquely determine the future state, the reduced variables may no longer be Markovian. Because the reduced variables $i(x)$ may no longer constitute a Markov chain, we cannot use equation 7.1 to test whether our simulation obeys detailed balance.

We use the general form of detailed balance for a stochastic variable, $p(\Delta, \tau; \Delta', 0) = p(\Delta', \tau; \Delta, 0) \forall \tau$, where $p(\Delta, \tau; \Delta', 0)$ is the joint probability density of transitioning from Δ' into Δ over a time-interval τ [10]. Specifically, for our slip-link model system we monitor the loop-size $\Delta(\tau)$ trapped by a slip-link (Figure 7.5a). The polymer dynamics influences slip-link positioning, so by monitoring Δ we are verifying detailed balance of the *full* slip-link–polymer system. We collected statistics of loop-sizes $\Delta = 1$ and $\Delta = 3$ (Figure 7.5b) and generated histograms of $p(1, \tau; 3, 0), p(3, \tau; 1, 0)$. As can be seen in Figure 7.5c, these distributions match within statistical error, indicating that detailed balance is obeyed for all time points considered.

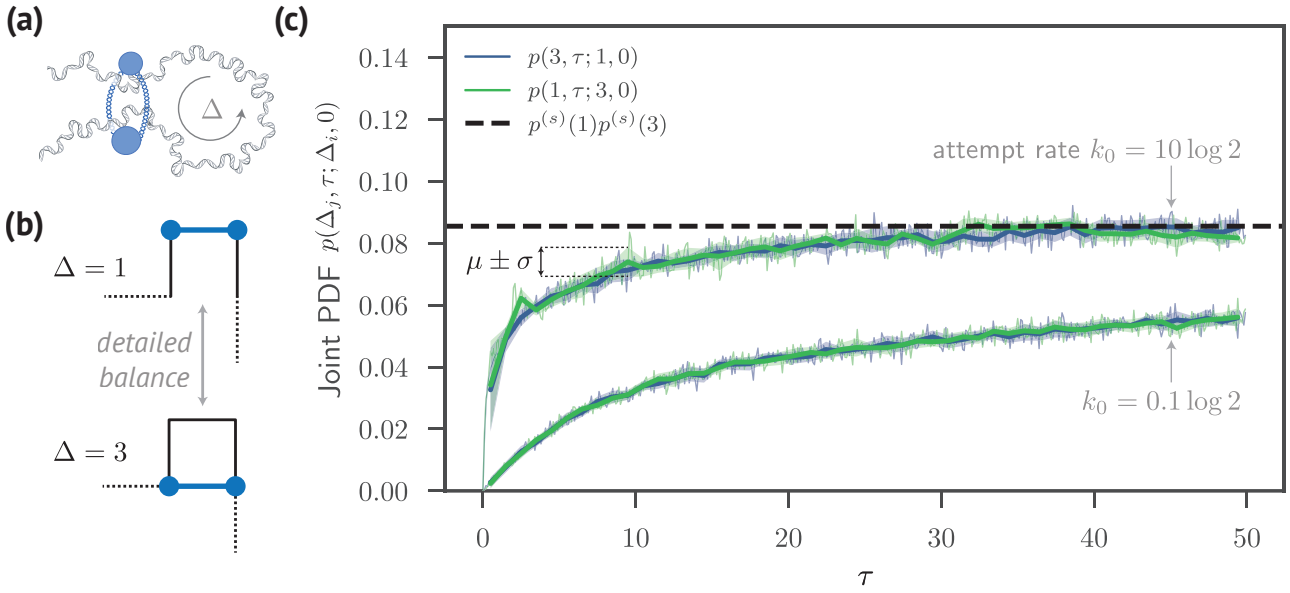

Figure 7.5: **Coarse-grained variables can be used to verify that our LKMC satisfies detailed balance in thermal equilibrium. (a)** We monitor the size Δ of a DNA loop trapped by a slip-link. **(b)** We collected statistics of loop-sizes $\Delta = 1$ and $\Delta = 3$. **(c)** Detailed balance is obeyed if $p(1, \tau; 3, 0) = p(3, \tau; 1, 0)$ for all τ, which is indeed the case for our LKMC data within one standard deviation (blue and green curves). A lower slip-link diffusion attempt rate k_0 (compare upper and lower curves) simply increases the decorrelation time. For large times, the steady-state distributions satisfy $p(\Delta, \tau; \Delta', 0) \to p^{(s)}(\Delta)p^{(s)}(\Delta')$ (dashed line) since the system is characterized by a finite amount of memory.

7.4 Control on Particle Dynamics in Potential Landscapes

We implemented the effect of energetic differences between states on kinetics using the Metropolis-Hastings algorithm (section 6.5). As a simple test of this algorithm, we simulated a particle that diffuses in a one-dimensional harmonic potential well. At $t = 0$, we release the particle in the middle of potential wells of various stiffnesses and record the particle trajectories. A data-collapse shows that the standard deviation $\sigma_i(t)$ of an ensemble of these trajectories (Figure 7.6) agrees well with the theoretical value calculated from the Fokker-Planck equation $\sigma_{i,\text{theor.}}(t) \sim 1/\sqrt{k}$ [33]. This benchmark simulation of the Ornstein–Uhlenbeck process illustrates that these 'Metropolis-Hastings kinetics' indeed correctly sample the stochastic dynamics of a particle diffusing in a harmonic potential well.

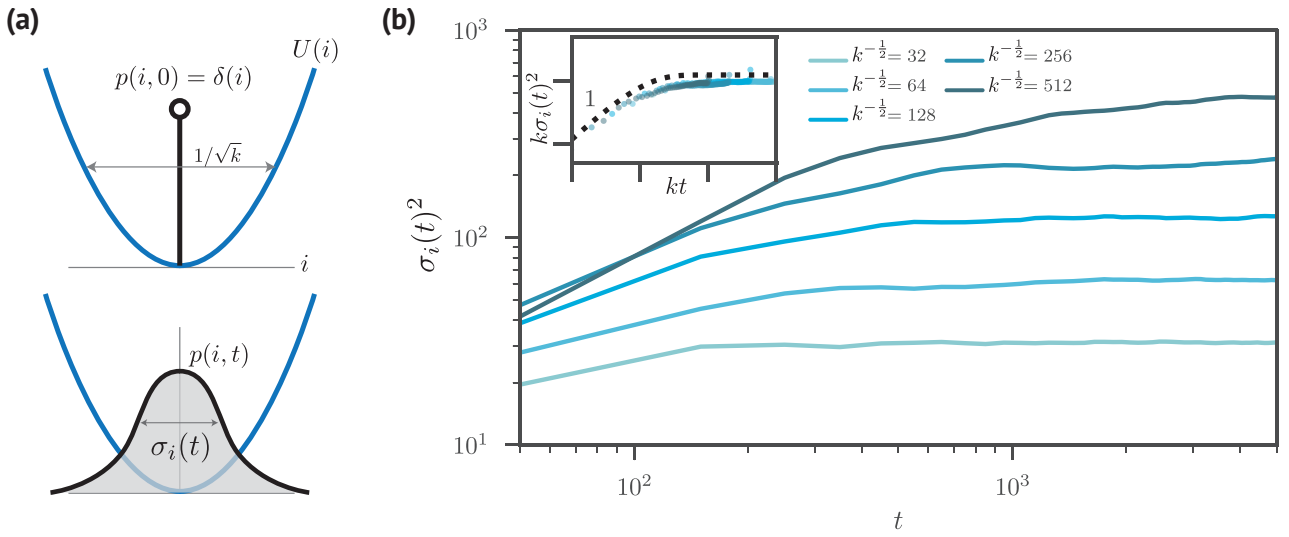

Figure 7.6: **'Metropolis-Hastings kinetics' samples overdamped dynamics of particles diffusing in an energy landscape.** **(a)** Schematic of benchmark set-up with a particle that diffuses in a harmonic potential well $U(i) = \frac{1}{2}ki^2$, initial condition $p(i,0) = \delta(i)$ and time-dependent standard deviation $\sigma_i(t)$ [33]. **(b)** Mean-square displacement of particles are consistent with the solution of the Einstein-Smoluchowski equation, verified by a data collapse (inset) using the theoretical rescaling [33].

7.5 Controls on Particle and Polymer Dynamics out of Equilibrium

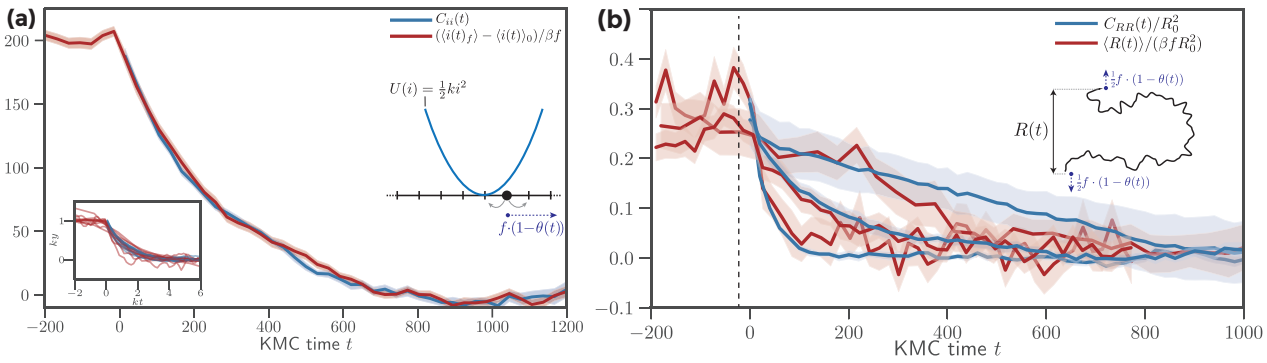

Figure 7.7: **Both single particles and polymer dynamics subject to time-dependent external forces obey the fluctuation-dissipation theorem (FDT).** A particle diffuses inside a potential well $U = \frac{1}{2}ki^2$ with time-dependent force $f(1-\theta(t))$. Shown are both the scaled positional dynamics $\langle \delta i(t)\rangle_f/\beta f$ due to the applied force (red) and the position autocorrelation $C_{ii}(t)$ (blue). These two curves overlap within the uncertainty (twice the standard error, shaded area), indicating that the FDT is obeyed. Inset: By rescaling the data by the intrinsic time-scale $\tau \sim 1/k$ of the potential for various k as indicated in the figure, all data collapses onto a single master-curve, showing that the system exhibits the expected relaxational dynamics. **(b)** Dynamic response with time-dependent force $\mathbf{f} = (0, 0, f(1-\theta(t))$. Relaxation towards equilibrium $\langle R\rangle_f/\beta f$ (red) is equal to the autocorrelation function $C_{RR}(t)$ (blue) within the statistical uncertainty (standard error in the mean, shaded area), indicating that the FDT is obeyed. We verified the FDT for $J = 0\ldots4$ and $N = 12\ldots120$; the data in this plot have parameters $(J, N) = (1, 64)$ (top), $(0, 48)$ (middle) and $(0, 24)$ (bottom). Data was scaled to the equilibrium variance to have an amplitude independent of N.

Our slip-link model system can be driven out of equilibrium by motor proteins such as SMC condensins [14, 29, 45], which can exert forces onto the DNA polymer (Figure 6.1a). When these proteins are no longer performing enzymatic activity, the system must relax back to equilibrium. The converse must of course also hold—motor proteins that are *switched on* drive the system away from equilibrium. Luckily, relaxation towards and away from equilibrium are characterized by the same decay time in the regime of linear response [12]. We arbitrarily choose to check relaxation towards equilibrium. Thus, we establish that our LKMC approaches equilibrium if there are no active forces are dynamically switched off in the system, and that within the linear response regime the system's relaxation towards equilibrium satisfies the fluctuation-dissipation theorem [33].

We first verify that our LKMC with MH-kinetics is in agreement with the FDT in the presence of an energy landscape and time-dependent forces applied to a single particle. We do this by first applying a constant force f to a particle in a harmonic potential $U(i) = \frac{1}{2}ki^2$. After letting the system equilibrate in the presence of the force, we switch off the force at $t = 0$ and evolve the system using MH-kinetics. The relaxation towards the unforced equilibrium is then related to the spontaneous fluctuations as $\langle i(t)\rangle_f - \langle i(t)\rangle_0 = \beta f C_{ii}(t)$ for $t > 0$ [33]. Here, $\langle i(t)\rangle_f$ is the ensemble average of $i(t)$ in the presence of a force f and $C_{ii}(t) = \langle i(t)i(0)\rangle - \langle i\rangle^2$ is the autocorrelation function of an unperturbed particle. Indeed, we find that the FDT is accurately obeyed for this system (Figure 7.7a). Moreover, since $k\langle i\rangle_f = f$ with an intrinsic relaxation time-scale $\tau \sim 1/k$, we verify that the particle displays the expected relaxational dynamics for all energy landscapes considered (Figure 7.7a, inset).

We have now verified that single particles subject to time-dependent forces obey the FDT, and polymers in our LKMC obey linear response with respect to time-independent forces. As a final control, we test whether the dynamic response out-of-equilibrium of polymers in our LKMC also follows the FDT. We therefore first equilibrate a polymer with an external force f that we turn off at $t = 0$, and monitor relaxation towards equilibrium. The FDT for this process is $\langle R(t)\rangle_f - \langle R(t)\rangle_0 = \beta f C_{RR}(t)$ for $t > 0$, with $C_{RR}(t) = \langle R(t)R(0)\rangle_0 - \langle R\rangle_0^2$ the spontaneous autocorrelation function [33]. We find that both sides of this equation are equal within our statistical accuracy (Figure 7.7b), indicating that the dynamical response in our LKMC obeys the FDT.

7.6 Comparison of LKMC with Brownian Dynamics for Non-Equilibrium Loop Extrusion

Next, we bring all aspects of our LKMC simulation together by considering a toy-model for DNA-organization by actively loaded slip-links. The active loading mechanism consists of binding at a particular loading site on the DNA, but spontaneous dissociation (rate k_-) anywhere (Figure 7.8a). This binding/unbinding asymmetry breaks detailed balance, driving the polymer dynamics away from equilibrium. We consider two popular models for the movement of slip-links over DNA: diffusive and ballistic motion. The latter models DNA loop-extrusion by enzymes such as SMC condensin [6, 7, 18, 29], which is believed to be important for chromosome segregation and cell-fate in both prokaryotic and eukaryotic DNA [14, 20, 21, 29, 42–44]. Although both sub-systems, slip-links and DNA, exhibit well-understood dynamics that we have already described (Figures 6.3 and 6.4), the combination of these sub-systems exhibits interesting emergent behavior [7, 7, 18, 29].

The out-of-equilibrium DNA–slip-link system can be characterized by the loop-size distribution $p(\Delta)$. Unlike the power-law behavior observed in equilibrium polymers [11], we observe that $p(\Delta)$ of the non-equilibrium slip-linked polymers is approximately described by an exponential decay (Figure 7.8b). This dependence indicates that the active slip-link loading imparts a characteristic length-scale onto the polymer. In prior work it was argued, using both Brownian dynamics simulations and the corresponding Fokker-Planck equation, that the auxiliary function $\tilde{p}(\Delta) = p(\Delta)N/(N - \Delta)$ decays exponentially with a characteristic length scale $\langle\Delta\rangle_{\tilde{p}} \sim k_-^{-\alpha}$ ($\alpha = 1$ for ballistic slip-links, and $\alpha = \frac{1}{2}$ diffusive slip-links) [7]. We tested this predicted scaling with our LKMC simulation data; a corresponding data-collapse reveals that there is good agreement with this scaling form up to $k_- \approx 0.05$ (Figure 7.8c), for which the typical loop-sizes $\langle\Delta\rangle_{\tilde{p}} \lesssim 3$ border on the lattice discretization. The agreement with the observations from Brackley et al. [7] indicates that the non-equilibrium dynamics of slip-linked polymers in our LKMC simulation is consistent with the corresponding Fokker-Planck equation and Brownian dynamics simulations, but that discretization effects are observed for loop-sizes $\lesssim 3$.

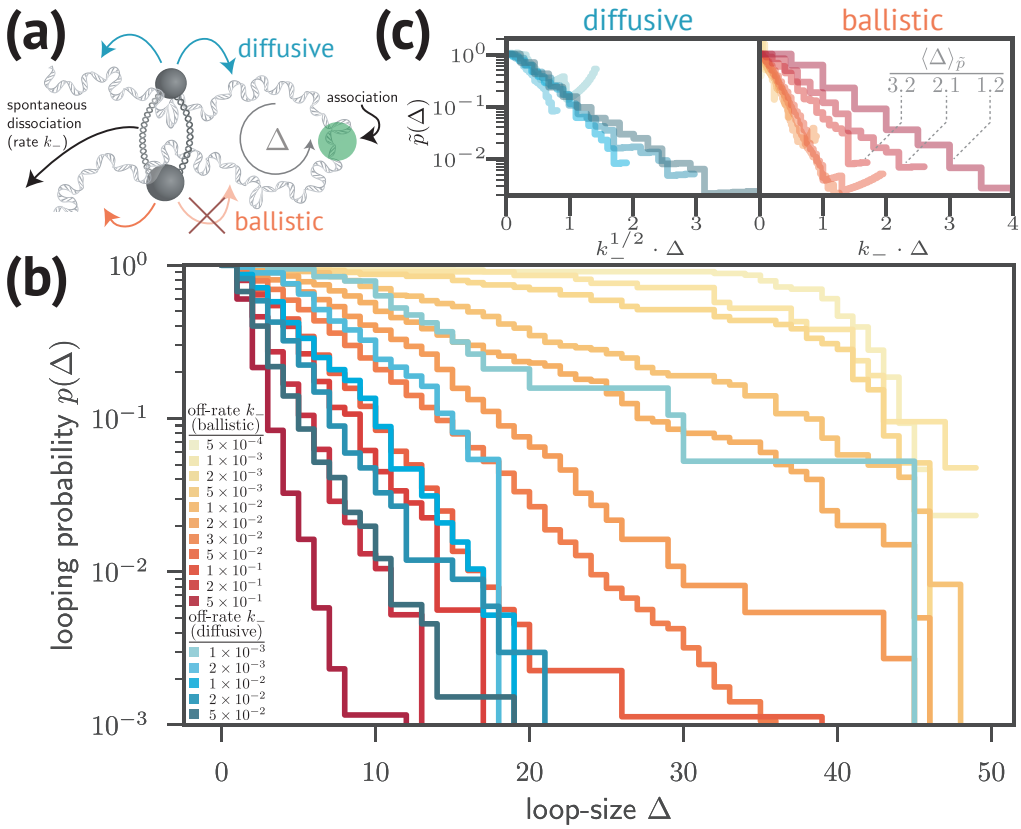

Figure 7.8: **Non-equilibrium dynamics of DNA–slip-link toy model is consistent with Brownian dynamics simulations. (a)** A single slip-link binds to a particular location on the polymer (green) and dissociates with rate k_-. The loop-size Δ is defined as the chain-size trapped by the slip-link. This set-up closely models the Brownian dynamics simulations from Brackley et al. [7]. **(b)** The loop-size distribution is shown for diffusive (green-blue) and ballistic (yellow-red) slip-links (k_- indicated in legend). **(c)** The data from panel (b) was used to compute the auxiliary function $\tilde{p}(\Delta) = p(\Delta) \cdot N/(N - \Delta)$ and data-collapse by the rescaling of Δ from Brackley et al. [7].

8

Probing the Limits of LKMC for Non-Equilibrium Systems

Chapter summary: *The limits of LKMC are tested by driving both a single particle as well as the full slip-linked polymer system far out of equilibrium. We show that Metropolis-Hastings kinetics cannot be driven arbitrarily far from equilibrium, and that the lattice discretization can generate unphysical artifacts far from equilibrium.*

8.1 Metropolis-Hastings Kinetics Limits the Maximum Speed of Particle Movement

To verify that MH-kinetics can also be used to study far-from-equilibrium dynamics, we start by simulating the overdamped dynamics of a single particle on a ring with periodic boundary conditions that experiences an external force according to two protocols:

(i) A particle moving along a potential ramp of slope $\Delta E_{\mathrm{MH}}/\ell \equiv -\phi_{\mathrm{MH}}$ according to Metropolis-Hastings kinetics.

(ii) A particle that is subject to an external force f in the form of an additional ballistic displacement move with attempt rate $k_+ \sim f$.

In either protocol, the fluctuation-dissipation theorem (FDT) can be stated as $FD = \langle v \rangle k_B T$, where D is the diffusion coefficient, $\langle v \rangle$ is the average velocity and F the force that the particle experiences due to the potential ramp (protocol (i)) or external force (protocol (ii)) [33].

In protocol (ii), the force F in the FDT is simply the external force f; for protocol (i), F depends on the energy landscape. To determine this dependency, we calculate the relationship between velocity $\langle v \rangle$ and the steepness set by $\beta \Delta E_{\mathrm{MH}}$. Denoting the probability of a forward, backward step by respectively p_+, p_-, the average velocity $\langle v \rangle$ is $\langle v \rangle = \ell \langle k \rangle (p_+ - p_-)$. The probabilities in Metropolis-Hastings kinetics are defined as $p_\pm = \min(1, e^{\mp \beta \Delta E_{\mathrm{MH}}})$, where the average stepping rate is $\langle k \rangle = \int \mathrm{d}k \, k p(k) = K$ for exponentially distributed rates $p(k) = K^{-1} \exp(-k/K)$. The total rate depends on ΔE_{MH} as $K = k_0 p_- + k_0 p_+$, for which we can find a closed expression using the $p_\pm$ as defined before:

$$K = k_0(\min(1, e^{-\beta \Delta E_{\mathrm{MH}}}) + \min(1, e^{+\beta \Delta E_{\mathrm{MH}}})) \tag{8.1}$$

$$= k_0(1 + e^{-\beta |\Delta E_{\mathrm{MH}}|}). \tag{8.2}$$

Combining the previous results, we find the average velocity to be

$$\langle v \rangle = \ell k_0 (1 + e^{-\beta |\Delta E_{\mathrm{MH}}|}) \frac{\min(1, e^{-\beta \Delta E_{\mathrm{MH}}}) - \min(1, e^{+\beta \Delta E_{\mathrm{MH}}})}{1 + e^{-\beta |\Delta E_{\mathrm{MH}}|}} \tag{8.3}$$

$$= \ell k_0 \left(\min(1, e^{-\beta \Delta E_{\mathrm{MH}}}) - \min(1, e^{+\beta \Delta E_{\mathrm{MH}}}) \right) \tag{8.4}$$

$$= \ell k_0 \mathrm{sgn}(\Delta E_{\mathrm{MH}})(e^{-\beta |\Delta E_{\mathrm{MH}}|} - 1). \tag{8.5}$$

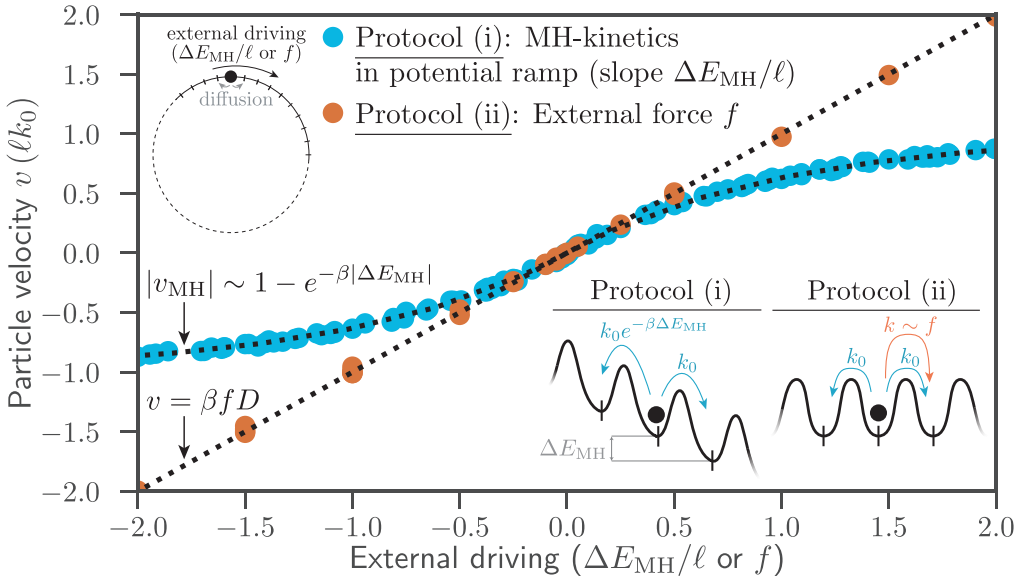

Figure 8.1: **Particle that moves in an external field according to Metropolis-Hastings kinetics obeys the fluctuation-dissipation theorem (FDT), but only in the small field limit.** A particle with position $i(t)$ moves on a ring with periodic boundary conditions. Average velocity $\langle v\rangle = \langle i'(t)\rangle$ of the particle using two protocols: (i) MH-kinetics with a potential ramp (force $\phi_{\mathrm{MH}} = -\Delta E_{\mathrm{MH}}/\ell$) (blue) and (ii) an external force f in the form of a renormalized attempt rate (orange). For small external fields $|\Delta E_{\mathrm{MH}}| \ll k_B T$, MH-kinetics obeys the FDT $\langle v\rangle = \beta f D$; for $\Delta E_{\mathrm{MH}} \gtrsim 0.5 k_B T$, the data deviates from the FDT with a maximum velocity $|v_{\mathrm{max}}| \to \ell k_0$ (k_0: particle diffusion attempt rate). A mean-field theory accurately describes these data (dashed curve, see appendix S3.3). Protocol (ii) is consistent with the FDT at all applied forces.

We find that the maximum velocity in Metropolis-Hastings kinetics is ℓk_0, and is therefore fundamentally limited by the microscopic attempt rate k_0. For small external driving $\beta|\Delta E_{\mathrm{MH}}| \ll 1$ we have $\exp(-\beta\Delta E_{\mathrm{MH}}) \approx 1 - \beta\Delta E_{\mathrm{MH}}$. This gives $\langle v\rangle \approx -\mathrm{sgn}(\Delta E_{\mathrm{MH}})\ell k_0 \beta|\Delta E_{\mathrm{MH}}| = -\ell k_0 \beta \Delta E_{\mathrm{MH}}$. Furthermore, we have for the diffusion coefficient $D = k_0 \ell^2$ and $\Delta E_{\mathrm{MH}} = -\phi_{\mathrm{MH}}\ell$ with ϕ_{MH} the steepness of the potential ramp. We combine these last results to find

$$\langle v\rangle \approx \beta \phi_{\mathrm{MH}} D, \tag{8.6}$$

Importantly, we find that Metropolis-Hastings kinetics is consistent with the fluctuation-dissipation theorem with a force $F = \phi_{\mathrm{MH}}$, but only in the limit of a potential ramp with small slope $\beta|\Delta E_{\mathrm{MH}}| \ll 1$.

We find that the FDT is obeyed for both protocols in the small field limit, but—consistent with the above calculations—the MH-kinetics displays non-linearities for $|\Delta E_{\mathrm{MH}}| \gtrsim 0.5 k_B T$ (Figure 8.1a, blue). These non-linearities stem from the fact that the maximum velocity v_{max} in MH-kinetics is rate-limited by the microscopic attempt rate k_0 as $v_{\mathrm{max}} = \ell_0 k_0$ and agrees excellently with our theoretical estimate (Figure 8.1a, dashed curve). Protocol (ii) with an external force obeys the FDT at all forces considered (Figure 8.1a, orange). This analysis shows that MH-kinetics can be used to approximately model non-equilibrium dynamics due to external forces, but that the magnitude of the dynamics will be underestimated at large field strengths.

8.2 Metropolis-Hastings Kinetics Underestimates the Entropy Production at Large Forces

To further investigate the validity of the stochastic dynamics in our LKMC far from equilibrium, we test whether a particle subject to external forces obeys the *steady-state fluctuation theorem* (SSFT) [35, 36, 38]

$$\log[p(+\Delta s)/p(-\Delta s)] = \Delta s,$$

where

$$\Delta s[x(\tau)] = D^{-1} \int_0^t \mathrm{d}\tau\ \dot{x}(\tau) v_s(x(\tau)) \tag{8.7}$$

is the total entropy production of a particle with trajectory $x(\tau)$ and steady-state velocity $v_s(x)$. The SSFT with this expression for Δs holds for a steady-state one-dimensional system arbitrarily far from equilibrium, and therefore serves as a good benchmark of the correctness of LKMC. We test the SSFT for the overdamped dynamics of a particle moving on a ring in an external field using the same two protocols as used in Figure 8.1a.

For small external fields $|\Delta E_{\mathrm{MH}}| \ll k_B T$, the data using MH-kinetics agrees well with the SSFT (Figure 8.2, light blue curves). However, for larger external fields $|E_{\mathrm{MH}}| \gtrsim 0.5 k_B T$, significant deviations from the SSFT can be observed (Figure 8.2, dark blue curves). The source of these deviations can be traced back to the maximum possible velocity in MH-kinetics: the maximum velocity $v_{\max} = \ell k_0$ at high $|E_{\mathrm{MH}}| \gg k_B T$ corresponds to a well-defined upper bound for the entropy production, $\Delta s_{\max} = t D^{-1} (\ell k_0)^2$ from equation (8.7). Since the particle in the limit $|E_{\mathrm{MH}}| \gg k_B T$ always moves with $v \approx v_{\max}$, the distribution $p(\Delta s)$ becomes increasingly peaked around $\Delta s_{\max}$. In other words, the upper bound on velocity in MH-kinetics results in an upper bound on entropy generation per unit time. By contrast, for the protocol (ii) with an explicit external force f, the data agrees with the SSFT at all forces considered (Figure 8.2, red curves). Our analysis shows that LKMC does agree with these fundamental results from stochastic thermodynamics, but at large external fields MH-kinetics will overestimate the entropy production probability for $\Delta s < \Delta s_{\max}$ and underestimate the entropy production probability for $\Delta s > \Delta s_{\max}$.

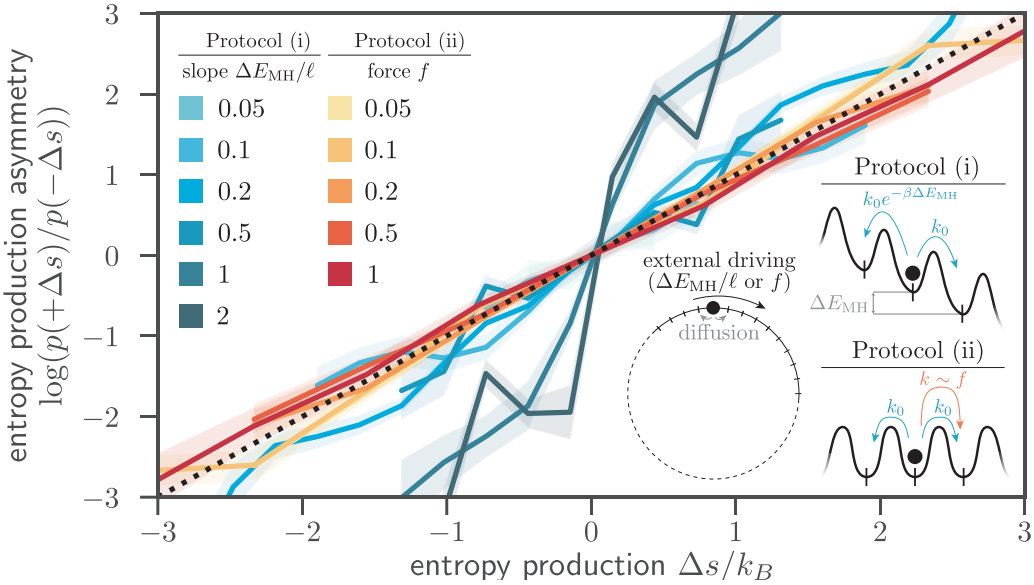

Figure 8.2: **Our LKMC with Metropolis-Hastings kinetics obeys the steady-state fluctuation theorem (SSFT), but only close to equilibrium.** We simulated the steady-state dynamics of a diffusive particle (stepping attempt rate k_0) on a ring subject to an external field. For the blue curves, the external field is a potential ramp, coupled to the particle motion using Metropolis-Hastings kinetics. For small external field strength $|\Delta E_{\mathrm{MH}}| \ll k_B T$, this potential ramp corresponds to a force $\phi_{\mathrm{MH}} = -\Delta E_{\mathrm{MH}}/\ell$. Indeed, we observe agreement with the SSFT for $|\Delta E_{\mathrm{MH}}| \ll k_B T$, but deviations occur from $\Delta E_{\mathrm{MH}} \gtrsim 0.5 k_B T$. For the red curves, the particle is subject to an external force f, which was included by adding an LKMC move for ballistic motion with attempt rate $k_+ \sim f$. For these data, we observe good agreement with the SSFT for all f considered.

8.3 Lattice Discretization can Result in Unphysical Jamming far from Equilibrium

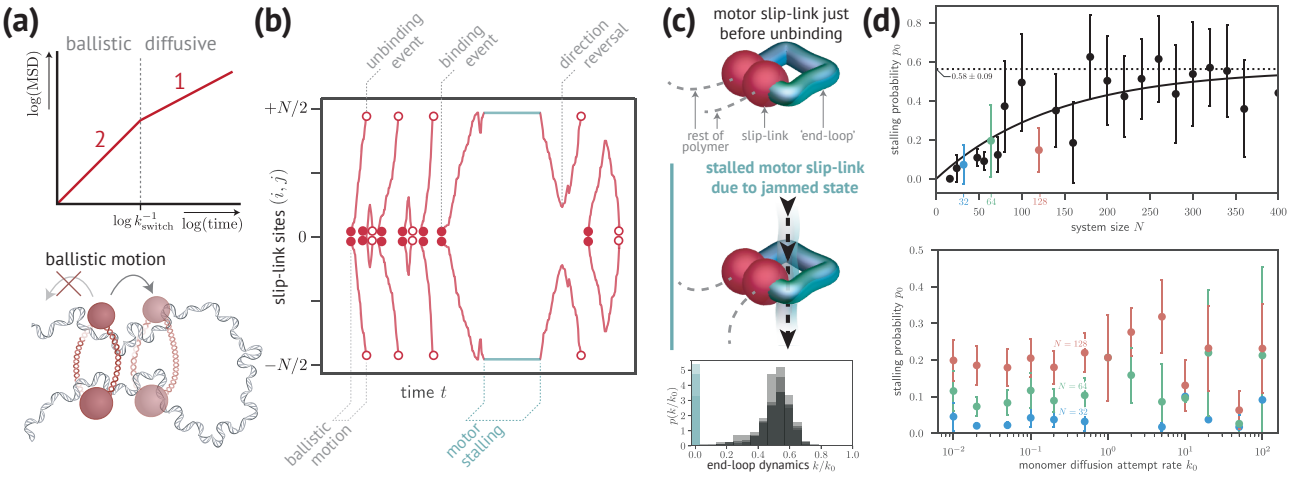

Figure 8.3: **Loop-extruding slip-links can stall due to sterically jammed configurations, dramatically reinforcing irreversibility. (a):** Implementation of motor slip-links as persistent random walkers. Motor slip-links move in one direction, but that direction reverses on average every $\langle t_{\text{switch}} \rangle = k_{\text{switch}}^{-1}$. **(b):** Inspection of kymographs of motor slip-links on circular polymers shows binding, unbinding and direction reversal events (for visual clarity, we centered all traces around locations of their respective binding events). The motor dynamics displays two distinct types of motion: the expected ballistic motion, but also long stretches of time where the motor appears to be *stalled* (turquoise). **(c):** Representative 3D polymer configurations of the 'end-loop' (green tube) for motor slip-links (red dumbbells) just before unbinding (top) and when stalled (middle). The stalled slip-link encloses an 'end-loop' that has a polymer strand running through it. This loop-threading results in locally jammed configurations, thereby stalling the motor. A histogram of the local polymer dynamics (bottom) reveals that there is indeed a sizeable portion of 'end-loops' that are completely frozen, $k \to 0$ (turquoise colored bin). **(d):** We computed the prior probability of stalling p_0 by repeatedly binding a single hyperpersistent slip-link ($k_{\text{switch}} = 0$) to the polymer, and measuring the fraction of traces that end in a stalled state. The stalling probability depends on the polymer size and converges to $p_0 = 0.58 \pm 0.09$ (error: square-root of parameter covariance). p_0 does not depend within error (twice standard error of the mean) on the monomer diffusion attempt rate k_0. Colors blue, green, red correspond to system-sizes $N = 32, 64, 128$. **Note:** For all sub-figures, we used the limit of $k_{\text{motor}} \gg k_0$.

Next, we consider how far a toy-model for DNA-organization can be driven out of equilibrium by loop-extruding enzymes. DNA loop-extrusion by enzymes such as SMC condensin is believed to be important for chromosome segregation and cell-fate in both prokaryotic and eukaryotic DNA [14, 20, 21, 29, 42–44]. We model these loop-extruding factors as slip-link dimers such as those in Figure 6.4, but with persistent random motion instead of diffusive motion (Figure 8.3a). The persistence of these motor slip-links is regulated by the rate k_{switch} of switching direction. The motor slip-links randomly bind to a circular polymer, extrude loops by performing persistent random motion, and can unbind when they enclose a polymer loop of size $|i - j| = 1$. Unlike our study of a single particle on a ring (Figures 8.1 and 8.2), where the particle and polymer dynamics evolve independently, the extrusion activity of these motor slip-links couples to the polymer dynamics, thereby driving the polymer out of equilibrium.

Motor slip-links in our LKMC mostly displayed ballistic motion, as expected (Figure 8.3b). Infrequently, however, we observe a surprising stalling behavior close to the end of the polymer (Figure 8.3b, turquoise). Images of the 3D polymer configurations show that these two distinct types of slip-link motion can be attributed to two distinct types of 'end-loops' enclosed by the slip-link (Figure 8.3c). Normal, ballistic motion over the full course of slip-link motion was associated with end-loops such as the top image in Figure 8.3c. The stalled slip-links, however, surround polymer loops that encircle a polymer strand from a different section of the polymer (Figure 8.3c, middle). Histograms of the total rate k of the 'end-loop' reveal that these end-loops are often kinetically arrested, $k = 0$, (Figure 8.3c, bottom), indicating that jammed configurations exist. The jamming is caused by steric repulsion that prevents any movement within the Verdier-Stockmayer move-set. Note that these states also occur when the polymer is in thermal equilibrium, but they exist only transiently since the motor can diffuse backwards, allowing the jammed end-loop to unravel.

We hypothesize that the irreversible motion of motor slip-links traps jammed configurations until the motor slip-link reverses its direction of movement. We quantitatively verified this by comparing the measured fraction of time spent in a stalled state to an estimate that takes into account motor switching. In detail, assume that the motor has two possible states: ballistic movement with velocity v and stalled motion at the end of the polymer (position $\approx N/2$). The time spent in the ballistic regime is then $\langle t_{\text{ballistic}} \rangle \approx N/v$, where the motor velocity in such a regime is $v \approx C^2 k_0$ with $C \approx 3/16$ the probability of two monomer bonds to be aligned (Figure 11.3). Once the motor slip-link stalls, the time spent in that stalled position is $\approx 1/k_{\text{switch}}$, so the average time spent in a stalled state is $\langle t_{\text{stalled}} \rangle \approx p_0/k_{\text{switch}}$, where we took p_0 directly from the data (Figure 8.3d). An estimate for the probability θ of a motor to be in a stalled state is then simply the weighted average of these two lifetimes:

$$\theta \approx \frac{\langle t_{\text{stalled}} \rangle}{\langle t_{\text{ballistic}} \rangle + \langle t_{\text{stalled}} \rangle} \approx \frac{p_0 v}{p_0 v + k_{\text{switch}} N}, \tag{8.8}$$

This estimate fits the data quite well, except for very small k_{switch} (Figure 8.4). The systematic deviation stems from the way that we prepare the system: The motor slip-link is bound to the polymer without any extruded loop. This slightly biases the data.

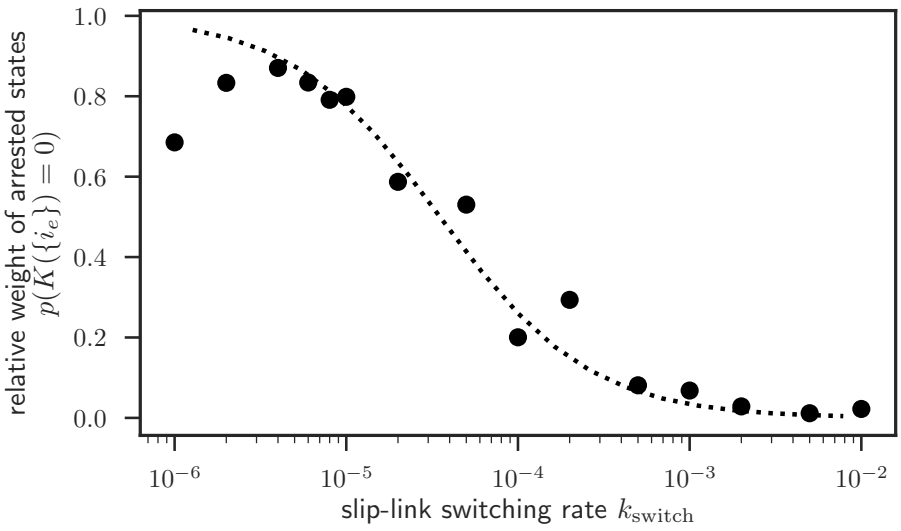

Figure 8.4: **The relative time that a motor slip-link spends in a stalled position depends on a balance between the direction switching time and the motor velocity.** Shown are the fractional time spent in a stalled state (black circles) for various rates k_{switch} of the motor-slip switching its direction of movement. A stalled state is defined as $K(i_e) = 0$, where $K(i_e)$ is the total rate of the loop (sites i_e) that surrounds a slip-link. Dashed line: mean-field approximation (8.8).

The images in Figure 8.3c suggest that the two types of end-loops are topologically distinct. However, the Verdier-Stockmayer for self-avoiding walks cannot change the polymer topology, since neither of the moves for a circular polymer (Figure 6.3a) can ever cross another strand. Indeed, movies of the 3D configuration before and during motor stalling reveal that the jamming of end-loops by motor slip-links is not a topological effect, but rather irreversible tightening of a large sub-chain that threads the loop trapped by the slip-link (supplementary movies 1–4)[1]. We hypothesize that in the limit of fast motor slip-links $k_{\text{motor}} \gg k_0$, this is a purely geometric—rather than kinetic—effect that depends only on the probability of such loop-threading. We evaluate this hypothesis with two independent tests (Figure 8.3d). As a first test, the probability of loop-threading depends on the size of the loops involved, and therefore also on the system size. Indeed, we observe that

[1]URL to movies is encoded in the following QR code:

the prior probability p_0 of jammed end-loops increases with system size, saturating to $p_0 \approx 0.58$ (Figure 8.3d, top). Second, we verify that p_0 is independent of the attempt rates of polymer dynamics (Figure 8.3d, bottom), consistent with loop threading being a geometric effect.

To the best of our knowledge, jammed end-loops have not been reported. However, the lattice topology combined with steric repulsion does imply the existence of other frozen, so-called 'non-ergodic', states [2, 26, 27, 37]. Non-ergodic states are distinct from the jammed end-loops in Figure 8.3c in that non-ergodic states can never be reached using the Verdier-Stockmayer move-set [27], but jammed end-loops clearly can be, since they are frequently observed (Figure 8.3). Our analysis of slip-linked polymers shows that including *irreversible* slip-link dynamics can dramatically increase the importance of frozen states compared to thermal equilibrium. In sum, great care must be taken when adding active agents in LKMC to systems with steric hindrance to avoid possibly unphysical, sterically jammed configurations.

Bibliography

[1] GibsonMichael A. and Jehoshua Bruck. Efficient Exact Stochastic Simulation of Chemical Systems with Many Species and Many Channels. 2000.

[2] Org Baschnagel, Joachim P Wittmer, Hendrik Meyer, J Baschnagel, J P Wittmer, and H Meyer. Monte Carlo Simulation of Polymers: Coarse-Grained Models. *Computational Soft Matter*, 23:83–140, 2004.

[3] G. Bell. Models for the specific adhesion of cells to cells. *Science*, 200(4342):618–627, may 1978. ISSN 0036-8075.

[4] Somendra M Bhattacharjee, Achille Giacometti, and Amos Maritan. Flory theory for Polymers. *Journal of physics: Condensed Matter*, 25:503101, 2013.

[5] A.B. Bortz, M.H. Kalos, and J.L. Lebowitz. A new algorithm for Monte Carlo simulation of Ising spin systems. *Journal of Computational Physics*, 17(1):10–18, jan 1975. ISSN 0021-9991.

[6] C. A. Brackley, J. Johnson, D. Michieletto, A. N. Morozov, M. Nicodemi, P. R. Cook, and D. Marenduzzo. Extrusion without a motor: a new take on the loop extrusion model of genome organization. *Nucleus*, 9(1):95–103, jan 2018. ISSN 1949-1034.

[7] Chris A Brackley, James Johnson, Davide Michieletto, Alexander N Morozov, Mario Nicodemi, Peter R Cook, and Davide Marenduzzo. Non-equilibrium chromosome looping via molecular slip-links. *Physical Review Letters*, 119(13):138101, 2017.

[8] C. P. Broedersz, X. Wang, Y. Meir, J. J. Loparo, D. Z. Rudner, and N. S. Wingreen. Condensation and localization of the partitioning protein ParB on the bacterial chromosome. *Proceedings of the National Academy of Sciences*, 111(24):8809–8814, jun 2014. ISSN 0027-8424.

[9] T Chou, K Mallick, and R K P Zia. Non-equilibrium statistical mechanics: from a paradigmatic model to biological transport. *Reports on Progress in Physics*, 74(11):1–41, 2011. ISSN 0034-4885.

[10] Crispin Gardiner. *Stochastic Methods: A Handbook for the Natural and Social Sciences*. Springer, Berlin, 2009.

[11] Pierre-Gilles de. Gennes. *Scaling concepts in polymer physics*. Cornell University Press, 1979. ISBN 080141203X.

[12] M. Doi and S. F. Edwards. *The Theory of Polymer Dynamics*. Clarendon Press, Oxford, 1986.

[13] Kristen A. Fichthorn and W. H. Weinberg. Theoretical foundations of dynamical Monte Carlo simulations. *The Journal of Chemical Physics*, 95 (2):1090–1096, jul 1991. ISSN 0021-9606.

[14] Mahipal Ganji, Indra A Shaltiel, Shveta Bisht, Eugene Kim, Ana Kalichava, Christian H Haering, and Cees Dekker. Real-time imaging of DNA loop extrusion by condensin. *Science*, 360(6384):102–105, feb 2018. ISSN 1095-9203.

[15] Daniel T Gillespie. A general method for numerically simulating the stochastic time evolution of coupled chemical reactions. *Journal of Computational Physics*, 22(4):403–434, dec 1976. ISSN 0021-9991.

[16] Daniel T. Gillespie. Exact stochastic simulation of coupled chemical reactions. *The Journal of Physical Chemistry*, 81(25):2340–2361, dec 1977. ISSN 0022-3654.

[17] Daniel T. Gillespie, Andreas Hellander, and Linda R. Petzold. Perspective: Stochastic algorithms for chemical kinetics. *The Journal of Chemical Physics*, 138(17):170901, may 2013. ISSN 0021-9606.

[18] Anton Goloborodko, Maxim V Imakaev, John F Marko, and Leonid Mirny. Compaction and segregation of sister chromatids via active loop extrusion. *eLife*, 5, may 2016. ISSN 2050-084X.

[19] Anthony J Guttmann. Self-Avoiding Walks and Polygons – An Overview. *Asia Pacific Mathematics Newsletter*, 2(4), 2012.

[20] Tatsuya Hirano. At the heart of the chromosome: SMC proteins in action. *Nature Reviews Molecular Cell Biology*, 7(5):311–322, may 2006. ISSN 1471-0072.

[21] Tatsuya Hirano. Condensin-Based Chromosome Organization from Bacteria to Vertebrates. *Cell*, 164:847–857, 2016.

[22] P. C. Hohenberg and B. I. Halperin. Theory of dynamic critical phenomena. *Reviews of Modern Physics*, 49(3):435–479, jul 1977. ISSN 0034-6861.

[23] Mehran Kardar. *Statistical Physics of Particles*. Cambridge University Press, Cambridge, New York, 2007. ISBN 9780521873420.

[24] Peter Kratzer. Monte Carlo and kinetic Monte Carlo methods - a tutorial. Technical report, 2009.

[25] Werner Krauth. *Statistical Mechanics: Algorithms and Computations*. Cambridge University Press, 2006. ISBN 9780198515357.

[26] Kurt Kremer and Kurt Binder. Monte Carlo simulation of lattice models for macromolecules. *Computer Physics Reports*, 7(6):259–310, jun 1988. ISSN 0167-7977.

[27] Neal Madras and Alan D. Sokal. Nonergodicity of local, length-conserving Monte Carlo algorithms for the self-avoiding walk. *Journal of Statistical Physics*, 47(3-4):573–595, may 1987. ISSN 0022-4715.

[28] Thomas F Middleton and David J Wales. Comparison of kinetic Monte Carlo and molecular dynamics simulations of diffusion in a model glass former. *Journal of Chemical Physics*, 120(17):8134, 2004.

[29] Christiaan A. Miermans and Chase P. Broedersz. Bacterial chromosome organization by collective dynamics of SMC condensins. *Journal of The Royal Society Interface*, 15(147):20180495, oct 2018. ISSN 1742-5689.

[30] Uri Moran, Rob Phillips, and Ron Milo. SnapShot: Key Numbers in Biology. *Cell*, 141:1262–1262, 2010.

[31] Debabrata Panja and Gerard T Barkema. Passage Times for Polymer Translocation Pulled through a Narrow Pore. *Biophysical Journal*, 94, 2008.

[32] Debabrata Panja and Gerard T. Barkema. Rouse Modes of Self-avoiding Flexible Polymers. *The Journal of Chemical Physics*, 131:154903, aug 2009.

[33] L. E. Reichl. *A Modern Course in Statistical Physics*, volume 67. Wiley, 4 edition, 2016. ISBN 978-3-527-40782-8.

[34] Michael Rubinstein and Ralph H. Colby. *Polymer Physics*. Oxford University Press, 2003.

[35] Udo Seifert. Entropy Production along a Stochastic Trajectory and an Integral Fluctuation Theorem. *Physical Review Letters*, 95(4):040602, jul 2005. ISSN 0031-9007.

[36] Udo Seifert. Stochastic thermodynamics, fluctuation theorems and molecular machines. *Reports on Progress in Physics*, 75(12):126001, dec 2012. ISSN 0034-4885.

[37] Nicholas D. Socci and José Nelson Onuchic. Folding kinetics of proteinlike heteropolymers. *The Journal of Chemical Physics*, 101(2):1519–1528, jul 1994. ISSN 0021-9606.

[38] T Speck, V Blickle, C Bechinger, and U Seifert. Distribution of entropy production for a colloidal particle in a nonequilibrium steady state. *Europhysics Letters (EPL)*, 79(3):30002, aug 2007. ISSN 0295-5075.

[39] Peter H. Verdier and W. H. Stockmayer. Monte Carlo Calculations on the Dynamics of Polymers in Dilute Solution. *The Journal of Chemical Physics*, 36(1):227–235, jan 1962. ISSN 0021-9606.

[40] D. G. Vlachos, L. D. Schmidt, and R. Aris. Kinetics of faceting of crystals in growth, etching, and equilibrium. *Physical Review B*, 47(9):4896–4909, mar 1993. ISSN 0163-1829.

[41] Arthur F. Voter. INTRODUCTION TO THE KINETIC MONTE CARLO METHOD. In *Radiation Effects in Solids*, pages 1–23. Springer Netherlands, Dordrecht, 2007.

[42] Xindan Wang and David Z Rudner. Spatial organization of bacterial chromosomes. *Current Opinion in Microbiology*, 22:66–72, 2014.

[43] Xindan Wang, Paula Montero Llopis, and David Z Rudner. Organization and segregation of bacterial chromosomes. *Nature Reviews Genetics*, 14: 191–203, 2013.

[44] Xindan Wang, Hugo B. Brandão, Tung B. K. Le, Michael T. Laub, and David Z. Rudner. Bacillus subtilis SMC complexes juxtapose chromosome arms as they travel from origin to terminus. *Science*, 355(6324), 2017.

[45] Xindan Wang, Olive W. Tang, Eammon P. Riley, and David Z. Rudner. The SMC Condensin Complex Is Required for Origin Segregation in Bacillus subtilis. *Current Biology*, 24(3):287–292, apr 2018. ISSN 0960-9822.

[46] G Witz, K Rechendorff, J Adamcik, and G Dietler. Conformation of Circular DNA in 2 Dimensions. *Physical Review Letters*, 101(14):148103, 2008.

Part III

Bacterial Chromosome Organization by Condensin

9

Minimal Models for DNA Organization by SMC

Movies for this chapter are found at the URL encoded in this QR code.

Chapter summary: *We present two minimal models for the action of SMC using diffusive and motor slip-links.*

On large length-scales, a prominent feature of chromosome organization in many bacteria is the emergence of a cross-diagonal in Hi-C maps spanning the whole length of the genome, indicating anomalously high contact probabilities between opposing pairs of DNA-loci positioned on the left and right chromosomal arms. Such a cross-diagonal is observed in *B. subtilis* and *C. crescentus* [24, 42, 44, 45], but not in *E. coli* [25]. The measured cross-diagonal indicates a robust juxtaposition of the left and right arms of the chromosome [24, 42, 44, 45], an organizational feature that is important for faithful chromosome segregation [18, 19, 28, 38, 43]. This juxtaposed organization is largely controlled by the highly conserved ATPase SMC condensin [28, 44, 45]. While much is known about condensin at the molecular level [7, 11, 13, 20, 21, 36], it is unclear how small numbers of condensins (3–30 per chromosome [47]) are capable of collectively organizing the chromosome over such a range of length-scales. Thus, the physical principles underlying the juxtaposed organization of the chromosome remain elusive.

The functional capability of SMC condensins to organize the chromosome into a juxtaposed state crucially depends on two factors:

(i) The presence of a specific loading site on the chromosome [32, 44].

(ii) The ability of condensin to bind and hydrolyze ATP [32, 47].

In *B. subtilis*, the loading site is established by a large nucleoprotein complex composed of ParB proteins bound around *parS* close to the origin of replication (*ori*) [5, 26, 33, 39]. Condensins are recruited to this ParB*S* region, and from there propagate deep into the bulk of the DNA polymer [32, 47]. Removing the loading site results in a loss of the cross-diagonal in Hi-C maps, and adding additional loading sites disrupts the cross-diagonal [44, 45]. Moreover, the translocation of condensins away from the loading site depends on their ATPase activity; condensin mutants that cannot bind ATP only weakly associate with DNA, and mutants that do not hydrolyze ATP do not efficiently propagate away from the ParB*S* loading site (appendix A.1 and [32, 47]). With a ring-like topology of $25 - 50\,\mathrm{nm}$ in diameter, the condensin ring is large enough to trap a DNA loop by threading a DNA duplex through it [7, 8, 8, 11, 13, 20, 36, 47]. It has been proposed that the possibility of condensins to trap DNA-loops would enable them to align the chromosomal arms by progressively extruding DNA-loops from the origin to the terminus region [28, 44, 45].

Important clues on the role of ATPase activity in SMC condensin come from *in vitro* single-molecule experiments. These experiments revealed that *Saccharomyces cerevisiae* condensin is a molecular motor, and performs active translocation over DNA duplexes [40]. Kymographs showed that the direction of movement of yeast condensin is *a priori* random, and

switches direction after a typical time-scale; in other words, yeast condensin performs persistent random motion over DNA. In fact, recent single-molecule experiments have revealed that such yeast condensin performs active loop extrusion [16]. Similar experiments have not yet observed such motor activity for bacterial condensin [23]. Nevertheless, it has been widely speculated that the ATPase activity of bacterial condensin is also directed towards motor activity [8, 11, 14, 47]. In this picture, condensin would actively extrude DNA-loops, possibly by feeding DNA duplexes through its ring-like structure [1, 3, 15, 35]. In contrast, other models have been proposed in which the ATPase activity of condensin is directed towards regulating its association with DNA [2, 3, 32, 47]. Thus, it remains an open question whether bacterial condensin also acts as a loop extruding enzyme, or whether the ATPase activity primarily regulates the DNA-recruitment of condensins.

To elucidate the role of condensin ATPase activity on bacterial chromosome organization, we develop two minimal models for condensin–DNA interactions, where we describe SMC condensin as a slip-link that non-topologically traps a DNA-loop (Figure 9.1). In these models, we analyze the complex interplay between the molecular-scale dynamics of SMC condensins and large-scale chromosome organization. In the most basic model, condensin activity is assumed to be directed towards regulating its DNA-recruitment, while the dynamics of condensin slip-links on the DNA is diffusive. Although the motion of individual slip-links on the DNA is purely diffusive, their active recruitment to DNA results in non-equilibrium collective motion of slip-links. Interestingly, we find that such *diffusive slip-links* can organize the chromosome into a juxtaposed state, but not within physiological constraints (section 11.1). Next, we expand the model to include *motor slip-links* that perform persistent random motion on DNA, as observed for yeast condensin *in vitro* [40]. We find that these motor slip-links are much more effective in organizing the entire chromosome. In particular, our motor slip-link model requires at least 2–3 orders of magnitude fewer condensins to organize the chromosome than in the diffusive slip-link model. In addition, the development of the juxtaposed state exhibits sub-diffusive dynamics in the diffusive slip-link model, in contradiction with the rapid re-organization observed *in vivo* [45] (chapter 12.1). We show that such a fast re-organization of the chromosome can be achieved by motor activity in the form of active loop extrusion. More generally, we provide a quantitative model to address key questions in bacterial chromosome organization, such as the role of an exclusive loading site, cell confinement, motor activity and interaction of SMC condensin with other DNA-bound factors.

Our model of condensin–DNA interactions (Figure 9.1) contains two main ingredients:

(i) A circular DNA polymer;

(ii) Multiple SMC condensins that interact with the DNA;

which we explore in combination with possible additional ingredients, such as ellipsoidal confinement (chapter 10). We employ a lattice polymer with a lattice constant set by the persistence length of DNA (appendix A). Condensins are modeled as slip-links: elastic rings that trap a DNA-loop by encircling two DNA duplexes. Importantly, we consider both diffusive and motor slip-links. Diffusive slip-links move randomly (stepping rate k_0) over the DNA (Figure 9.1, inset); motor slip-links perform persistent random motion (translocation rate k_{motor}) with a persistence time-scale $\tau_{\text{switch}} = k_{\text{switch}}^{-1}$. These persistent dynamics enable motor slip-links to actively extrude DNA loops.

To simulate the dynamics of both the DNA polymer and the slip-links, we use the Lattice Kinetic Monte-Carlo (LKMC) algorithm that we developed in part II. Our LKMC algorithm simulates the Rouse dynamics of DNA [12, 46], the associated stochastic motion of slip-links on the DNA, as well as the microscopic reactions in which slip-links bind to (rate k_+) or unbind from (rate k_-) the DNA. For simplicity, we assume instantaneous slip-link binding $k_+ \to \infty$, justified by the relatively fast cytosolic diffusion of condensin [37]. Because the number of condensins on the bacterial chromosome is thought to be limited to $3 - 30$ per chromosome [47], we additionally fix a maximum number of slip-links N_p that can bind to the DNA.

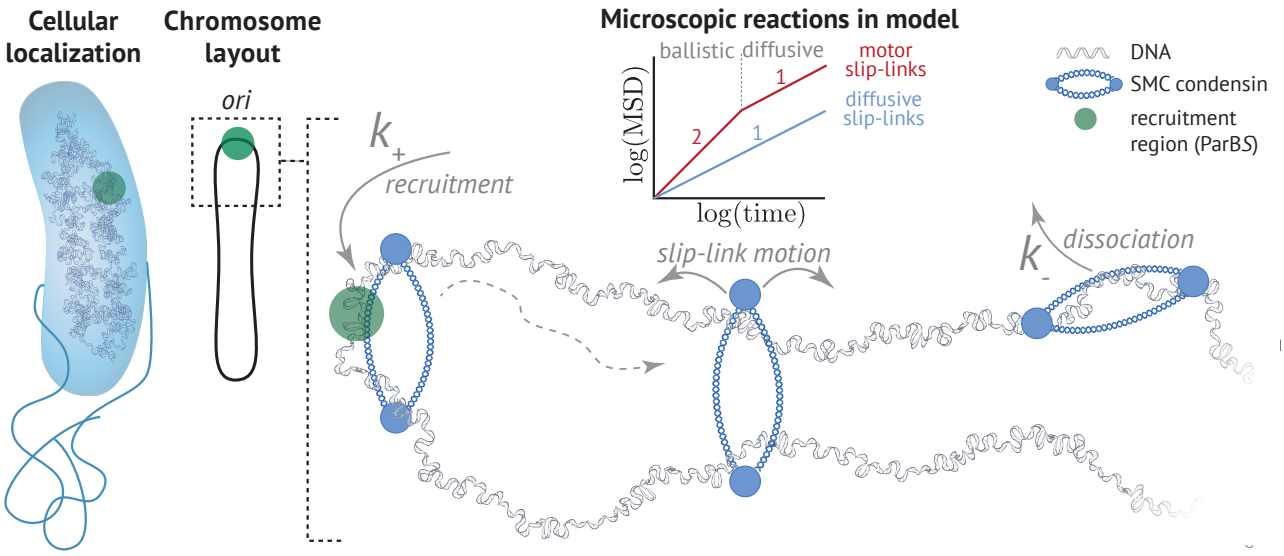

Figure 9.1: **Schematic of slip-link model for SMC condensin–DNA interactions. Left**: The bacterial chromosome has a circular topology. SMC condensins are loaded onto the DNA by the ParB*S* complex located near the origin of replication (*ori*, green). **Right**: Microscopic reactions in our model with associated rate constants. Condensins are represented as slip-links, which either perform diffusive or more persistent, motorized movement (inset). Our computational method simulates the stochastic interplay between DNA dynamics and slip-link positioning.

9.1 Quantifying Loop Topology

Although a single slip-link can only encircle DNA loops non-topologically in our model (Figure 9.1), multiple slip-links do form a loop network. Loop networks of slip-linked polymers can have a variety of loop network topologies [30]. In particular, slip-links that surround other slip-links transiently trap loops by steric interactions: for the trapped slip-link to unbind, its neighboring slip-links have to unbind first. Thus, loop relaxation is a nested process, so we call these loops 'nested loops'.

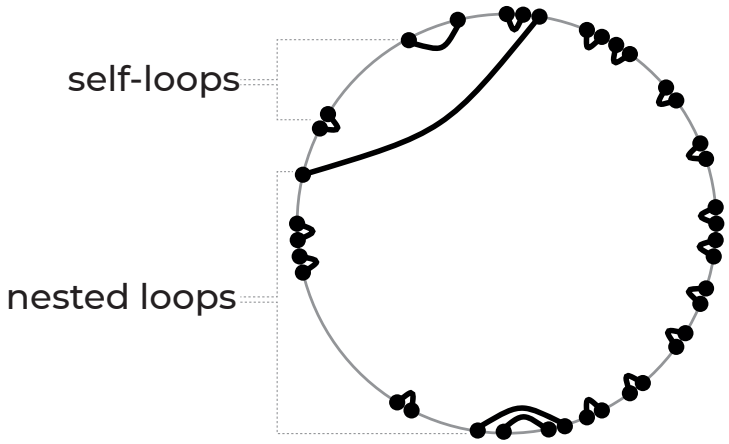

Figure 9.2: **Slip-links can enclose loops in topologically distinct ways: nested and non-nested.** Self-loops are not trapped by additional slip-links. Nested loops, on the other hand, are topologically trapped by other slip-links, which need to unbind before the loop can become non-nested.

To investigate the role of slip-link kinetics on loop topology more quantitatively, we employ a metric that captures the

nestedness of these nested loops, an essential topological difference between the loop network of random and juxtaposed polymers (compare Figure 11.1b to Figs. 11.1c–d). To this end, we define the order parameter $\theta \in [0, 1]$ as the fraction of nested loops (Figure 9.2). Below we have reproduced a pseudocode to measure θ:

Algorithm 9.1 Pseudocode for computing the loop-network order parameter θ. In this algorithm, we use the convention $|\Delta| = \min(\Delta, N_m - \Delta)$, which encodes the periodic boundary conditions of circular polymers.

Input : slip-link sites $\{(i, j)_n\}, n = 1, \ldots, N_p$ (with N_p the number of slip-links).
output: loop network topology order parameter $\theta \in [0, 1]$

$n_{\text{nested}} \leftarrow 0$
for $n \leftarrow 1$ **to** N **do**
  get slip-link sites (i_n, j_n) of slip-link n
  compute self-loop-size of slip-link n: $\Delta_{\text{self}} \leftarrow |i - j|$
  get sites $(i, j)_{n-1,n+1}$ of neighboring slip-links $n - 1, n + 1$
  compute nested-loop-size between slip-link n and $n - 1, n + 1$:

$$\Delta_{(n,n-1)} = |i_n - i_{n-1}| + |j_n - j_{n-1}|$$
$$\Delta_{(n,n+1)} = |i_n - i_{n+1}| + |j_n - j_{n+1}|$$

  $\Delta_{\text{nested}} \leftarrow \min(\Delta_{(n,n-1)}, \Delta_{(n,n+1)})$
  if $\Delta_{\text{nested}} < \Delta_{\text{self}}$ **then**
    $n_{\text{nested}} \leftarrow n_{\text{nested}} + 1$
  end
end

$\theta \leftarrow n_{\text{nested}}/N_p$
return θ

The order parameter θ is defined for a slip-link–polymer network, so that we can measure θ for each time-point t, i.e. $\theta(t)$ is well-defined. Variances (varθ) were computed as the variance of the time-sequence $\{\theta(t_1), \theta(t_2), \ldots\}$. Whenever we refer to θ in the main manuscript without explicit reference to the time-dependence, we imply $\theta = \langle\theta(t)\rangle$ where we used a time average for $\langle\cdot\rangle$.

10

Slip-Linked Polymers in Equilibrium do not Display Juxtaposed Organization

Chapter summary: *By showing that several equilibrium models fail to produce juxtaposed organization under physiological constraints, we make plausible that the juxtaposition is unlikely to originate from an equilibrium mechanism.*

10.1 Equilibrium Implementation of Diffusive Slip-Links do not Produce Juxtaposed Organization

As a first test of the effect of slip-links on chromosome organization, we examine the impact of diffusive slip-links on the loop sizes and loop topology. Loop sizes were quantified through the looping contact probability $p(\Delta)$ for loops of size Δ; the loop topology was captured by the loop topological order parameter θ (section 9.1). We implemented a system with diffusive slip-links that can bind and unbind anywhere, so that this system obeys detailed balance and hence relaxes into thermodynamic equilibrium. Since this corresponds to the absence of a specific ParB*S* loading site, we abbreviate this system as ΔParB*S*. The scaling $p \sim \Delta^{1.7}$ we observe for the ΔParB*S* scenario (Figure 10.1a, left) is nearly identical to that of a random polymer $p \sim \Delta^{d\nu}, d\nu \approx 1.8$ [9]. The distribution of the loop-topological order parameter θ (section 9.1) is highly peaked at $\theta = 0$, showing that the diffusive slip-links almost always enclose self-loops and almost never enclose nested loops (Figure 10.1a, right). The system with diffusive slip-links that can only bind to the loading site breaks detailed-balance, but we find that for slow dissociation kinetics, the resulting distribution of loop-sizes $p \sim \Delta^{1.8}$ is nevertheless consistent with that of a random polymer (Figure S10.1b).

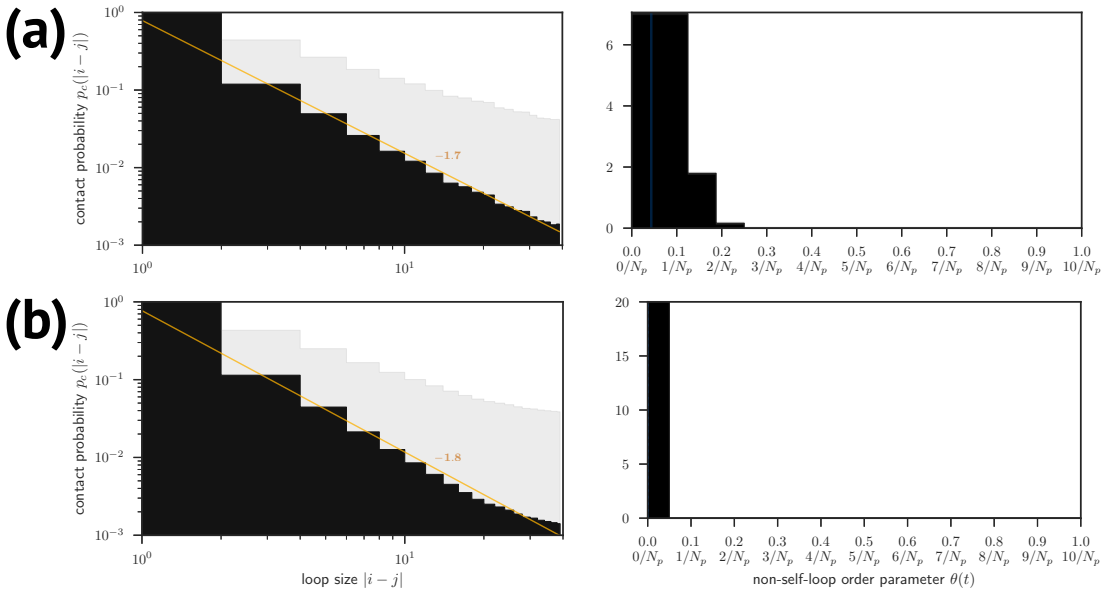

Figure 10.1: Left panels: Contact distribution $p(\Delta)$ for loop-size Δ. Yellow lines: linear regressions of the log-transformed data $(\log \Delta, \log p(\Delta))$. Right panels: Distributions $p(\theta)$ of loop nesting parameter θ. **(a):** Diffusive slip-links that bind non-specifically to the polymer (ΔParBS). **(b):** Diffusive slip-links that bind exclusively to the loading site, but with slow dissociation kinetics ($k_- = 10^{-6} k_0$).

10.2 Confinement and Diffusive Slip-Links do not Produce Juxtaposed Organization

Some authors have argued that large-scale chromosome organization can be effected by purely geometrical factors [6, 29]. In more detail, Monte-Carlo studies demonstrate that spatially fixing one or a few loci, in combination with compaction proteins that organize DNA into topological domains, produce a linear global arrangement of self-avoiding polymers [6, 29]. These data show that substantial large-scale organization can be produced even by factors that do not consume ATP. It is an open question, however, whether the linear arrangement of chromosomal loci presented by Buenemann and Lenz [6] also implies the existence of juxtaposed chromosomal arms. To address this, we test whether slip-linked self-avoiding polymers that are forced into a linear arrangement by an elongated confining potential also display a robust cross-diagonal in contact maps.

To investigate the role of an anisotropic confinement on juxtaposed organization, we use an ellipsoidal harmonic potential,

$$V_{\text{conf.}}(x, y, z) = \frac{1}{2}\left(k_x x^2 + k_y y^2 + k_z z^2\right),$$

where the $k_{x,y,z}$ specify the 'spring-constants' of the confinement for monomers with positions x, y, z. The ellipsoidal potential simulates the combined action of the cell membrane and crowding agents. We assume cylindrical symmetry [28], $x^2 = y^2 = r^2$ where r is the radius of the cylindrical confinement. We use a length-to-width ratio of 4, slightly larger than the typical length-to-width ratio ≈ 3 of many bacteria [34].

A confinement alone cannot produce a cross-diagonal in thermodynamic equilibrium, since we haven't yet included any breaking of translational invariance.[1] Indeed, bacteria such as *B. subtilis* and PopZ in *C. crescentus* contain DivIVA proteins that localize *ori* to one of the cell poles [43]. To simulate such a breaking of translational symmetry in our simulations, we additionally include a spring-like tether. We use equilibrium Monte-Carlo simulations [5] to investigate the organization of DNA in the presence of a confinement potential and tether. We find that the contact maps do not exhibit a pronounced cross-diagonal in the absence of slip-links (Figure 10.2a).

So far, we have shown that neither an ellipsoidal potential (Figure 10.2a), nor equilibrium slip-links (section 10.1) separately introduce anomalously large loops. But, since slip-link positioning can respond to polymer geometry in a non-

[1] Linear polymers strictly break translational invariance by their endpoints. In bacteria, the DNA exists in a circular configuration, making the system invariant under global translations $i \to i'$ in polymer site.

trivial way [30, 31], it is possible that the *combination* of these two ingredients introduces organizational features that are absent in the system with these ingredients separately. However, the addition of N_p slip-links mostly appears to increase the number of contacts (compare Figs. 10.2a–b). This slight asymmetry resembles a cross-diagonal under conditions of large N_p and small polymer-length N_m, but only becomes visually apparent in our contact maps when the density of slip-links is 10%, $>$ 100 times higher than the SMC condensin density *in vivo* [47]. Even so, even at this unphysiologically high concentration of slip-links, the asymmetry in the contact maps is very diffuse compared to that of the *in vivo* Hi-C maps (Figure 10.2a–b). The width of the off-diagonal structure broadens as we increase N_m. Indeed, the cross-diagonal for $N_m = 200$ is only clearly resolved when we increase the asymmetry of the confinement potential to unrealistically high values $\sqrt{z^2/r^2} > 30$ (Figure 10.2c–d). In sum, our simulations indicate that ellipsoidal confinement and tethering alone cannot be responsible for a cross-diagonal under physiological constraints.

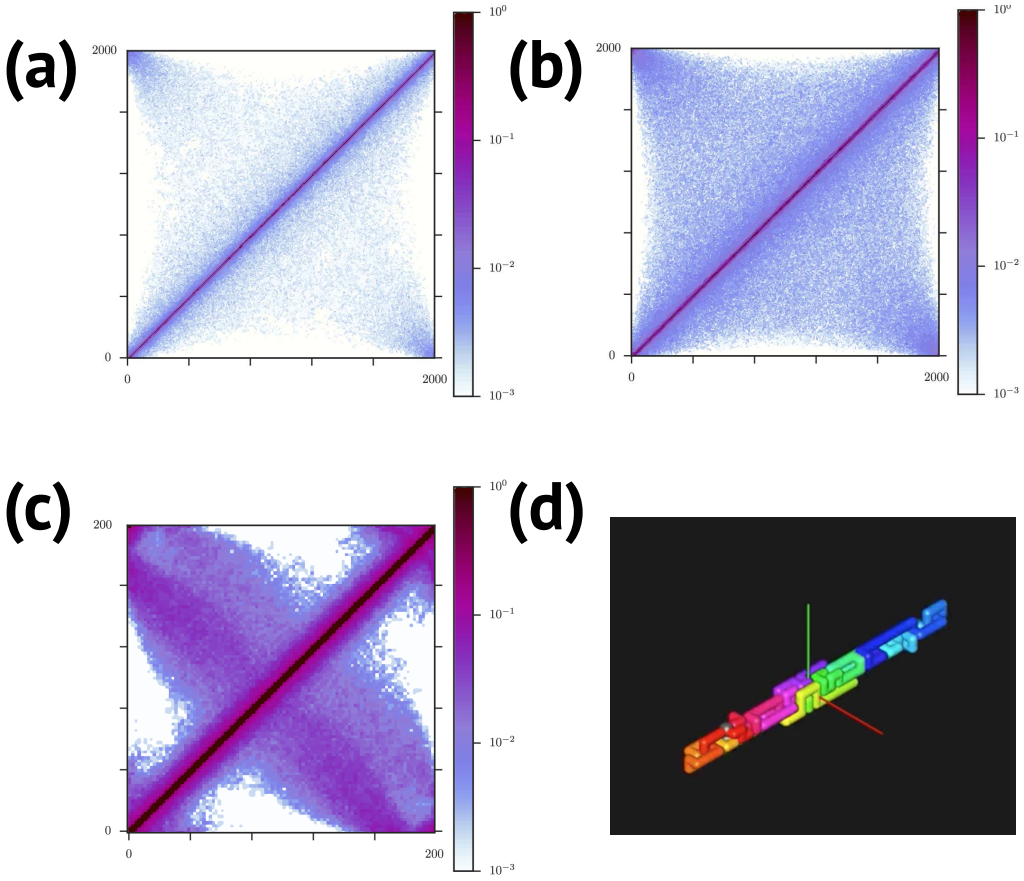

Figure 10.2: **Physiologically relevant confinement potentials do not result in a cross-diagonal. (a–b):** contact maps from polymers with $N_p = 0$ (a) and $N_p = 100$ (b) equilibrium slip-links with a confinement potential of widths $(\sqrt{x^2}, \sqrt{y^2}, \sqrt{z^2}) = (5\ell_0, 5\ell_0, 20\ell_0)$, where ℓ_0 is the monomer length. Polymer length $N_m = 2000$. **(c–d):** Simulation with a confinement potential of anisotropy ratio $\sqrt{100} \approx 31.6$. Polymer length $N_m = 200$. See SI movie 6 for a movie of the polymer for various other anisotropies.

11

Steady-State Organization by Diffusive and Motor Slip-Links Out of Equilibrium

Chapter summary: *We show that diffusive slip-links can effect organization due to a surprising non-equilibrium loop selection mechanism, but not at physiological densities. Slip-links with active loop extrusion organizes the whole chromosome at all densities.*

11.1 Diffusive Slip-Links Can Organize the Chromosome at High Densities

Diffusive slip-links in equilibrium do not display juxtaposed organization in our models (Figure 10.2). We therefore introduce active binding of slip-links to a ParB*S* loading site (Figure 9.1, left), modeling the effect of actively regulated association of condensin to the DNA [2, 3, 32, 47]. Before we examine the role of a ParB*S* loading site, we first develop some intuition for the phenomenology for the simpler case of no specific loading site. In this ΔParB*S* model, diffusive slip-links can bind and unbind anywhere on the DNA (Figure 11.1a, ΔParB*S*). This assumption results in a homogeneous binding probability $p_p(i)$ (Figure 11.1a, bottom). Importantly, in the ΔParB*S* scenario, all microscopic reactions are fully reversible, implying that the system relaxes into thermodynamic equilibrium. In equilibrium, small loops are strongly favored, owing to the increasing entropic cost of loop formation with larger loop size. This tendency to form small loops is reflected in the loop diagrams (Figure 11.1a, top). Indeed, the loop sizes trapped by the slip-links are consistent with the equilibrium loop-size distribution (section 10.1). Furthermore, in this scenario the contact maps are structureless and only exhibit a single main diagonal (Figure 11.1a, middle), as for a random polymer. These results demonstrate that our KMC model with reversible microscopic reactions evolves towards thermodynamic equilibrium. Consistent with our previous data (section 10.2), we conclude that diffusive slip-links that can easily bind over the full extent of the polymer but do not organize the chromosome.

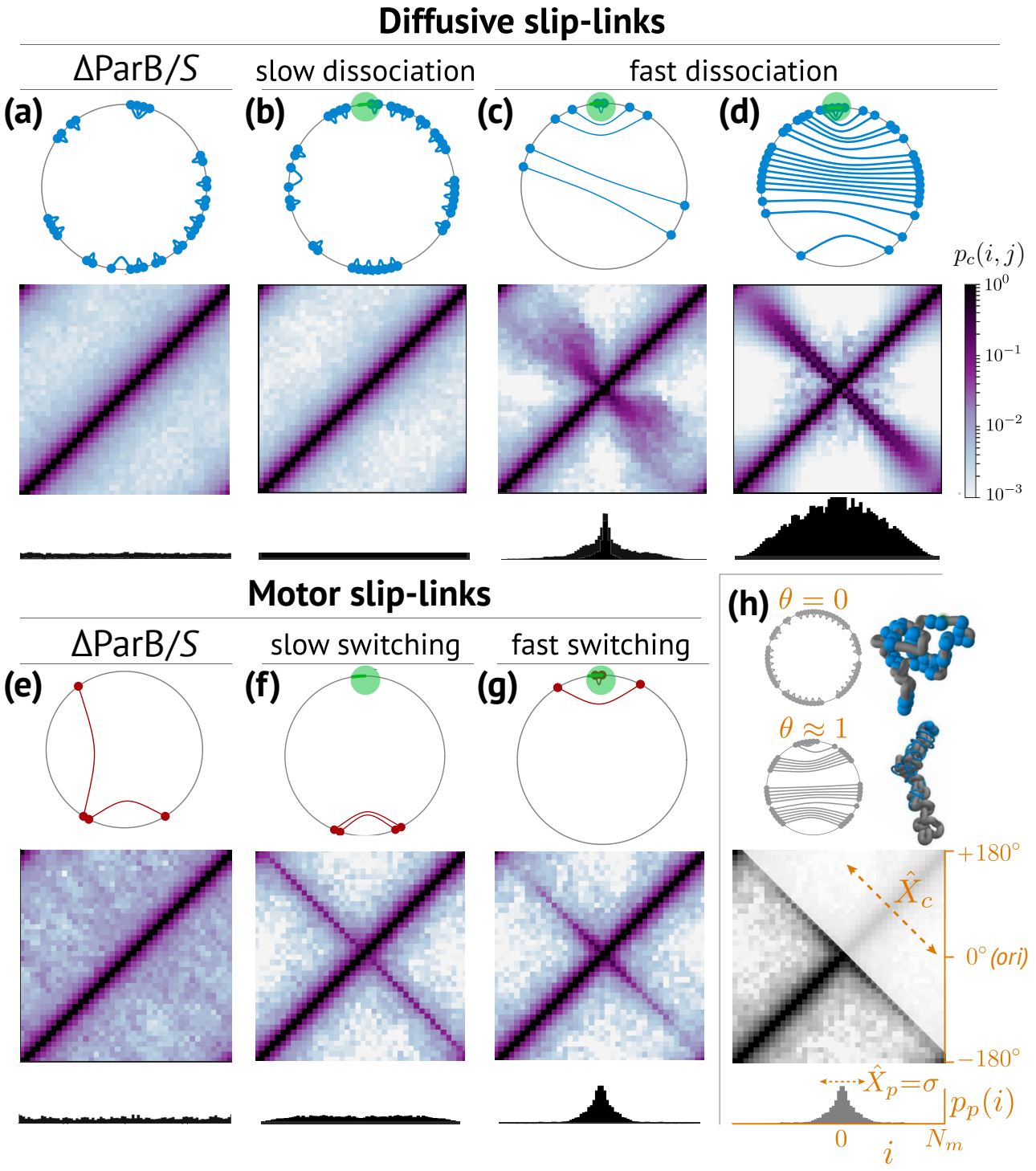

Figure 11.1: **Steady-state organization of a circular chromosome by diffusive and motor slip-links.** For all sub-figures (a)–(h): top panels show a loop diagram that illustrates the loop structure induced by slip-links, middle panels the contact map $p_c(i,j)$, and bottom panels the binding profile $p_p(i)$ of slips-links along the DNA. **Diffusive slip-links, (a)–(d)**: (a) lacks a specific loading site (ΔParB*S*), (b) $k_- = 10^{-6}k_0$, (c)–(d) $k_- = k_0$ with $N_p = 5$ in (c) and $N_p = 25$ in (d). **Motor slip-links, (e)–(g)** (e) lacks a specific loading site (ΔParB*S*), (f) $k_{\text{switch}} = 10^{-6}k_{\text{motor}}$, (g) $k_{\text{switch}} = 10^{-1}k_{\text{motor}}$. All simulations were performed with a circular polymer polymer of length $N_m = 80$. Maximum number of polymer-bound slip-links from (a)–(g) are respectively $N_p = 16, 20, 5, 25, 2, 2, 2$. **Legend, (h)**: We use the fraction of nested loops (θ), cross-diagonal length ($\hat{X}_c$, see appendix A.2) and the slip-link propagation distance ($\hat{X}_p = \sqrt{\text{var } p_p(i)}$) to quantify polymer organization. The slip-link loading site (when present) is positioned in the center of the contact map, so that the axes run from $-\frac{1}{2}N_m \ldots + \frac{1}{2}N_m$.

We next investigate how the presence of a ParB*S* slip-link loading site [18, 32, 44, 45, 47] impacts steady-state chromosome organization. Note, while recruitment of slip-links in our model is exclusive to *ori*, unbinding can occur anywhere on the DNA. This implies that the reactions involving slip-link binding/unbinding are partially irreversible. Hence, detailed balance is broken [17], and the system may no longer evolve towards thermodynamic equilibrium. Nevertheless, for slow dissociation kinetics (small k_-), we observe an unstructured contact map (Figure 11.1b), similar to the equilibrium system lacking a specific loading site (Figure 11.1a). Moreover, the loop diagrams again show that the slip-links mostly encircle small loops (Figure 11.1b, top). In sum, we see that, although detailed balance is broken on the level of slip-link binding/unbinding, the diffusive slip-links with slow dissociation kinetics do not appear to organize the DNA polymer.

Interestingly, increasing the dissociation kinetics of slip-links results in dramatically different contact maps. We observe the emergence of a prominent cross-diagonal, which either disperses away from the loading site (Figure 11.1c) or remains clearly resolved over the whole polymer (Figure 11.1d), depending on the density of slip-links. The loop diagrams for these systems exhibit a topology distinct from the equilibrium configuration; slip-links trap DNA-loops in a cooperative, nested manner. Movies of the loop diagrams and contact maps clearly demonstrate that these nested loops propagate away from the loading site, dynamically driving a juxtaposition of the two polymer arms (SI movies 3a–b). This dynamical arm–arm alignment is a distinct out-of-equilibrium phenomenon, and thus requires the exclusive binding of slip-links to the loading site. Thus, our observations show that diffusive slip-links with fast dissociation kinetics in conjunction with a loading site can, in principle, generate a non-equilibrium polymer organization similar to that found in living cells [24, 28, 44, 45].

We observe a sigmoidal relation between θ and the dissociation rate k_- for diffusive slip-links, with θ transitioning from low to high values with increasing k_- (Figure 11.2a, blue). The change in the average θ is associated with a transition from a distribution around $\theta \approx 0$ to a distribution around $\theta \approx 1$ (Figure 11.2b). This surprising link between k_- and θ can ultimately be traced to collective interactions between slip-links: steric hindrance between slip-links drives loops away from the loading site, resulting in ballistic collective motion of slip-links (SI Movie 3b). The lifetime τ_{NS} of nested loops depends on both the velocity of the ballistic movement and on the polymer length N_m. We argue below that the increase in τ_{NS} due to these two factors quantitatively accounts for the increase of θ with k_-.

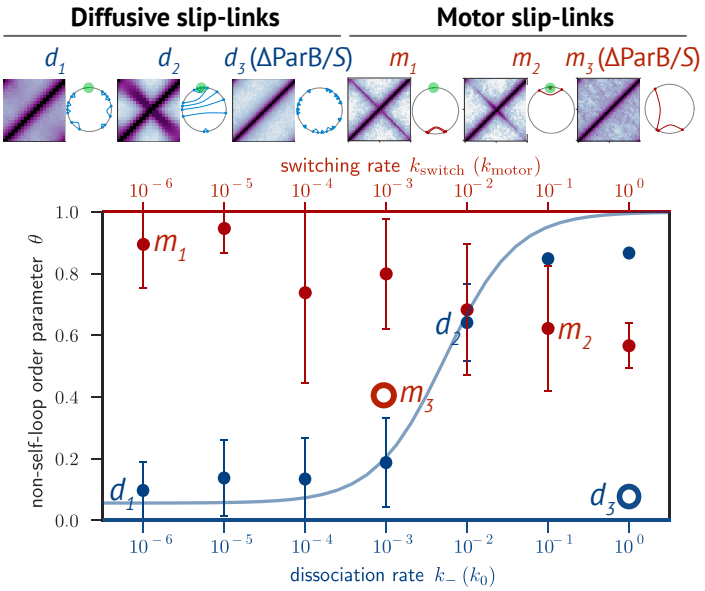

(a) **Loop network topology controls polymer organization.** The fraction of nested loops θ of diffusive slip-links (blue) is shown as a function of the dissociation rate k_- (in units of the slip-link diffusion rate k_0), and for motor slip-links (red) as a function of the switching rate k_{switch} (in units of the slip-link translocation rate k_{motor}). Error bars represent the standard deviation $\sqrt{\text{var}\theta}$. A mean-field model yields an estimate for θ of diffusive slip-links (blue curve). Representative loop diagrams and contact maps are indicated for different parameter choices, labeled d_1–d_3 for diffusive links and m_1–m_3 for motor slip-links. Also shown are θ for diffusive (d_3) and motor (m_3) slip-links with non-specific slip-link binding (ΔParBS). Polymer lengths N_m and slip-link numbers N_p are $N_m = 40, N_p = 10$ (diffusive slip-links) and $N_m = 80, N_p = 2$ (motor slip-links).

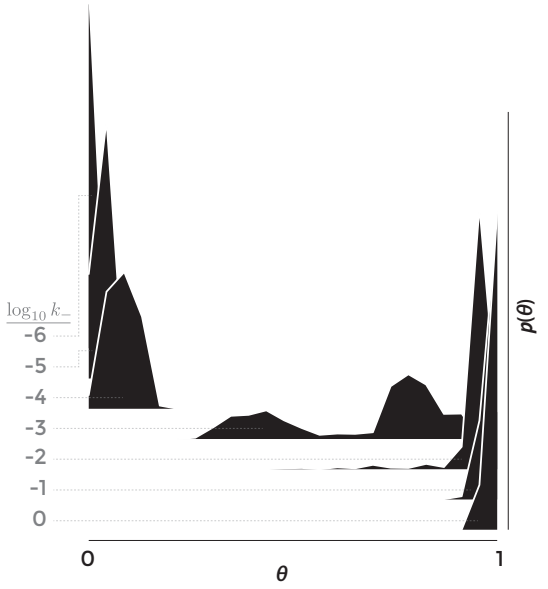

(b) **Theta is characterized by a narrow distribution at low and high dissociation rates.** Shown is the distribution $p(\theta)$ for logarithmically spaced k_-. These data show that the transition in the mean $\langle\theta\rangle$ for increasing k_- is associated with a transition from a narrow distribution around $\theta \approx 0$ to a distribution around $\theta \approx 1$.

Figure 11.2

To understand the impact of loop lifetime on θ more quantitatively, we model the loop topology of the slip-links as N_p independent two-state systems: (i) self-loop (S) with a lifetime τ_S; (ii) nested loop (NS) with a lifetime τ_{NS}. From this mean-field perspective, the fraction of nested loops $\langle\theta\rangle$ is simply the weighted lifetime of a nested loop:

$$\langle\theta\rangle \approx \frac{p_{NS}\tau_{NS}}{p_{NS}\tau_{NS} + p_S\tau_S}, \tag{11.1}$$

where p_S and p_{NS} are the probabilities for a diffusive slip-link to enclose a self and nested loop respectively after loading to *ori*. Before a slip-link encloses nested loop, two conditions have to be fulfilled: (i) the two bonds away from the loading site have to be aligned and (ii) the slip-link now has to randomly move both slip-link sides away from the loading site, instead of sideways. Once these two conditions are fulfilled, the arbitrarily fast binding $k_+ \to \infty$ (chapter 9) guarantees that a new slip-link will bind to the origin, generating a nested loop. To find the probability for step (i), we propose a simple counting argument. We count the total number of configurations of two bonds, excluding global symmetries, as 16, of which three have both bonds aligned (Figure 11.3). Thus, the prior probability of bond alignment is $C \approx 3/16$. Then, there are three possibilities for double-sided slip-link movement: two possibilities to move sideways (left or right) and one possibility to move both sides away from the loading site. Thus, the probability of the slip-link enclosing the loop, assuming there is one, is 1/3. In sum, the prior probability for a slip-link that was just loaded to randomly enclose a loop is $\frac{1}{3}C \approx \frac{1}{16}$.

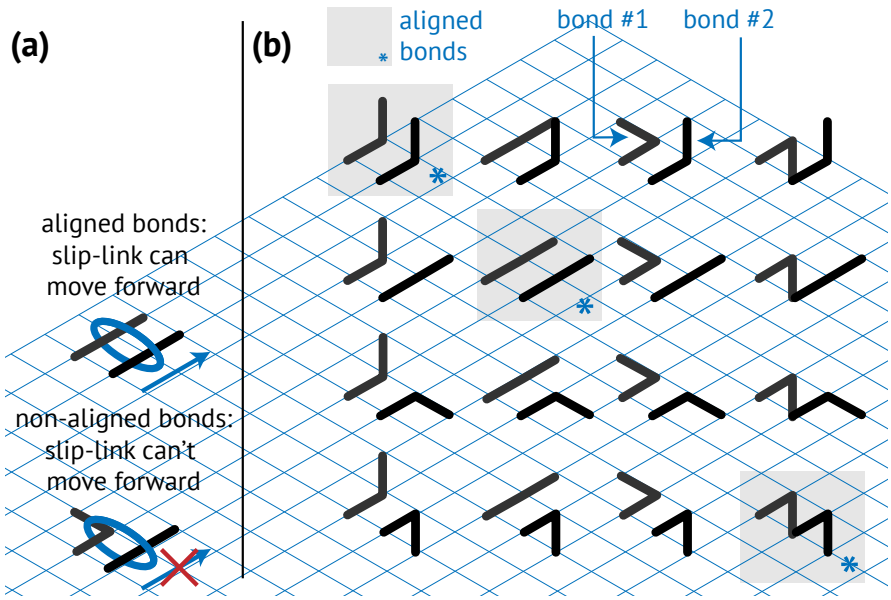

Figure 11.3: **Illustration of our simple counting argument for estimating C, the probability for two bonds to be aligned parallel. (a)**: A stiff slip-link can translocate in a certain direction (arrow) if the two polymer bonds in that direction are parallel. **(b)**: We count three possible configurations (marked "*") for bonds #1, #2 that allow slip-link movement out of a possible 16 configurations. This implies that $C \approx 3/16$.

Now that we have $p_{\mathrm{NS}} \approx \frac{1}{3}C$ (and, by extension $p_{\mathrm{S}} = 1 - p_{\mathrm{NS}}$), we need to find the loop lifetimes $\tau_{\mathrm{S}}, \tau_{\mathrm{NS}}$ to find a closed form for equation (11.1). The lifetime of a self-loop can be approximated as $\tau_{\mathrm{S}} \approx k_-^{-1}$.[1] Since the nested loops propagate ballistically in the high density phase (Figure 11.4a; SI movie 3b), there exists a well-defined mean velocity $\langle v \rangle$. Note that $\langle v \rangle$ is well-defined, but not known *a priori* since it is a collective property of the system that might depend on system size, looping entropy and slip-link density. We approximate the dynamics of a slip-link enclosing non-self-loops as a two step process: (i) Ballistic motion from the loading site to a point opposite thereto with velocity $\langle v \rangle$, and (ii) Random unbinding (waiting time $\tau_S \approx k_-^{-1}$) once the slip-link has traversed the entire system. Assuming step (ii) follows step (i), and that the two steps are independent, we estimate the lifetime of a nested loop by

$$\tau_{\mathrm{NS}} \approx \frac{\frac{1}{2}N_m}{\langle v \rangle} + k_-^{-1}.$$

For the unknown parameter $\langle v \rangle$, we empirically find for $\phi_p = 0.4$ that $\langle v \rangle \approx c k_0 / N_m^2$ where k_0 is the slip-link movement attempt rate and $c \approx 9$ (Figure 11.4a). This $1/N_m^2$ scaling is distinct from the $1/N_m$ scaling observed in the Simple Symmetric Exclusion Process [10], likely due to polymer loop entropy that impedes the movement of slip-links away from the loading site.

In sum, our estimate for $\langle \theta \rangle$ is

$$\langle \theta \rangle \approx \frac{\frac{1}{3}C\left(\frac{1}{2}cN_m^3 k_0^{-1} + k_-^{-1}\right)}{\frac{1}{3}C\left(\frac{1}{2}cN_m^3 k_0^{-1} + k_-^{-1}\right) + (1 - \frac{1}{3}C)k_-^{-1}}. \tag{11.2}$$

From this, we determine that nested loops start to dominate the loop topology from a characteristic dissociation rate $k_-^\star \sim N_m^{-3}$. The dependency of θ on k_- reveals that the irreversible loading mechanism functions as a *kinetic filter*: The fast dissociation kinetics filters out self-loops, only allowing nested loops to propagate through the system. Since c in Eq. (11.2)

[1] The estimate $\tau_{\mathrm{S}} \approx k_-^{-1}$ is not exact due to the fact that not all self-loops can directly unbind. To be able to unbind, a slip-link has to enclose a loop of size $\Delta = 1$ and—although the majority of slip-links falls in this category—some have a larger loop size $\Delta > 1$. The slip-links with $\Delta > 1$ have to first diffuse to a $\Delta = 1$ before they can unbind, increasing the lifetime of these self-loops. For very low $k_- \ll T_D^{-1}$, where T_D is the typical time needed to diffuse back to a loop of size $\Delta = 1$, the approximation $\tau_{\mathrm{S}} \approx k_-^{-1}$ will be excellent. For increasing k_-, the finite diffusion time T_D will worsen the estimate $\tau_{\mathrm{S}} \approx k_-^{-1}$.

can be determined from a measurement of $\langle v \rangle$, this form for $\langle \theta \rangle$ does not contain any free fit-parameters, and collapses data for various N_m, k_- onto a single master curve (Figure 11.4b).

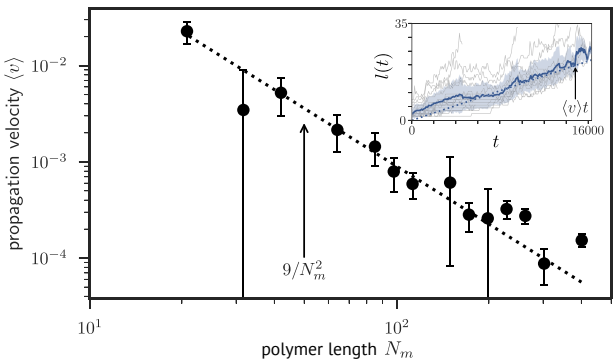

(a) Diffusive slip-links propagate ballistically over a polymer in the juxtaposed state with a velocity $\langle v \rangle \sim 1/N_m^2$. **Main panel**: Averaged velocities of tracer slip-links $\langle v \rangle$ (markers) for different system sizes N_m (error bars: twice the standard error in the mean). The dashed line $\langle v \rangle \approx 9k_0/N_m^2$ is shown together with data computed in the high-density and fast-dissociation regime ($\phi_p = 0.4, k_- = k_0$). **Inset**: Trajectories of diffusive slip-links $l(t)$ (thin, gray) with ensemble average $\langle l(t) \rangle$ (thick, blue; shaded region is the standard deviation), where $l(t)$ is the distance traversed by a tracer slip-link at time t after loading onto the polymer.

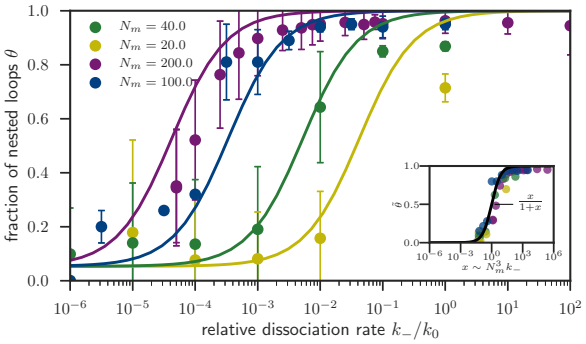

(b) A single master curve approximately describes the fraction of nested loops. **Main panel**: Loop parameter $\langle \theta \rangle$ (markers) for different system sizes N_m as indicated (error bars: $\sqrt{\mathrm{var}\theta}$) together with mean-field (Eq. (11.2)) estimate (solid curves). All data were measured in the high-density regime ($\phi_p = 0.4$ for $N_m = 20, 40, 200$ and $\phi_p = 0.38$ for $N_m = 100$). **Inset**: The mean-field estimate for θ (Eq. (11.2)) collapses the data onto a single master-curve $x/(1+x)$. The reduced parameters are: $\tilde{\theta} = (\theta - \theta_{\min})/(\theta_{\max} - \theta_{\min}), \theta_{\max} = 1, \theta_{\min} = \frac{1}{3}C$ and $x = \frac{C}{3-C}(\frac{1}{2}cN_m^3 k_-/k_0 + 1)$ with $x \sim N_m^3 k_-$ for $N_m \gg 1$.

Figure 11.4

We find that the characteristic dissociation rate at the inflection point of θ coincides with the transition from a random polymer to a juxtaposed organization with a cross-diagonal in contact maps (d_1 vs. d_2 in Figure 11.2a). In addition, we observe that the equilibrium implementation of diffusive slip-links that bind non-specifically to the DNA (ΔParB*S*) yields $\theta \approx 0$ (d_3 in Figure 11.2a), confirming our previous observation that the loading site is necessary for creating large, nested loops. Thus, in the presence of a loading site, diffusive slip-links appear to drive a dynamical transition between phases of weak and strong nesting of DNA-loops, and this transition is crucial to establish the juxtaposed state of the chromosome.

The loop topological order parameter θ remains close to the equilibrium value $\theta \ll 1$ for low k_- (Figure 11.4b). However, at lower k_-, the collective dynamics are much slower—in other words, the decreased θ at low k_- could be simply due to insufficient simulation time. To investigate this, we *prepared* the system at low k_- in a high θ state, and monitor whether these loops remain nested. We did this by positioning immobilized slip-links at regular intervals along the polymer but nevertheless allowing for polymer relaxation (Figure 11.5a). After we turned on slip-link movement, we recorded kymographs of the cross-diagonal.

Kymographs clearly reveal that the cross-diagonal in the regime of slow dissociation propagates away from the loading site (Figure S11.5b). The region around *ori* in the contact maps slowly loses the anomalously high contact probabilities over time, meaning that the cross-diagonal disappears for diffusive slip-links in the slow dissociation regime. For slip-links in the fast dissociation regime, however, the cross-diagonal persists and remains stable over time for N_p above a critical value (Figure 11.5c). Ensemble averaged movies of contact maps for $N_p = 1, 2, 4, 8, 16, 32$ confirm that the cross-diagonal only persists in the fast dissociation regime (SI movies 4[a-f] for fast dissociation and 5[a-f] for slow dissociation). These data show that the dependency of θ on k_- is not due to lack of simulation time, but rather an emergent feature of the collective dynamics.

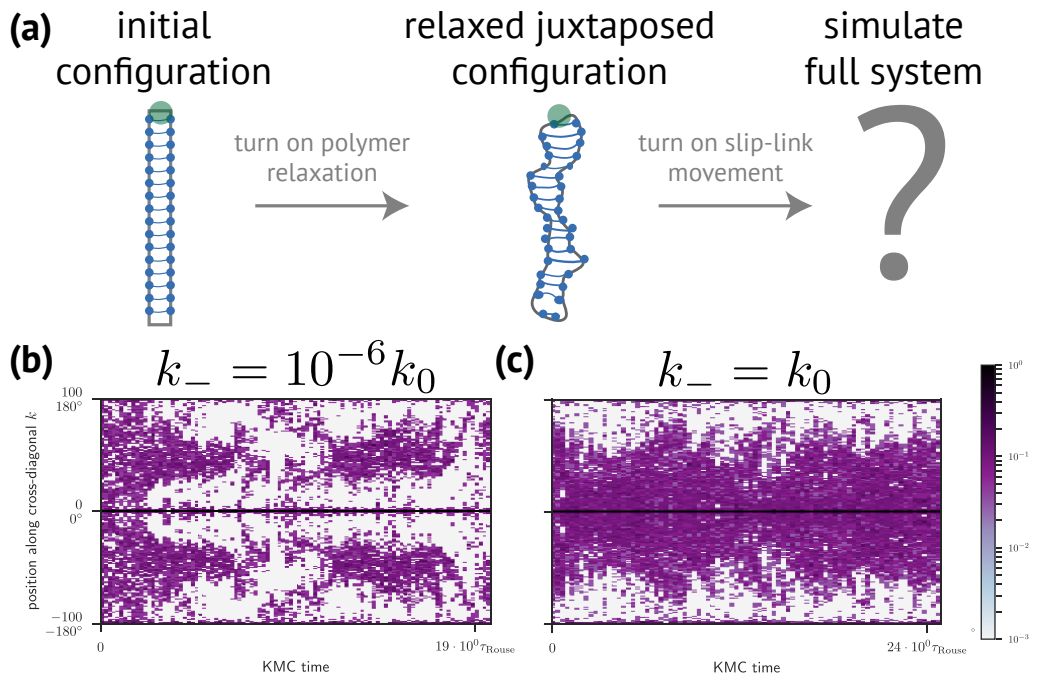

Figure 11.5: **The juxtaposed organization is only stable for fast dissociation kinetics. (a)**: Illustration of our simulation to text the stability of the juxtaposed organization. We first initialize a polymer in the juxtaposed organization with immobilized diffusive slip-links, but allow for polymer relaxation. We then turn on slip-link diffusion along the polymer, and recorded kymographs of the cross-diagonal from contact maps. **(b)**: Kymograph of the cross-diagonal for slow dissociation kinetics. The cross-diagonal disappears over time (see also SI movies 5[a–f]). **(c)**: Kymograph of the cross-diagonal for fast dissociation kinetics. The cross-diagonal persists (see also SI movies 4[a–f]). For both kymographs (b–c) we used $N_m = 200, N_p = 32$.

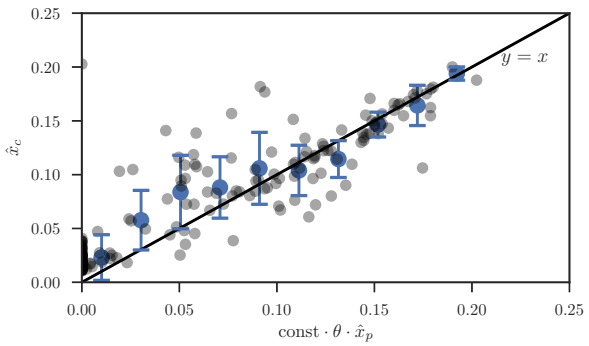

(a) The relative cross-diagonal width is $\approx$ const.$\theta\hat{x}_p$ with const. = 1.3. Error bars: standard deviation $\sqrt{\text{var}\hat{x}_c}$.

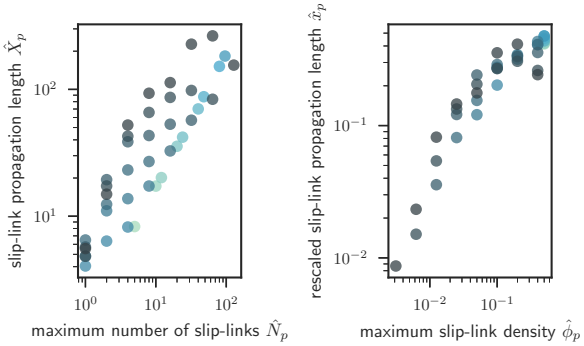

(b) **Left**: The data of $\hat{X}_p$ is not a single-valued function of $\hat{N}_p$, but also depends on N_m. **Right**: Rescaling both axes to intensive quantities $\hat{x}_p, \hat{\phi}_p$ (see text) collapses the data onto a single master curve.

Figure 11.6

Importantly, in our model with diffusive slip-links, we find that having many nested loops is a necessary, but not sufficient condition to organize the polymer into a juxtaposed state. These loops also need to propagate into the bulk of the polymer. In particular, our simulations reveal that the cross-diagonal length $\hat{x}_c$ is well approximated by an 'and-gate' of θ and $\hat{x}_p$ (Figure 11.6a). This shows that one needs cooperative loops (high θ) that also propagate deep into the bulk of the

polymer (high $\hat{x}_p$). Additionally, we find that the propagation of diffusive slip-links is a density-driven process: the nested loops only propagate over the full length of the polymer for very high slip-link densities (Figure 11.6b). This can be clearly seen in the binding profiles $p_p(i)$; at low slip-link densities, the binding profile is sharply peaked around the loading site (Figure 11.1c, bottom), whereas this peak broadens as we increase the slip-link density (Figure 11.1d, bottom). We stress that this points to a fundamental limitation of organization by diffusive slip-links: since the collective dynamics are density driven, many slip-links will be needed to organize large DNA polymers.

Whether condensins could be pushed in file in the way we describe here *in vivo* is uncertain; single condensins actually move across DNA-bound obstacles *in vivo* [4] and multiple condensins can traverse one another *in vitro* [22]. In sum, sterically interacting diffusive slip-links can juxtapose chromosomal arms at high slip-link density through a combination of active loading and fast dissociation, but whether such a mechanism is possible in live cells is unclear.

11.2 Motor Slip-Links are Effective at Organizing the Chromosome at all Densities

Motivated by recent observations of motor activity of yeast condensin in single-molecule experiments [16, 40], we next explore how such activity impacts the ability of slip-links to organize the chromosome. In our model, motor slip-links are assumed to perform persistent random motion (Figure 9.1, inset). Such persistent slip-links actively extrude loops [1, 3, 15, 16, 35]. The active dynamics of motor slip-links is characterized by the *switching rate* k_{switch}. For $k_{\text{switch}} \to 0$, the motor slip-links never reverse direction, whereas for $k_{\text{switch}} \gg k_{\text{motor}}$ they behave as diffusive slip-links with a diffusion coefficient that depends on the motor stepping speed k_{motor}. We find that motor slip-links with small k_{switch} organize a system-spanning cross-diagonal (Figure 11.1f), whereas the cross-diagonal retracts for increasing k_{switch} (Figure 11.1g).

Overall, we observe that the persistence of such motor slip-links renders them much more effective at producing the cross-diagonal (Figs. 11.1f–g). Even for low slip-link densities, a system-spanning cross-diagonal is formed together with an extended binding profile (Figure 11.1f). Indeed, motor slip-links can readily drive the chromosome into a state with a high degree of loop nesting. Even in the absence of a loading site (m_3 in Figure 11.2a), motor slip-links efficiently create nested loops. However, the degree of loop nesting θ is sensitive to k_{switch} (Figure 11.2a, red). We observe a decline of θ with increasing k_{switch}, although θ remains above 50% even if the motor slip-link on average switches direction with each step ($k_{\text{switch}} = k_{\text{motor}}$). Since a high degree of loop nesting is necessary for establishing the juxtaposed state (Figure 11.6a), the rate of directional switching must remain sufficiently small for the motor slip-links to organize the chromosome.

In the absence of a specific loading site, motor slip-links still extrude large loops and efficiently propagate along the polymer, as reflected in the higher contact probability away from the main diagonal (Figure 11.1e). However, there is no breaking of translational symmetry by a loading site, resulting in a leveled time-averaged contact map. Interestingly, we observe that systems without a loading site can organize *transiently* into a juxtaposed state, a phenomenon that we discuss in section 12.3.

In vivo experiments have demonstrated that condensins propagate far from their loading site [32, 47]. To quantify the distribution of condensins on the chromosome in our model, we measure the extent $\hat{X}_p$ of slip-link propagation as the standard deviation of the binding profile $p_p(i)$ (Figure 11.1h). We eliminate the system-size dependence by considering the scaled propagation length $\hat{x}_p = \hat{X}_p / \frac{1}{2} N_m$ (Figure 11.6b) as a function of slip-link density $\phi_p = 2N_p/N_m$.

The scaled propagation length of diffusive slip-links only approaches the *in vivo* value, $\hat{x}_p \approx 0.5$ ([32, 47] and appendix A), when we use slip-link densities $\gtrsim$10% in our simulations (Figure 11.7a, blue). Importantly, this slip-link density would correspond to thousands of condensins on the chromosome, 2–3 orders of magnitude more than reported *in vivo* [47]. This further illustrates that diffusive slip-links are not efficient at forcing the nested loops into the bulk of the polymer at low densities. In contrast, motor slip-links propagate over the full length of the polymer at all slip-link densities we considered (red data in Figure 11.7), as observed experimentally in cells ([32, 47] and appendix A).

Our results are summarized in a "state diagram" (Figs. 11.7b–c), indicating the scaled extent $\hat{x}_c = \hat{X}_c / \frac{1}{2} N_m$ of the cross-diagonal in contact maps. *Diffusive* slip-links require both fast dissociation kinetics as well as a high slip-link density to bring the polymer into the juxtaposed state (Figure 11.7b). For high densities of *motor* slip-links $\phi_p \gtrsim 10\%$ and low k_{switch}, the slip-links readily juxtapose the DNA polymer (e.g. m_1 in Figure 11.7c). Contrarily, for increasing k_{switch}, motor slip-links antagonize each other's translocation (e.g. m_2 in Figure 11.7c), impeding the collective propagation of slip-links away from the loading site, thereby resulting in a reduced $\hat{x}_c$ (compare m_1, m_2 in Figure 11.7c; SI movies 10a–b). In the limit $k_{\text{switch}} \gg k_{\text{motor}}$, motor slip-links effectively behave as diffusive slip-links with enhanced unbinding kinetics, placing them in the fast dissociation regime (data for $k_{\text{switch}} \gtrsim 10 k_{\text{motor}}$ in Figure 11.7c). In contrast, for $\phi_p \lesssim 10\%$, motor slip-links only require k_{switch} to be sufficiently low. We estimate that wild-type condensin is indeed in this slow switching regime ("exp." in Figure 11.7c). In sum, our simulations indicate that condensins at physiological densities can drive nested loops into the

bulk of the polymer, crucial for establishing arm–arm alignment, only if they perform motorized, persistent motion.

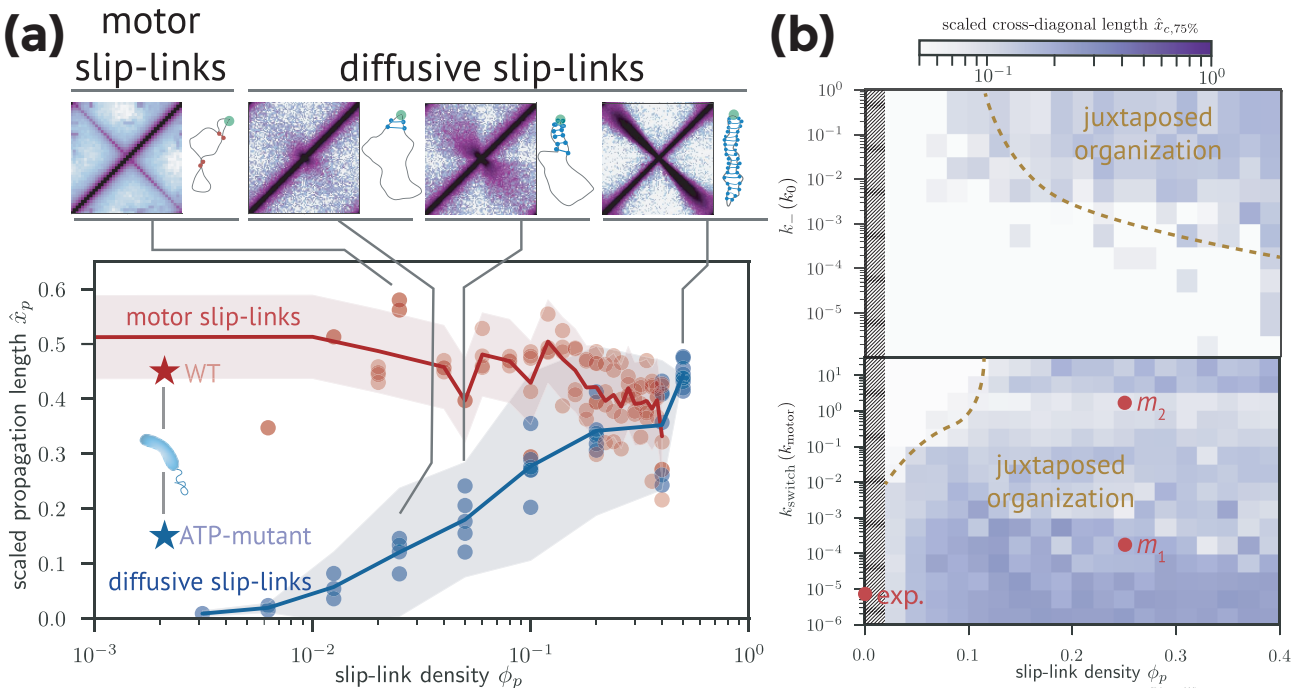

Figure 11.7: Propagation length of slip-links and associated arm–arm juxtaposition **(a)** Scaled propagation length $\hat{x}_p \equiv \hat{X}_p / \frac{1}{2} N_m$ as a function of slip-link density ϕ_p for diffusive (blue) and motor (red) slip-links. Indicated are also experimental measurements from [32] for wild-type cells ("WT", red star) and mutants whose SMC condensins have suppressed ATPase activity ("ATP-mutant", blue star) (appendix A). **(b)**: State diagram of scaled cross-diagonal length $\hat{x}_c = \hat{X}_c / \frac{1}{2} N_m$ for diffusive slip-links as a function of dissociation rate k_- (in units of k_0) and ϕ_p. **(c)**: State diagram of scaled cross-diagonal length $\hat{x}_c$ for motor slip-links as a function of the switching rate k_{switch} (in units of k_{motor}) and ϕ_p. Both (b–c) have $N_m = 100$. Marker "exp.": is an estimate of WT behavior (Table A.1). Markers m_1 (SI movie 10a) and m_2 (SI movie 10b) are respectively at low and high k_{switch}. Hatched area indicates values that we did not reach computationally. We define $\hat{x}_c$ as the 75$^{\text{th}}$ percentile of the cross-diagonal contacts (appendix A).

Asymmetrically translocating condensins produce a star-shaped motif in contact maps

Experiments of SMC condensin propagation in *B. subtilis* suggest that two condensin complexes might link together in a hand-cuff topology, with each of the two condensins in the dimer actively extruding a separate DNA duplex [41, 45]. In our model, motor slip-links extrude DNA in a symmetrical fashion, as expected for condensins in a hand-cuff configuration: both sides of a slip-link move over a separate DNA duplex with the same translocation rate. However, in recent *in vitro* assays, single yeast condensin complexes actively extrude DNA loops asymmetrically: one end of the complex appears anchored at a DNA locus, while the opposite end actively translocates over DNA [16]. Interestingly, contact maps of such asymmetric motor slip-links[2] contain a star-shaped pattern around the loading site (Figure 11.8), a feature that is also visible in Hi-C maps of *B. subtilis* [28, 44]. This suggests that there is at least some fraction of condensins performing asymmetric translocation. An equally tantalizing explanation is that the movement of one of the condensins in a dimer is impeded by other DNA-bound factors, thereby forcing a condensin-dimer to propagate asymmetrically. Indeed, there is growing evidence that the movement of SMC complexes can be antagonized by oncoming transcription factors [41, 44, 45].

[2]The protocol we used for asymmetric translocation is: 1. a slip-link is added to the loading site; 2. one of the two sides of the slip-link is immobilized; 3. the side of the slip-link that is not immobilized is assigned a random translocation direction (i.e. positive or negative) and 4. the particle actively translocates until it unbinds (when $|i - j| = 1$), after which we return to step 1.

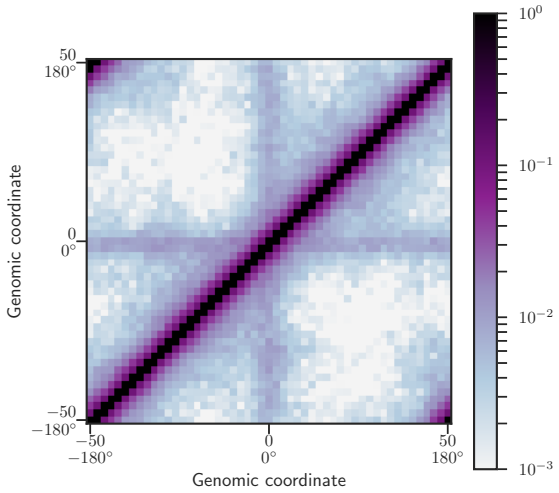

Figure 11.8: **Asymmetric loop extrusion results in a star-shaped pattern in contact maps.** For these data, we bound one asymmetric highly persistent motorized slip-link to the loading site. Note, in this simulation, none of the slip-links perform *symmetric* loop extrusion, which is the type of motor activity discussed in the other sections of this chapter.

12

Dynamic Re-Organization of Chromosomes by Diffusive and Motor Slip-Links

Chapter summary: *Diffusive slip-links re-organize the chromosome with sub-diffusive scaling, whereas the velocity of motor slip-links is independent of system size, making only motor slip-links fast enough to account for the experimental data. Only at unphysiologically high motor velocities does polymer relaxation become rate-limiting for the speed of chromosome organization.*

12.1 SMC condensin requires motor activity to rapidly re-organize the chromosome

SMC induction experiments revealed that condensin can propagate from the loading site into the bulk of the DNA, thereby organizing an entire bacterial chromosome in a timespan of only $T_{\mathrm{WT}} \approx 24\,\mathrm{min}$ (appendix A and [45]). Based on these experiments, we estimate that condensins translocate away from their loading site with a velocity of $\approx 300\,\mathrm{nm/s}$. To understand the origin of these remarkably fast dynamics, we compute time-traces $X_p(t)$ of the width of the slip-link binding profile for our minimal models. From these traces, we extract a typical propagation time T for slip-links to establish a steady-state binding profile on a DNA polymer of physical length $L = aN_m$ (Figure 12.1, inset), where $a \approx 50\,\mathrm{nm}$ is the size of one monomer (Table A.1). Importantly, the propagation time T does not represent the time needed for a slip-link to move through the full system in the steady state—rather, it is the time needed for slip-links to collectively organize the chromosome, starting from a random configuration. This computational set-up mimics the situation in the SMC induction experiments from Wang et al. [45].

The propagation time of diffusive slip-links scales strongly with DNA length: $T \sim L^x$, with $x \approx 2.5$ (Figure 12.1, blue). This scaling differs from simple diffusive motion ($x = 2$, black in Figure 12.1), which we attribute to the loop-entropic forces that impede slip-link movement away from their loading site. Based on this observed scaling of T, we estimate that diffusive slip-links propagate several orders of magnitude slower over the DNA than observed in live cells (Figure 12.1, "WT"). In contrast, the propagation time of motor slip-links exhibits ballistic scaling, $T = L/v$ (Figure 12.1, red), where v is the effective translocation velocity.

Interestingly, our model prediction of motor slip-links, $T = L/v$, is remarkably close to the observed propagation time *in vivo* (Figure 12.1, "WT"). Indeed, recent single-molecule experiments have revealed that yeast condensin can extrude DNA loops with a velocity of up to 425 nm/s [16]. These data combined with our simulations, strongly indicate that rapid re-organization of the chromosome by SMC condensin requires fast and active loop extrusion.

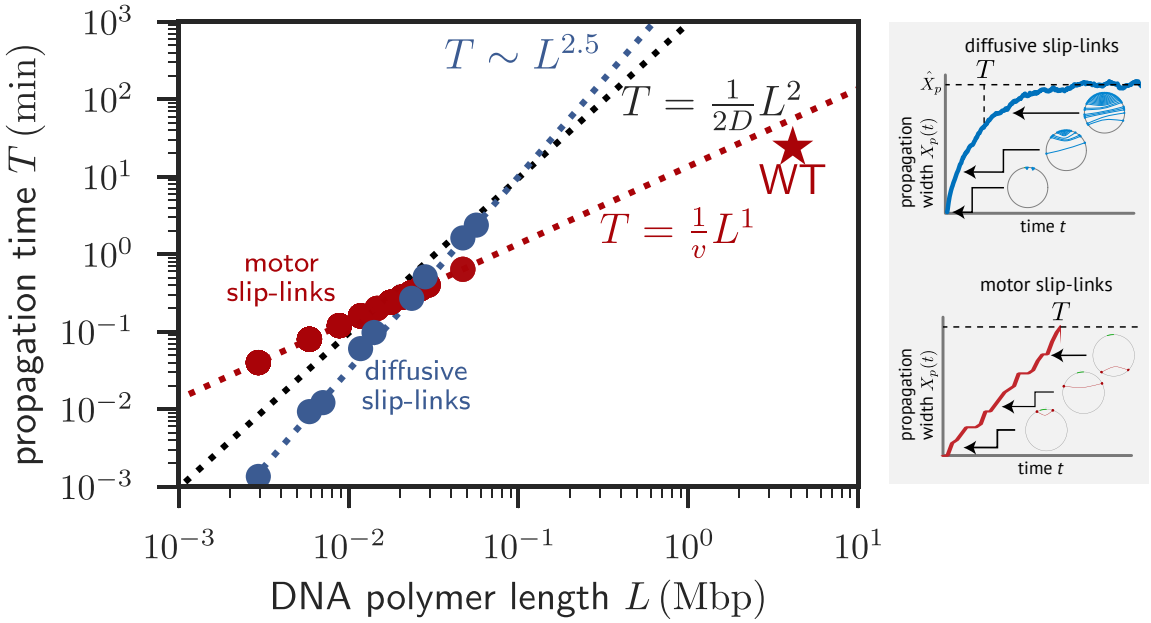

Figure 12.1: Propagation dynamics of slip-links and comparison with wild-type cells. For diffusive slip-links (blue), we quantify the propagation time-scale T by an exponential fit to the propagation length $X_p(t)$ (legend, top). For motor slip-links (red), we computed the average translocation velocity v and define $T = L/v$ (legend, bottom). Diffusive slip-links exhibit sub-diffusive scaling $T \sim L^{2.5}$ (blue, dashed); diffusive scaling $T \sim L^2$ is shown for comparison (black, dashed). The extrapolation of the simulated data for motor slip-links (red) is in accord with *in vivo* data ("WT"). Simulation units were converted to real units as described in appendix A.1.

12.2 DNA Relaxation Dynamics Can Limit Slip-Link Velocity

In figure 12.1, we link the speed of dynamic re-organization of large polymers (through T) by motor slip-links to the observed speed for small polymers (through v). Thus, we tacitly assumed that the speed of *collective* motion is independent of system size. For the system sizes in figure 12.1, this assumption holds for motor, but not diffusive slip-links. This begs the question, does the simple relation $T = L/v$ we found always hold—even for motor slip-links? In addition, can highly processive motors whose speed of movement exceeds local polymer dynamics, $k_{\text{motor}} \gg k_0$, also organize the polymer at speeds $v \sim k_{\text{motor}}$?

To address the aforementioned questions, we examine the relationship between the slip-link translocation attempt rate k_{motor}, the monomer diffusion attempt rate k_0, the polymer size N_m, and the effective motorized slip-link translocation velocity v. We distinguish two regimes: a *fast* relaxation regime $k_{\text{motor}} \ll k_0$ and a *slow* relaxation regime $k_{\text{motor}} \gg k_0$. In both regimes, for a stiff slip-link to make a step, the two polymer bonds in the direction of movement need to be parallel. If we denote the prior probability of observing these two polymer bonds to be parallel by $C \approx 3/16$ (Figure 11.3), then the effective rate of bond–bond alignment is $k_0^{\text{eff}} \approx Ck_0$. In our estimate for the rate k_0^{eff} we neglect the force that motor slip-links might exert on these bonds, because *in vitro* experiments indicate that the stalling force of yeast condensin is very small [16]. Hence, the characteristic rate $k^\star_{\text{motor}}$ that sets the transition from the fast relaxation to the slow relaxation regime occurs at $k^\star_{\text{motor}} = k_0^{\text{eff}}$. Consistent with the prediction that k_{motor} only depends on *local* kinetics, our data shows that k_{motor} is independent of the system size (Figure 12.2a).

In the fast relaxation regime, the rate-limiting factor is k_{motor}. In this case, the velocity v of slip-links is approximated by $v_{\text{fast}}(k_{\text{motor}}) \approx C\ell k_{\text{motor}}$. In the slow relaxation regime, $k_{\text{motor}} > k^\star_{\text{motor}}$, polymer relaxation becomes the rate-limiting factor, so that $v_{\text{max}} \approx v_{\text{fast}}(k^\star_{\text{motor}}) \approx C^2\ell k_0$. This argument suggests that the scaling form of dimensionless variables $\tilde{v} \equiv v/(\ell k_0)$, $\tilde{k} \equiv k_{\text{motor}}/k_0$ will collapse the data of k_{motor}, v, k_0 onto a universal curve $\tilde{v} = C\tilde{k}$ for $\tilde{k} < C$ and $\tilde{v} = C^2$ for $\tilde{k} \geq C$. Indeed, our numerical data is well-described by this scaling form (Figure 12.2b). By combining *in vitro* with *in vivo* empirical data, we estimate that SMC condensin in *B. subtilis* is well within the fast relaxation regime $k_{\text{motor}} < 10^{-5}k_0 \ll k_0$.

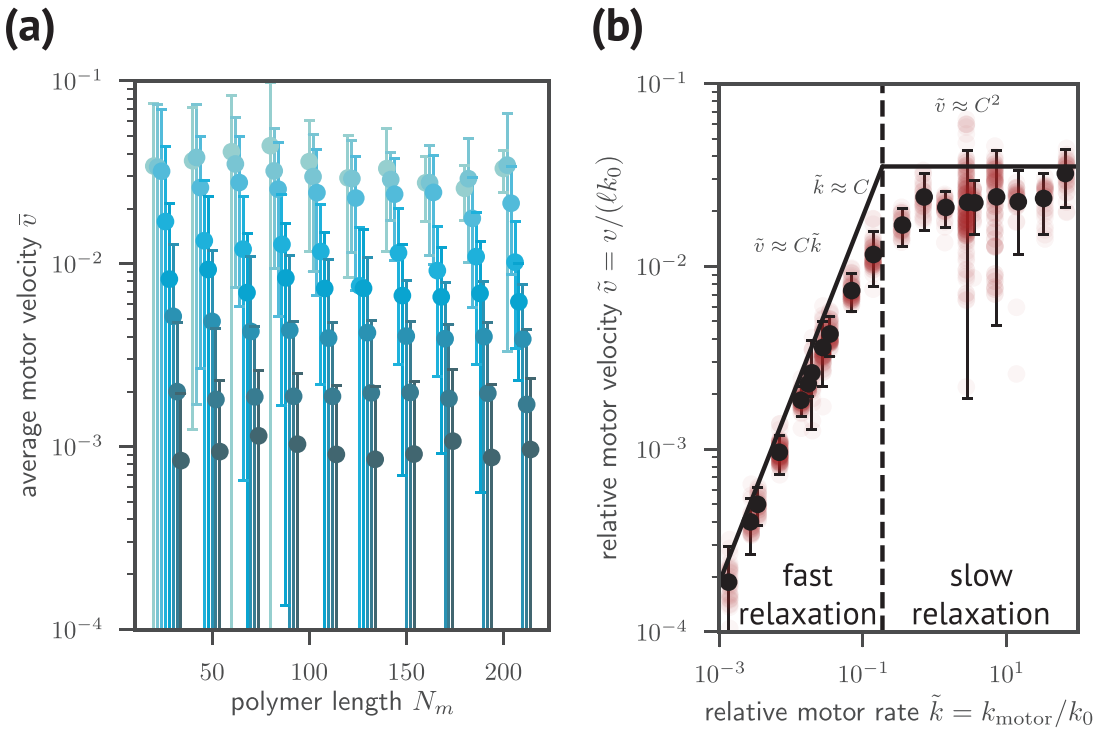

Figure 12.2: DNA relaxation dynamics limits the maximum velocity of motor slip-links. **(a):** The average motor velocity (error bars: standard deviation) for various translocation attempt rates (turquoise to dark blue, $k_{\mathrm{motor}} = 100 \ldots 0.01$) and various system sizes N_m. For clarity, we shifted the datapoints for decreasing k_{motor}; the value of N_m used is always the datapoint corresponding to $k_{\mathrm{motor}} = 100$ (turquoise). **(b):** Rescaled motor velocity as a function of relative motor rare for the data shown in panel a). Propagation of wild-type condensins is within the "fast relaxation" regime ($\tilde{k} = 6.8 \times 10^{-6}$) using data from appendix A.

12.3 Motor condensins without a loading site transiently juxtapose the polymer

Time-averaged contact maps of a polymer with motor slip-links but no loading site (ΔParBS) are, apart from the main diagonal, homogeneous (Figure 11.1e). Upon closer inspection, however, movies of the contact maps (SI movie 7a) suggest a diffusing cross-diagonal. Additionally, movies of the loop diagrams show that the motor slip-links extrude large loops until they collide and block further motion (SI movie 7b). To investigate this quantitatively, we perform Hough transforms of the contact maps. The Hough transform maps Cartesian space (x, y) into Hough-space (r, θ). Lines in Cartesian can be represented as $r = x \cos\theta + y \sin\theta$, and the Hough transformed image is simply the image of these (r, θ).

Before we examine the data for dynamic organization by motors, what do we expect for unorganized and juxtaposed polymers? The main diagonal in contact maps corresponds to an angle $\theta = 45°$ that starts at the origin, $r = 0$. Since the main diagonal is a feature of local persistence and will hence always be there, there should be always be a locus at $(r, \theta) = 0, 45°$ in Hough transforms of contact maps. Juxtaposed organization is characterized by lines in contact maps of an angle perpendicular to the main diagonal, i.e. $\theta = -45°$, and the position of the fold is captured by r. Thus, we can numerically establish both the presence and location of juxtaposed organization in our contact maps.

Intuitively, Hough transformed contact maps of this system with one motorized slip-link $\hat{N}_p = 1$ only contain a locus that corresponds to the main diagonal (Figure S12.3aa). Interestingly, however, when we have two motor slip-links $\hat{N}_p = 2$, there appears a very clear additional locus in the Hough transformed contact maps whose position diffuses randomly over time (Figure S12.3ab and SI movie 8).

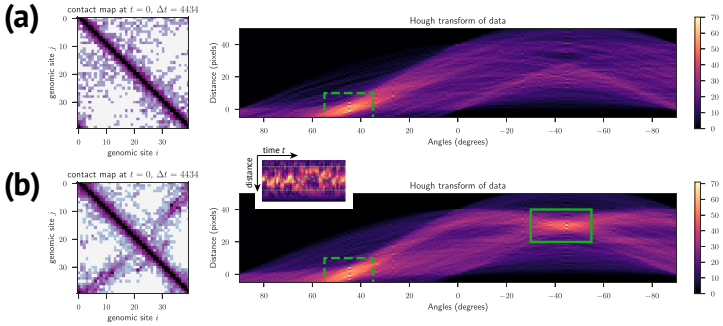

(a) **Left panels**: Representative contact map at a time t averaged over a time-interval Δt. **Right panels**: The Hough transform of the contact map. **(a):** Simulation was performed with $\hat{N}_p = 1$ with persistence time $\tau_{\text{switch}} = 10^{-3}$. **(b):** Simulation was performed with $\hat{N}_p = 2$ with persistence time $\tau_{\text{switch}} = 10^{-3}$. The Hough transforms in (b) displays an additional locus in the area $\theta = 40° \ldots 50°, r = 14 \ldots 42$ px. This locus diffuses randomly over time (inset).

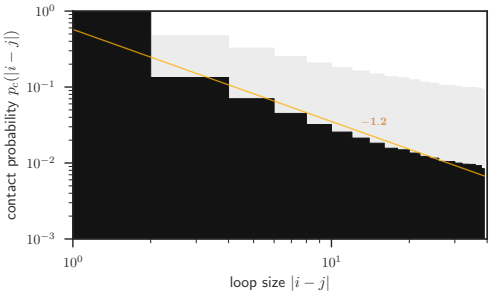

(b) Contact distribution $p(\Delta)$ for loop-size Δ of a polymer with $N_p = 10$ motor slip-links but lacking a loading site (ΔParB*S*).

Figure 12.3

The distribution of loop-sizes $p(\Delta)$ for the ΔParB*S* system with motor slip-links appears to be characterized by an approximate power-law behavior for intermediate loop-sizes (Figure S12.3b). With the same number of slip-links, the exponent of this powerlaw for the system with motor slip-links is smaller than that of the system with diffusive slip-links (compare Figs. S10.1 and S12.3b). This change in the exponent associated to the power-law behavior of $p(\Delta)$ indicates that the ΔParB*S* system with motor slip-links is characterized by a qualitatively different loop organization than that of a random polymer or that of a polymer organized by diffusive slip-links. This is reminiscent of the DNA loops observed in *E. coli*, an organism where the SMC complex MukBEF forms large loops without a specific loading complex [27].

Bibliography

[1] Elnaz Alipour and John F Marko. Self-organization of domain structures by DNA-loop-extruding enzymes. *Nucleic acids research*, 40(22):11202–12, dec 2012. ISSN 1362-4962.

[2] C A Brackley, J Johnson, D Michieletto, and D Marenduzzo. Effect of chromatin flexibility on diffusive loop extrusion via molecular slip-links. *bioRxiv*, page 275214, 2018.

[3] Chris A Brackley, James Johnson, Davide Michieletto, Alexander N Morozov, Mario Nicodemi, Peter R Cook, and Davide Marenduzzo. Non-equilibrium chromosome looping via molecular slip-links. *Physical Review Letters*, 119(13):138101, 2017.

[4] Hugo B Brandão, Payel Paul, Aafke A van den Berg, David Z Rudner, Xindan Wang, and Leonid A Mirny. RNA polymerases as moving barriers to condensin loop extrusion. *Proceedings of the National Academy of Sciences of the United States of America*, 116(41):20489–20499, oct 2019. ISSN 1091-6490.

[5] C. P. Broedersz, X. Wang, Y. Meir, J. J. Loparo, D. Z. Rudner, and N. S. Wingreen. Condensation and localization of the partitioning protein ParB on the bacterial chromosome. *Proceedings of the National Academy of Sciences*, 111(24):8809–8814, jun 2014. ISSN 0027-8424.

[6] Mathias Buenemann and Peter Lenz. A Geometrical Model for DNA Organization in Bacteria. *PLoS ONE*, 5(11), 2010.

[7] Frank Bürmann, Ho-Chul Shin, Jérôme Basquin, Young-Min Soh, Victor Giménez-Oya, Yeon-Gil Kim, Byung-Ha Oh, and Stephan Gruber. An asymmetric SMC-kleisin bridge in prokaryotic condensin. *Nature Structural & Molecular Biology*, 20(3):3–7, 2013.

[8] Frank Bürmann, Alrun Basfeld, Roberto Vazquez Nunez, Marie-Laure Diebold-Durand, Larissa Wilhelm, and Stephan Gruber. Tuned SMC Arms Drive Chromosomal Loading of Prokaryotic Condensin. *Molecular Cell*, 65(5):861–872.e9, mar 2017. ISSN 10972765.

[9] Pierre-Gilles de. Gennes. *Scaling concepts in polymer physics*. Cornell University Press, 1979. ISBN 080141203X.

[10] Bernard Derrida. Non-equilibrium steady states: fluctuations and large deviations of the density and of the current. *Journal of Statistical Mechanics: Theory and Experiment*, 2007(07):P07023–P07023, jul 2007. ISSN 1742-5468.

[11] Marie-Laure Diebold-Durand, Hansol Lee, Laura B. Ruiz Avila, Haemin Noh, Ho-Chul Shin, Haeri Im, Florian P. Bock, Frank Bürmann, Alexandre Durand, Alrun Basfeld, Sihyun Ham, Jérôme Basquin, Byung-Ha Oh, and Stephan Gruber. Structure of Full-Length SMC and Rearrangements Required for Chromosome Organization. *Molecular Cell*, 67(2):334–347.e5, jul 2017. ISSN 10972765.

[12] M. Doi and S. F. Edwards. *The Theory of Polymer Dynamics*. Clarendon Press, Oxford, 1986.

[13] Jorine M. Eeftens, Allard J. Katan, Marc Kschonsak, Markus Hassler, Liza de Wilde, Essam M. Dief, Christian H. Haering, and Cees Dekker. Condensin Smc2-Smc4 Dimers Are Flexible and Dynamic. *Cell Reports*, 14(8):1813–1818, 2016. ISSN 22111247.

[14] Jorine M Eeftens, Shveta Bisht, Jacob Kerssemakers, Christian H Haering, and Cees Dekker. Real-time detection of condensin-driven DNA compaction reveals a multistep binding mechanism. *bioRxiv*, 2017.

[15] Geoffrey Fudenberg, Maxim Imakaev, Carolyn Lu, Anton Goloborodko, Nezar Abdennur, and LeonidÂ A. Mirny. Formation of Chromosomal Domains by Loop Extrusion. *Cell Reports*, 15(9):2038–2049, 2016. ISSN 22111247.

[16] Mahipal Ganji, Indra A Shaltiel, Shveta Bisht, Eugene Kim, Ana Kalichava, Christian H Haering, and Cees Dekker. Real-time imaging of DNA loop extrusion by condensin. *Science*, 360(6384):102–105, feb 2018. ISSN 1095-9203.

[17] Federico Gnesotto, Federica Mura, Jannes Gladrow, and Chase Broedersz. Broken detailed balance and non-equilibrium dynamics in living systems: a review. *Reports on Progress in Physics*, 81(6):066601, mar 2018. ISSN 0034-4885.

[18] Stephan Gruber and Jeff Errington. Recruitment of condensin to replication origin regions by ParB/SpoOJ promotes chromosome segregation in B. subtilis. *Cell*, 137(4):685–96, may 2009. ISSN 1097-4172.

[19] Stephan Gruber, Jan-Willem Veening, Juri Bach, Martin Blettinger, Marc Bramkamp, and Jeff Errington. Interlinked Sister Chromosomes Arise in the Absence of Condensin during Fast Replication in B. subtilis. *Current Biology*, 24:293–298, 2014.

[20] Michiko Hirano and Tatsuya Hirano. Opening closed arms: long-distance activation of SMC ATPase by hinge-DNA interactions. *Molecular cell*, 21(2):175–86, jan 2006. ISSN 1097-2765.

[21] Katsuhiko Kamada, Masayuki Su'etsugu, Hiraku Takada, Makoto Miyata, and Tatsuya Hirano. Overall Shapes of the SMC-ScpAB Complex Are Determined by Balance between Constraint and Relaxation of Its Structural Parts. *Structure*, 2017. ISSN 18784186.

[22] Eugene Kim, Jacob Kerssemakers, Indra A. Shaltiel, Christian H. Haering, and Cees Dekker. DNA-loop extruding condensin complexes can traverse one another. *bioRxiv*, page 682864, jun 2019.

[23] HyeongJun Kim and Joseph J. Loparo. Multistep assembly of DNA condensation clusters by SMC. *Nature Communications*, 7:10200, jan 2016. ISSN 2041-1723.

[24] Tung B K Le, Maxim V Imakaev, Leonid A Mirny, and Michael T Laub. High-Resolution Mapping of the Spatial Organization of a Bacterial Chromosome. *Science*, 342(6159):731–734, nov 2013. ISSN 0036-8075.

[25] Virginia S Lioy, Axel Cournac, Olivier Espé, Fré Dé, Ric Boccard, Romain Koszul Correspondence, Martial Marbouty, Sté Phane Duigou, Julien Mozziconacci, and Romain Koszul. Multiscale Structuring of the E. coli Chromosome by Nucleoid-Associated and Condensin Proteins. *Cell*, 172: 771–783, 2018.

[26] Jonathan Livny, Yoshiharu Yamaichi, and Matthew K Waldor. Distribution of Centromere-Like parS Sites in Bacteria: Insights from Comparative Genomics . *Journal of Bacteriology*, 189(23):8693–8703, dec 2007.

[27] Jarno Mäkelä and David J. Sherratt. The SMC complex, MukBEF, organizes the Escherichia coli chromosome by forming an axial core. *bioRxiv*, page 696872, jul 2019.

[28] Martial Marbouty, Antoine Le Gall, Diego I Cattoni, Axel Cournac, Alan Koh, Jean-Bernard Fiche, Julien Mozziconacci, Heath Murray, Romain Koszul, and Marcelo Nollmann. Condensin- and Replication-Mediated Bacterial Chromosome Folding and Origin Condensation Revealed by Hi-C and Super-resolution Imaging. *Molecular Cell*, 59(4):588–602, aug 2015. ISSN 1097-4164.

[29] Mathias Buenemann and Peter Lenz. Geometrical ordering of DNA in bacteria. *Communicative & Integrative Biology*, 4(3), 2011.

[30] Ralf Metzler, Andreas Hanke, Paul G Dommersnes, Yacov Kantor, and Mehran Kardar. Tightness of slip-linked polymer chains. 2002.

[31] Ralf Metzler, Yacov Kantor, and Mehran Kardar. Force-Extension Relations for Polymers with Sliding Links. *Physical Review E*, 66(2):022102, 2002.

[32] Anita Minnen, Frank Bürmann, Larissa Wilhelm, Anna Anchimiuk, Marie-Laure Diebold-Durand, and Stephan Grüber. Control of Smc Coiled Coil Architecture by the ATPase Heads Facilitates Targeting to Chromosomal ParB/parS and Release onto Flanking DNA. *Cell Reports*, 14, 2016.

[33] Dane A Mohl and James W Gober. Cell Cycle-Dependent Polar Localization of Chromosome Partitioning Proteins in Caulobacter crescentus. *Cell*, 88(5):675–684, mar 1997. ISSN 0092-8674.

[34] Uri Moran, Rob Phillips, and Ron Milo. SnapShot: Key Numbers in Biology. *Cell*, 141:1262–1262, 2010.

[35] Adrian L Sanborn, Suhas S P Rao, Su-Chen Huang, Neva C Durand, Miriam H Huntley, Andrew I Jewett, Ivan D Bochkov, Dharmaraj Chinnappan, Ashok Cutkosky, Jian Li, Kristopher P Geeting, Andreas Gnirke, Alexandre Melnikov, Doug McKenna, Elena K Stamenova, Eric S Lander, and Erez Lieberman Aiden. Chromatin extrusion explains key features of loop and domain formation in wild-type and engineered genomes. *Proceedings of the National Academy of Sciences*, 112(47):E6456–E6465, nov 2015. ISSN 0027-8424.

[36] Young-Min Soh, Frank Bürmann, Ho-Chul Shin, Takashi Oda, Kyeong Sik Jin, Christopher P. Toseland, Cheolhee Kim, Hansol Lee, Soo Jin Kim, Min-Seok Kong, Marie-Laure Durand-Diebold, Yeon-Gil Kim, Ho Min Kim, Nam Ki Lee, Mamoru Sato, Byung-Ha Oh, and Stephan Gruber. Molecular Basis for SMC Rod Formation and Its Dissolution upon DNA Binding. *Molecular Cell*, 57(2):290–303, 2015. ISSN 10972765.

[37] Johannes Stigler, Gamze Ç Amdere, Douglas E Koshland, and Eric C Greene. Single-Molecule Imaging Reveals a Collapsed Conformational State for DNA-Bound Cohesin. *Cell Reports*, 15:988–998, 2016.

[38] Nora L Sullivan, Kathleen A Marquis, and David Z Rudner. Recruitment of SMC by ParB-parS Organizes the Origin Region and Promotes Efficient Chromosome Segregation. *Cell*, 137(137):697–707, 2009.

[39] Jennifer A Surtees and Barbara E Funnell. Plasmid and chromosome traffic control: how ParA and ParB drive partition. *Current topics in developmental biology*, 56:145–80, 2003. ISSN 0070-2153.

[40] Tsuyoshi Terekawa, Shveta Bisht, Jorine Eeftens, Cees Dekker, Christian Haering, and Eric Greene. The Condensin Complex Is A Mechanochemical Motor That Translocates Along DNA. *Science*, 358(6363):672–676, 2017.

[41] Ngat T Tran, Michael T Laub, and Tung B K Le. SMC progressively aligns chromosomal arms in Caulobacter crescentus but is antagonized by convergent transcription.

[42] Mark A. Umbarger, Esteban Toro, Matthew A. Wright, Gregory J. Porreca, Davide Baù, Sun-Hae Hong, Michael J. Fero, Lihua J. Zhu, Marc A. Marti-Renom, Harley H. McAdams, Lucy Shapiro, Job Dekker, and George M. Church. The Three-Dimensional Architecture of a Bacterial Genome and Its Alteration by Genetic Perturbation. *Molecular Cell*, 44(2):252–264, 2011. ISSN 10972765.

[43] Xindan Wang and David Z Rudner. Spatial organization of bacterial chromosomes. *Current Opinion in Microbiology*, 22:66–72, 2014.

[44] Xindan Wang, Tung B K Le, Bryan R. Lajoie, Job Dekker, Michael T. Laub, and David Z. Rudner. Condensin promotes the juxtaposition of dna flanking its loading site in Bacillus subtilis. *Genes and Development*, 29(15):1661–1675, 2015. ISSN 15495477.

[45] Xindan Wang, Hugo B. Brandão, Tung B. K. Le, Michael T. Laub, and David Z. Rudner. Bacillus subtilis SMC complexes juxtapose chromosome arms as they travel from origin to terminus. *Science*, 355(6324), 2017.

[46] Stephanie C Weber, Andrew J Spakowitz, and Julie A Theriot. Bacterial chromosomal loci move subdiffusively through a viscoelastic cytoplasm. *Physical review letters*, 104(23):238102, jun 2010. ISSN 1079-7114.

[47] Larissa Wilhelm, Frank Bürmann, Anita Minnen, Ho-Chul Shin, Christopher P Toseland, Byung-Ha Oh, Stephan Gruber, E. Alipour, JF. Marko, P. Arumugam, and S. Gruber. SMC condensin entraps chromosomal DNA by an ATP hydrolysis dependent loading mechanism in Bacillus subtilis. *eLife*, 4:11202–11212, may 2015. ISSN 2050-084X.

Part IV

Force-Extension Behavior of the ParB-DNA System

13

Polymer Looping affects the Force-Extension Relation of the DNA-ParB System

Chapter summary: *Large loops emanate from ParB condensates on DNA, which we hypothesize affects the force-extension relation of the full system in a non-trivial way. The results in this chapter have not been peer reviewed.*

ParB nucleoid-associated proteins can bind to DNA in both a specific and non-specific fashion [6, 14]. In live cells, ParBs robustly aggregate into a single large ParB-DNA condensate composed of $\sim 10^3$ ParBs [7]. On a molecular level, ParB proteins can make *spreading bonds* to other ParBs that are adjacent along the DNA in addition to *bridging bonds* to other ParBs on different parts of the DNA molecule (Figure 13.1a) [2–5, 13]. Computer simulations indicate that it is probably only through a combination of both spreading and bridging bonds that such a condensate can be generated under physiological constraints [1]. However, this ParB-DNA condensate does not live in isolation inside the cell: other actors live inside the cell that push and pull on DNA. A notable example of this concerns ParA enzymes that are believed to pull on the ParB cluster during replication and segregation [8, 12, 15, 16]. Here, however, we restrict ourselves to forces that are exerted directly on the DNA endpoints (Figure 13.1b). Thus, we seek out to understand the force-extension behavior of a DNA molecule with a large ParB cluster bound to it (Figure 13.1b).

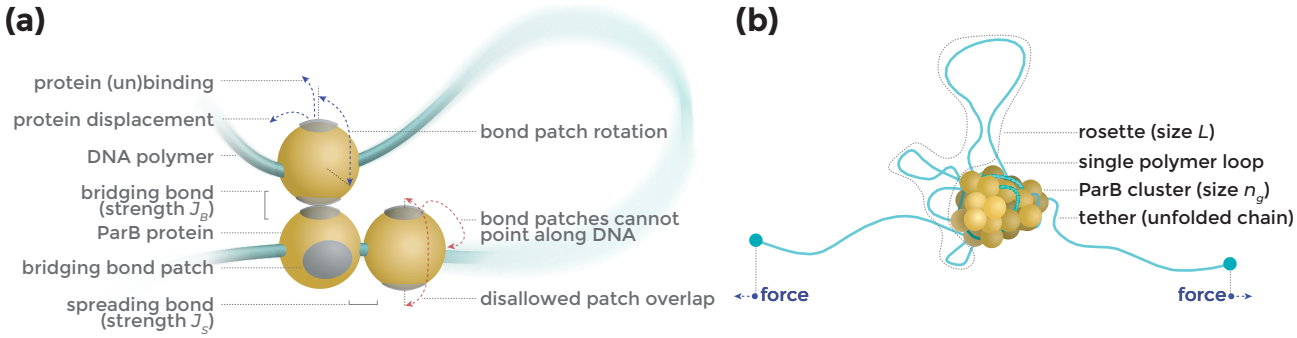

Figure 13.1: **Outline of model for ParB condensate formation on DNA. (a)** Schematic of minimal model for DNA polymer (turquoise) with ParB proteins (yellow) that interact with each other via spreading (along chain) and bridging (orthogonal to chain) interactions. Indicated are example directions for the bridging bonds (gray patches) for a bridging valency $q_B = 2$ per particle. Bridging bonds randomly rotate (blue arrow, right), but more than one bridging bond in a given direction is disallowed (red arrow, right). Bridging bonds are not allowed to overlap with spreading bonds. **(b)** An external force f is exerted on the ParB-DNA system (projected length z). The collection of all loops that emanate from the cluster is called the 'rosette'.

To investigate the elastic properties of DNA molecules that have a large ParB condensate bound to it, we use a lattice

simulation of a polymer with patchy particles (Figure 13.1a). Two neighboring proteins form a bond if two bond patches touch, and do not bond otherwise—i.e. if the bond patches do not point in opposite directions (Figure 13.1a). The bond patches consist of spreading bonds (strength J_S) that can only be formed with other proteins adjacent along the DNA ($|i-j|=1$), and bridging bonds (strength J_B), which can only bond to particles that are neighboring in space but not neighboring along the DNA ($|\mathbf{r}_i-\mathbf{r}_j|=1, |i-j|\neq 1$). The total number of bridging patches q_B and spreading patches q_S is fixed; in what follows we use $q_S=2, q_B=4$, such that the total number of patches equals the coordination number ($q_S+q_B=z_c$). We first tested that our simulations can accurately capture the equilibrium statistics for these very dense phases (appendix D). We quantify the elastic properties of the system by submitting the projected end-to-end distance z to a force f (Figure 13.1b), and measuring the spring constant k at small extensions $k=\partial_z f|_{f\to 0}$. This computational set-up mimics the *in vitro* force-extension experiments from Fisher et al. [3].

What do we expect for a system composed of naked polymer tethers, and a dense globular state? Homopolymers with attractive interactions in a fixed length ensemble can display a 'tadpole' geometry: tethers (unfolded chains of combined size $n-n_g$, extension $z_{\text{tether}}(n-n_g)$) that emerge from and coexist with a single condensed 'head' in a globular state (size n_g, extension $z_{\text{glob.}}(n_g)$) [10, 11]. Because the head and tethers are in distinct phases in this phase coexistence, the full extension then obeys a superposition principle $z_{\text{full}}(n,n_g)\approx z_{\text{glob.}}(n_g)+z_{\text{tether}}(n-n_g)$.[1] Surprisingly, however, our ParB-DNA system does not obey such a superposition principle (Figure 13.2a). To the contrary, the full system has a *smaller* extension than the tethers alone ($|z_{\text{full}}(n,n_g)|<|z_{\text{tether}}(n-n_g)|$), despite the full system being larger in length ($n>n-n_g$)! This surprising fact is because the ParB cluster suctions in DNA from the tethers, producing slack loops that emanate from the ParB cluster (Figure 13.1b). Because of this interaction between the cluster and tether, the ParB-DNA system cannot be straightforwardly mapped to a homopolymer description, and the force-extension behavior will likely be affected by the looping statistics in the rosette.

We start by quantifying the number of loops $N(\ell)$ of size ℓ that emanate from the ParB cluster. Loops are defined as naked stretches of DNA that start *and* end on the cluster (i.e. the tethers are not loops, as they only either start *or* end on the cluster), with the size $\ell=|i-j|-2$, where i,j are the first, last monomer in the loop; the term -2 is to discount the loop monomers which are occupied by proteins. Although the loop-sizes ℓ and -frequencies $N(\ell)$ are random variables, we assume that their ensemble averages are well-defined and tacitly characterize the looping statistics by their mean-field values, $\ell=\langle\ell\rangle, N(\ell)=\langle N(\ell)\rangle$.[2] The very stiff globule barely expands for small forces, so that a single loop emanating from the cluster does not feel the force f directly. Hence, although the total amount of DNA in the rosette L is a function of f, each single loop is mostly slack. Thus, we expect a loop-size distribution that maximizes the total looping entropy, conditioned on a total length $L(f)$. In section 4 we presented a heuristic argument for the distribution that follows from this constraint for a single polymer, namely $N_{\text{th.}}(\ell)=N_0(\ell/\ell_0)^{-\nu d}$ (d : dimension, ν : Flory exponent), where the prefactor N_0 sets the total number of loops at a length-scale cut-off which we can conveniently set to $\ell_0=1$ for our lattice simulation. For all values of f considered, we indeed find a distribution of this form $N_{\text{th.}}(\ell)$ up to an upper length-scale $\ell_{\max}$ after which the decay of $N(\ell)$ is faster than a power-law (Figure 13.2b). For a given total amount of DNA L in the rosette, the largest possible loop-size is L. This results in the falsifiable prediction $\ell_{\max}=L$. First by expressing $N_{\text{th.}}(\ell)$ in terms of L using the constraint $\int \mathrm{d}\ell\,\ell N_{\text{th.}}(\ell)\equiv L$, we can test this prediction by collapsing all $N(\ell)$ onto a universal form, independent of L (Figure 13.2b, inset). The good agreement between the measured data $N(\ell)$ and the loop distribution of a single polymer $N_{\text{th.}}(\ell)$ shows that the rosette can be regarded as a single polymer of size $L(f)$ whose looping statistics do not experience the external force.

[1] This superposition principle expresses negligible interactions between the two phases. In general, for a phase coexistence and phases A,B, the free energy can be written $F_{\text{full}}=F_A+F_B+F_{AB}$, where F_{AB} is a mixture term that increases sub-extensively, and can therefore be neglected in the thermodynamic limit. In our case, the interactions at the phase boundary consist of excluded volume interactions between the globule and the tethers. Since the excluded volume of the globule scales slower ($\sim n_g^{1/d}$) than that of the tethers ($\sim (n-n_g)^{\nu d}$), the globule only takes up a vanishing fraction of the accessible volume for the tethers as $n\to\infty$. Thus, neglecting the globule-tether excluded volume interactions is an appropriate approximation in the thermodynamic limit.

[2] Since an upper bound for ℓ is n, the first moment of ℓ is necessarily well-defined for any system size. Similarly, an upper bound on N is the number of loops that can possibly be formed, equal to the surface area of the globule. This too, is bounded by the system size.

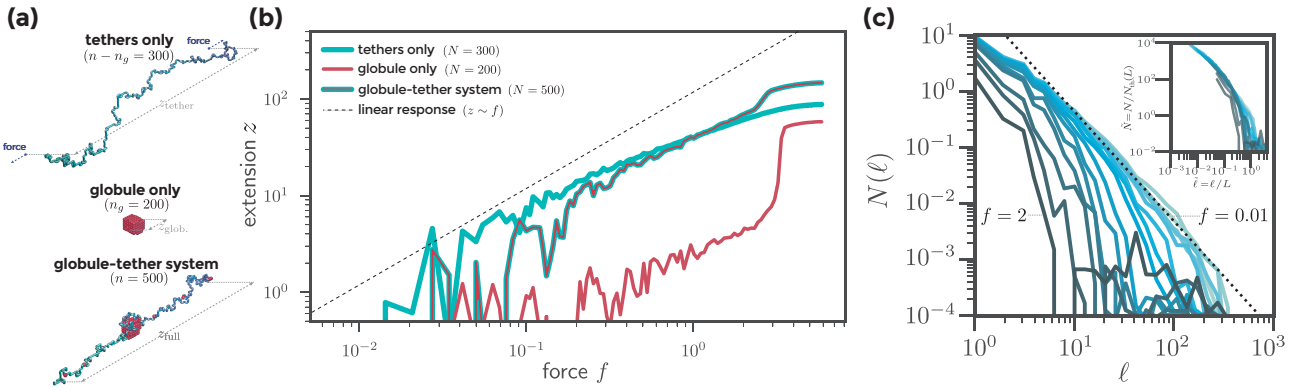

Figure 13.2: **The ParB condensate absorbs DNA** . **(a)** Set-up of experiment to test the superposition principle $z_{\text{full}} = z_{\text{glob.}} + z_{\text{tether}}$, based on the extension of a naked polymer (size $n - n_g$), a condensed 'protein droplet' (size n_g) and a system with both a globular and unfolded part (size n). **(b)** The extensions of the three systems is shown for various external forces. **(c)** Internal looping statistics of the full system for various forces $f = 0.01 \ldots 2$ (light to dark). Inset: collapse onto universal curve. The total amount of DNA in the rosette $L = \int \mathrm{d}\ell\, \ell N(\ell)$ was numerically integrated from $N(\ell)$ to rescale ℓ to $\tilde{\ell} = \ell/L$ and to find the closed form of $N_{\text{th.}}(\ell) = N_0 \ell^{-\nu d}$. The vertical axis $\tilde{N}(\tilde{\ell})$ was rescaled such that all curves at $\tilde{\ell} = 1$ lie at $\tilde{N} = 1$.

Although the loops in the rosette can freely exchange DNA in order to maximize their looping entropy, the *number* of loops is not only subject to entropic constraints. Rather, spreading interactions between adjacent ParB proteins (Figure 13.1a) can control the total number of loops N_0, largely independent of how much entropy is contained in those loops [1]. Thus, we can expect a dependency of the spring constant k on J_S. In agreement with this, the spring constant for a system with zero loops ($J_S \to -\infty$) scales as $k_0 \sim 1/N$, whereas the spring constant for a polymer with a single loop of size $\langle \ell \rangle_f$ is $k_1 \sim 1/(N - \langle \ell \rangle_f)$ [9]. Despite the loop itself in this example being slack, it makes the full system *stiffer*, $k_1 > k_0$. Although we do not have a quantitative theory for a rosette with an arbitrary number of loops, the ordering $k_1 > k_0$ does suggest that favored looping (higher J_S) results in a larger spring constant. In agreement with this, $k(J_S)$ increases with increasing J_S (Figure 13.3a). We hypothesize that the spring constant of the ParB-DNA system depends on J_S because spreading interactions control N_0, thereby affecting the amount of DNA in the rosette. However, we see a surprising additional dependency on J_B, with k increasing with decreasing J_B (Figure 13.3), albeit with a poor data quality. We stress that this dependency on J_B appears to be opposite to that of J_S.

The dependency of k on J_B is probably not due to an increased stiffness of the globule.[3] It is also not obvious how the dependency of k on J_B could be due to changes in the internal geometry of the globule: for a given number of looping sites, DNA can reptate from the tethers into the rosette without breaking any bridging bonds. Additionally, since a piece of DNA on the surface of the globule that does not yet form a loop must have $|i - j| = 1$, we do not see how the number of looping sites could be affected by the internal geometry of the globule.

Instead, we hypothesize that k depends on J_B because the nucleation of a loop does not only break a spreading bond; it also allows for the possibility of the formation of an additional bridging bond (Figure 13.3b). The net energy upon creating a looping site is thus $\Delta E = -2J_S + 2J_B$ (the factor 2 stems from *both* proteins changing their number of bonds), which has an opposite dependency on J_S compared to J_B. Based on this, we predict that the spring constant is not a function of J_S alone, but rather a function of $\Delta E \sim J_S - J_B$ (Figure 13.3b). Indeed, when plotting k as a function of ΔE, the data for different J_B do show substantially more overlap (Figure 13.3a, inset). These data suggest that a large contribution to k is the net energy of loop nucleation, with more looping (ΔE negative and $|\Delta E|$ increasing) increasing the stiffness of the full system.

[3] The formula that relates stress and strain shows $z_{\text{glob.}} = fR/(AE) \sim 1/R$, where $R \sim M^{1/d}$ is the radius, E is the globule's elastic modulus and $A \sim R^2$ is the globule's cross-section. Thus, although the spring constant of the globule itself does depend on J_B through E, the stiffness of the globule increases as $\sim M_g^{1/d}$ [10]. In contrast, the spring constant of the tethers *decreases* as $1/(N - M_g)$. Hence, in the thermodynamic limit, the globular part of the system becomes arbitrarily stiff compared to the tethers. Thus, we can neglect the globular contribution to the spring constant for large enough system sizes.

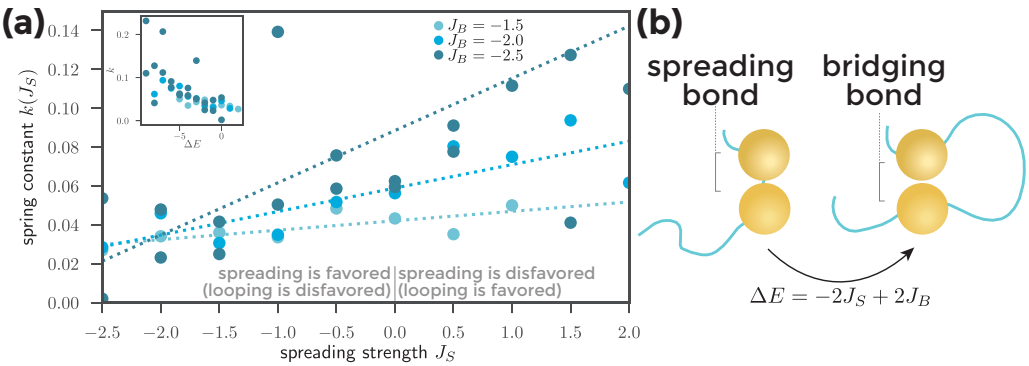

Figure 13.3: **Both spreading and bridging interactions affect the stiffness of the ParB-DNA system. (a)** We measured the spring constant $k = \partial_z f|_{f\to 0}$ from the initial slope of a force ramp for various values J_S, J_B. Dashed lines correspond to a linear regression on the datapoints with the same color. Inset: Spring constant expressed as a function of the net energy change upon loop creation $\Delta E = -2J_S + 2J_B$. Polymer length $N = 120$, number of proteins $M = 60$, maximum number of bridging bonds $q_B = 4$. **(b)** Creating a loop site breaks a spreading bond (left), but allows for the formation of an additional bridging bond (right). Thus, the net energy of loop creation is ΔE as indicated, neglecting any possible entropy changes.

Bibliography

[1] C. P. Broedersz, X. Wang, Y. Meir, J. J. Loparo, D. Z. Rudner, and N. S. Wingreen. Condensation and localization of the partitioning protein ParB on the bacterial chromosome. *Proceedings of the National Academy of Sciences*, 111(24):8809–8814, jun 2014. ISSN 0027-8424.

[2] Bo-Wei Chen, Ming-Hsing Lin, Chen-Hsi Chu, Chia-En Hsu, and Yuh-Ju Sun. Insights into ParB spreading from the complex structure of Spo0J and parS Data deposition: The atomic coordinates and structure factors have been deposited in the Protein Data Bank, www.pdb.org (PDB ID code 4UMK). *PNAS*, 112(21):6613–6618, 2015.

[3] Gemma L M Fisher, César L Pastrana, Victoria A Higman, Alan Koh, James A Taylor, Annika Butterer, Timothy D Craggs, Frank Sobott, Heath Murray, Matthew P Crump, Fernando Moreno-Herrero, and Mark S Dillingham. The C-terminal domain of ParB is critical for dynamic DNA binding and bridging interactions which condense the bacterial centromere. .

[4] Gemma LM Fisher, Cé L sar Pastrana, Victoria A Higman, Alan Koh, James A Taylor, Annika Butterer, Timothy Craggs, Frank Sobott, Heath Murray, Matthew P Crump, Fernando Moreno-Herrero, and Mark S Dillingham. The structural basis for dynamic DNA binding and bridging interactions which condense the bacterial centromere. .

[5] Thomas G W Graham, Xindan Wang, Dan Song, Candice M Etson, Antoine M van Oijen, David Z Rudner, and Joseph J Loparo. ParB spreading requires DNA bridging. *Genes & Development*, 28(11):1228–38, jun 2014. ISSN 1549-5477.

[6] Stephan Gruber and Jeff Errington. Recruitment of condensin to replication origin regions by ParB/SpoOJ promotes chromosome segregation in B. subtilis. *Cell*, 137(4):685–96, may 2009. ISSN 1097-4172.

[7] Baptiste Guilhas, Jean-Charles Walter, Jerome Rech, Gabriel David, Niels Walliser, John Palmeri, Carine Mathieu-Demaziere, Andrea Parmeggiani, Jean-Yves Bouet, Antoine Le Gall, and Marcelo Nollmann. ATP-Driven Separation of Liquid Phase Condensates in Bacteria. *SSRN Electronic Journal*, oct 2019. ISSN 1556-5068.

[8] Hoong Chuin Lim, Ivan Vladimirovich Surovtsev, Bruno Gabriel Beltran, Fang Huang, Jörg Bewersdorf, and Christine Jacobs-Wagner. Evidence for a DNA-relay mechanism in ParABS-mediated chromosome segregation. *eLife*, 3:e02758, jan 2014. ISSN 2050-084X.

[9] Ralf Metzler, Yacov Kantor, and Mehran Kardar. Force-Extension Relations for Polymers with Sliding Links. *Physical Review E*, 66(2):022102, 2002.

[10] Alexey A Polotsky, Mohamed Daoud, Oleg Borisov, and Tatiana M Birshtein. A Quantitative Theory of Mechanical Unfolding of a Homopolymer Globule. Technical report.

[11] Alexey A Polotsky, Elizaveta E Smolyakova, and Tatiana M Birshtein. Theory of mechanical unfolding of homopolymer globule: all-or-none transition in force-clamp mode vs phase coexistence in position-clamp mode. Technical report, 2012.

[12] Conrad W Shebelut, Jonathan M Guberman, Sven van Teeffelen, Anastasiya A Yakhnina, and Zemer Gitai. Caulobacter chromosome segregation is an ordered multistep process. *Proceedings of the National Academy of Sciences of the United States of America*, 107(32):14194–8, aug 2010. ISSN 1091-6490.

[13] Dan Song, Kristen Rodrigues, Thomas GW Graham, Joseph J Loparo, and Harvard A John. A network of cis and trans interactions is required for ParB spreading. *Nucleic Acids Research*, 45(12):7106–7117, 2017.

[14] James A. Taylor, Cesar L. Pastrana, Annika Butterer, Christian Pernstich, Emma J. Gwynn, Frank Sobott, Fernando Moreno-Herrero, and Mark S. Dillingham. Specific and non-specific interactions of ParB with DNA: implications for chromosome segregation. *Nucleic Acids Research*, 43(2): 719–731, jan 2015. ISSN 1362-4962.

[15] Esteban Toro, Sun-Hae Hong, Harley H McAdams, and Lucy Shapiro. Caulobacter requires a dedicated mechanism to initiate chromosome segregation. *Proceedings of the National Academy of Sciences of the United States of America*, 105(40):15435–40, oct 2008. ISSN 1091-6490.

[16] Xindan Wang, Paula Montero Llopis, and David Z Rudner. Organization and segregation of bacterial chromosomes. *Nature Reviews Genetics*, 14: 191–203, 2013.

Part V

Conclusion and Outlook

14

Conclusion

In this thesis, we compared several minimal models for how bacterial condensin could organize the whole chromosome using a tailored Lattice Kinetic Monte-Carlo framework. We describe the benefits and limitations of this simulation methodology in detail. Based on our results, we argue that motor activity on the level of single condensins is able to organize an entire bacterial chromosome.

To address this puzzle, we develop a *lattice kinetic Monte-Carlo* (LKMC) method in part II to simulate spatially heterogeneous non-equilibrium processes on a lattice. In particular, we frequently make use of a DNA–slip-link system as a toy model to illustrate and test features of our LKMC framework. For our DNA–slip-link toy model, the microscopic processes consist of both polymer moves which affect the local configuration of DNA, as well as NAP (un)binding and displacement moves. We use the theory of stochastic processes to compute the proper attempt rates of displacement moves that affect multiple degrees of freedom simultaneously. We show that, at least for intermediate system sizes, locality of the kinetics can be leveraged to greatly enhance the computational efficiency of LKMC. For larger system sizes, other effects (such as hash-table lookups and/or performing the tower sampling) can become the limiting factor.

We address in detail two major challenges in designing LKMC for simulating far-from-equilibrium dynamics. The first of these is the sampling of all possible states. It is known that the Verdier-Stockmayer move-set does not sample all states for self-avoiding walks. Fortunately, the equilibrium dynamics appears to display the same dynamics for both strict and partial self-avoidance, suggesting that the lack of ergodicity is not an issue for close-to-equilibrium systems. Far from equilibrium, however, we do see the appearance of—to the best of our knowledge, previously unreported—unphysical states, jammed states. We propose that these states are jammed because loop-extrusion factors can irreversibly tighten loops into a state, where none of the Verdier-Stockmayer lattice moves can be performed. We propose possible solutions to this problem, include allowing partial polymer overlap, including a small extrusion reversal direction and a small extruder unbinding rate. We believe that awareness of this issue is important when using LKMC to simulate organization of DNA by molecular motors, since we frequently (with a $\approx 60\%$ probability) observed jammed states for highly persistent motors.

The second major challenge of LKMC that we address is simulating far-from-equilibrium dynamics. We show that Metropolis-Hastings kinetics, which assumes that the dynamics of microscopic processes only depends on energy differences of those microscopic changes, can not be taken arbitrarily far from equilibrium. The maximum velocity of particle movement is rate-limited by the attempt rate of a microscopic process, and leads to a breakdown of the fluctuation-dissipation theorem that holds close to equilibrium. We also show that Metropolis-Hastings kinetics disobeys the generally applicable steady-state fluctuation theorem at large external forces. In particular, the maximum velocity of particle movement in Metropolis-Hastings leads to an underestimation of the entropy production at large external forces. We show that both the maximum velocity and entropy production display the expected behavior if the attempt rate of microscopic processes is renormalized to include the external force.

In part III, we use our LKMC framework to elucidate chromosome organization by *structural maintenance of chromosomes* (SMC) proteins, which are responsible for the arm–arm alignment and anomalously large looping probability in many bacteria. We show that the asymmetric confinement does lead to a slight arm–arm alignment if the chromosome is tethered at one of the cell poles, but that this alignment is not nearly enough to account fo the experimental data. Adding model SMCs in the form of slip-links does not produce more observed organization; the looping probability remains similar

to that of an equilibrium polymer.

Surprisingly, merely adding active loading to otherwise diffusive slip-links does produce robust arm–arm alignment and the formation of large, nested DNA loops. Diffusive slip-links juxtapose the chromosomal arms through collective motion driven by the active loading, in combination with steric repulsion between the individual slip-links. Because this mechanism depends on mutual steric repulsion, its efficacy depends on slip-link density. Indeed, we find that the propagation length of slip-links into the chromosome is only similar to that of live cells for slip-links densities of $\gtrsim$ 10%—orders of magnitude higher than the densities of SMC reported *in vivo*. Besides needing a very high density, dynamic re-organization by diffusive slip-links is slow, needing orders of magnitude more time to organize the full chromosome than live cells. In sum, we find that diffusive slip-links with active loading can organize the chromosome in principle, but that both its efficiency and speed are too low to account for the experimental data.

Adding motor activity to slip-link motion in the form of persistent random motion makes the slip-links much more effective at organizing the chromosome. Their function does not depend on collective motion, but rather on the persistence of single extruders—explaining why only a small number of SMCs can organize an entire chromosome. We show that the speed of dynamic re-organization by motor slip-links is independent of system size for low slip-link density and physiologically relevant motor speeds. This is not true for all motor speeds, since local polymer dynamics can be the rate-limiting factor at high motor speeds, but only at motor speeds orders of magnitude faster than physiologically relevant. Because motor speed appears independent of system size, our measurement of dynamic re-organization of a full chromosome agrees well with the time observed *in vivo*. In sum, although motor activity has been experimentally demonstrated in yeast SMC but not bacterial SMC, our data points to the presence of motor activity in bacterial SMC.

Finally, we study the force-extension behavior of ParB condensates on DNA. A naive *Ansatz* for such a system is a stiff globule in series with two naked tethers. *In vitro* data of the force-extension curve of the ParB–DNA system display striking differences with such a model, suggesting that the combined system is more complex. Indeed, we show that large polymer loops emanate from ParB condensates on DNA, making the combined system qualitatively different to a globule in series with two tethers. We hypothesize that loop the spring constant is related to the energetic penalty associated with loop creation and annihiliation. In agreement with this, the spring constant appears to be only a function of the net energy of creating a loop. Although these data are far from conclusive, they do show that the force-extension behavior of ParB–DNA system might be far more interesting than a simple homopolymer.

This work takes a step towards understanding the physical principles of chromosome organization by diffusively sliding or loop-extruding complexes. This field has received a surge interest in recent years: both much experimental data has been gathered on these systems *in vitro* [60, 61, 64, 71, 72, 82] and *in vivo* [53, 55, 58, 68, 69, 75, 79, 86–89, 91, 92]; and theoretical modeling has been published on both diffusive slip-links [50–52] and loop-extrusion factors [47, 63, 65, 66]. Our core contribution to this field is a quantitative comparison of the collective effect of condensins with and without motor activity on chromosome organization.

15

Outlook

15.1 Rouse Dynamics of Circular Polymer Chains

In the literature of Rouse dynamics of circular polymers, the normal modes have been assumed to be Fourier modes (see appendix B and [84, 90]). However, we find that these modes are not *perfectly* normal; there appears to be a small mode–mode coupling in the random forces in mode space (appendix B). The amplitude of this off-diagonal coupling scales as 1/(system size) compared to the on-diagonal coupling (equation B.10), and hence may be irrelevant for large system sizes. The mode–mode coupling in our discussion of circular polymers ultimately stems from our definition of the noise autocorrelator $\langle \mathbf{f}(n,t)\mathbf{f}(m,t')\rangle$ (equations (B.7) and (B.8)), which assumes that—since they lie at the same position in space—both polymer end-points $n = 0, N$ receive the same random force kicks from the heat bath. These noise correlations are, however, not present in the work by Watanabe et al. [90] or Tsolou et al. [84]. Since our definition is different to the one used in the literature, it is currently unclear whether the noise end-point correlations *should* be included and, if so, what the consequences of the mode–mode coupling might be.

Another interesting property of the Rouse dynamics of circular chains is the response function of the end-to-end distance $\mathbf{R}_\Delta(t)$ of sub-chains (size $\Delta \leq N/2$). We observe a *plateau* in the response function, perhaps due to the relaxation of the chain complement with size $N - \Delta \geq \Delta$ (Figure C.1). If true, this offers the possibility to measure a *global* geometrical property (namely polymer size N) by looking at a *non-global* dynamical property. The other way round, for known polymer sizes N, the size of the plateau in Figure C.1 could be used to infer the size of the sub-chain Δ.

15.2 Impact of Looping on Force-Extension Behavior of ParB-DNA System

We have shown that large DNA loops emanate out of ParB clusters on DNA (chapter 13). We argued that the difficulty of loop creation and annihilation affects the force-extension behavior of this system, even at small external forces. Our data seems to indicate that the probability of loop creation and annihiliation is controlled by the strength of spreading and bridging interactions J_S, J_B (Figure 13.3). Importantly, these spreading and bridging interactions are measurable quantities generated by the specific molecular structure of ParB [56, 80], and can be manipulated by point mutations of these proteins [54, 56, 67, 70]. In figure 13.3, we hypothesize that the spring constant k for ParBs with a valency $q = 6$ only depends on these interaction strengths as a function of a single parameter $\Delta E \sim J_S - J_B$. The hypothesis that $k = k(J_S - J_B)$ stemmed from the fact that creating an additional loop can create a bridging bond at the expense of a spreading bond. For ParB proteins with a lower valency $q < 6$, this is no longer always the case, since a particle on the outside of the cluster can have all bridging bonds satisfied. However, a spreading bond can still be broken, so we expect $k \approx k(J_S)$.[1] This hypothesis can be tested by measuring k for different valency proteins.

[1] The dependence on J_S is likely imperfect, because some particles will still have not all bridging bonds satisfied, as in the $q = 6$ case. Additionally, a protein may be positioned on the loop with a single spreading bond but no bridging bonds. Such spreading-only proteins are pruned away in our graph-theoretical loop measurement process since spreading bonds do not constrain the localization of DNA.

Additionally, we did not directly test whether the *amount* of DNA in the rosette L_R affects the spring constant. Since the entropy reduction of a loop scales sub-extensively (as $\Delta S(\Delta) \sim \log \Delta$), large loops are 'entropically soft': it is much more entropically favored to remove the same amount of DNA from a small loop than from a large one. Everything else being equal, this should make it *easier* to pull DNA from the small loops than large loops. However, since the different loops in the rosette can exchange DNA—and they do, see Figure 13.2—it is not obvious how to control the size of a single loop for a fixed system size. But, since the system size does increase L_R, perhaps the relation between L_R and the force-extension behavior can be tested by varying the total polymer length. Alternatively, L_R could be controlled by adding two ParB binding sites on the DNA with a binding energy ϵ. For sites that favor ParB binding ($\epsilon < 0$), the ParB cluster will try to suction the DNA up to these two sites into it, thereby increasing L_R (Figure 15.1). For sites with $\epsilon > 0$, the cluster will try to expel the DNA up to those two sites, decreasing L_R. ParB binding sites such as these, in fact, exist in real bacteria in the form of *parS* sites [85]. Thus, pulling experiments of a ParB–DNA system with binding sites not only allows testing the impact of rosette size on the force-extension behavior—they could also offer insight into whether *parS* sites affect the elastic properties of the ParB–DNA system.

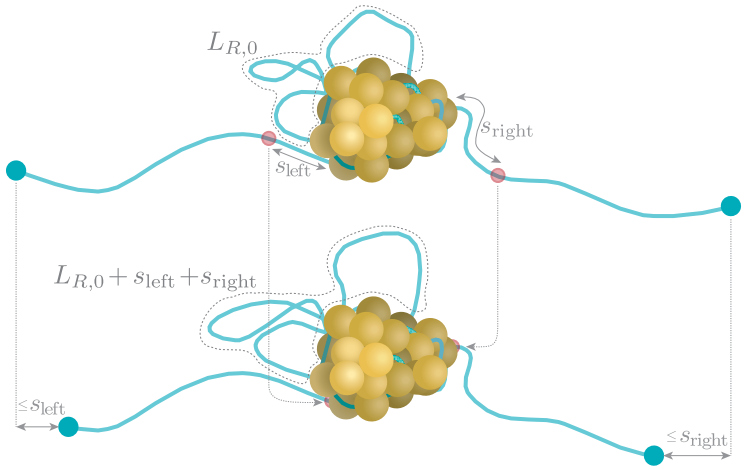

Figure 15.1: **ParB binding sites could possibly be used to regulate the amount of DNA in the rosette.** Top: Two hypothetical attractive ParB sites are positioned on the tethers, distances $s_{\text{left}}, s_{\text{right}}$ outside of the clustered region. $s_{\text{left}}, s_{\text{right}}$ are random variables that depend on the binding strength, cluster size, etc. Bottom: Occupying these sites will suction in DNA from the tethers into the rosette, increasing the size of the rosette by an amount $\approx s_{\text{left}} + s_{\text{right}}$ (this is only the approximate change, as the cluster does not always occupy the binding sites, or even more DNA could be suctioned into the cluster). The net displacement of the tether endpoints will be $s_{\text{left}}, s_{\text{right}}$ for perfectly straight tethers, less otherwise.

Based on the data of the impact of looping on the force-extension behavior of the ParB-DNA system that we present in chapter 13, we propose the following research questions:

- For ParBs with a bridging valency $q = 6$, does the spring constant of the ParB–DNA system only depend on $J_S - J_B$?
- For ParBs with a bridging valency $q < 6$:
  - Do the clusters have have an increased probability of loop creation, since loop creation is not necessarily accompanied by breaking of a bridging bond?
  - Is loop creation now no longer accompanied by the breaking of a bridging bond? If so, does the spring only depend on J_S and not on J_B?
- Possibly controlled by system size or by using ParB binding sites (Figure 15.1), how does the amount of DNA in the rosette impact the force extension behavior?
- Force-extension curves of the ParB–DNA system *in vitro* are not consistent with a worm-like chain model [62]. Can part of this inconsistency be resolved based on the inclusion of DNA loops that emanate from the ParB cluster?

15.3 Interaction Between Slip-Links

We have discussed how local polymer relaxation can affect the slip-link translocation velocity (section 12.2) of a single slip-link. At higher densities of slip-links, however, the slip-links can *interact* with each other through the polymer loop that runs between two slip-links. In particular, a part of the polymer that a motor slip-link recently moved over will be partially straightened, potentially creating a 'track' for a next slip-link to more quickly move over. Such an interplay between polymer relaxation dynamics and slip-link translocation will only exist during the relaxation time of that loop τ_R. For times $t \gg \tau_R$, the motor slip-links move adiabatically over the polymer.

If true, an interplay between relaxation dynamics and slip-link movement would open up the possibility for accelerated translocation through the polymer substrate. This phenomenon will likely not take place at any density—as we discussed in section 11.2, motor slip-links engange in antagonistic movement at very high densities. To the contrary, a naive *Ansatz* suggests that mutual slip-link attraction could take place even at low densities. Namely, for Rouse relaxation of a loop of size L, we have $\tau_R \sim L^2$ [59]; the distance between motors in units of time is $t_{\text{betw. SLs}} \approx L/v \sim L$, because v typically does not depend on system size (Figure 12.2). This naive calculation suggests that the impact of a finite polymer relaxation time could be greater at larger system sizes. Stated otherwise, for the same system size, a lower density increases the disparity between $t_{\text{betw. SLs}}$ and τ_R. At the same time, a higher density of slip-links does increase the amount of DNA organization, as measured by the number of long-range contacts (Figure 11.7). We have not investigated this possible mutual slip-link attraction, but it offers the exciting possibility of motors that can collectively organize DNA faster than at the single-motor speed measured *in vitro* [64]. In particular, we propose the following research question:

Do multiple motors accelerate one another, when they follow each other in file?

To address this question, we propose the following three experiments:

1. Attractive interactions between multiple slip-links simultaneously on the DNA
   - Slip-links are loaded onto the DNA at a particular location.
   - First, measure the speed v_1 of a single motor slip-link over the DNA by setting the slip-link association rate very low $k_+ \to 0$.
   - Now increase the number of slip-links by increasing k_+. Does the speed $v_{>1}$ increase, $v_{>1} > v_1$?
2. Directly measuring the effect of polymer relaxation on the movement of a single slip-link, *accelerated* translocation.
   - At most a single slip-link is bound to the DNA, always loaded onto the DNA at a *particular* location.
   - First, set $k_+ \to 0$ and measure the speed $v(0)$ of the slip-link. In this case, the DNA has plenty of time to relax into a random configuration until the next binding event.
   - Now, increase k_+ and measure the speed $v(k_+)$; does it *increase* $v(k_+) > v(0)$? This suggests that the polymer is quenched in a favorable configuration for slip-link translocation.
3. Directly measuring the effect of polymer relaxation on the movement of a single slip-link, testing whether other quenched polymer configurations can inhibit slip-link movement.
   - At most a single slip-link is bound to the DNA, always loaded onto the DNA at a *random* location.
   - First, set $k_+ \to 0$ and measure the speed $v(0)$ of the slip-link. In this case, the DNA has plenty of time to relax into a random configuration until the next binding event.
   - Now, increase k_+ and measure the speed $v(k_+)$; does it *increase* $v(k_+) > v(0)$ or *decrease* $v(k_+) < v(0)$?

Bibliography

[47] Elnaz Alipour and John F Marko. Self-organization of domain structures by DNA-loop-extruding enzymes. *Nucleic acids research*, 40(22):11202–12, dec 2012. ISSN 1362-4962.

[48] Tadashi Ando and Jeffrey Skolnick. Crowding and hydrodynamic interactions likely dominate in vivo macromolecular motion. *Proceedings of the National Academy of Sciences of the United States of America*, 107(43):18457–62, oct 2010. ISSN 1091-6490.

[49] S Bicknese, N Periasamy, S B Shohet, and A S Verkman. Cytoplasmic Viscosity Near the Cell Plasma Membrane: Measurement by Evanescent Field Frequency-Domain Microfluorimetry. *Biophysical Journal Volume*, 65:1272–1282, 1993.

[50] C A Brackley, J Johnson, D Michieletto, and D Marenduzzo. Effect of chromatin flexibility on diffusive loop extrusion via molecular slip-links. *bioRxiv*, page 275214, 2018.

[51] C. A. Brackley, J. Johnson, D. Michieletto, A. N. Morozov, M. Nicodemi, P. R. Cook, and D. Marenduzzo. Extrusion without a motor: a new take on the loop extrusion model of genome organization. *Nucleus*, 9(1):95–103, jan 2018. ISSN 1949-1034.

[52] Chris A Brackley, James Johnson, Davide Michieletto, Alexander N Morozov, Mario Nicodemi, Peter R Cook, and Davide Marenduzzo. Non-equilibrium chromosome looping via molecular slip-links. *Physical Review Letters*, 119(13):138101, 2017.

[53] Hugo B Brandão, Payel Paul, Aafke A van den Berg, David Z Rudner, Xindan Wang, and Leonid A Mirny. RNA polymerases as moving barriers to condensin loop extrusion. *Proceedings of the National Academy of Sciences of the United States of America*, 116(41):20489–20499, oct 2019. ISSN 1091-6490.

[54] C. P. Broedersz, X. Wang, Y. Meir, J. J. Loparo, D. Z. Rudner, and N. S. Wingreen. Condensation and localization of the partitioning protein ParB on the bacterial chromosome. *Proceedings of the National Academy of Sciences*, 111(24):8809–8814, jun 2014. ISSN 0027-8424.

[55] Frank Bürmann, Alrun Basfeld, Roberto Vazquez Nunez, Marie-Laure Diebold-Durand, Larissa Wilhelm, and Stephan Gruber. Tuned SMC Arms Drive Chromosomal Loading of Prokaryotic Condensin. *Molecular Cell*, 65(5):861–872.e9, mar 2017. ISSN 10972765.

[56] Bo-Wei Chen, Ming-Hsing Lin, Chen-Hsi Chu, Chia-En Hsu, and Yuh-Ju Sun. Insights into ParB spreading from the complex structure of Spo0J and parS Data deposition: The atomic coordinates and structure factors have been deposited in the Protein Data Bank, www.pdb.org (PDB ID code 4UMK). *PNAS*, 112(21):6613–6618, 2015.

[57] Pierre-Gilles de. Gennes. *Scaling concepts in polymer physics*. Cornell University Press, 1979. ISBN 080141203X.

[58] Marie-Laure Diebold-Durand, Hansol Lee, Laura B. Ruiz Avila, Haemin Noh, Ho-Chul Shin, Haeri Im, Florian P. Bock, Frank Bürmann, Alexandre Durand, Alrun Basfeld, Sihyun Ham, Jérôme Basquin, Byung-Ha Oh, and Stephan Gruber. Structure of Full-Length SMC and Rearrangements Required for Chromosome Organization. *Molecular Cell*, 67(2):334–347.e5, jul 2017. ISSN 10972765.

[59] M. Doi and S. F. Edwards. *The Theory of Polymer Dynamics*. Clarendon Press, Oxford, 1986.

[60] Jorine M. Eeftens, Allard J. Katan, Marc Kschonsak, Markus Hassler, Liza de Wilde, Essam M. Dief, Christian H. Haering, and Cees Dekker. Condensin Smc2-Smc4 Dimers Are Flexible and Dynamic. *Cell Reports*, 14(8):1813–1818, 2016. ISSN 22111247.

[61] Jorine M Eeftens, Shveta Bisht, Jacob Kerssemakers, Christian H Haering, and Cees Dekker. Real-time detection of condensin-driven DNA compaction reveals a multistep binding mechanism. *bioRxiv*, 2017.

[62] Gemma L M Fisher, César L Pastrana, Victoria A Higman, Alan Koh, James A Taylor, Annika Butterer, Timothy D Craggs, Frank Sobott, Heath Murray, Matthew P Crump, Fernando Moreno-Herrero, and Mark S Dillingham. The C-terminal domain of ParB is critical for dynamic DNA binding and bridging interactions which condense the bacterial centromere. .

[63] Geoffrey Fudenberg, Maxim Imakaev, Carolyn Lu, Anton Goloborodko, Nezar Abdennur, and LeonidÂ A. Mirny. Formation of Chromosomal Domains by Loop Extrusion. *Cell Reports*, 15(9):2038–2049, 2016. ISSN 22111247.

[64] Mahipal Ganji, Indra A Shaltiel, Shveta Bisht, Eugene Kim, Ana Kalichava, Christian H Haering, and Cees Dekker. Real-time imaging of DNA loop extrusion by condensin. *Science*, 360(6384):102–105, feb 2018. ISSN 1095-9203.

[65] Anton Goloborodko, Maxim V Imakaev, John F Marko, and Leonid Mirny. Compaction and segregation of sister chromatids via active loop extrusion. *eLife*, 5, may 2016. ISSN 2050-084X.

[66] Anton Goloborodko, John F Marko, and Leonid A Mirny. Chromosome Compaction by Active Loop Extrusion. *Biophysical Journal*, 110, 2016.

[67] Thomas G W Graham, Xindan Wang, Dan Song, Candice M Etson, Antoine M van Oijen, David Z Rudner, and Joseph J Loparo. ParB spreading requires DNA bridging. *Genes & Development*, 28(11):1228–38, jun 2014. ISSN 1549-5477.

[68] Stephan Gruber and Jeff Errington. Recruitment of condensin to replication origin regions by ParB/SpoOJ promotes chromosome segregation in B. subtilis. *Cell*, 137(4):685–96, may 2009. ISSN 1097-4172.

[69] Stephan Gruber, Jan-Willem Veening, Juri Bach, Martin Blettinger, Marc Bramkamp, and Jeff Errington. Interlinked Sister Chromosomes Arise in the Absence of Condensin during Fast Replication in B. subtilis. *Current Biology*, 24:293–298, 2014.

[70] Adam S. B. Jalal, Ngat T. Tran, and Tung B. K. Le. ParB spreading on DNA requires cytidine triphosphate in vitro. *bioRxiv*, page 2019.12.11.865972, dec 2019.

[71] Eugene Kim, Jacob Kerssemakers, Indra A. Shaltiel, Christian H. Haering, and Cees Dekker. DNA-loop extruding condensin complexes can traverse one another. *bioRxiv*, page 682864, jun 2019.

[72] HyeongJun Kim and Joseph J. Loparo. Multistep assembly of DNA condensation clusters by SMC. *Nature Communications*, 7:10200, jan 2016. ISSN 2041-1723.

[73] Tung B K Le, Maxim V Imakaev, Leonid A Mirny, and Michael T Laub. High-Resolution Mapping of the Spatial Organization of a Bacterial Chromosome. *Science*, 342(6159):731–734, nov 2013. ISSN 0036-8075.

[74] Erez Lieberman-Aiden, Nynke L van Berkum, Louise Williams, Maxim Imakaev, Tobias Ragoczy, Agnes Telling, Ido Amit, Bryan R Lajoie, Peter J Sabo, Michael O Dorschner, Richard Sandstrom, Bradley Bernstein, M A Bender, Mark Groudine, Andreas Gnirke, John Stamatoyannopoulos, Leonid A Mirny, Eric S Lander, and Job Dekker. Comprehensive mapping of long-range interactions reveals folding principles of the human genome. *Science (New York, N.Y.)*, 326(5950):289–93, oct 2009. ISSN 1095-9203.

[75] Anita Minnen, Frank Bürmann, Larissa Wilhelm, Anna Anchimiuk, Marie-Laure Diebold-Durand, and Stephan Grüber. Control of Smc Coiled Coil Architecture by the ATPase Heads Facilitates Targeting to Chromosomal ParB/parS and Release onto Flanking DNA. *Cell Reports*, 14, 2016.

[76] Uri Moran, Rob Phillips, and Ron Milo. SnapShot: Key Numbers in Biology. *Cell*, 141:1262–1262, 2010.

[77] Michael Rubinstein and Ralph H. Colby. *Polymer Physics*. Oxford University Press, 2003.

[78] SB Smith, L Finzi, and C Bustamante. Direct mechanical measurements of the elasticity of single DNA molecules by using magnetic beads. *Science*, 258(5085), 1992.

[79] Young-Min Soh, Frank Bürmann, Ho-Chul Shin, Takashi Oda, Kyeong Sik Jin, Christopher P. Toseland, Cheolhee Kim, Hansol Lee, Soo Jin Kim, Min-Seok Kong, Marie-Laure Durand-Diebold, Yeon-Gil Kim, Ho Min Kim, Nam Ki Lee, Mamoru Sato, Byung-Ha Oh, and Stephan Gruber. Molecular Basis for SMC Rod Formation and Its Dissolution upon DNA Binding. *Molecular Cell*, 57(2):290–303, 2015. ISSN 10972765.

[80] Dan Song, Kristen Rodrigues, Thomas GW Graham, Joseph J Loparo, and Harvard A John. A network of cis and trans interactions is required for ParB spreading. *Nucleic Acids Research*, 45(12):7106–7117, 2017.

[81] Johannes Stigler, Gamze Ç Amdere, Douglas E Koshland, and Eric C Greene. Single-Molecule Imaging Reveals a Collapsed Conformational State for DNA-Bound Cohesin. *Cell Reports*, 15:988–998, 2016.

[82] Tsuyoshi Terekawa, Shveta Bisht, Jorine Eeftens, Cees Dekker, Christian Haering, and Eric Greene. The Condensin Complex Is A Mechanochemical Motor That Translocates Along DNA. *Science*, 358(6363):672–676, 2017.

[83] J Tothova, B Brutovsky, and V Lisy. Monomer motion in single-and double-stranded DNA coils.

[84] Georgia Tsolou, Nikos Stratikis, Chunggi Baig, Pavlos S. Stephanou, and Vlasis G. Mavrantzas. Melt Structure and Dynamics of Unentangled Polyethylene Rings: Rouse Theory, Atomistic Molecular Dynamics Simulation, and Comparison with the Linear Analogues. *Macromolecules*, 43 (24):10692–10713, dec 2010. ISSN 0024-9297.

[85] Xindan Wang, Paula Montero Llopis, and David Z Rudner. Organization and segregation of bacterial chromosomes. *Nature Reviews Genetics*, 14: 191–203, 2013.

[86] Xindan Wang, Tung B K Le, Bryan R. Lajoie, Job Dekker, Michael T. Laub, and David Z. Rudner. Condensin promotes the juxtaposition of dna flanking its loading site in Bacillus subtilis. *Genes and Development*, 29(15):1661–1675, 2015. ISSN 15495477.

[87] Xindan Wang, Hugo B. Brandão, Tung B. K. Le, Michael T. Laub, and David Z. Rudner. Bacillus subtilis SMC complexes juxtapose chromosome arms as they travel from origin to terminus. *Science*, 355(6324), 2017.

[88] Xindan Wang, Anna C. Hughes, Hugo B. Brandão, Benjamin Walker, Carrie Lierz, Jared C. Cochran, Martha G. Oakley, Andrew C. Kruse, and David Z. Rudner. In Vivo Evidence for ATPase-Dependent DNA Translocation by the Bacillus subtilis SMC Condensin Complex. *Molecular Cell*, 71(5):841–847.e5, sep 2018. ISSN 1097-2765.

[89] Xindan Wang, Olive W. Tang, Eammon P. Riley, and David Z. Rudner. The SMC Condensin Complex Is Required for Origin Segregation in Bacillus subtilis. *Current Biology*, 24(3):287–292, apr 2018. ISSN 0960-9822.

[90] Hiroshi Watanabe, Inoue Tadashi, and Yumi Matsumiya. Transient Conformational Change of Bead–Spring Ring Chain during Creep Process. *Macromolecules*, 39(16):5419—-5426, 2006.

[91] Larissa Wilhelm, Frank Bürmann, Anita Minnen, Ho-Chul Shin, Christopher P Toseland, Byung-Ha Oh, Stephan Gruber, E. Alipour, JF. Marko, P. Arumugam, and S. Gruber. SMC condensin entraps chromosomal DNA by an ATP hydrolysis dependent loading mechanism in Bacillus subtilis. *eLife*, 4:11202–11212, may 2015. ISSN 2050-084X.

[92] Pawel Zawadzki, Mathew Stracy, Katarzyna Ginda, Katarzyna Zawadzka, Christian Lesterlin, Achillefs N. Kapanidis, and David J. Sherratt. The Localization and Action of Topoisomerase IV in Escherichia coli Chromosome Segregation Is Coordinated by the SMC Complex, MukBEF. *Cell Reports*, 13(11):2587–2596, dec 2015. ISSN 22111247.

Appendices

A

Measurement of Simulation and Empirical Data

Our simulation parameters and units are clarified in Table A.1. Because cytosolic diffusion of condensin is fast compared to diffusion of condensin over dsDNA [81], we assume a regime in which the condensin binding rate is much higher than the slip-link movement attempt rate, $k_+ \gg k_0$. We implemented loading to the ParB*S* region [75] by binding slip-links only to a predetermined loading site (*ori*) on the polymer. Slip-links can, however, unbind anywhere on the DNA, as long as the slip-link encircles a loop of only one lattice width.

A.1 Converting Empirical Data to Simulation Parameters

Motor direction switching time in yeast condensin

In vitro DNA curtain experiments have shown that a fraction of condensins can reverse their active motion within a time τ_r [82]. In these experiments, the condensins can only be monitored over a maximum distance $L_{\text{assay}} = 16.49\,\mu\text{m}$. The time a condensin can be observed to move with a constant velocity $v \approx 20\,\text{nm/s}$ is, therefore $t^\star = L_{\text{assay}}/v \approx 825\,\text{s}$ [82]. In [82], the probability for the motor to be reversed at least once within this time $t^\star$ has been measured to be $p_r(t^\star) \approx 6\%$. Assuming Poissonian statistics, the probability of the condensin having reversed within a time $t^\star$ is

$$p_r(t^\star) = 1 - \exp(-t^\star/\tau_r),$$

from which we estimate a typical switching time for yeast condensin $\tau_r \approx 222\,\text{min}$. Based on a typical velocity of $v \approx 20\,\text{nm/s}$ [64], we estimate that a yeast condensin travels on average a distance $L_{\max} = v\tau_r \approx 266\,\mu\text{m} \approx 785\,\text{kpb}$ before switching direction. Crowding on the DNA by other proteins *in vivo* could affect these estimates.

Measuring propagation length of condensin in *B. subtilis*

We analyzed ChIP-seq data from [75] of the strains "WT" (wild-type), "ATP_" (mutant with strongly suppressed ATP hydrolysis) and ΔParB (mutant without ParB). As a baseline for the SMC signal, we used the ΔParB data for both the WT and ATP_ strains and computed the difference in their SMC ChIP-Seq signals $c_{\text{SMC}}(i)$ (Fig. SA.1),

$$\begin{aligned}\Delta c_{\text{SMC,WT}}(i) &= c_{\text{SMC,WT}}(i) - c_{\text{SMC,}'\text{ParB}}(i)\\ \Delta c_{\text{SMC,ATP_}}(i) &= c_{\text{SMC,ATP_}}(i) - c_{\text{SMC,}'\text{ParB}}(i).\end{aligned}$$

We then smoothed the data with a Savitzky-Golay-filter of window 21 and order 2 and extracted typical widths $\hat{X}_{\text{SMC}}$, defined as the standard deviation of the smoothed ChIP profiles. We computed the typical widths $\hat{X}_{\text{SMC,WT}} \approx 7000\ell_0$, $\hat{X}_{\text{SMC,ATP_}} \approx 2000\ell_0$—or, when scaled by the system size $\hat{x}_{\text{SMC,WT}} \approx 13\%$, $\hat{x}_{\text{SMC,ATP_}} \approx 45\%$.

Table A.1: The parameters used in the simulations and comparisons with WT data.

Quantity	Expression	Value	Reference
Lattice constant (persistence length of dsDNA)	ℓ_0	50 nm	[78]
Size of slip-link	$25 - 50\,\mathrm{nm}$	set to ℓ_0	[55, 60]
Size of *B. subtilis* genome	$L_{\mathrm{gen.}}$	4 Mbp	[75]
Length of *B. subtilis* genome in sim. units	$N_{m,\mathrm{WT}} = L_{\mathrm{gen.}}/\ell_0$	$28 \cdot 10^3$	rest of table
Radius of dsDNA	b	2 nm	[76]
Thermal energy	$k_B T$	4.2 pN nm	[76]
Cytosolic viscosity	η	1 mPa/s	[48?, 49]
Diff. coeff. of dsDNA-bound cohesin	D	$1\,\mu\mathrm{m}^2/\mathrm{s}$	[81]
Diffusion time of slip-link over monomer	$\tau_{\mathrm{diff.slip-link}} \approx \ell_0^2/2D$	$1250\,\mu\mathrm{s}$	rest of table
Loop extrusion velocity of yeast condensin	v	425 nm/s	[64]
Translocation time of condensin over a monomer	$\tau_{\mathrm{motor.slip-link}} \approx \ell_0/v$	0.12 s	rest of table
Yeast condensin switching rate	k_{switch}	$222\,\mathrm{min}^{-1}$	SI A.1
Relative SMC propagation length, WT	$\hat{x}_{\mathrm{SMC,WT}}$	45%	SI A.1
Relative SMC propagation length, -ATP	$\hat{x}_{\mathrm{SMC,ATP_}}$	13%	SI A.1
Monomer relaxation time	$\tau_{\mathrm{mon.}} = \frac{2}{\pi}\ell_0^2 b\eta/k_B T$	$0.8\,\mu\mathrm{s}$	[77, 83]
Number of condensins per chromosome	$N_{p,\mathrm{WT}}$	3–30	[91]
SMC density per simulation monomer	$\phi_{p,\mathrm{WT}} = \frac{2N_{p,\mathrm{WT}}}{N_{m,\mathrm{WT}}}$	$10^{-4} - 10^{-3}$	rest of table

A.2 Converting Simulation Data to Metrics

Measuring condensin propagation timescale

Recent *in vivo* experiments have been performed in which ChIP-seq data was measured at various time-points after induction of SMC condensin [87]. From these ChIP-seq data, the typical width $\hat{X}_p(t)$ of condensin propagation was measured as a function of time. Since the curve of $\hat{X}_p(t)$ was well approximated by an exponential curve, we extracted a typical timescale of ≈ 24 min from these curves (Fig. SA.2).

Determination of typical length of cross-diagonal

We first extract an 'unprocessed' cross-diagonal probability $p_{c,\mathrm{unprocessed}}(k) \in [0, 1]$ as illustrated in Fig. SA.3. Neither the moments $\langle k^n \rangle$ nor the $p-$th percentile of the 'unprocessed' distribution $p_{c,\mathrm{unprocessed}}(k)$ correlated well with the cross-diagonal width based on visual inspection. The reason for this is that $p_{c,\mathrm{unprocessed}}(k)$ contains large flanks at $|k| \approx N_m/2 \gg 1$ (Figure A.3d) that were found to significantly impact estimates of $\hat{X}_c$.

The flanks in $p_{c,\mathrm{unprocessed}}(k)$ (Figure A.3d) arise due to the circular topology of the polymer, with an increasing contact probability for $|k| \approx N_m/2 \gg 1$. A naive estimate of the flanks is a power-law with Flory-scaling $p_{c,\mathrm{naive}} \sim (\frac{1}{2}N_m - |k|)^{d\nu}, d = 3, \nu \approx 3/5$ [57]. Subtracting this naive estimate from $p_{c,\mathrm{unprocessed}}(k)$, was found to sometimes lead to negative probabilities. To avoid this, we instead subtracted an underestimate of the flanks, namely a power-law with 50% stronger scaling than the naive estimate: $p_{c,\mathrm{underest.}}(k) \sim (\frac{1}{2}N_m - |k|)^{-1.5d\cdot\nu} \leq p_{c,\mathrm{naive}}$ (Figure A.4, compare black and blue histograms). By visual inspection on a variety of representative test-cases, we found that this method indeed suppressed the flanks of $p_{c,\mathrm{unprocessed}}(k)$, but left the cross-diagonal itself intact (Figure A.4, blue histogram).

After subtracting the flanks from $p_c(k)$ (Fig. SA.4, blue histogram), we calculate the typical length $X_{c,p} = \frac{1}{2}m_p$ with parameter p as the $p-$th percentile of the distribution $p_c(k)$. We computed various percentiles $\{m_{50\%}, m_{75\%}, m_{90\%}, m_{95\%}\}$ on a representative collection of contact maps and empirically found by visual inspection that $m_{75\%}$ was a good measure for the typical length of the cross diagonal in contact maps.

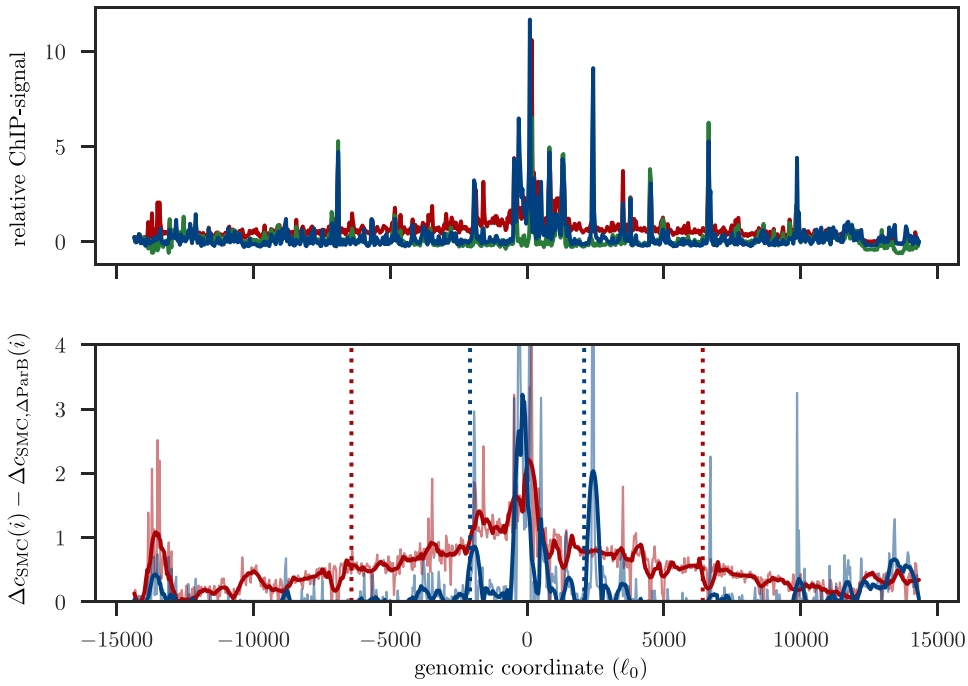

Figure A.1: **Determination of typical SMC propagation width from SMC ChIP-seq data.**. **Top**: Raw relative ChIP-seq data $c_{\mathrm{SMC}}(i) - c_{\mathrm{SMC}}(\frac{1}{2}N_m)$ (i.e. we subtracted the ChIP-signal at *ter*) of three strains from [75]: "WT" (wild-type, red), "ATP_" (mutant with strongly suppressed ATP hydrolysis, blue) and ΔParB (mutant lacking ParB, green). **Bottom**: We use the ΔParB signal as a baseline for the SMC ChIP-signal. The WT and ATP_ signals with the ΔParB signal subtracted (thin curves) and with an additional smoothing using a Savitzky-Golay filter (window: 21, order: 2) (thick curves). The typical width of these graphs was then defined as $\sqrt{\mathrm{var}[c_{\mathrm{SMC}}(i)]}$ (dotted vertical lines). Lengths are in units of polymer bond lengths $\ell_0 = 50\,\mathrm{nm}$ (see Table A.1). ChIP-seq data were taken from the ArrayExpress database at EMBL-EBI (www.ebi.ac.uk/arrayexpress) under accession number E-GEOD-76949.

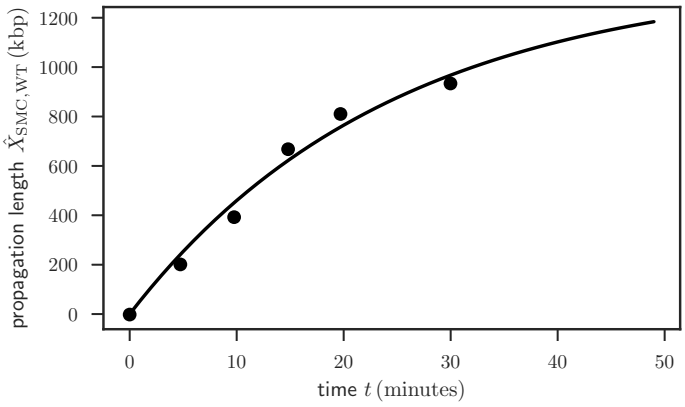

Figure A.2: The ChIP-seq data of the SMC condensin propagation width has a typical timescale of ≈ 24 min. Fit parameters $\tau \approx 24\,\mathrm{min}$, amplitude ≈ 1368 kbp were found by fitting the data from [87] with an exponential.

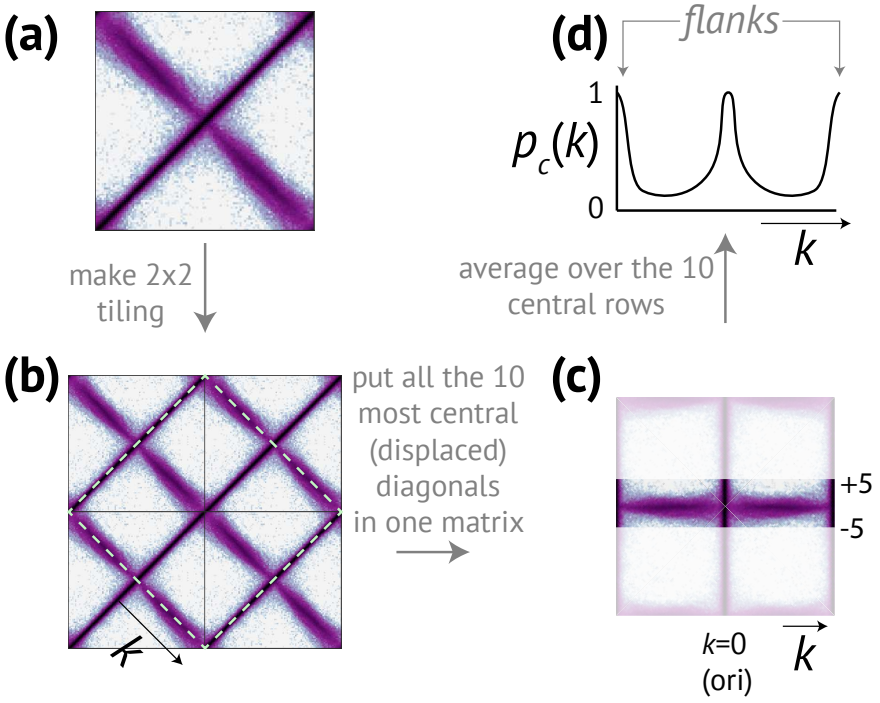

Figure A.3: Illustration of our procedure to extract the cross diagonal from a contact map. **(a)**: A single contact map. **(b)**: Make a 2×2 tiling of contact maps. **(c)**: Extract the 10 most central cross-diagonal rows (similar to the procedure published in [73, 87]). **(d)**: Average the data from step (c) over the 10 rows, returning a cross-diagonal probability $p_c(k)$ where $k = -\frac{1}{2}N_m, \ldots, +\frac{1}{2}N_m$ is the distance from *ori*. In order to isolate the cross-diagonal from the rest of the contact map, we select the 10 most central rows from the contact map (i.e. $|k| \leq 5$).

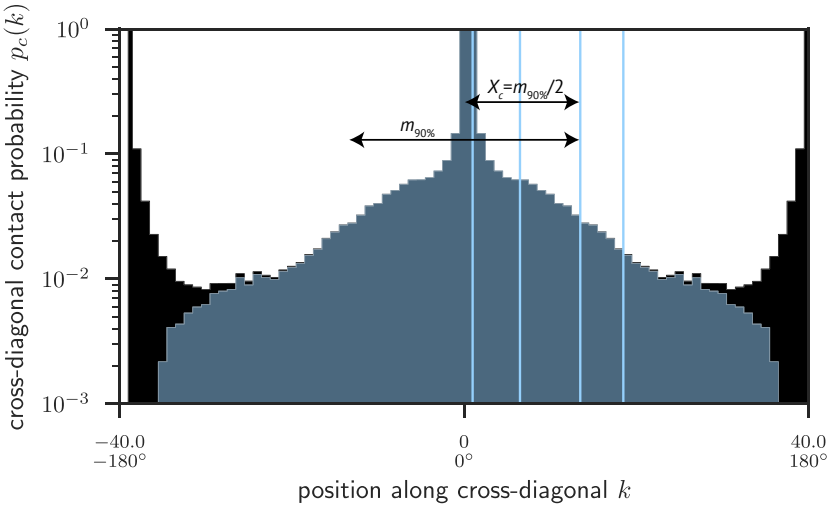

Figure A.4: **Computation of the length of the cross-diagonal using the p−th percentile.** We first measured the 'unprocessed' cross-diagonal contact probability $p_{c,\text{unprocessed}}(k)$ from contact maps (black, see Fig. SA.3 for the procedure). Then, we subtract an estimate for the left and right flanks (blue, see section A.1) and computed the p−th percentile m_p of $p_c(k)$. The half-width of the p−th percentile $\frac{1}{2}m_p$ is shown for $p = 50, 75, 90, 95\%$ (blue vertical lines, from left to right), and the typical width of the curve is defined as $X_c \equiv \frac{1}{2}m_p$.

B

Rouse Model for Circular Polymer Chains

The results in this chapter have not been peer reviewed.

The dynamics of a *circular* Rouse chain of size N (i.e. a polymer lacking hydrodynamic and excluded volume interactions) can be described in the continuum limit by the *Edward-Wilkinson* equation:

$$\gamma \partial_t \mathbf{r}(n,t) = k \partial_n^2 \mathbf{r}(n,t) + \mathbf{f}(n,t), \tag{B.1}$$

where the position of the nth monomer $\mathbf{r}(n,t)$ is a stochastic variable with boundary conditions from the circularity of the polymer $\mathbf{r}(0,t) = \mathbf{r}(N,t), \mathbf{r}'(0,t) = \mathbf{r}'(N,t)$ and noise $\mathbf{f}(n,t) = (f_\alpha(n,t))_\alpha$ is white noise from a heat bath with the properties

$$\begin{aligned} \left\langle f_\alpha(n,t) \right\rangle &= 0, \\ \left\langle f_\alpha(n,t) f_\beta(m,t') \right\rangle &= 2\gamma k_B T \delta_{\alpha\beta} \delta(t-t') \delta(n - \mod(m,N)), \end{aligned} \tag{B.2}$$

is delta-correlated in time, between the different dimensions and along the chain—the modulo operator enforces the periodic boundary conditions that arise from having the endpoints connected. As in [59], we seek a solution for normal modes $\mathbf{X}_p(t) = \int_0^N \mathrm{d}n\, \phi_p(n) \mathbf{r}(n,t)$ of the form

$$\gamma_p \partial_t \mathbf{X}_p = -k_p \mathbf{X}_p + \mathbf{F}_p, \tag{B.3}$$

where $\mathbf{F}_p$ is projection of the noise on normal mode space. We note that the problem is identical to Rouse modes for a linear chain, except for a difference in boundary conditions. Thus, we re-use the solutions presented by Doi and Edwards [59]:

$$\frac{\gamma_p}{\gamma} k \partial_n^2 \phi_p = -k_p \phi_p, \tag{B.4}$$

$$\left(\mathbf{r}_n \partial_n \phi_p\right)\Big|_{n=0}^{N} = 0, \tag{B.5}$$

$$\mathbf{F}_p(t) = \frac{\gamma_p}{\gamma} \int_0^N \mathrm{d}n\, \phi_p(n) \mathbf{f}(n,t), \tag{B.6}$$

with the coefficients γ_p, k_p given by Doi and Edwards [59]. The boundary conditions for a linear Rouse chain only allow for cosine modes. For a circular chain, the normal modes from the literature also include sine modes $\phi_p^+ = N^{-1} \cos q_p n, \phi_p^- = N^{-1} \sin q_p n$ [84, 90]. The boundary condition in equation (B.5), $\mathbf{r}_0(\partial_n \phi_p(n))(0) = \mathbf{r}_N(\partial_n \phi_p(n))(N)$ (with $\mathbf{r}_0 = \mathbf{r}_N$ due to circularity), implies $q_p = 2\pi p/N$ as opposed to $q_p^{\text{linear}} = \pi p/N$ for a linear chain. In short: the normal modes for circular chains still live in 'momentum space', but only the even modes $q_p = 2\pi p/N$ are consistent with circularity.

What is the correlation structure of the normal mode noise amplitudes $\mathbf{F}_p$? For this, we cannot directly use the solution for a linear chain, because the noise autocorrelator in the real-space description $\left\langle f_\alpha(n,t) f_\beta(m,t') \right\rangle$ contains a modulo

operator (equation B.2) that is absent for linear chains. Since the integrals that we use always run from $n, m = 0 \ldots N$, we simplify the modulo operator by writing

$$\delta(n - \mod(m, N)) = \delta(n - m) + \delta_\epsilon(n)\delta_\epsilon(m - N) + \delta_\epsilon(m)\delta_\epsilon(n - N), \tag{B.7}$$

where $\delta_\epsilon(x) = \delta(x - \epsilon)$ with $\epsilon \to 0$; i.e. we assume that the random forces that the heat bath exerts arbitrarily close to the end-points are highly correlated. This has a clear physical interpretation if we choose for $\epsilon = 2\ell_{\text{solvent}}$ twice the size of a solvent molecule ℓ_{solvent}, since a single solvent molecule will then exert forces on both $n = 0 - \epsilon, N - \epsilon$.

Using the form in equation (B.7), we have the noise correlator $G_{pq,\alpha\beta}(t - t')$ in normal mode space:

$$\begin{aligned} G_{pq,\alpha\beta}(t - t') &\equiv \left\langle F_{p\alpha}(t) F_{q\beta}(t') \right\rangle \\ &= \frac{\gamma_p \gamma_q}{\gamma^2} \int \mathrm{d}n\mathrm{d}m \; \phi_p(n)\phi_q(m) \left\langle f_{n\alpha}(t) f_{m\beta}(t') \right\rangle \\ &= 2\gamma k_B T \delta_{\alpha\beta}\delta(t - t') \frac{\gamma_p \gamma_q}{N^2\gamma^2} \int \mathrm{d}n\mathrm{d}m \; \phi_p(n)\phi_q(m)[\delta(n - m) + \qquad (B.8) \\ &\quad \delta_\epsilon(n)\delta_\epsilon(m - N) + \delta_\epsilon(m)\delta_\epsilon(n - N)], \qquad (B.9) \end{aligned}$$

where we substituted the normal modes $\phi_p(n)$ and the noise correlator (equation (B.7)). Each of the additional noise terms have the form

$$\begin{aligned} \int \mathrm{d}n\mathrm{d}m \; g_p(n) g_q(m) \delta_\epsilon(n)\delta_\epsilon(m - N) &= \int \mathrm{d}n \; g_p(n)\delta_\epsilon(n) \cdot \int \mathrm{d}m \; g_q(m)\delta_\epsilon(m - N) \\ &= g_p(0) \cdot g_q(N), \end{aligned}$$

where $g(x)$ is some test function that is continuous at $n \to 0, N$ and we tacitly took the limit $\epsilon \to 0$. Thus, we find

$$\begin{aligned} G_{pq,\alpha\beta}(t - t') &= 2\gamma k_B T \delta_{\alpha\beta}\delta(t - t') \frac{\gamma_p \gamma_q}{N^2\gamma^2} \cdot \left[N\delta_{pq} \frac{1 + \delta_{p0}}{2} + \cos 2\pi q + \cos 2\pi p \right] \\ &= 2\gamma k_B T \delta_{\alpha\beta}\delta(t - t') \frac{\gamma_p \gamma_q}{N^2\gamma^2} \cdot \left[N\delta_{pq} \frac{1 + \delta_{p0}}{2} + 2 \right], \end{aligned}$$

where the sine modes ϕ_p^- at the boundaries dropped out because $\sin 2\pi p = 0$. Importantly, the second term in brackets does not have a Kronecker delta prefactor δ_{pq}: The noise correlator $G_{pq,\alpha\beta}(t - t')$ in momentum space contains correlations also between *different* normal modes. It can be visualized in matrix form:

$$\mathbf{G}_{\alpha\beta}(t - t') = 2\gamma k_B T \delta_{\alpha\beta}\delta(t - t') \frac{\gamma_p \gamma_q}{N^2\gamma^2} \begin{bmatrix} N + 2 & 2 & 2 & \cdots \\ 2 & \frac{1}{2}N + 2 & 2 & \cdots \\ 2 & 2 & \frac{1}{2}N + 2 & \cdots \\ \vdots & \vdots & \vdots & \ddots \end{bmatrix}. \tag{B.10}$$

Thus, the periodic boundary conditions in the real space (B.1) equation is transformed into a linear ordinary differential equation in momentum space, but with coupled noises for the different modes. This should be contrasted with Rouse dynamics for a linear chain, where the random forces of normal modes are completely uncoupled. It is important to note that the coupling is weak, and decreases as $1/N$ compared to the on-diagonal correlations.

Through the mode coupling introduced by the off-diagonal elements in equation (B.10), the polymer modes themselves also become coupled. Although the mode coupling is weak ($1/N$ weaker than the on-diagonal correlations), this does introduce the possibility to excite modes indirectly. In principle, this could be used for dynamic DNA re-organization on e.g. large length-scales can be effected by driving a shorter length-scale mode. Unlike the dynamics of linear chains, where driving one mode slightly increases the temperature of all modes but doesn't result in coherent motion of those other modes, the motion of different modes in circular polymers are positively correlated. Of course, whether this is desirable depends on the context.

C

Response Function of Sub-Chains of Circular Polymers

The results in this chapter have not been peer reviewed.

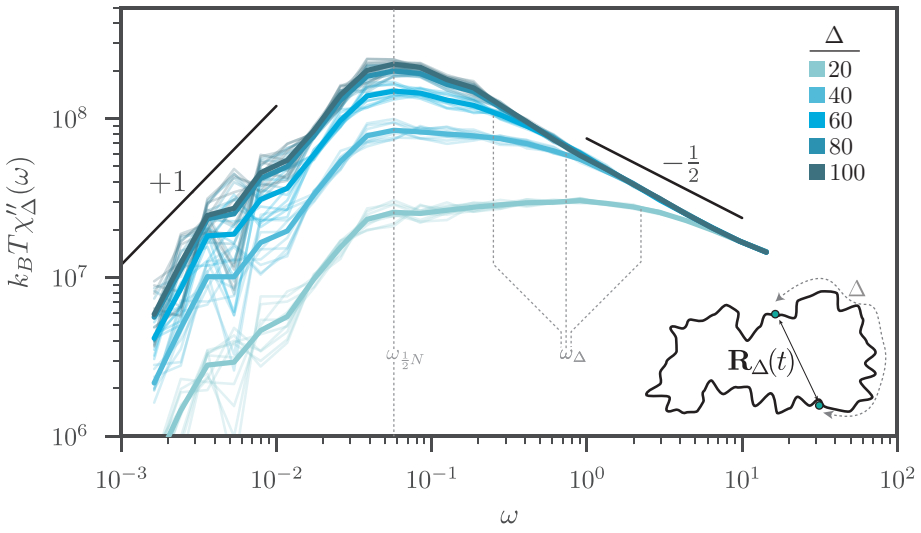

Figure C.1: **Response function of sub-chains of circular polymers.** Shown is the imaginary part of the response function $\chi_\Delta = \chi'_\Delta + i\chi''_\Delta$ in frequency space. We computed χ''_Δ using the fluctuation-fissipation theorem $\chi''_\Delta = \frac{1}{2}\beta\omega\left\langle|\mathbf{R}_\Delta(\omega)|^2\right\rangle$, where $\mathbf{R}_\Delta(\omega)$ is the Fourier transform of the end-to-end vector of a sub-chain of size Δ (inset). The size defined here is the *smallest* distance between two monomers. Approximate frequencies at which the plateau in χ''_Δ transitions to a $\sim \omega^{-1/2}$ scaling. Full polymer length $N = 200$.

We measured the response function of sub-chains of a circular polymer for various sub-chain sizes Δ (Figure C.1). After measuring the end-to-end vector $\mathbf{R}_\Delta(t)$, we compute the imaginary part of the response function $\chi''_\Delta(\omega)$ using the fluctuation-dissipation theorem $\chi''_\Delta = \frac{1}{2}\beta\omega\left\langle|\mathbf{R}_\Delta(\omega)|^2\right\rangle$. In agreement with [84], we find that sub-chains the size of the largest possible sub-chain in the system ($\Delta = N/2$) exhibit the same form as for a linear chain: for ω up to the whole-polymer relaxation frequency $\omega_{\max} \sim N^{-2}$ [84, 90] the response scales as $\chi''_\Delta \sim \omega$ and as $\chi''_\Delta \sim \omega^{-1/2}$ for $\omega > \omega_{\max}$. Interestingly,

however, sub-chains of circular polymers display a *plateau* for $\omega > \omega_{\max} = \omega_{\frac{1}{2}N}$ up to the point $\omega = \omega_\Delta$ where the plateau intersects with $\chi''_{\frac{1}{2}N}$; an implicit definition for ω_Δ is thus $\chi''_\Delta(\omega_{\max}) \approx \chi''_{\frac{1}{2}N}(\omega_\Delta)$. Using the scaling forms for $\chi''_{\frac{1}{2}N}$ shown in Figure C.1 in combination with extensivity of the response function at small frequencies ($\chi_\Delta(\omega < \omega_{\max}) \sim \Delta$), we find $\omega_\Delta \approx \omega_{\frac{1}{2}N} \cdot (N/\Delta)^2$. Since $\omega_{\frac{1}{2}N} \sim N^{-2}$, we thus find $\omega_\Delta \sim \Delta^{-2}$. In other words, at the fastest timescale in the plateau $\tau_\Delta = \omega_\Delta^{-1}$, the sub-chain Δ itself has relaxed; at the slowest timescale in the plateau $\tau_{\max} = \omega_{\frac{1}{2}N}^{-1}$, the largest length-scale in the whole polymer has relaxed.

If our above scaling analysis, then relaxation of the sub-chain at intermediate frequencies $\omega \in \langle \omega_{\frac{1}{2}N}, \omega_\Delta \rangle$ must 'wait' for relaxation of all other length-scales in the full polymer.. Thus, there is a link between *semi-local* dynamical properties and *global* geometrical properties. Then, inspecting the dynamics of two DNA loci, their relative genomic distance Δ/N can be inferred. This might be leveraged to infer binding sites of proteins on plasmids, based only on looking at the time-trace of their interparticle vector $\mathbf{R}_\Delta(t)$. Instead, if their binding sites are known, the same data could be used to infer plasmid size N.

D

Controls on Equilibrium Monte-Carlo Model for Globular Polymers

D.1 Force-Extension of Naked Polymer

Derivation of Force-Extension Curve

To compute the force-extension curve, we decompose the walk into three parts across the different dimensions: n_x, n_y, n_z. The entropy is now

$$S = S_x + S_y + S_z,$$

where $S_i = n_i^+ \log n_i^+ + (n_i - n_i^+)\log(n_i - n_i^+)$ with n_i^+ the steps in the positive direction. We use a Lagrange multiplier μ to constrain the total length:

$$\begin{aligned} F &= -TS - \mu(\sum_i n_i - N) + f(n_z^+ - n_z^- - L) \\ &= \left[\sum_i T n_i^+ \log n_i^+ + T(n_i - n_i^+)\log(n_i - n_i^+) + \mu n_i + \delta_{i,z} f(2n_i^+ - n_i - L)\right]. \end{aligned}$$

In thermodynamic equilibrium, we have to tune μ, f such that this free energy will be minimized with respect to all response variables n_i^+, n_i. This is seemingly an overdetermined problem, but the x, y equations are actually identical. We have the constraints:

$$\begin{aligned} (i)\sum_i n_i &= N \\ (ii) 2n_z^+ - n_z &= L \\ (iii)\partial_{n_i} F &= 0 \\ (iv)\partial_{n_i^+} F &= 0 \end{aligned}$$

Equation (iii) gives us

$$T\log(n_i - n_i^+) + T + \mu - f\delta_{i,z} = 0.$$

From that equation we find the chemical potential:

$$\mu = -T - T\log(n_x - n_x^+),$$

but since the x, y symmetries are not broken by the force along the $z-$direction, we have $n_x - n_x^+ = \frac{1}{2}n_x$, so

$$\begin{aligned}\mu &= -T - T\log(n_x/2)\\ &= T(\log 2 - 1 - \log n_x).\end{aligned}$$

Since μ is a global property and does not depend on the x, y, z coordinates, we can actually solve the equation (iii) for also the z direction, and this gives us:

$$\mu = f - T - T\log(n_z - n_z^+) = f - T(1 + \log(n_z - n_z^+)) = T(\log 2 - 1 - \log n_x).$$

Remember, μ controls the total amount of particles, so we can utilize this equation by solving it for n_x as a function of n_z and using that everywhere:

$$n_x = \exp\left[-\frac{f}{T} + \log(n_z - n_z^+) + \log 2\right].$$

Equation (iv) gives us:

$$T\log n_i^+ + T - T\log(n_i - n_i^+) - T + 2f\delta_{i,z} = 0.$$

For $n_i = n_{x,y}$ this gives, using $n_i^+ = \frac{1}{2}n_i$,

$$\begin{aligned}0 &= T\log n_i^+ + T - T\log(n_i - n_i^+) - T\\ &= T\log(n_i/2) - T\log(n_i/2)\\ &= 0,\end{aligned}$$

trivially. No surprise there, because equation (iv) basically dictates how the force distributes the n_z^+ over the n_z. For $n_i = n_z$,

$$0 = -T\log\frac{n_z - n_z^+}{n_z^+} + 2f.$$

From that equation follows

$$n_z = n_z^+(1 + \exp\frac{2f}{T}).$$

So the constraint of total particle number is

$$\begin{aligned}N &= dn_x + n_z\\ &= d\exp\left[-\frac{f}{T} + \log(n_z - n_z^+) + \log 2\right] + n_z^+(1 + \exp\frac{2f}{T}),\end{aligned}$$

where $n_z - n_z^+ = n_z^+ e^{2f/T}$ so

$$\begin{aligned}N &= d\exp\left[-\frac{f}{T} + \log n_z^+ + \frac{2f}{T} + \log 2\right] + n_z^+(1 + e^{2f/T})\\ &= 2dn_z^+ e^{f/T} + n_z^+(1 + e^{2f/T})\\ &= n_z^+ e^{f/T}(2d + e^{-f/T} + e^{f/T}).\end{aligned}$$

From this we find

$$n_z^+ = N\frac{e^{-f/T}}{2d + e^{-f/T} + e^{f/T}},$$

so

$$\begin{aligned} L &= 2n_z^+ - n_z \\ &= n_z^+ + (n_z^+ - n_z) \\ &= n_z^+ - (n_z - n_z^+) \\ &= n_z^+(1 - e^{2f/T}) \\ &= N\frac{e^{-f/T}}{2d + e^{-f/T} + e^{f/T}}(1 - e^{2f/T}) \\ &= N\frac{e^{-f/T} - e^{f/T}}{2d + e^{-f/T} + e^{f/T}} \\ &= N\frac{-2\sinh(f/T)}{2d + 2\cosh(f/T)}. \end{aligned}$$

In sum, we find

$$\frac{L}{N} = -\frac{\sinh(f/T)}{d + \cosh(f/T)},$$

or

$$\frac{|L|}{N} = \frac{\sinh \tilde{f}}{d + \cosh \tilde{f}}, \tag{D.1}$$

where $\tilde{f} = |f|/T$.

Check of Theory with Simulations

We now compare equation (D.1) with simulation data. We simulated self-avoiding linear polymers of various lengths (Figure D.1). The self-avoiding and random walks are not in the same universality class, with linear response of random polymers scaling as $f \sim \langle R \rangle / N^{1/2}$ and for self-avoiding polymers as $f \sim \langle R \rangle / N^{0.588}$ (section 7.1). At small extensions, we therefore expect that steric effects could violate equation (D.1). For larger extensions, polymer crossings will be much less frequent, so the agreement with equation (D.1) should gradually improve for larger forces. Indeed, we find that equation (D.1) holds well under large forces, but breaks down at $f \to 0$ (Figure D.1).

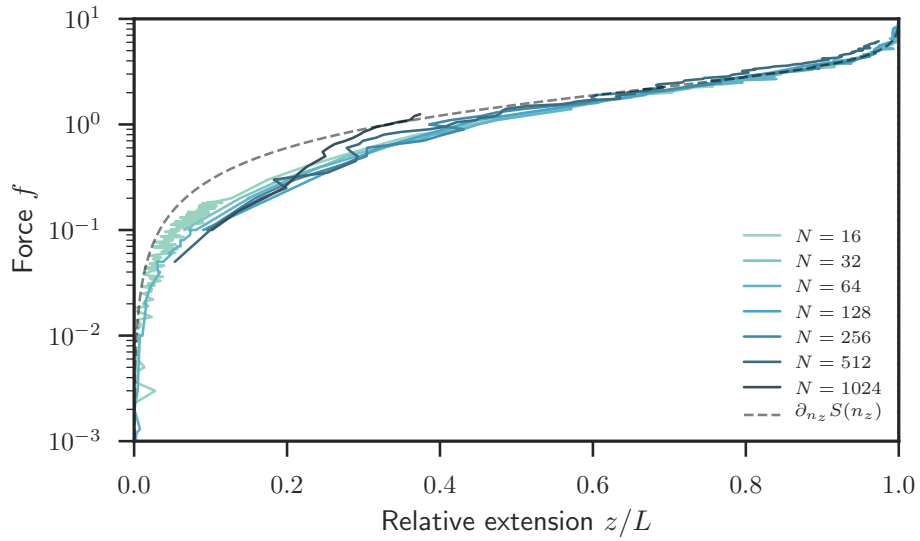

Figure D.1: **Force-extension curve appears to match with theory.** Linear self-avoiding polymers of various lengths were simulated and compared with the theoretical result (equation (D.1)). The fit is excellent for large forces, at which steric effects no longer play a role. The fit is poor at low forces, which is to be expected since steric effects play an important role there.

D.2 Binding Isotherm of Non-Interacting, Repulsive Particles

To test the validity of sampling of the grand canonical ensemble in our simulations, we simulated random binding events of particles without any binding patches to a polymer. To make the test as realistic as possible, we turned on both polymer and protein Monte-Carlo moves. Since there is no protein-protein interaction (except for steric interactions), we can factorize the partition function Z over all binding sites on the polymer. The single-particle partition function is $Z_1 = \sum_{\phi=0,1} \exp(\beta\mu\phi) = 1 + e^{\beta\mu}$. The average occupation is therefore $\langle\phi\rangle = \sum_\phi \phi p(\phi)/Z = e^{\beta\mu}/(1 + e^{\beta\mu}) = 1/(1 + e^{-\beta\mu})$, which is simply the Fermi-Dirac distribution—as it should be, since sterically repelling particles are fermions. Similarly, we can compute the standard deviation of $p(\phi)$, $\sqrt{\mathrm{var}[\phi]}$ which is $\sqrt{\phi(1-\phi)/N}$ (this can easily be seen from again a mean-field description, which is exact since Z factorizes).

The theoretical prediction for the mean and standard deviation of the particle occupation matches perfectly with the data (Figure D.2).

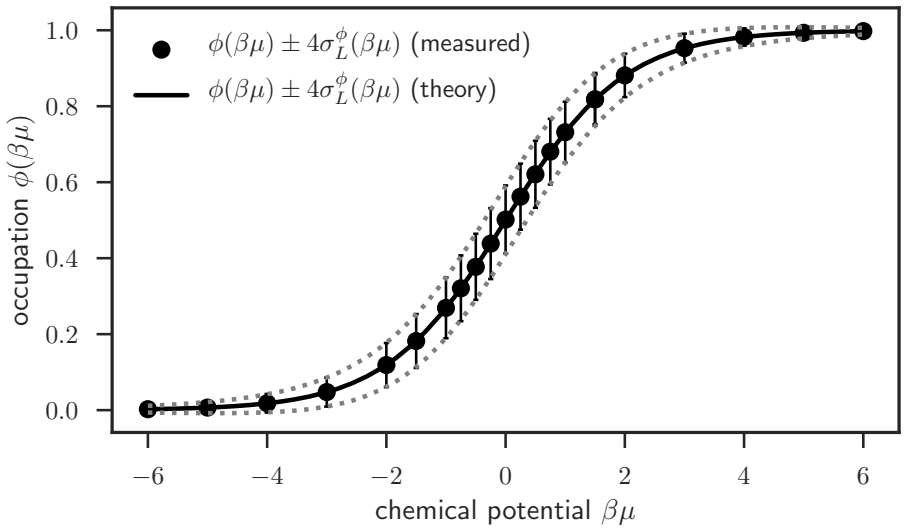

Figure D.2: **The binding probability of sterically interacting particles matches with theory**. Shown is the fractional occupation on a polymer for various chemical potentials in a grand canonical simulation. Polymer size $N = 500$. Gray lines: four times the theoretical standard deviation agree perfectly with the measured value (error bars).

D.3 Binding Isotherm of Particles with Spreading Interactions

Now that we have established that sterically repelling particles have the expected binding probability across different chemical potentials, we also verify that spreading bonds have the appropriate effect on the binding probability. To compute the theoretical binding curve, we utilize the fact that the one-dimensional spreading bonds can be formally mapped to the one-dimensional Ising model, which has an exact solution. The free energy for the one-dimensional Ising model is $\beta f \approx -\log \lambda_+$, where $\lambda_+ = e^K \cosh B + \sqrt{(e^K \sinh B)^2 + (e^{-}K)^2}$, where $K = \frac{1}{4}J, B = \frac{1}{2}J + \frac{1}{2}\mu$ with σ_i a spin-like variable. The magnetization $m = \langle \sigma_i \rangle$ is found by using $m = -\partial_B f$ and then plugging this value for m into $\phi = \frac{1}{2}(\sigma_i + 1)$.

We tested agreement with the one-dimensional Ising model in two ways: (i) by setting the bridging bonds to 'phantom bonds' with $J_B = 0$ and (ii) by setting the number of bond patches to zero. For (i), the presence of these phantom bonds should only contributes a constant addition to the free energy, equal to the entropy contained in the number of possible bond path rotations. Indeed, we find that the phantom bridging bonds and absence of bonds have an identical binding curve (Figure D.3, gray vs. black markers). Moreover, we find excellent agreement between the data for ϕ and the analytical result from the one-dimensional Ising model (Figure D.3).

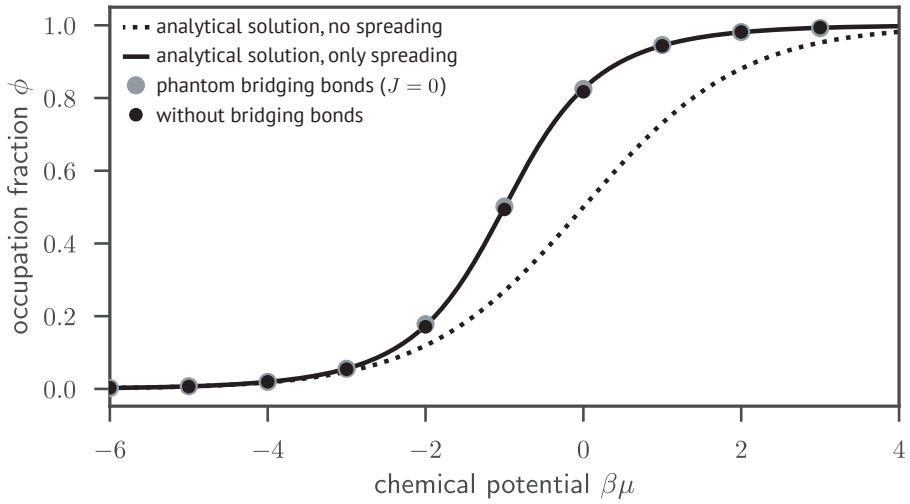

Figure D.3: **The binding probability of spreading particles matches with theory**. Shown is the fractional occupation of particles that can have spreading interactions ($J_S = -1$) and either $q_B = 4$ phantom bridging bonds with zero binding energy $J_B = 0$ (gray) or no bridging bonds at all (black). Both datasets match extremely well with the theory from the one-dimensional Ising model (black curve).

D.4 Binding Isotherm of Particles with Bridging Interactions

To test the validity of bridging interactiions, immobilized polymers were prepared in the form of a 'harmonica', forming a square plane. We assume that $\mu \gg k_B T$, so that there is at most one particle not bound to the polymer. Thus, we ignore collective effects, greatly simplifying the problem. The partition function of this system is $Z = \sum_\phi \exp(-\beta H), \phi = 0, 1$ and $H = \phi \cdot (-\beta\mu + \beta z J)$ (z: coordination number) so that $Z = 1 + \exp(\beta\mu - \beta z J)$ with binding probability $p(\phi) = \exp(\beta\mu - \beta z J)^\phi / Z$. Thus, the first two moments are found to be

$$\langle \phi \rangle = \frac{1}{1 + \exp(-\beta\mu + \beta z J)} \tag{D.2}$$

and $\langle \phi^2 \rangle = \sum_\phi \phi^2 p(\phi) = \sum_\phi \phi p(\phi) = \langle \phi \rangle$. The result $\langle \phi^2 \rangle = \langle \phi \rangle$ is a hallmark of Poisson distributed random variables. The single-site standard deviation is then

$$\sigma_\phi = \langle \phi^2 \rangle - \langle \phi \rangle^2 = \langle \phi \rangle (1 - \langle \phi \rangle).$$

The single-site statistics will be noisy, because we assumed that at most one hole is present across the whole polymer. We therefore collect statistics on the hole probability *averaged* over the whole polymer. However, the standard deviation in the average hole probability over a sheath of size N follows a different distribution. In particular, if the individual sites are i.i.d. random variables (a good approximation in the limit of dilute holes $1 - \langle \phi \rangle \to 0$), then the central-limit-theorem dictactes that the expected standard deviation is reduced by a factor $1/\sqrt{N}$. Indeed, we find that this mean-field estimate of the standard deviation closely matches the experimentally observed data (Figure D.4).

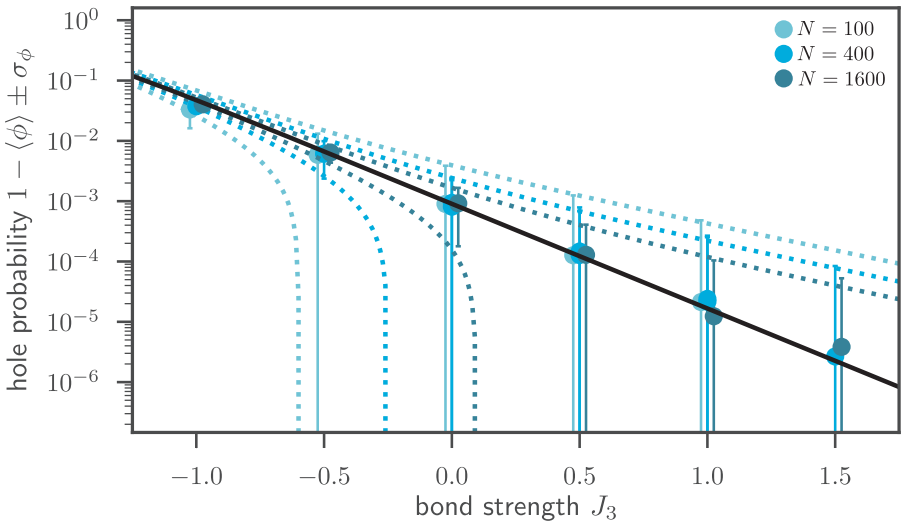

Figure D.4: **Bridging bonds display the correct statistics, as inferred from the hole probability for varying bridging strength.** Shown are data from the whole-polymer hole probability ϕ for various bridging bond strengths J_3 on an immobilized polymer. Black: analytical estimate of $\langle\phi\rangle$ from the partition function (equation (D.2)); dashed lines, analytical estimate of σ_ϕ. Datapoints are slightly shifted horizontally for visual clarity.

D.5 Internal Scaling of Globular Polymer

We now test the ability of our simulation to capture the internal scaling of a self-avoiding globular polymer. Most Monte-Carlo moves will be rejected in such a dense, globular phase, so the previous controls we have performed do not guarantee the validity of scaling in the globular phase.

We generated polymers with a protein coverage of $c = 0.5$ and varying system size N and full valency ($q_1 = 2, q_3 = 4$) with interaction parameters below the phase boundary ($J_1 = J_3 = -2$). We then extracted all protein clusters from the data by first constructing a graph of the protein bonds, and then partitioning these into subgraphs (a subgraph is called a "cluster"). We then analyzed the relation between the distance Δ between two nodes i, j in all subgraphs $\Delta = |i - j|$ and the mean Euclidean distance between these two proteins R_{ij}. The should have an initial slope of $\sim \Delta^{1/2}$ [74], which it does, and should saturate at the largest possible distance for a Euclidean object $R^* \sim N^{1/3}$. The saturation at $\Delta = \Delta^*$ should kick in once the sub-chain of size Δ has typically traversed a distance R^*, which is according to our scaling at $R^* \approx \ell(\Delta^*)^{1/2}$ or $\Delta^* \sim (R^*)^2$. We indeed observe these scalings (Figure D.5).

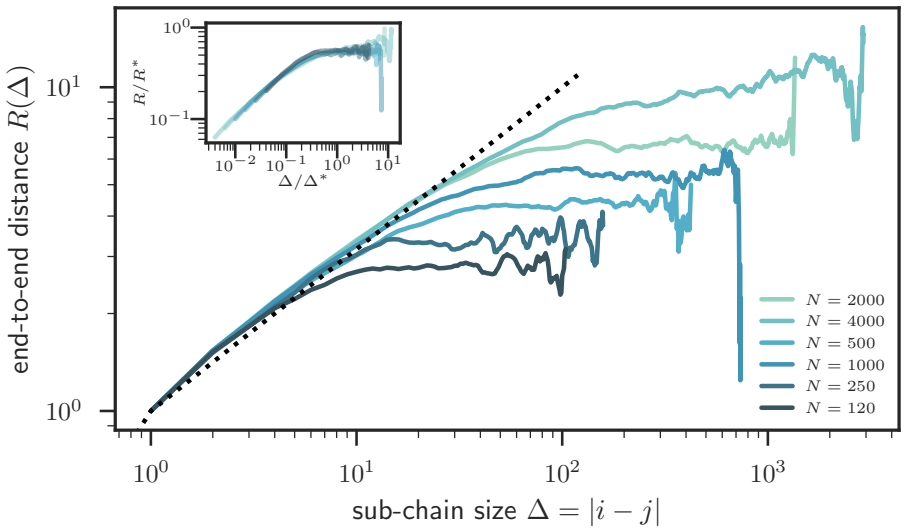

Figure D.5: **Internal scaling of globular polymers follows the expected dependency on system-size and sub-chain size.** Shown are end-to-end distances of various sub-chains (size Δ) inside a globular polymer for various total system-sizes N. Data collapse (inset) using $R^* \sim N^{1/3}, \Delta^* \sim (R^*)^2$.

Bibliography

[47] Elnaz Alipour and John F Marko. Self-organization of domain structures by DNA-loop-extruding enzymes. *Nucleic acids research*, 40(22):11202–12, dec 2012. ISSN 1362-4962.

[48] Tadashi Ando and Jeffrey Skolnick. Crowding and hydrodynamic interactions likely dominate in vivo macromolecular motion. *Proceedings of the National Academy of Sciences of the United States of America*, 107(43):18457–62, oct 2010. ISSN 1091-6490.

[49] S Bicknese, N Periasamy, S B Shohet, and A S Verkman. Cytoplasmic Viscosity Near the Cell Plasma Membrane: Measurement by Evanescent Field Frequency-Domain Microfluorimetry. *Biophysical Journal Volume*, 65:1272–1282, 1993.

[50] C A Brackley, J Johnson, D Michieletto, and D Marenduzzo. Effect of chromatin flexibility on diffusive loop extrusion via molecular slip-links. *bioRxiv*, page 275214, 2018.

[51] C. A. Brackley, J. Johnson, D. Michieletto, A. N. Morozov, M. Nicodemi, P. R. Cook, and D. Marenduzzo. Extrusion without a motor: a new take on the loop extrusion model of genome organization. *Nucleus*, 9(1):95–103, jan 2018. ISSN 1949-1034.

[52] Chris A Brackley, James Johnson, Davide Michieletto, Alexander N Morozov, Mario Nicodemi, Peter R Cook, and Davide Marenduzzo. Non-equilibrium chromosome looping via molecular slip-links. *Physical Review Letters*, 119(13):138101, 2017.

[53] Hugo B Brandão, Payel Paul, Aafke A van den Berg, David Z Rudner, Xindan Wang, and Leonid A Mirny. RNA polymerases as moving barriers to condensin loop extrusion. *Proceedings of the National Academy of Sciences of the United States of America*, 116(41):20489–20499, oct 2019. ISSN 1091-6490.

[54] C. P. Broedersz, X. Wang, Y. Meir, J. J. Loparo, D. Z. Rudner, and N. S. Wingreen. Condensation and localization of the partitioning protein ParB on the bacterial chromosome. *Proceedings of the National Academy of Sciences*, 111(24):8809–8814, jun 2014. ISSN 0027-8424.

[55] Frank Bürmann, Alrun Basfeld, Roberto Vazquez Nunez, Marie-Laure Diebold-Durand, Larissa Wilhelm, and Stephan Gruber. Tuned SMC Arms Drive Chromosomal Loading of Prokaryotic Condensin. *Molecular Cell*, 65(5):861–872.e9, mar 2017. ISSN 10972765.

[56] Bo-Wei Chen, Ming-Hsing Lin, Chen-Hsi Chu, Chia-En Hsu, and Yuh-Ju Sun. Insights into ParB spreading from the complex structure of Spo0J and parS Data deposition: The atomic coordinates and structure factors have been deposited in the Protein Data Bank, www.pdb.org (PDB ID code 4UMK). *PNAS*, 112(21):6613–6618, 2015.

[57] Pierre-Gilles de. Gennes. *Scaling concepts in polymer physics*. Cornell University Press, 1979. ISBN 080141203X.

[58] Marie-Laure Diebold-Durand, Hansol Lee, Laura B. Ruiz Avila, Haemin Noh, Ho-Chul Shin, Haeri Im, Florian P. Bock, Frank Bürmann, Alexandre Durand, Alrun Basfeld, Sihyun Ham, Jérôme Basquin, Byung-Ha Oh, and Stephan Gruber. Structure of Full-Length SMC and Rearrangements Required for Chromosome Organization. *Molecular Cell*, 67(2):334–347.e5, jul 2017. ISSN 10972765.

[59] M. Doi and S. F. Edwards. *The Theory of Polymer Dynamics*. Clarendon Press, Oxford, 1986.

[60] Jorine M. Eeftens, Allard J. Katan, Marc Kschonsak, Markus Hassler, Liza de Wilde, Essam M. Dief, Christian H. Haering, and Cees Dekker. Condensin Smc2-Smc4 Dimers Are Flexible and Dynamic. *Cell Reports*, 14(8):1813–1818, 2016. ISSN 22111247.

[61] Jorine M Eeftens, Shveta Bisht, Jacob Kerssemakers, Christian H Haering, and Cees Dekker. Real-time detection of condensin-driven DNA compaction reveals a multistep binding mechanism. *bioRxiv*, 2017.

[62] Gemma L M Fisher, César L Pastrana, Victoria A Higman, Alan Koh, James A Taylor, Annika Butterer, Timothy D Craggs, Frank Sobott, Heath Murray, Matthew P Crump, Fernando Moreno-Herrero, and Mark S Dillingham. The C-terminal domain of ParB is critical for dynamic DNA binding and bridging interactions which condense the bacterial centromere. .

[63] Geoffrey Fudenberg, Maxim Imakaev, Carolyn Lu, Anton Goloborodko, Nezar Abdennur, and LeonidÂ A. Mirny. Formation of Chromosomal Domains by Loop Extrusion. *Cell Reports*, 15(9):2038–2049, 2016. ISSN 22111247.

[64] Mahipal Ganji, Indra A Shaltiel, Shveta Bisht, Eugene Kim, Ana Kalichava, Christian H Haering, and Cees Dekker. Real-time imaging of DNA loop extrusion by condensin. *Science*, 360(6384):102–105, feb 2018. ISSN 1095-9203.

[65] Anton Goloborodko, Maxim V Imakaev, John F Marko, and Leonid Mirny. Compaction and segregation of sister chromatids via active loop extrusion. *eLife*, 5, may 2016. ISSN 2050-084X.

[66] Anton Goloborodko, John F Marko, and Leonid A Mirny. Chromosome Compaction by Active Loop Extrusion. *Biophysical Journal*, 110, 2016.

[67] Thomas G W Graham, Xindan Wang, Dan Song, Candice M Etson, Antoine M van Oijen, David Z Rudner, and Joseph J Loparo. ParB spreading requires DNA bridging. *Genes & Development*, 28(11):1228–38, jun 2014. ISSN 1549-5477.

[68] Stephan Gruber and Jeff Errington. Recruitment of condensin to replication origin regions by ParB/SpoOJ promotes chromosome segregation in B. subtilis. *Cell*, 137(4):685–96, may 2009. ISSN 1097-4172.

[69] Stephan Gruber, Jan-Willem Veening, Juri Bach, Martin Blettinger, Marc Bramkamp, and Jeff Errington. Interlinked Sister Chromosomes Arise in the Absence of Condensin during Fast Replication in B. subtilis. *Current Biology*, 24:293–298, 2014.

[70] Adam S. B. Jalal, Ngat T. Tran, and Tung B. K. Le. ParB spreading on DNA requires cytidine triphosphate in vitro. *bioRxiv*, page 2019.12.11.865972, dec 2019.

[71] Eugene Kim, Jacob Kerssemakers, Indra A. Shaltiel, Christian H. Haering, and Cees Dekker. DNA-loop extruding condensin complexes can traverse one another. *bioRxiv*, page 682864, jun 2019.

[72] HyeongJun Kim and Joseph J. Loparo. Multistep assembly of DNA condensation clusters by SMC. *Nature Communications*, 7:10200, jan 2016. ISSN 2041-1723.

[73] Tung B K Le, Maxim V Imakaev, Leonid A Mirny, and Michael T Laub. High-Resolution Mapping of the Spatial Organization of a Bacterial Chromosome. *Science*, 342(6159):731–734, nov 2013. ISSN 0036-8075.

[74] Erez Lieberman-Aiden, Nynke L van Berkum, Louise Williams, Maxim Imakaev, Tobias Ragoczy, Agnes Telling, Ido Amit, Bryan R Lajoie, Peter J Sabo, Michael O Dorschner, Richard Sandstrom, Bradley Bernstein, M A Bender, Mark Groudine, Andreas Gnirke, John Stamatoyannopoulos, Leonid A Mirny, Eric S Lander, and Job Dekker. Comprehensive mapping of long-range interactions reveals folding principles of the human genome. *Science (New York, N.Y.)*, 326(5950):289–93, oct 2009. ISSN 1095-9203.

[75] Anita Minnen, Frank Bürmann, Larissa Wilhelm, Anna Anchimiuk, Marie-Laure Diebold-Durand, and Stephan Grüber. Control of Smc Coiled Coil Architecture by the ATPase Heads Facilitates Targeting to Chromosomal ParB/parS and Release onto Flanking DNA. *Cell Reports*, 14, 2016.

[76] Uri Moran, Rob Phillips, and Ron Milo. SnapShot: Key Numbers in Biology. *Cell*, 141:1262–1262, 2010.

[77] Michael Rubinstein and Ralph H. Colby. *Polymer Physics*. Oxford University Press, 2003.

[78] SB Smith, L Finzi, and C Bustamante. Direct mechanical measurements of the elasticity of single DNA molecules by using magnetic beads. *Science*, 258(5085), 1992.

[79] Young-Min Soh, Frank Bürmann, Ho-Chul Shin, Takashi Oda, Kyeong Sik Jin, Christopher P. Toseland, Cheolhee Kim, Hansol Lee, Soo Jin Kim, Min-Seok Kong, Marie-Laure Durand-Diebold, Yeon-Gil Kim, Ho Min Kim, Nam Ki Lee, Mamoru Sato, Byung-Ha Oh, and Stephan Gruber. Molecular Basis for SMC Rod Formation and Its Dissolution upon DNA Binding. *Molecular Cell*, 57(2):290–303, 2015. ISSN 10972765.

[80] Dan Song, Kristen Rodrigues, Thomas GW Graham, Joseph J Loparo, and Harvard A John. A network of cis and trans interactions is required for ParB spreading. *Nucleic Acids Research*, 45(12):7106–7117, 2017.

[81] Johannes Stigler, Gamze Ç Amdere, Douglas E Koshland, and Eric C Greene. Single-Molecule Imaging Reveals a Collapsed Conformational State for DNA-Bound Cohesin. *Cell Reports*, 15:988–998, 2016.

[82] Tsuyoshi Terekawa, Shveta Bisht, Jorine Eeftens, Cees Dekker, Christian Haering, and Eric Greene. The Condensin Complex Is A Mechanochemical Motor That Translocates Along DNA. *Science*, 358(6363):672–676, 2017.

[83] J Tothova, B Brutovsky, and V Lisy. Monomer motion in single-and double-stranded DNA coils.

[84] Georgia Tsolou, Nikos Stratikis, Chunggi Baig, Pavlos S. Stephanou, and Vlasis G. Mavrantzas. Melt Structure and Dynamics of Unentangled Polyethylene Rings: Rouse Theory, Atomistic Molecular Dynamics Simulation, and Comparison with the Linear Analogues. *Macromolecules*, 43 (24):10692–10713, dec 2010. ISSN 0024-9297.

[85] Xindan Wang, Paula Montero Llopis, and David Z Rudner. Organization and segregation of bacterial chromosomes. *Nature Reviews Genetics*, 14: 191–203, 2013.

[86] Xindan Wang, Tung B K Le, Bryan R. Lajoie, Job Dekker, Michael T. Laub, and David Z. Rudner. Condensin promotes the juxtaposition of dna flanking its loading site in Bacillus subtilis. *Genes and Development*, 29(15):1661–1675, 2015. ISSN 15495477.

[87] Xindan Wang, Hugo B. Brandão, Tung B. K. Le, Michael T. Laub, and David Z. Rudner. Bacillus subtilis SMC complexes juxtapose chromosome arms as they travel from origin to terminus. *Science*, 355(6324), 2017.

[88] Xindan Wang, Anna C. Hughes, Hugo B. Brandão, Benjamin Walker, Carrie Lierz, Jared C. Cochran, Martha G. Oakley, Andrew C. Kruse, and David Z. Rudner. In Vivo Evidence for ATPase-Dependent DNA Translocation by the Bacillus subtilis SMC Condensin Complex. *Molecular Cell*, 71(5):841–847.e5, sep 2018. ISSN 1097-2765.

[89] Xindan Wang, Olive W. Tang, Eammon P. Riley, and David Z. Rudner. The SMC Condensin Complex Is Required for Origin Segregation in Bacillus subtilis. *Current Biology*, 24(3):287–292, apr 2018. ISSN 0960-9822.

[90] Hiroshi Watanabe, Inoue Tadashi, and Yumi Matsumiya. Transient Conformational Change of Bead–Spring Ring Chain during Creep Process. *Macromolecules*, 39(16):5419—-5426, 2006.

[91] Larissa Wilhelm, Frank Bürmann, Anita Minnen, Ho-Chul Shin, Christopher P Toseland, Byung-Ha Oh, Stephan Gruber, E. Alipour, JF. Marko, P. Arumugam, and S. Gruber. SMC condensin entraps chromosomal DNA by an ATP hydrolysis dependent loading mechanism in Bacillus subtilis. *eLife*, 4:11202–11212, may 2015. ISSN 2050-084X.

[92] Pawel Zawadzki, Mathew Stracy, Katarzyna Ginda, Katarzyna Zawadzka, Christian Lesterlin, Achillefs N. Kapanidis, and David J. Sherratt. The Localization and Action of Topoisomerase IV in Escherichia coli Chromosome Segregation Is Coordinated by the SMC Complex, MukBEF. *Cell Reports*, 13(11):2587–2596, dec 2015. ISSN 22111247.